Numerieke en experimentele modellering van overvloeipluimen in de nabijheid van het baggertuig

Numerical and Experimental Modelling of Near-Field Overflow Dredging Plumes

Boudewijn Decrop

Promotoren: prof. dr. ir. T. De Mulder, prof. dr. ir. E. Toorman
Proefschrift ingediend tot het behalen van de graden van
Doctor in de Ingenieurswetenschappen (Universiteit Gent) en
Doctor in de Ingenieurswetenschappen (Katholieke Universiteit Leuven)

Vakgroep Civiele Techniek
Voorzitter: prof. dr. ir. P. Troch
Faculteit Ingenieurswetenschappen en Architectuur

UNIVERSITEIT GENT

Departement Burgerlijke Bouwkunde
Voorzitter: prof. dr. ir. G. Degrande
Faculteit Ingenieurswetenschappen

KU LEUVEN

Academiejaar 2015 - 2016

ISBN 978-90-8578-823-2
NUR 956
Wettelijk depot: D/2015/10.500/67

Numerical and Experimental Modelling of Near-Field Overflow Dredging Plumes

by

Boudewijn Decrop

Composition of the Examination Committee:

prof. dr. ir. T. De Mulder (promotor, UGent)
prof. dr. ir. E.A. Toorman (promotor, KULeuven)
prof. dr. ir. L. Taerwe (co-chairman, UGent)
prof. dr. ir. P. Van Houtte (co-chairman, KULeuven)
prof. dr. ir. J. Berlamont (KULeuven)
prof. dr. ir. J.H. Jensen (DHI)
prof. dr. ir. J. Meyers (reading committee, KULeuven)
ir. M. Sas (assessor, IMDC)
prof. dr. ir. P. Troch (assessor, UGent)
prof. dr. ir. C. van Rhee (reading committee, TU Delft)
prof. dr. ir. J. Vierendeels (reading committee, UGent)

The research presented in this Ph.D. thesis has been funded by the Agency for Innovation by Science and Technology (IWT) and by International Marine and Dredging Consultants (IMDC).

Abstract

Throughout modern history, the interference of human developments with the natural environment has ever increased. This can be largely associated with an exponential population increase, the growth of the world's economy and technological development. In the early stages of the industrial development, efforts concentrated on the increase of productivity and living standards. In more recent times, developed countries have reached a stage in which the accumulated technological aids and wealth have lead to an increased availability of time and resources for environmental awareness.

In this light, the attention for environmental aspects of dredging projects has increased and regulations have become increasingly stringent in the past decades. Nowadays, governments, owners and contractors are cooperating to execute projects in a way that adverse effects to the natural environment are maximally avoided. More specifically, the potential increase of turbidity during dredging projects - and the ways to avoid it - are the topic of this research. Turbid sediment plumes can cause adverse effects to the natural environment when reaching sensitive areas such as coral reefs, sea grass fields and intertidal areas. One of the main sources of turbidity during fairway deepening, land reclamation or minerals mining is the overflowing of excess water from Trailing Suction Hopper Dredgers. In the recent past, the use of this type of dredger has been on the rise, for example due the well-known developments of artificial islands and land reclamation in the Middle-East and Asia.

In order to minimise environmental impacts of turbidity, from the early stages of planning until the project execution, turbidity prediction tools are necessary. In this way, the production methods, project site organisation and the planning of works can be optimised in advance to achieve a minimum generation of turbidity. To this end, numerical models are the most effective tools in the prediction of the sea currents and sediment dispersion (on the scale of coastal regions or an estuary). Neither simulation models at this scale,

nor the behaviour of the sludge in the hopper of the dredger are the subject of this study, but the near-field plume dynamics below and directly behind the sailing hopper dredgers is. This near-field dynamics has been a source of uncertainty in the far-field predictions. Accurate input of the vertical and horizontal distributions of sediment at the source location are paramount to obtain reliable prediction results at the environmentally sensitive areas further away. In this research, physical and numerical modelling are used as a tool to determine the three-dimensional flows of water, sediment and air bubbles directly after release from the overflow shaft.

In a first stage, laboratory experiments with dynamically scaled sediment plumes have been investigated, including the influence of a schematised ship hull and air bubbles. In order to capture turbulent properties of the water-sediment mixture, a new processing technique was developed for Acoustic Doppler Velocimeter (ADV) data. This processing technique corrects for high-frequency noise in the signals of velocity and sediment concentration. In this way the turbulent fluctuations of sediment concentration and the turbulent fluxes of sediment could be measured.

It was shown in the experiments that a fine sediment plume behaves in a very similar way to a buoyant jet. It was also shown that both the stern section of a ship hull and air bubbles can strip off part of the plume, to form a secondary plume near the surface. The set of experiments resulted in a large data set against which the results of the numerical models can be compared.

In a second stage, a highly detailed, three-dimensional mathematical model has been built in different steps of increasing complexity. As a starting point, a numerical model of the simplified geometry of the laboratory experiments was set up. Using this geometry, first a vertical sediment plume without crossflow was simulated and compared with the experimental results. Afterwards, crossflow was added and the results were again compared to experimental results. Subsequently, the same was done after adding a schematised dredging vessel hull. The plume trajectory as well as the turbulent structures in the flow field were reproduced accurately by the model. Additionally, the model performance was evaluated by comparing the simulation results with experimental data drawn from the literature. It was shown that the model could reproduce time averaged and turbulent characteristics of cases with buoyant jets in crossflow, air bubble plumes in a crossflow and a wall-impinging sediment-laden jet.

In a third stage, the laboratory-scale model was resized to the scale of se-

diment plumes released by hopper dredgers, i.e. the prototype scale. The Reynolds number-independence of the plume trajectories was therefore investigated. It was found that with a similar number of computational cells, the trajectories of plumes a factor 100 larger were equivalent to the small-scale plumes. In a next step, a real-life hopper dredger geometry was implemented in the model, as well as two propellers. The propellers were implemented using the actuator disk method. The simulated decay of the axial and tangential velocity components in the propeller jet have been validated against experimental data drawn from literature.

In order to allow a validation of this prototype-scale simulation model, a campaign has been organised to obtain field measurement data. Using a survey boat, monitoring instruments were lowered in the water column while sailing behind a Trailing Suction Hopper Dredger at work. The most interesting data gathered consisted of detailed vertical profiles of the sediment concentration using the SiltProfiler instrument, taken from the water surface down to the last few centimetres above the sea bed. In this way, not only the plume in the central part of the water column was monitored, but also the sediment concentration in a density current near the sea bed was recorded. It was also found that when using acoustic profilers (ADCP) for dredging plumes, it is often hard to distinguish between air bubble plumes and sediment plumes.

In order to compare the data set of the field measurements, simulations with exactly the same boundary conditions have to be set up. To this end, also the sediment loading in the overflow shaft was measured onboard the dredging vessel. The detailed data set was then used to compare a number of plume cases with the simulation results. It was found that - notwithstanding the complexity of the flows - the numerical simulation results compared well with the observed data.

A number of additional applications of the model were undertaken. It could be confirmed that an extension of the overflow shaft below the keel has the potential to reduce surface concentrations, but more research is needed to conclude on this matter.

Further, it was found that a rectangular cross section of overflow shaft also reduces the surface plume concentrations. The efficiency of the environmental valve was investigated in detail. It was found that the valve is very efficient in many cases, but that under a number of conditions, the efficiency drops to very low values.

Subsequently, the developed model has been utilised to investigate the behaviour of the near-field overflow plume in a range of conditions. A large number of simulations has been carried out in which only one boundary condition or overflow configuration aspect was altered at a time. This has lead to a wealth of insights in the influencing factors on near-field overflow plume behaviour. Some observations found in the model results were expected, such as the increase in surface plume turbidity due to higher sailing (or current) speed and the presence of air bubbles. Other observations were revealing new insights such as a reduction in surface concentrations due to a more concentrated overflow mixture at the same volume discharge. Overflows located near the stern of the vessel or located away from the axis of the hull are also found to have an adverse effect on overflow concentration in some cases.

The non-linear interaction between the different boundary conditions makes that a simple regression analysis in which one parameter is analysed at a time does not lead to the correct relationships. The degree of correlation between one boundary condition and the behaviour of the plume is indeed a function of one or more other boundary conditions. This leads to the fourth and last step in the presented developments.

In the last step, a simplified grey-box model was developed. In order to fit the parameters in this model, a large set of numerical simulations was carried out in which the boundary conditions, overflow positions, water depths, dredging speeds, sediment concentration, air bubbles and number of overflows were varied. The model uses both theoretical plume solutions and multivariate regression analysis. In a holistic approach, the complete data set of numerical model sediment concentration fields was fed in a grey-box model training algorithm in which the non-linear interactions between the multitude of influence factors is represented. Despite its simplicity and speed, it was demonstrated that the grey-box model can still predict the vertical distribution of the plume sediment flux in a relatively accurate way.

The goal of this research is to improve the predictions of dredging-induced turbidity in both the planning and execution phases of a dredging project. To improve the predictions of the model on the scale of an estuary or coastal region, more accurate predictions of the source terms are needed. This is achieved with the near-field models developed in this study. In the planning phase, time is available to perform detailed numerical simulations of specific field conditions. This can now be achieved with the three-dimensional model developed in this research. In the project execution phase, it is important to perform real-time predictions of the fate of the plumes being generated

day-by-day. To make forecasts of the plume dispersion, the daily planning of dredging production must be incorporated on a daily basis. The marine conditions may vary with time scales less than one hour. At this stage, no time is available for extensive numerical simulations of the near-field behaviour. For this purpose, the grey-box model is developed, which can be implemented as an internal module in the large-scale modelling software.

Samenvatting

Doorheen de moderne geschiedenis is de interferentie van de menselijke ontwikkelingen met de natuurlijke omgeving enkel toegenomen. Dit kan grotendeels worden geassocieerd met een exponentiële toename van de bevolking, de groei van de wereldeconomie en de technologische vooruitgang. In het begin van de industriële revolutie was men voornamelijk begaan met de verhoging van de productiviteit en de levensstandaard. In het meer nabije verleden, zijn de ontwikkelde landen in een fase gekomen waarin de geaccumuleerde technologische hulpmiddelen en de welvaart hebben geleid tot een grotere beschikbaarheid van tijd en middelen voor het ontwikkelen van een milieubewustzijn.

Ook de aandacht voor milieuaspecten van baggerprojecten is hierdoor toegenomen, terwijl de regelgeving steeds strenger werd in de afgelopen decennia. Tegenwoordig werken overheden, projectontwikkelaars en aannemers samen om projecten uit te voeren op een manier waarop negatieve milieueffecten maximaal worden vermeden. Meer in het bijzonder de potentiële toename van de troebelheid van het zeewater tijdens baggerprojecten - en de manieren om dit te vermijden - zijn het onderwerp van dit onderzoek. Troebele sedimentpluimen kunnen nadelige effecten op het milieu veroorzaken wanneer deze gevoelige gebieden bereiken zoals bijvoorbeeld koraalriffen, zeegrasvelden en intergetijdegebieden. Eén van de belangrijkste bronnen van troebelheid tijdens het verdiepen van vaargeulen, landwinning of zandwinning is het afvoeren van overtollig water uit sleephopperzuigers via een overvloei. Het gebruik van dit type baggerschip is sterk toegenomen in het recente verleden, bijvoorbeeld bij de bekende voorbeelden van de aanleg van kunstmatige eilanden en landwinning in het Midden-Oosten en Azië.

Om de milieueffecten van troebelheid te beperken worden van in een vroeg stadium van de planning tot bij de uitvoering van het project voorspellingsmodellen gebruikt. Op deze wijze kunnen de productiemiddelen, de ruimtelijke organisatie en de planning van de werken worden geoptimaliseerd

teneinde een minimale hoeveelheid troebelheid te genereren. Daartoe zijn grootschalige numerieke modellen (niveau kustregio, estuarium) het meest efficiënte alternatief, onder andere bij het voorspellen van de zeestromingen en het sediment transport. Noch modellen op deze grote schaal, noch het gedrag van de specie in beun van het baggerschip zijn echter het onderwerp van dit onderzoek, doch wel de dynamiek van de straal bij het verlaten van het schip en de pluim net achter de sleephopperzuiger. Deze dynamiek is een bron van onzekerheid in de voorspellingen op grote schaal. Nauwkeurige vertikale en horizontale verdelingen van deze brontermen voor sediment zijn van groot belang voor het bekomen van betrouwbare voorspellingen rond de ecologisch kwetsbare gebieden op grotere afstand van de werkzaamheden. In dit onderzoek werden fysische en numerieke modellen gebruikt om de driedimensionale stromen van water, sediment en luchtbellen te bepalen in de directe nabijheid van het schip.

In een eerste fase werden laboratoriumexperimenten uitgevoerd met dynamisch geschaalde sedimentpluimen, inclusief de invloed van een geschematiseerde scheepsromp en luchtbellen. Om de turbulente eigenschappen van het water-sediment mengsel te kunnen opmeten, werd een nieuwe verwerkingstechniek ontwikkeld voor gegevens uit het Acoustic Doppler Velocimeter (ADV) instrument. Deze verwerkingstechniek corrigeert hoogfrequente ruis in de signalen van snelheid en sedimentconcentratie. Hierdoor kunnen de turbulente fluctuaties van de sedimentconcentratie en de turbulente flux van sediment worden bepaald.

De experimenten toonden onder andere aan dat een pluim bestaande uit fijne sedimenten zich in de nabijheid van het lozingspunt op een gelijkaardige manier gedraagt als een pluim bestaande uit een vloeistof die zwaarder is dan haar omgeving. Ook werd aangetoond dat zowel de achtersteven van een scheepsromp als luchtbellen een deel van de hoofdpluim kan afscheuren, en een secundaire pluim nabij het oppervlak veroorzaken. De reeks van proeven resulteerde in een grote verzameling gegevens waarmee de resultaten van de numerieke modellen kunnen worden vergeleken.

In een tweede fase werd een zeer gedetailleerd, driedimensionaal wiskundig model opgebouwd in verschillende stappen van toenemende complexiteit. Een numeriek model met de vereenvoudigde geometrie van de experimenten werd opgesteld. In een eerste stap werd een verticale sedimentpluim zonder achtergrondstroming gesimuleerd en vergeleken met de experimentele resultaten. Daarna werd achtergrondstroming toegevoegd en de resultaten werden opnieuw vergeleken met experimentele resultaten. Vervolgens werd deze pro-

cedure herhaald na het toevoegen van een geschematiseerde scheepsromp. Telkens werden de nodige bijsturingen aan het model uitgevoerd. Het traject van de pluim en de turbulente structuren in het stromingsveld bleken nauwkeurig gereproduceerd te worden door het model. Bovendien werd de kwaliteit van het model geëvalueerd door de simulatieresultaten te toetsen aan experimentele gegevens uit de literatuur.

In een derde fase werd dit model opgeschaald naar de afmetingen van sedimentpluimen van sleephopperzuigers, de prototypeschaal. Daarom werd onderzocht of de nauwkeurigheid van de gesimuleerde pluimtrajecten onafhankelijk is van het Reynoldsgetal. Uit de resultaten bleken de gesimuleerde trajecten van pluimen op prototypeschaal equivalent te zijn aan de experimentele pluimen. In een volgende stap werd een realistische geometrie van een sleephopperzuiger geïmplementeerd in het model, evenals de twee schroeven. Het gesimuleerde verval van de axiale en tangentiële snelheidscomponenten in het snelheidsveld achter de schroeven werd gevalideerd aan de hand van experimentele gegevens uit de literatuur.

Om een validatie van dit wiskundig model op prototypeschaal mogelijk te maken, werd een veldcampagne georganiseerd voor het verzamelen van meetgegevens. Met behulp van een meetvlet werden meetinstrumenten ontplooid in de pluim achter een opererende sleephopperzuiger. De meest interessante gegevens bestaan uit gedetailleerde verticale profielen van de sedimentconcentratie, gemeten met de SiltProfiler, en dit vanaf het wateroppervlak tot op enkele centimeters boven de zeebodem. Op deze wijze kon niet enkel de pluim in het centrale deel van de waterkolom worden opgemeten, maar ook de sedimentconcentratie in een dichtheidsstroom nabij de zeebodem. Tevens bleek tijdens deze veldmetingen dat bij gebruik van akoestische profilers (ADCP's) voor het opmeten van baggerpluimen, het vaak moeilijk is om een onderscheid te maken tussen luchtbellen en sedimentpluimen.

Om de dataset van de veldmetingen te kunnen vergelijken met wiskundige simulaties, moet men simulaties opzetten met precies dezelfde randvoorwaarden als tijdens de veldmetingen. Daartoe werd tevens de sedimentconcentratie in de overvloeischacht opgemeten, aan boord van het baggerschip. De gedetailleerde dataset werd vervolgens gebruikt om voor een aantal cases de vergelijking met de simulatieresultaten te maken. Er werd vastgesteld dat - niettegenstaande de complexiteit van de stromingen - de numerieke simulatieresultaten de vergelijking met de veldmetingen goed doorstonden.

Een aantal toepassingen van het numeriek model werden uitgevoerd. Er kon worden bevestigd dat een extensie van de overvloeipijp onder de kiel het potentieel heeft om de turbiditeit te verminderen. Meer onderzoek is echter noodzakelijk om te bepalen onder welke omstandigheden dit het geval is en onder welke omstandigheden niet.

Er werd tevens gevonden dat een rechthoekige vorm voor de dwarsdoorsnede van de overvloeipijp tot een lagere turbiditeit kan leiden. Daarnaast werd de efficiëntie van de milieuklep nader onderzocht. Er kon worden geconcludeerd dat deze klep in veel gevallen zeer efficiënt is, maar in een heel aantal andere omstandigheden slechts een beperkte efficiëntie heeft.

Vervolgens werd het ontwikkelde model gebruikt om het gedrag van de overvloeipluim in nabijheid van het schip onder verschillende omstandigheden te onderzoeken. Een groot aantal simulaties werd uitgevoerd waarbij telkens slechts één randvoorwaarde of overvloei-eigenschap werd gewijzigd. Dit heeft geleid tot een groot aantal inzichten in de invloedsfactoren op het gedrag van overvloeipluimen nabij het schip. Een aantal vaststellingen uit de modelresultaten werden a priori verwacht, zoals de concentratietoename in de oppervlaktepluim door hogere vaar- of stroomsnelheid en de aanwezigheid van luchtbellen. Andere vaststellingen zijn nieuwe inzichten, zoals de lagere oppervlakteconcentraties als gevolg van een meer geconcentreerd overvloeimengsel (bij hetzelfde volumedebiet). Een overvloei gelegen nabij de achtersteven van het schip of weg van het langse symmetrievlak van het schip zorgt tevens voor hogere concentraties.

De niet-lineaire interactie tussen de verschillende randvoorwaarden zorgt ervoor dat een eenvoudige regressieanalyse waarbij elke parameter apart wordt onderzocht niet tot de juiste relaties leidt. De mate waarin één randvoorwaarde een effect heeft op de pluim hangt namelijk af van één of meerdere andere randvoorwaarden. Deze vaststelling leidt tot de vierde en laatste stap in de gepresenteerde ontwikkelingen.

In de laatste stap werd een vereenvoudigd 'grey-box' model ontwikkeld. Teneinde de parameters in dit model te kunnen fitten werd een groot aantal numerieke simulaties uitgevoerd, waarin de randvoorwaarden, overvloeipositie, waterdiepte, vaarsnelheid, sedimentconcentratie, aanwezigheid van luchtbellen en het aantal overvloeien werden gevarieerd. Het model maakt gebruik van zowel theoretische oplossingen als van multivariate regressieanalyse. Een holistische aanpak werd aangewend waarin de parameters werden gevonden met een 'model-training' op basis van de grote hoeveelheid pluimoplossingen

uit het numeriek model. Ondanks zijn eenvoud en snelheid werd aangetoond dat het grey-box model de verticale verdeling van de sedimentflux in de pluim op een relatief nauwkeurige manier voorspelt.

Het doel van dit onderzoek was om de voorspellingen van troebelheid in zowel de plannings- als de uitvoeringsfase van een baggerproject te verbeteren. Om de voorspellingen van de pluimverspreiding op de schaal van een estuarium of kustgebied te verbeteren, zijn meer accurate voorspellingen van de brontermen nodig. Net dat objectief werd in dit onderzoek bereikt met de ontwikkeling van modellen op verschillende detailniveaus. In de planningsfase is tijd beschikbaar is om gedetailleerde numerieke simulaties van specifieke omstandigheden uit te voeren. Dit kan nu worden bereikt, zoals het driedimensionale model uit dit onderzoek aantoont. Tijdens de uitvoeringsfase is het belangrijk real-time voorspellingen van de pluimverspreiding uit te voeren. Door voorspellingen van de pluimverspreiding uit te voeren op basis van de dagelijkse baggerplanning tijdens een project, kan eventueel worden bijgestuurd wanneer een overschrijding van de limieten voor turbiditeit wordt voorspeld. De omstandigheden op zee kunnen variëren van uur tot uur, zeker in geval van sterk getij. In dit stadium is geen tijd beschikbaar voor uitgebreide numerieke simulaties van de brontermen. Voor deze real-time toepassingen kan het grey-box model als interne module in de software voor grootschalige modellen (kustregio, estuarium) worden geïmplementeerd.

Contents

Chapter 1

Introduction

1.1 General situation

Throughout the history of mankind, the interference of human developments with the natural environment has ever increased. This can be largely associated with an exponential population increase, the growth of the world's economy and technological development. In the early stages of the industrial development, efforts concentrated on the increase of productivity and living standards. In more recent times, developed countries have reached a stage in which the accumulated technological aids and wealth have lead to an increased availability of time and resources for environmental awareness. A second important motivation for environmental impact reductions is the increasing stress of environmental degradation on human health and the quality of life.

In this light, the attention for environmental aspects of dredging projects has increased and regulations have become increasingly stringent in the past decades. More specifically, the potential generation of turbidity by dredging projects, and the ways to avoid it, are the topic of this research. One of the main sources of turbidity during fairway deepening, land reclamation or minerals mining is the overflowing of excess water from Trailing Suction Hopper Dredgers. In the recent past, the use of this type of dredger has been on the rise, for example due the well-known developments of artificial islands and land reclamation in the Middle-East and Asia.

The growing attention for dredging-induced turbidity, combined with the challenging aspects of the prediction thereof, has lead to conceiving this research project. The processing power of nowadays high-performance comput-

ing systems has generated a potential for much more detailed simulations and predictions of the turbidity generated by a Trailing Suction Hopper Dredger. In the research presented below, the exploitation of this potential towards tools for a better environmental impact assessment is described.

1.2 The Trailing Suction Hopper Dredger

The topic of this thesis is the sediment-water plume released through the overflow shaft of a trailing suction hopper dredger (TSHD). The latter type of dredger is a self-propelled, seagoing vessel and is widely applied worldwide. While trailing a drag head across the sea bed, a sediment-water mixture is pumped through a suction pipe and into the hopper with discharge Q_p and sediment mass concentration C_p (figure 1.1). Whereas the coarser sediment particles settle in the hopper, the finest sediment fractions can stay in suspension and flow overboard with the excess water through a vertical dropshaft, the overflow. The volume discharge through the overflow is denoted Q_0 and the sediment mass concentration in the mixture as C_0.

The exit of the overflow shaft is usually mounted flush with the keel of the vessel's hull. As a consequence, a negatively buoyant plume of water, air bubbles and fine sediment particles is released vertically below the vessel. Due to the sailing speed of the vessel and/or the ambient currents, the generated plumes are subjected to a crossflow.

The hypothesis is that part of the sediment plume can be stripped off the main density current by means of air bubbles, propellers and crossflow. This fraction of the total sediment discharge, Q_s, is subsequently moved to a surface plume. These surface plumes are often visible on aerial photography.

To enable proper assessment of the environmental impact of the plumes it is important to predict its fate and dispersion in the water column (Bray, 2008).

1.3 Environmental impacts of dredging with overflow

The turbidity generated by dredging with overflow potentially leads to adverse environmental impacts (Bray, 2008). When a surface plume is formed with relatively low sediment concentration, and thus low excess density, it

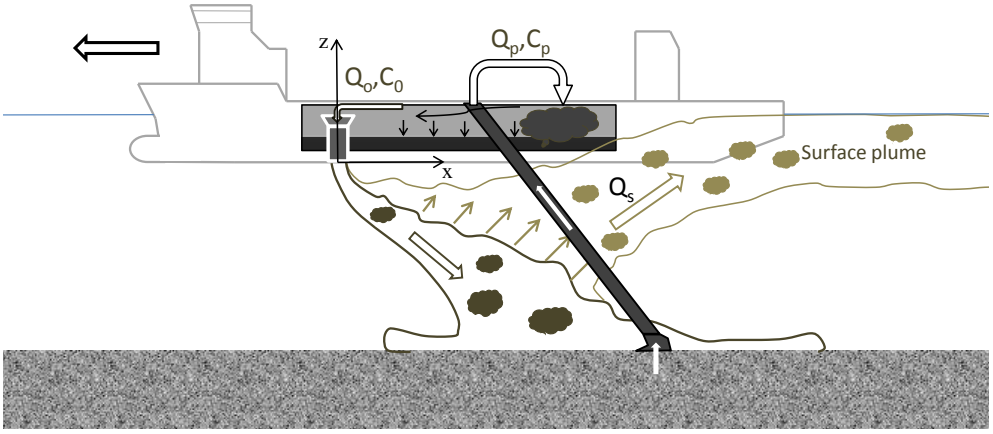

Figure 1.1: Sketch of a Trailing Suction Hopper Dredger with emphasis on the path of the water-sediment mixture. The sediments move from the sea bed through the suction pipe into the hopper and a fraction is discharged through the overflow, back into the sea.

will not have the ability to descent to the sea bed. In this case the surface plume can travel with tidal currents over distances of a few kilometers (Hitchcock and Bell, 2004; Breugem *et al.*, 2009; Leggett *et al.*, 2013). The reduced light penetration or sediment depositions can induce adverse effects to aquatic life such as coral reefs, hunting fish, sea grass patches and benthic organisms.

To prevent plumes to reach these valuable areas, an extensive turbidity monitoring programme is usually deployed during dredging projects. Alarm levels are defined above which turbidity is not allowed to rise. In case these levels are reached, the planning of works need to be revised or ultimately, the dredging works have to be suspended. To avoid such events, the dredging plumes caused by the operational vessels have to be forecasted by model simulations. In the past, a so-called environmental valve has been used in case severe adverse effects are likely. This valve chokes the flow in the overflow shaft, thereby avoiding the plunging jet and subsequent air bubble entrainment. It is generally believed this valve can reduce turbidity, but it is not known what level of efficiency can be expected throughout the range of possible field conditions.

1.4 Overflow dredging plumes

In their spatial evolution from overflow shaft to dissipation, overflow plumes can be divided in two zones. The zone closest to the release is subject to complex interactions between water, sediment, air bubbles, propeller jets and the bulk buoyancy of the plume. This zone is called the near field. In this zone, the plume is usually a dynamic plume, which is defined as a plume under influence of an increased bulk density compared to the surrounding sea water.

After a certain distance behind the TSHD, propeller- and ship-induced mixing have decayed, air bubbles have left the water column and the sediment concentration has reduced to levels at which the bulk density is very close the sea water density. This zone is called the far field. Here, the plume is no longer dynamic, but is referred to as a passive plume. It is this type of plume which can travel over long distances with the sea current.

1.5 Present-day numerical modelling of overflow dredging plumes

In order to assess the potential of plumes to reach sensitive areas in the phase of tendering, predictions of tidal currents and plume dispersion are needed. Also in the operational phase of dredging projects, real-time forecasting of plume dispersion is an advantage in avoiding suspension of works due to turbidity threshold violations.

To predict the path and concentration of turbidity plumes, numerical models are the only option. Large-scale hydrodynamic models are set up and calibrated to simulate the temporal evolution of tidal currents. When it is planned that a given dredging vessel with a given production will be working at a given location, the sediment source terms can be imposed in the numerical flow model. Based on the production rates and the percentage of fine sediment in the sea bed, a sediment flux through the overflow can be estimated, e.g. van Rhee (2002); Jensen and Saremi (2014).

The released sediments are subsequently dispersed through a complex flow pattern influenced by density gradients, air bubbles, propeller mixing and the flow around the TSHD. A fraction might reach the sea bed immediately and spread as a near-bed density current. The solution of these detailed processes is not feasible in a large-scale model stretching over a distance of typically

10 to 100 km. There are two main reasons: a number of assumptions in the equations and relatively large grid cells. Both aspects are needed to make predictive calculations feasible for such large timescales and spatial scales. At present, the bulk effect of all the complex near-field processes has to be condensed in one parameter: the fraction of the released sediments that is brought in suspension in the water column (Becker *et al.*, 2015). The vertical distribution of this fraction throughout the water column is also unknown. These factors forms the largest uncertainty in defining sediment source terms for overflow plume simulations.

In this work, a model is developed to perform highly-detailed, threedimensional simulations of the complex flows of the water-sediment-air mixture from overflow shaft to far field.

1.6 Review of in situ plume measurements

The subject of environmental impacts of dredging plumes has lead to a significant number of field surveys described in literature. Especially since optical and acoustic instruments became available in the 1990's, more detailed monitoring results have been published. Newell *et al.* (1999) measured sediment concentrations in plumes caused by overspills and reject chutes during marine aggregates mining along UK coasts. They found that in the water column most sediments had settled after 300 m. Sediment concentrations were found up to 1400 mg/l. Hitchcock and Bell (2004) also measured in overspill plumes from aggregate mining activities and found sediment concentrations above background levels up to about 800 m from the dredging location. They also found that a near-bed layer of highly concentrated sediments existed up to 4.5 km from the dredging area. In an extensive study on marine aggregate mining plumes from overspills, CoastlineSurveys (1998) measured sediment concentrations in the plumes between 10 mg/l and 2500 mg/l. The fraction of fine sediments ($<63\mu$m) was between 40 and 67%. These examples stem, however from overspill-related plumes, rather than the overflow released through a shaft in the keel of the vessel as studied in this thesis. These overspills (or reject chutes) lead to a plunging jet at the water surface and might therefore induce higher near-surface concentrations.

During scallop dredging, Black and Parry (1999) monitored a plume which consisted of a near-bed layer with concentrations up to 5 g/l at 0.25 m above the bed. Higher in the water column, concentrations were found up to 100

mg/l.

During field measurements in an overflow plume in the English Channel, Breugem *et al.* (2009) sampled the mixture inside the overflow shaft. In this way, the sediment concentrations found in the plume could be related to the source strength. They found initial concentrations between C_0=7 g/l and 40 g/l, with median grain sizes of d_{50}=7 μm. The sediment concentrations found in the plume were in the range 10-100 mg/l between 400 and 1200 m behind the dredger. The plume length was between 300 and 2200m, while the width of the plume was 85 to 280m. The lifetime of the plumes were estimated at 1200 to 2600 s.

In a very detailed field survey in the San Francisco Bay, Smith and Friedrichs (2011) determined not only suspended solids concentrations, but also settling velocities, particle size and particle density. They found that 20 to 50% of the material in the plume consisted of bed aggregates that were not fully separated during the hydraulic transport. The aggregates had settling velocities of 0.5 to 3 mm/s. Lower-density flocs accounted for 50-80% of the material, with settling velocity between 0.5 and 5 mm/s. These measurements were taken far behind the dredger since it is indicated that the plume was followed for 90 minutes after the dredging had stopped.

Finally, in a monitoring campaign Leggett *et al.* (2013) observed overflow plumes during a 4 year dredging project in the Thames Estuary, UK. Plume lengths between 300 and 1700 m and plume widths between 50 and 200 m were found. The plume-average increase in suspended solids concentration above the background was in the range 60-300 mg/l.

In general the length and width of the plumes as well as the sediment concentrations reported in literature seem to be consistent. However, in most cases described in literature, plume measurements have been executed at relatively large distance from the dredger. In this study, the behaviour of the near-field plume i.e. the first few 100 m behind the dredger, is studied. Therefore, an additional measurement campaign was executed during the course of this research.

1.7 Research objectives & methodology

Development of a Computational Fluid Dynamics model

The main goal of this research is to develop simulation methods for the prediction of overflow sediment plumes in the near-field, in order to improve the estimates of the sediment input to a passive, far-field plume. The overflow mixture characteristics as resulting from hopper processes have been studied in the past (van Rhee, 2002; Jensen and Saremi, 2014) and are considered as input data in this work.

The following work packages are identified to meet the CFD model objective:

1. **Laboratory tests** will provide a detailed data set to validate the characteristics of the simulated turbulent flow in the plume. The tests will also give indications of the influence of air bubbles and a ship hull on a plume in crossflow. In a simplified geometry, the comparison of the sediment plume in a crossflow with the much better studied single-phase buoyant jet in crossflow can be made. To allow for detailed measurements of the turbulent properties of the water-sediment mixture, new data-processing techniques need to be developed.

2. **CFD model at lab scale**: The primary tool to determine the detailed dynamics of near-field dredging plumes is a Computational Fluid Dynamics model (CFD). Given the numerous complexities related to a full-scale simulation of a TSHD with propellers and a sediment plume including air bubbles, the model will be developed in a number of steps with increasing complexity. In a first step, a CFD model with a simplified geometry will be developed. This model, with the geometry of the laboratory setup, can be validated in detail against experimental data. The model allows for the isolation of the relevant processes regarding a buoyant jet in crossflow with influence of a schematised ship hull.

3. In a second step, a **CFD model at prototype scale** will be developed, to describe in detail the behaviour of the water-sediment-air mixture. Additionally, **in situ measurements** will be performed to serve as validation data set for the prototype-scale simulations. The final objective of the numerical modelling exercise is to obtain a model able to predict both the amount of sediments entrained from the dense plume under the vessel as well as its distribution over the water column

further away from the vessel. In this way, the impact of a large number of influencing factors on the plume dispersion can be investigated.

Development of a grey-box parameter model

Finally, the most cost-effective sediment input prediction tool for use in engineering consultancy is the following: a fast and simplified model based on the patterns found in the CFD results, programmed and compiled in an executable to be used by engineers in consultancy work. The development and assessment of a black-box or grey-box model as a basis for such a tool is the second and final objective of this research. This type of tool will be more suitable for dredging plumes than the currently available jet-integrated or length-scale models which pre-define the cross-sectional shape of the plume and which do not take into account typical dredging plume processes such as air bubbles and propeller mixing (Van Eekelen, 2007). The tool will be validated against a large data set of CFD model results.

1.8 Outline of the thesis

In this section, the work flow of the research and the outline of this thesis are described, which is also visualised in figure 1.2.

In the chapter 2, a general introduction of buoyant jets and plumes is given. The classification of jets and plumes, as well as their relevant turbulent properties are shortly described. A brief overview is given of the multiphase aspects of the flows studied here. Readers who are familiar with these topics might omit these sections. At the end of chapter 2, propeller jets are discussed as well as previously reported Large-Eddy Simulations of jets and plumes.

In chapter 3, the experimental facility at the Hydraulics Laboratory of Ghent University is described. Afterwards, the measurement techniques applied in the laboratory are described (chapter 4), followed by a chapter on newly developed processing techniques to derive turbulent sediment flux data from ADV instruments (chapter 5). The results of the laboratory experiments of sediment plumes in a crossflow are described in detail in chapter 6.

Next, a CFD model is built with exactly the same geometry as the laboratory setup. This allows detailed assessment of the performance of the CFD model. The setup and validation of this lab-scale CFD model is described in

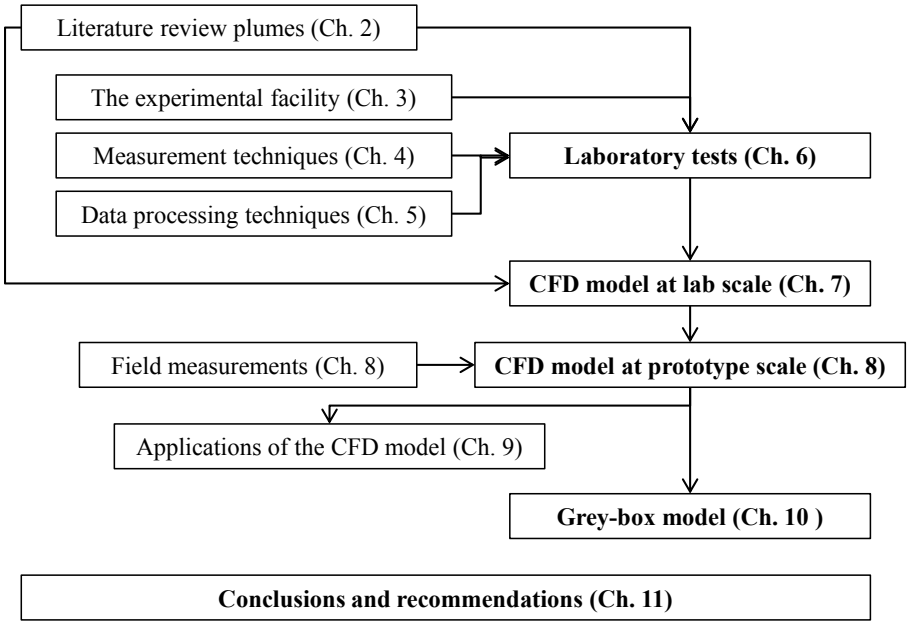

Figure 1.2: Flow chart of the research and outline of this thesis.

chapter 7.

After validation of the CFD model at lab-scale, the process of upscaling the CFD model to prototype scale is validated. The model is extended with a realistic TSHD geometry and schematised propellers. At that point, the model has the possibility to include the effect of the air bubble- and turbidity-reducing environmental valve. In chapter 8, the setup and validation of the prototype-scale model is given, including validation against in situ measurements. In chapter 9, three of the many potential applications of the CFD model are described: a study of the efficiency of the environmental valve, an analysis of a different shape for the overflow shaft and the potential of a telescopic overflow extension.

In chapter 10, the development and validation of a simplified, grey-box plume model is shown, which has the ability to rapidly generate predictions of the vertical profile of the overflow plume sediment flux, within its range of validity. Finally, general conclusions of this research and recommendations for future work are given in chapter 11.

Chapter 2

Jets and plumes

2.1 Introduction

Jets and plumes form a well-documented class of flows in fluid mechanics. Jets and plumes are intensively studied due to their occurrence in a wide range of scientific and engineering domains. They can be found in, among many others, the following flow phenomena: smokestacks, rocket steering, volcano eruptions, marine outfalls, fuel injection, submarine oil well blowouts and turbine film cooling.

In this chapter, a concise overview is given of the most important aspects of the present knowledge on jets and plumes, and more specifically on the buoyant jet in crossflow, to which the near-field overflow plume belongs.

2.2 Classification

Depending on the continuous or non-continuous release and on the injection of momentum and/or buoyancy in an ambient fluid, Cushman-Roisin (2010) defines the classification given in table 2.1, regardless of cross-flows or density stratification.

A near-field overflow plume is released with an initial momentum and an initial buoyancy flux. Most overflow dredging plumes can therefore be classified as buoyant jets or forced plumes.

Table 2.1: Terminology after Cushman-Roisin (2010)

	Continuous injection	Intermittent injection
Momentum only	Jet	Puff
Buoyancy only	Plume	Thermal
Momentum + Buoyancy	Buoyant Jet	Buoyant Puff

2.3 Integral properties

2.3.1 The buoyant jet in a still environment

A buoyant jet or forced plume is a plume in which both an initial momentum flux and a buoyancy flux govern the flow up to a certain distance from the release point (Morton *et al.*, 1956; Fischer, 1979). Pure plumes and pure jets, to the contrary, are only forced by a mass density difference and an intial momentum flux, respectively.

For round buoyant jets with top-hat velocity profile, initial volume, momentum and buoyancy fluxes can be written, respectively, as:

$$Q_0 = \frac{\pi}{4} D^2 W_0 \tag{2.1}$$

$$M_0 = \frac{\pi}{4} D^2 W_0^2 = W_0 Q_0 \tag{2.2}$$

$$B_0 = g_0' \frac{\pi}{4} D^2 W_0 = g_0' Q_0 \tag{2.3}$$

where D is the exit pipe diameter, W_0 is the (uniform) exit velocity and $g_0' = g(\Delta\rho/\rho_w)$ is the reduced gravity of the mixture being discharged in an ambient fluid. $\Delta\rho = \rho_m - \rho_w$ with ρ_w the mass density of the surrounding fluid (water), ρ_m the mass density of the plume mixture (figure 2.1).

In the case of overflow plumes, the buoyancy force is generated by the presence of particles in a mixture. Assuming the mass density of the fluid phase in the mixture is equal to the mass density of the ambient fluid, g_0' can be written as

$$g_0' = g\phi_0 \frac{\rho_s - \rho_w}{\rho_w} \tag{2.4}$$

where ϕ_0 is the initial particle volume concentration (m^3/m^3), ρ_s is the mass density of the particles and ρ_w is the mass density of the fluid phase in both

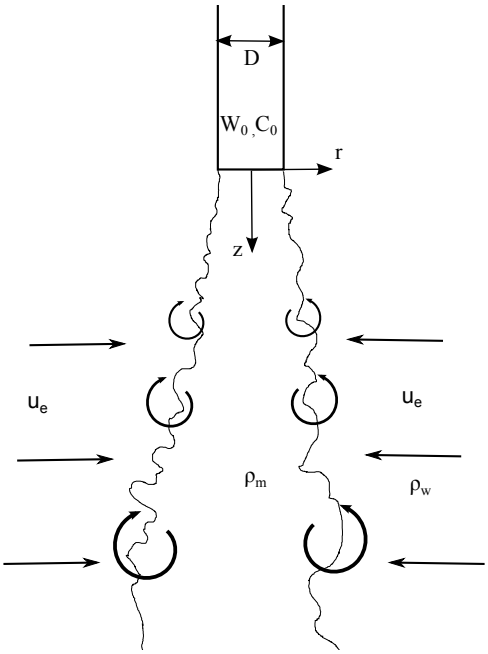

Figure 2.1: Sketch of the buoyant jet in a still ambient fluid. D is the exit pipe diameter, W_0 is the mean exit velocity, C_0 the exit concentration, ρ_w the mass density of the surrounding fluid and ρ_m the mass density of the buoyant jet mixture.

the mixture and the receiving ambient fluid.

The quantities Q_0, M_0 and B_0 are considered the primary variables in the study of turbulent jets, plumes and forced plumes (Fischer, 1979).

In figure 2.1, shear layer vortices are indicated. These vortices are responsible for entrainment of ambient fluid into the plume, with a velocity u_e. Often this velocity is defined as the mean vertical velocity in the plume multiplied by an entrainment rate. The turbulent entrainment of ambient fluid results in a Gaussian profile of vertical velocity and concentration. Plumes released from a circular pipe or orifice exhibit self-similarity in the region past the so-called zone of flow establishment, typically at about 6 to 10 pipe diameters (Morton *et al.*, 1956; Fischer, 1979). The radial profiles of flow velocity and tracer concentration collapse when normalised by the appropriate parameters. Radial profiles of axial velocity and tracer concentration exhibit a Gaussian distribution of the form:

$$W(z,r) = W_c(z)e^{-(r^2/b_w^2)} \tag{2.5}$$

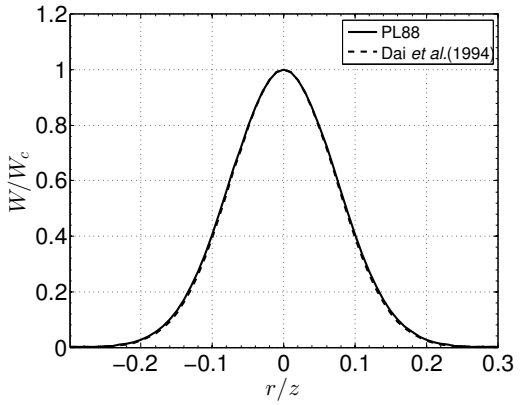

(a)

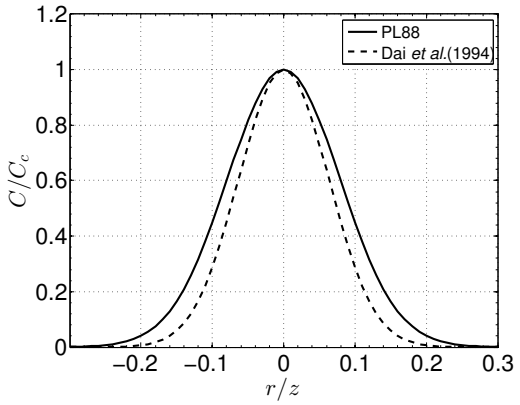

(b)

Figure 2.2: Radial profile of the axial velocity (a) and tracer concentration (b) in the self-similar region, Gauss curve fits by Papanicolaou and List (1988) and Dai et al. *(1994a).*

$$C(z,r) = C_c(z)e^{-(r^2/b_c^2)} \tag{2.6}$$

Where b_w and b_c are the distances from the axis at which the axial velocity (resp. concentration) has reduced to a value of $1/e$ times the axial value. These distances are referred to as half-widths. For the axial velocity, Papanicolaou and List (1988) and Dai *et al.* (1994a) find very similar values of respectively b_w=0.105z and b_w=0.104z (Figure 2.2a) in single-phase plumes. Apparently, $b_w \propto z$, the width of a vertical buoyant jet is thus proportional to the distance from the source.

For the concentration half-width, both authors find significantly different values, respectively b_c=0.111z and b_w=0.09z (Figure 2.2b). This means that in the measurements of Papanicolaou and List (1988), the concentration width of the plume was wider than the velocity width, indicating a turbulent Schmidt number $Sc_t > 1$, where the Schmidt number is the ratio of the turbulent viscosity ν_t to the turbulent diffusivity D_t. While in the measurements by Dai *et al.* (1994a), the opposite was found. In the next chapters, values for vertical sediment plumes are reported.

The self-similar property of buoyant jets in still environment allows researchers to compare experimental and numerical results of plumes of different Q_0, M_0 and B_0. In this work, the self-similarity property will be used to validate the LES model by simulating a vertical plume and comparing the results with measurements under the same circumstances, but also with plumes observed by other authors, i.e. the single-phase plume experiments by Papanicolaou and List (1988), Shabbir and George (1992) and Dai *et al.* (1994a).

2.3.2 The buoyant jet in a crossflow

When releasing a momentum and buoyancy source from a round pipe in an ambient fluid with uniform flow velocity and mass density, the round buoyant jet in crossflow is obtained. Most overflow plumes belong to this category.

Dimensional analysis leads to two main dimensionless numbers characterising plumes released in a crossflow with flow velocity U_0, the densimetric Froude number F_Δ and the jet-to-crossflow velocity ratio λ.

$$F_\Delta = \frac{W_0}{\sqrt{gD\Delta\rho/\rho_w}} \quad ; \quad \lambda = \frac{W_0}{U_0} \tag{2.7}$$

Trajectories followed by plumes in crossflow are determined by several possible flow regimes, see e.g. Wright (1984): jet regime, bent jet regime, plume regime and the bent plume regime. In some literature, these are referred to as momentum-dominated near field (MDNF), momentum-dominated far field (MDFF), buoyancy-dominated near field (BDNF) and buoyancy-dominated far field (BDFF) respectively.

The flow regimes characterising a plume from release to far field depend on a number of length scales. Length-scale l_M (eq. 2.8), determines the distance at which the buoyancy-generated momentum becomes dominant over the

initial momentum, or at which the MDNF regime transforms to a BDNF regime.

$$l_M = \frac{M_0^{3/4}}{B_0^{1/2}} \tag{2.8}$$

Height z_M (eq. 2.9) is the vertical distance at which the ambient crossflow velocity becomes more important than the initial vertical velocity at the exit, or at which a MDNF regime becomes transitional, moving to a MDFF regime (in case $z_M \ll l_M$).

$$z_M = \frac{M_0^{1/2}}{U_0} \tag{2.9}$$

Height z_B (eq. 2.10) is the height at which buoyancy-generated momentum dominance is taken over by crossflow dominance, or at which a BDNF regime transforms to a BDFF regime.

$$z_B = \frac{B_0}{U_0^3} \tag{2.10}$$

A plume in MDFF regime moves to a BDFF regime when the vertical distance becomes larger than z_C (eq. 2.11).

$$z_C = \left(\frac{M_0^2}{U_0 B_0}\right)^{1/3} \tag{2.11}$$

This number is only important when the plume has moved to MDFF regime first, in case $z_M > z_B$. Each flow regime is associated with a coefficient c and an exponent β in the exponential trajectory shape function $(z/L) = c(x/L)^\beta$, in which $L = z_M$ for momentum-dominated regimes and $L = z_B$ for buoyancy-dominated regimes.

The plumes studied in this work correspond to ranges of F_Δ and λ occurring in sediment plumes released from dredging vessels. Even though the initial relative density difference is usually in the order of 1 to 10%, the buoyancy is relatively weak compared to the crossflow in these cases, with the jet-to-crossflow velocity ratio usually in the range $0.25<\lambda<3$. Therefore, the momentum length scale z_M (eq. 2.9) is larger than the buoyancy length scale z_B (eq. 2.10) in most cases, leading to a plume trajectory sequence MDNF-MDFF-BDFF. However, in strong cross-flow cases both z_M/D and z_B/D are around or less than unity, due to which the plume transforms very rapidly to the BDFF regime. The plume trajectory in the two main regimes

occuring in the studied flows (MDFF, BDFF) scale with z_M and z_B, respectively.

2.4 Turbulence

2.4.1 General

In the present study, the Large-Eddy Simulation technique (LES) will be applied for the simulation of the overflow plumes. This technique partially resolves the turbulent motions in the flow field. Therefore, a number of basic concepts of turbulence need to be introduced.

A general theory for turbulence is not yet discovered, instead one must rely on a number of descriptive laws. When applying the Large-Eddy Simulation technique, the turbulent energy principles on which it is based must be understood. Kolmogorov (1941), postulated that at sufficiently high Reynolds number the statistics of the small-scale turbulent motions smaller than η are defined by the viscosity ν and the dissipation rate ϵ only. Here, η is the Kolmogorov length scale, at which viscous dissipation starts (eq. 2.12), see figure 2.3. Between the integral length scale l_0 and η the turbulent statistics can be defined by ϵ only. The integral scale is determined by the flow geometry and corresponds to the largest eddies. The Kolmogorov scale and the time and velocity scales associated with it can be estimated from

$$\eta \approx \left(\frac{\nu^3}{\epsilon}\right)^{1/4} \tag{2.12}$$

$$u_\eta \approx (\nu\epsilon)^{1/4} \tag{2.13}$$

$$t_\eta \approx \left(\frac{\nu}{\epsilon}\right)^{1/2} \tag{2.14}$$

Kolmogorov went on to describe the energy contained in the range of turbulent scales in Fourier space. Since the turbulent statistics in a certain region between l_0 and η are determined by ϵ only, the energy spectrum could be written in the following form:

$$E(\kappa) = c_e \epsilon^{2/3} \kappa^{-5/3} \tag{2.15}$$

where κ is the wave number of turbulent scales (m^{-1}). This is called the -5/3 power law of the turbulent energy cascade.

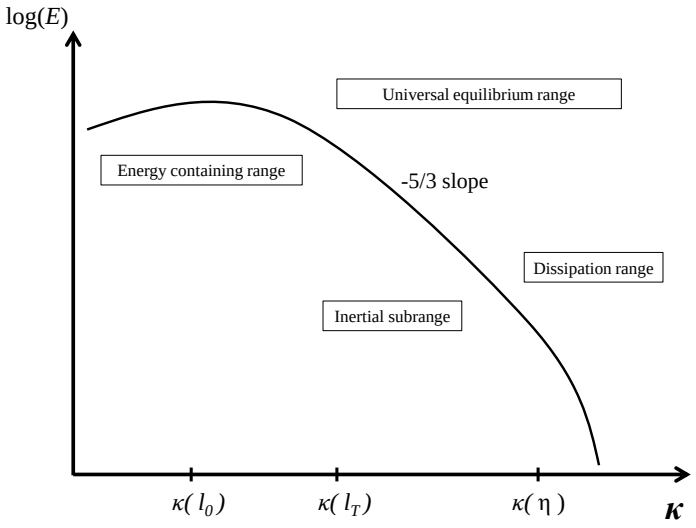

Figure 2.3: Energy spectrum as a function of the wave number κ, with the different characteristic turbulent length scales.

The total turbulent kinetic energy k is then defined by:

$$k = \int_0^\infty E(\kappa)\, d\,\kappa \tag{2.16}$$

The -5/3 power law can be found in measurements of turbulent flows. The energy is transferred from the energy-containing scales down to the smaller scales in the inertial subrange. At the Kolmogorov scale η, the molecular viscosity becomes important and viscous dissipation occurs. When the energy spectrum is expressed as a function of frequency f, a -2 power law is sometimes used. However, here it will be assumed the -5/3 power law can be retained.

Further, Kolmogorov's hypothesis of local isotropy is important here. It states that the small-scale turbulent motions are statistically isotropic. This means that these small scales should be more easily captured in a simplified model. This hypothesis is used in the definition of LES models.

In order to continue, first the Reynolds decomposition must be introduced. The result of turbulent motions is that fluctuations can be found in the instantaneous signals of velocity and scalar concentration measured at a fixed

point. The variations are due to the superposition of turbulent structures with different scales passing by an observation point. The Reynolds decomposition separates the time-averaged values of the velocity components and concentration (U, V, W and C, respectively), from the fluctuations u', v', w' and c':

$$u = U + u' \tag{2.17}$$

$$v = V + v' \tag{2.18}$$

$$w = W + w' \tag{2.19}$$

$$c = C + c' \tag{2.20}$$

The range of turbulent motions can be divided in an energy containing range and a universal equilibrium range. Even though it does not have a real physical meaning, the Taylor microscale is thought to be located near the start of the universal equilibrium range. The Taylor microscale can be defined as:

$$l_T^2 = \frac{\overline{u_i'^2}}{\overline{\left(\partial u_i/\partial x_i\right)^2}} \tag{2.21}$$

where the overbar represents averaging in time. l_T can be related to the integral scale by:

$$l_T \propto l_0 \mathrm{Re}_{l_0}{}^{-1/2} \tag{2.22}$$

where Re_{l_0} is the Reynolds number associated with an eddy with scale l_0, defined as $\mathrm{Re}_{l_0} = u' l_0/\nu$.

It is often assumed that the small scales with local isotropy are included in the universal equilibrium range. In the universal equilibrium range, the statistics of the turbulence is thought to be independent of the energy containing scales. The universal equilibrium range can be further divided in the inertial subrange (approximately at $l_T > l > \eta$) and the dissipation range (approximately at $l < \eta$). In Large-Eddy Simulation the turbulent motions of at least part of the inertial subrange is resolved on the numerical grid.

The turbulent kinetic energy present in the velocity fluctuations can then be determined as follows:

$$k = \frac{1}{2}(\overline{(u')^2} + \overline{(v')^2} + \overline{(w')^2}) \tag{2.23}$$

2.4.2 Turbulence in a jet in still environment

As discussed above, in jets and plumes released in a still environment, the radial profile of the time-averaged axial velocity has a Gaussian shape with maximum value at the jet axis. The radial profile of velocity fluctuations, to the contrary, shows double peaks away from the axis, as shown by, amongst many others, (Panchapakesan and Lumley, 1993; Dai *et al.*, 1995; Xu and Antonia, 2002; Westerweel *et al.*, 2009). These are related to the shear associated with the radial velocity gradients. The velocity gradient goes to zero at the axis, leading to a dip in turbulent intensity. A good review of experimental data on the turbulent properties of the round jet can be found in Lipari and Stansby (2011).

The radial profile of the Reynolds stresses shows opposite signs on either side of the plume. This shows the turbulent transport of streamwise momentum is always directed towards the edge of the jet. At the axis of the jet, this transport comes to a standstill and the Reynolds stress falls to zero.

Using dimensional reasoning and the basic equations of motion, Townsend (1976) derives the following law for free shear flows in jets in a still environment.

$$\frac{\overline{u_i'^2}}{W^2} \approx \frac{l}{L} \tag{2.24}$$

where l is the turbulent scale in the transverse direction and L the turbulent scale in the longitudinal direction.

For jets, this ratio is found to be about one to eight. This means that the turbulent intensity in jets can be considerably lower than one. It also shows that the turbulent scales in the transverse direction can be about an order of magnitude smaller compared to those in the longitudinal direction. That observation leads to some considerations for numerical grid design for simulations of jets and plumes. More, specifically, that the transverse grid spacing should be significantly smaller than the longitudinal one.

2.4.3 Turbulence in a buoyant jet in still environment

In jets, the variations of mixture fraction are governed by the inertial-advective momentum terms. In buoyant jets the turbulence in regions of varying density (like e.g. temperature or sediment concentration) is influenced by the

density gradients. The diffusion of mixture fractions is therefore expected to behave differently in buoyant jets as compared to non-buoyant jets.

Buoyant jets exhibit a similar turbulent structure compared to simple jets. Nevertheless, the buoyancy has an impact, also on the turbulent dissipation in the higher-frequency range. Like in most fully-developed turbulent flows, the -5/3 exponential law can be found in the frequency spectrum of the velocity signal and mixture fraction of plumes. This range is called the inertial-convective subrange for mixture fraction fluctuations. Kotsovinos (1991), Dai *et al.* (1994a) and Papanicolaou and List (1988) found that for plumes a -3 exponential law can be found between the -5/3 power law and the viscous dissipation. This zone cannot be found for simple jets without buoyancy differences. It is called the inertial-diffusive subrange, also described in Tennekes and Lumley (1972) for temperature fluctuations. It is argued that this zone stems from buoyancy-generated inertial forces resulting in a more rapid decay of the spectrum. It will be investigated in the present work whether this zone can also be found in LES simulations of buoyant jets consisting of fine sediments.

2.4.4 Turbulence in a buoyant jet in crossflow

The flow in plumes released vertically in a crossflow is characterised by different types of turbulent structures. These are related to a number of phenomena. Firstly, the blending of initial vertical momentum with crossflow horizontal momentum, leading to a counter-rotating vortex pair (CRVP), sometimes also called a kidney vortex pair, see e.g. experiments by Fric and Roshko (1994); Kelso *et al.* (1996). In these publications, the jet-to-crossflow velocity was however quite high compared to overflow plumes and the jet Reynolds number was not always high enough to ensure developed turbulent pipe flow. The shape of the plume exit opening is of importance for the plume trajectory turbulent behaviour. Haven and Kurosaka (1997) showed that for some rectangular shapes of the outflow hole, a so-called anti-kidney vortex pair is formed and the plume trajectory is significantly different from the round jet in crossflow case.

Secondly, Kelvin-Helmholtz instabilities result in leading-edge vortices and associated convection cells ejecting in the direction of the buoyancy force vector, e.g. Tian and Roberts (2003), Cambonie *et al.* (2013) and Diez *et al.* (2005)).

Additionally, a pattern of wake vortices similar to the vortices in the wake of a cylinder has been observed by Fric and Roshko (1994) and Muldoon and Acharya (2010) in the wake of a jet in cross flow. These vortices are, however, clearly distict from a von Karman vortex street since they originate from the crossflow boundary layer.

2.5 Multiphase jets and plumes

2.5.1 Particle-laden plumes

The two-liquid case of the buoyant jet in crossflow has been studied intensively, whereas turbulent plumes in which negative buoyancy is created by fine particles are not very well studied. Much of the large scale flow structure is expected to be similar to the intermiscible liquids case. However, turbulent diffusion of mass is expected to behave differently in dispersed two-phase flows. Different authors have shown that the turbulent Schmidt number, Sc_t has a different average value for particulate suspensions compared to the standard value of 0.7 for intermiscible liquids diffusion (Celik and Rodi, 1988; Mehta *et al.*, 1989; van Rijn, 1993; Toorman, 2008). The two-phase LES model developed in this research should resolve enough of the turbulent motions to provide a spreading rate associated with the diffusivity in a sediment plume. The sub-grid scale turbulent Schmidt number is derived from test-filtered turbulent fluxes (Lilly, 1992), as described in section 7.2.

In multiphase flows, the Stokes number is an important dimensionless number. It gives the ratio of a particle response time to a characteristic time scale of turbulent motions. It can be defined as follows:

$$\mathrm{St} = \frac{\rho_s d_s^2}{18\mu_w} \tag{2.25}$$

where d_s is the particle diameter and μ_w is the liquid dynamic viscosity. It can immediately be seen that the Stokes number is small for fine sediments, due to the small diameter. It is also relatively small for air bubbles in a water flow, due to the small mass density of air.

Much information can be found in literature on two-phase particle plumes with high phase-density ratios, such as solid particles in gases, gas bubbles in liquids and droplet sprays. Parthasarathy and Faeth (1987) performed

measurements in two-phase plumes with solid-to-liquid phase density ratio of 2.45, which is very similar to the value for sediment plumes (about 2.6). These flows are interesting cases of multi-phase flow, since all momentum transfer mechanisms are potentially important: virtual mass, drag, Saffman lift force and Basset history force, see e.g. Ishii and Hibiki (2006). For the cases studied in Parthasarathy and Faeth (1987), the particle diameter was 500 μm, a factor 50 higher compared to the presently studied cases of fine sediment plumes. This means the Stokes number is much smaller in the present cases. Nevertheless, it is interesting to verify whether the fine sediment plume measurements can be more closely related to the two-liquid cases or to the higher Stokes-number particle plumes. Parthasarathy and Faeth (1987) found that the radial profiles of $\overline{u_i'^2}$ did not show a significant dip near the axis, rather a flat section in the range r/z <0.1. Parthasarathy and Faeth (1990) also discuss turbulence modulation, a feature in multi-phase flows where the turbulence of the liquid phase is increased by the wakes of the particles moving through the liquid with a certain slip velocity. The footprint of this effect was indeed the increase in $\overline{u_i'^2}$ and k near the axis, compared to single-phase cases. Sheen *et al.* (1994) found that this effect was opposite, namely a reduction in turbulence intensity. The effect was also stronger with particles of 210 μm compared to coarser 780 μm particles. The reason for the opposite effect is probably due to the smaller phase density-ratio: 1.02.

2.5.2 Bubbly flows and bubble plumes

In overflow dredging plumes, air bubbles play an important role in the buoyancy force and dispersion of the plume. In overflow plumes, the air bubble rising velocity has the opposite direction compared to the initial momentum of the plume. In most experimental data available on bubbly plumes, both have the same direction (Kumar *et al.*, 1989; Socolofsky, 2001; Socolofsky and Adams, 2002; Neto *et al.*, 2008; Zhang, 2012; Zhang and Zhu, 2013). The reproduction by simulation of bubbly experiments carried out by other authors is quite challenging. The multiphase flow in the pipe forms the boundary condition for such model. This bubbly pipe flow shows already complex features (Kashinsky and Randin, 1999; Lelouvetel *et al.*, 2014). They showed that in downward bubbly pipe flows, the axial velocity has a maximum near the wall, rather than at the axis, especially for void fractions of more than 5%. This range of void fractions can also be expected in overflow shafts. Lelouvetel *et al.* (2014) showed that in downward bubbly pipe flow, the void fraction is maximal near the wall, while for upward bubbly pipe flow it is

maximal near the axis.

Before leaving the dredging vessel, the water-sediment mixture falls in a dropshaft (the overflow pipe) and entrains therefore a certain volume fraction of air. In the article by Ervine (1998), the maximum air bubble entrainment rate per unit jet width q_a in a vertical dropshaft is given by the equation

$$q_a = 0.00002(W_i - 1)^3 + 0.0003(W_i - 1)^2 + 0.0074(W_i - 1) - 0.0058 \quad (2.26)$$

where W_i is the impact velocity of the water jet impinging the water surface inside the dropshaft (m/s). W_i can be determined as:

$$W_i = \sqrt{2gH_d} \quad (2.27)$$

with H_d the vertical height the water falls in the overflow dropshaft before reaching the water surface.

Taking into account the typical ranges of H_d, pipe diameter D and overflow discharge Q_0, a range of maximum air bubble fractions can be found between 1% and 19% (figure 2.4). The upper limit of air fraction is found for the combination of D=1m and a free fall of 5 m. Since overflow shafts with small diameter are only found in smaller vessels, and since a narrow pipe will have a higher resistance, the 5 m drop to the water surface inside the overflow shaft is unlikely. The actual conditions inside an overflow shaft remain difficult to observe directly, but this range can give an indication of the volume fractions to take into account for the boundary conditions in overflow plume simulations.

In bubble plumes, the rise velocity of individual air bubbles is important. The rise velocity for bubbles, taking into account the non-spherical shape of the larger bubbles, was given by Talaia (2007). The diameter d_a for non-spherical bubble is defined as the sphere-equivalent diameter. Bubbles with a diameter much smaller than 1 mm are spherical. While for larger bubbles the change in shape and the surface tension need to be taken into account. The result is visualised in figure 2.5.

For larger bubbles up to 30 mm, the terminal rising velocity of a singular bubble $w_{t,a}$ is limited to about 0.4 m/s. This means even the larger bubbles will be able to travel trough the overflow pipe, with typical flow velocity between 1 and 3 m/s.

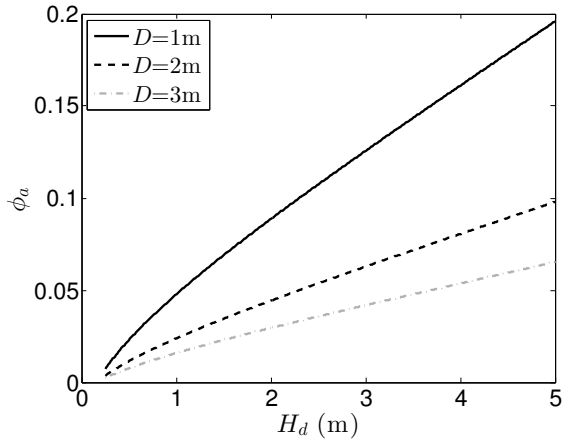

Figure 2.4: Air bubble entrainment into the overflow shaft, according to equations by Ervine (1998). $W_0 = Q_0/(0.25\pi D^2)$ is taken as 2 m/s.

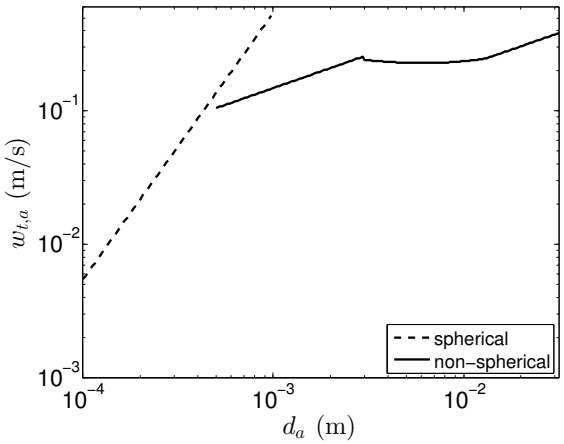

Figure 2.5: Air bubble terminal velocity $w_{t,a}$, according to fits by Talaia (2007).

However, in a bubble column or in a bubble plume with high air fraction, rising bubbles will be influenced by the wake of other bubbles. The actual slip velocity of the bubbles might therefore be higher in highly concentrated air bubble plumes (Neto *et al.*, 2008).

At high volume fractions of air, bubbles will collide frequently. This causes coalescence of the smaller bubbles to form larger ones. The air bubble population will clearly have a size distribution, which is unknown for overflow plumes. When large bubbles are allowed to form they could travel to the surface at a velocity of possibly 0.5 m/s or larger, in which case they could reach the surface after 10 to 20 seconds. The smaller bubbles of around 1 mm have a velocity of about 0.1 m/s, reaching the surface after about 100 seconds, when it is assumed turbulent motions have no influence. It is clear that a model will be needed to determine some kind of air bubble population density. A model for coalescence would be suitable, e.g. the model developed by O'Rourke (1981).

2.6 Propeller jets

Dredging vessels usually have two propellers, for reasons of manoeuvrability. The jets caused by these propellers are likely to have a significant impact on an overflow plume in many cases. Some experimental data about the velocity distributions near propeller jets is available (Lam *et al.*, 2010, 2011).

The rotating propellers initiate both an axial velocity component and a tangential component. The measurements by (Lam *et al.*, 2010) can be schematised as shown in figure 2.6. The axial component reaches a maximum at about halfway the propeller blade ($r/R_p \approx 0.5$), going to zero at the tip of the propeller ($r/R_p=1$). The tangential velocity is maximal near the axis and has a magnitude of about half the maximum axial component at $r/R_p=0.5$. These data are useful for the schematic implementation of the propellers in a numerical model.

In another article, Lam *et al.* (2011) measured the axial decay of the propeller jet velocity components (figure 2.7). In each measurement, the maximum value of a velocity component in a cross section of the jet was observed. This was done for different distances from the propeller. The axial component shown in figure 2.7a decays to about 50% of the initial value after about 3 propeller diameters ($x/D_p=3$). Afterwards a slower decay takes place. In

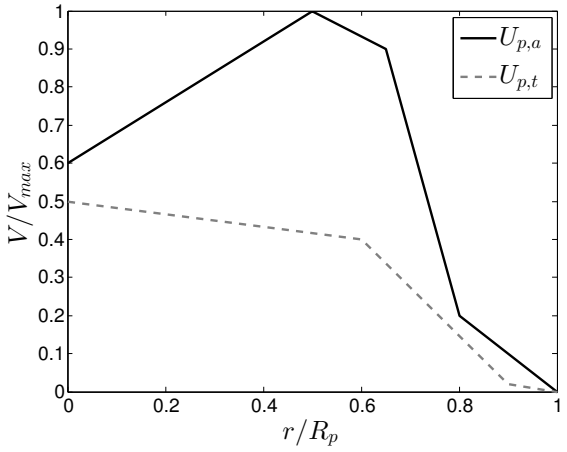

Figure 2.6: Radial profiles of axial and tangential velocity close to the propeller, based on (Lam et al.*, 2010).*

figure 2.7b, the tangential velocity decay is shown. At x/D_p=3, the tangential component has rapidly decayed to about 15% of the initial value. At x/D_p=6, only 5% of the initial tangential velocity is still present. These data are convenient for the validation of the approach for the implementation of a propeller jet in the numerical model described further in this thesis.

2.7 Large-eddy simulations of jets and plumes

The technique of Large-Eddy Simulation (LES) has been used for solving turbulent flow fields since many decades. The most practised form of LES is based on the spatial filtering of the Navier-Stokes equations (Leonard, 1974). A major factor influencing the accuracy of LES is the dependence of the turbulent flow solution on the sub-grid scale (SGS) stress model. For small-scale flows, the turbulent motions can be solved to a large extent and the SGS stress model has limited influence. For LES of large-scale engineering or geophysical flows, the fraction of energy in the scales filtered out is much larger (Galerpin and Orszag, 1996). The case of near-field overflow plumes has Reynolds numbers at the pipe exit of the order of magnitude 10^6 and can be considered as large-scale. The choice of a suitable SGS model will be important.

LES simulations of jets and plumes in a still environment have been reported repeatedly in the past (Zhou *et al.*, 2001; Webb and Mansour, 2000; Worthy,

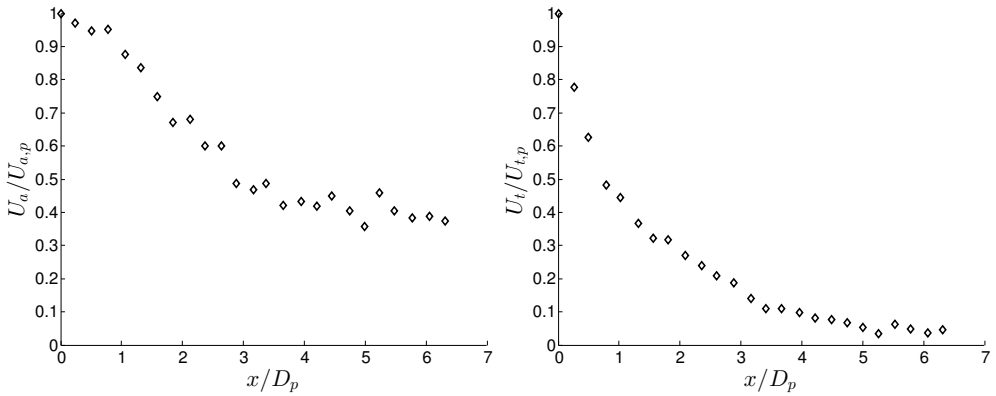

(a) (b)

Figure 2.7: Axial decay of axial and tangential velocity components of a propeller jet, measured by (Lam et al.*, 2011).*

2003). LES simulations of a dispersed two-phase plume in still environment were succesfully executed by Dimitrova *et al.* (2011). A limited number of studies, though, reports LES simulations of jets or single phase plumes in a crossflow, e.g. by Yuan *et al.* (1999), Recker *et al.* (2009) and Coussement *et al.* (2012). Muppidi and Mahesh (2007) and Muppidi and Mahesh (2008) performed Direct Numerical Simulations (DNS) simulations of transverse jets and passive scalar transport therein. LES of two-phase, small Stokes number particle plumes in crossflow did not receive much attention yet. LES simulations of dredging plumes have recently been executed by de Wit *et al.* (2014a); Saremi and Jensen (2014a). Using LES simulations of a TSHD overflow plume, de Wit *et al.* (2014c) showed that dredging speed, propeller turbulence and pulsing have a profound impact on the near-field dispersion of dredging plumes.

The particular form of the equations used for the LES model applied in this research are described in chapter 7.

Chapter 3

The experimental facility

3.1 Flume

A 15 m-long flume in the Hydraulics Laboratory of Ghent University was used to host the scaled overflow plume experiments (figure 3.1). The flume had a width of 0.8 m and a flow depth of about 0.6 m was used in all cases. The mean flow velocity U_0 was varied between 0.1 and 0.3 m/s. Profiles of the streamwise velocity component in the flume were verified using ADV measurements of lateral and vertical profiles. It was found that the lateral velocity profile in the flume was fairly uniform at more than 0.18 m from the flume walls. The flume side walls consist of smooth panels, but the joints between the panels are most likely the cause of the wider boundary layer velocity profile, as for rough walls. The vertical profile of the streamwise velocity exhibits a logarithmic profile. At 10 cm from the bottom wall, the streamwise velocity amounted to 90% of the maximum velocity.

The above observations lead to the conclusion that the studied plumes may preferrably not extend further than 0.2 m from the sidewalls and 0.1 m from the bottom wall before reaching the measurement sections.

The dredging plume experiments require the influence of a dredging vessel hull, with bow and stern section. The correct numerical simulation of the influence of mainly the stern section on the plume behaviour is an objective later in the research. Since the flume is too narrow to include a threedimensional vessel hull shape without significant influence of the flume wall proximity, a schematised, two-dimensional hull was designed. To this end, a 2.12 x 0.8 m polycarbonate plate was given a bow and stern section by folding the plate at 60°angles at both ends. The schematised hull is therefore

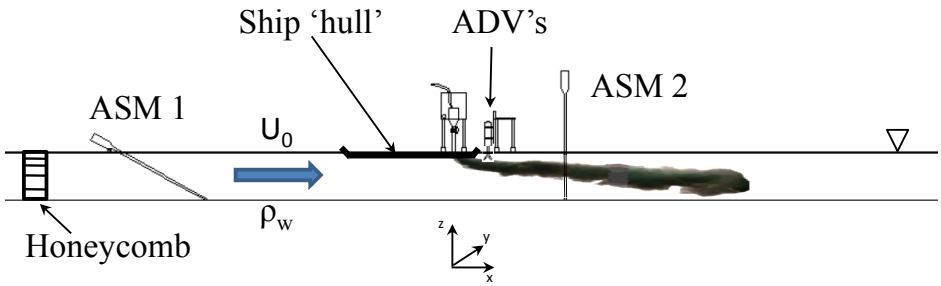

(a)

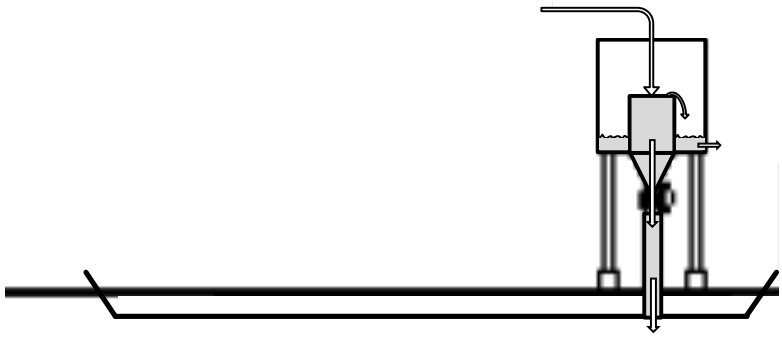

(b)

Figure 3.1: Top panel: Experimental setup, with a plume feeding mechanism containing a constant head vessel mounted on top of the flume. ADV and ASM2 instruments installed at respectively 0.5 m and 1.4 m from the plume exit. Lower panel: Detail of the schematised hull and constant head vessel.

laterally uniform and represents an infinitely wide vessel, in comparison to the overflow shaft pipe diameter. The overflow pipe was fitted flush with the schematised hull at a streamwise distance of 1.8 m downstream of the bow. Its axis was positioned in the direction normal to the hull plate. The stern section of the schematised hull is located at 0.32 m downstream of the overflow pipe.

A boundary layer will develop at the schematised hull before the flow reaches the plume exit point. The streamwise development of a smooth wall boundary layer thickness can be expressed as follows, see e.g. Douglas *et al.* (1995):

$$\delta_s = 0.37 x Re_x^{-1/5} \tag{3.1}$$

$$Re_x = \frac{\rho_w U_0 x}{\mu_w} \tag{3.2}$$

For a smooth wall, the boundary layer for flow velocity U_0=0.3 m/s has a thickness of about 0.047 m at the plume release point. Using the formula by Schlichting (1979),

$$\delta_r = 0.16 x Re_x^{-1/7}, \tag{3.3}$$

A δ_r=0.044 m is found, very close to the result using the formula by Douglas *et al.* (1995).
The value found for δ_r is of the same order of magnitude as the release pipe diameter D (between 0.034 and 0.060 m). The expected dimensionless boundary layer thickness δ/D is thus about 0.8 to 1.4.

In realistic situations, a TSHD dredger's hull can be considered as a rough wall. For a rough boundary layer, δ_r should no longer be dependent on the viscosity μ_w, but rather on a wall roughness height z_0. Elliott (1958) finds an exponent of 0.8 on x, for the thickness of a growing internal boundary layer in the atmosphere:

$$\delta_r = 0.86 x^{0.8} z_0^{0.2} \tag{3.4}$$

This is basically the same power as in the formula by Douglas *et al.* (1995). For typical distances between 50 to 80 m from the bow, using sea water density ρ=1025 kg/m^3 and a sailing speed of 2 knots, δ_r is between 0.63 m and 0.95 m using the equation by Schlichting (1979). Using the formula by Elliott (1958), with $z_0 = k_s/30$ and equivalent sand grain roughness k_s=0.1

mm, 1.6 m $< \delta_r <$ 2.3 m is found. Considering typical overflow shaft diameters between 1 m and 2 m, the dimensionless keel boundary layer thickness δ/D is thus between 0.3 and 2.3.

It can be concluded that for the chosen setup, the influence of the boundary layer on the plume extends to about 1 to 2 pipe diameters D, both in the realistic protype-scale situation as in the experimental situation.

3.2 Sediment minerals

Commercially available kaolin (China clay) was chosen for the fine sediment experiments for (i) its relatively low cation exchange capacity and (ii) its narrow grain size distribution. The first aspect eases the production of homogeneous mixtures, while the latter facilitates interpretation of the acoustic response, albeit that primary kaolin particles form microflocs due to their electrical charge. A second mineral was considered for execution of the plume experiments: quartz powder (ground sand M300, produced by Sibelco Benelux) was considered in the experiments for its absence of electrical charges responsible for flocculation and its particle size distribution being comparable to clays. The particle size distributions of both minerals have been determined with a Mastersizer laser diffraction device and are depicted in figure 3.2.

The quartz powder was not chosen for the main plume experiment, notwithstanding its inert property due to which it does not flocculate. The particle size distribution showed some fraction of larger particles, of $d >$60 μm. This fraction tends to settle in the different vessels used for mixing and transporting the water-sediment mixture, reducing the control over the particle size distribution reaching the plume. The quartz powder was used in separate experiments for the development and validation of a novel technique for the determination of turbulent fluxes of sediment (chapter 5).

The kaolin was selected for the main sediment plume experiments. The disadvantage is its flocculating behaviour. It was, however, assumed that no macroflocs occur in the mixing tank (see further shear stress analysis), and that the time to reach the plume exit and the subsequent lifetime inside the plume are too short to form large flocs. Any microflocs will have a very low settling velocity. Therefore they will not be able to influence the plume, since it is present within the measurement section of the experiments during

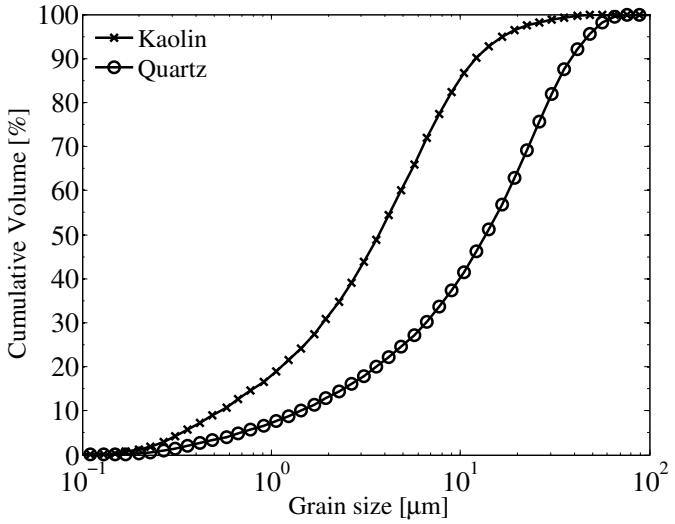

Figure 3.2: Cumulative particle size distribution (by volume) of the kaolin clay and quartz powder used for the experiments.

a maximum time of about 10 seconds.

3.3 Sediment mixing tank

To ensure a steady plume of which the statistics stabilise over time, the water-clay mixture for the plume release is required to stay homogeneous during the course of an experiment. This was achieved by using a mixing vessel (Figure 3.3).

The 0.3 m^3 cylindrical mixing vessel has been designed for being capable of keeping a mixture of fine sediments in suspension, while providing sufficient free space for instruments to be installed and containing sufficient water-sediment mixture for a 20-minute plume experiment. A 7,500 l/h submersible pump was installed for this purpose near the bottom of the vessel. This pump is positioned with its nozzle in the centre and blows towards the bottom from a height of 10 cm, generating the required circulation at a total shear stress of about 2.5 Pa (as measured by the ADV) in the centre of the vessel. Even though concentrations are high, at this level of shear stress macroflocs are not formed, see Manning and Dyer (2007) and Winterwerp *et al.* (2006) for estuarine mud data. In this way, a narrow size distribution of small microflocs improves reproducibility. Moreover, the mixture was

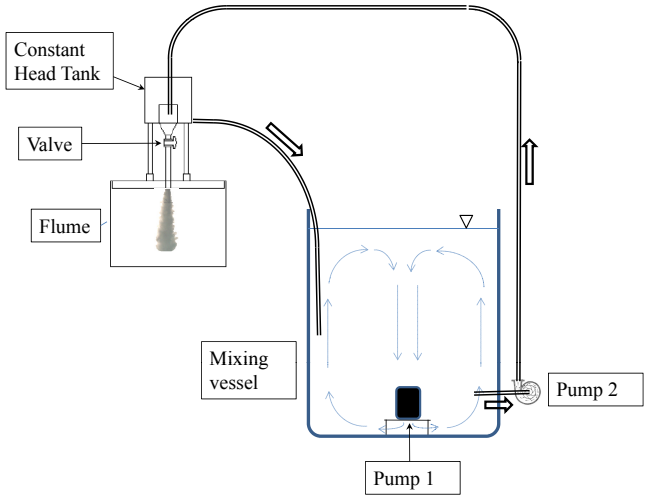

Figure 3.3: Plume feeding mechanism including a mixing tank, pumps and constant head vessel.

running through the submerged pump with a circulation time of 2 minutes, further reducing the chance of large flocs in the population.

The capacity of the tank and submerged pump to keep mixtures with various sediment concentration in a homogeneous state was monitored during a number of tests. In these tests, an ASM instrument (Argus, 2007) was positioned in the tank during full-length test runs. For a description of the ASM instrument, please refer to section 4.3.1. The measurements using the ASM equipment demonstrated that no significant vertical sediment concentration gradient develops during the course of an experimental run of about 20 minutes. The average concentration in the tank did not change either. After the test runs, some sediment deposits were found in the tank. The deposits were dried and weighed to determine the dry mass. The deposits accounted for a maximum fraction of the initial dry sediment mass of about 0.1%.

During the course of each experiment run, an infrared instrument (ParTech, see section 4.3.1) monitored continuously the sediment concentration in the

center of the tank to verify the constant level of the sediment concentration.

The water-sediment mixture is subsequently pumped towards a constant head vessel above the flume, described in the next section.

3.4 Constant head vessel

The constant head vessel is positioned in the experimental setup as shown in figure 3.3. It is mounted on top of the flume's sidewalls, above the schematised hull. The constant head vessel is fed with a discharge slightly larger than the plume discharge at any time. The excess discharge is flowing over the edge of the inner vessel and is returned to the mixing tank. In this way, the pressure head in the vessel is constant. The constant head vessel was calibrated using clear tap water, at temperatures between 13 and 15°C. It demonstrated the vessel is capable of maintaining a constant flow. Since the flow discharge through an orifice is a function of the kinematic viscosity, it can vary using different temperature and sediment concentration. Therefore, after each plume experiment the plume release discharge was determined by dividing the released volume of mixture by the time elapsed.

Different discharges can be obtained using orifices with different diameter, mounted inside the release pipe. Streamlining is ensured further down the overflow pipe (between constant head vessel and the plume release point) by means of three smaller pipes fitted in parallel inside the main pipe. This is considered as a necessary feature since it was shown in the past that swirling motions in the pipe flow can lead to significantly different turbulent structures and plume spreading rates (Pham *et al.*, 2006). Weak control of these motions would lead to reduced chances of reproducing the experimental plume dynamics in a numerical model, developed in a later stage of this PhD research.

In order to produce plume trajectories comparable to a full-scale situation, the pipe Reynolds number $Re_p = W_0 D/\nu_m$ should be considered. In realistic situations, Re_p is typically of the order 10^6 to 10^7. This cannot be achived in experimental conditions, unless a fluid with extremely low viscosity would be used. The pipe Reynolds number is thus maintained at a level to ensure a turbulent pipe outflow at any times (Re_p >4000). This corresponds to a minimum outflow velocity of W_0=0.1 m/s for the pipe with D=0.034 m and of W_0=0.067 m/s for the D=0.06 m pipe.

The constant head vessel's orifices were dimensioned in order to achieve overflow pipe velocities higher than these thresholds.

3.5 Air bubble injection

In the specific tests during which the influence of air bubbles is assessed, air bubbles are injected in the overflow pipe with an injection needle connected to a compressor. The injection occurs at a pressure of 3 bar and produces bubbles of various diameters in the overflow pipe. Controlling the size of air bubbles is difficult. However, only air bubbles having a rise velocity smaller than the flow velocity in the exit pipe will be released. During the air bubble experiments described in this thesis, the exit velocity was 0.3 m/s. Air bubbles in a water-sediment mixture of density ρ_m equal to 1020 kg/m^3 have a terminal rise velocity of 0.3 m/s at a diameter of about 3 mm according to Talaia (2007). Only bubbles with diameter of 3 mm or smaller will travel down the overflow pipe, larger bubbles rise in the constant head vessel before entering the overflow pipe. This fixes the upper limit of air bubble rise velocity to scale with the maximum air bubble rise velocity in reality. Unfortunately, the lower end of the bubble rise velocity distribution is unknown in real dredging conditions and difficult to control in an experiment. Images were taken of the air bubbles released from the overflow pipe (Figure 3.4) without sediment in the pipe flow. In a single image, no information is available about the distance of the air bubble from the camera. However, the distance from the camera to the center of the pipe is 40 cm and the width of the area containing air bubbles is about the same as the pipe diameter at short distance from the pipe. Therefore, the uncertainty on the air bubble diameter measured in this way is about 10%. Using the pipe diameter as a ruler, the air bubble diameter is estimated to range from 0.5 mm to 3 mm. A small number of larger bubbles are present due to coalescence of primary bubbles.

Further, the volume concentration of the air bubbles is determined as follows. The volume discharge released from the calibrated constant head vessel is known. First, the volume discharge of water-sediment mixture Q_0 is measured by timing the release of a given volume of mixture from the reservoir, of which the result has to be in accordance with the constant head vessel calibration. Then the air bubble release mechanism is turned on, after which the same measurement is taken, resulting in the volume discharge of the mixture in the presence of air bubbles $Q_{m,a}$. The air bubble volume concentration or void fraction θ_a is determined from

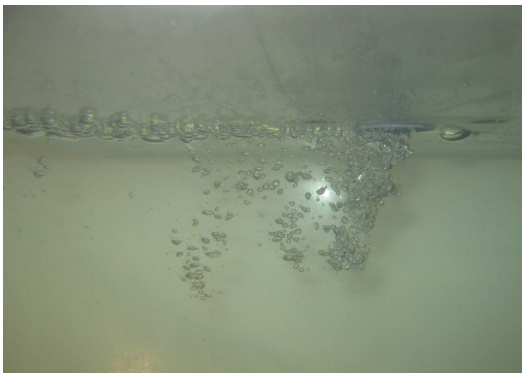

Figure 3.4: Image of air bubbles released from the overflow exit pipe in a plume without sediment at the same exit flow velocity as in the sediment plume experiments.

$$Q_a = \theta_a Q_0 = Q_0 - Q_{m,a} \quad . \tag{3.5}$$

The void fraction obtained in the present experiments was between 9% and 30%. Shortly after release, the larger air bubbles rise to the bottom of the polycarbonate plate representing the TSHD hull, whereas the smaller bubbles are ejected further from the exit and are entrained with the mean flow. However, since the rise velocity of the bubbles is of the same order of magnitude as the horizontal mean flow the bubbles reach the hull plate relatively fast: at most after 4 to 6 pipe diameters.

Given the limitations in the measurements of air bubble characteristics inside the turbid plume, only a qualitative evaluation of the influence of air bubbles in the experimental plumes will be given in the present research.

Chapter 4

Measurement techniques

4.1 Introduction

During the course of the experiments carried out for a sediment-laden plume in crossflow, both flow velocity components and sediment concentration were monitored. The background sediment concentration is monitored upstream the plume to take into account any sediment in the background flow in the flume. Since the data generated serve only for small corrections with slow variation, this type of measurement can be taken with low sampling frequency. The calibration range of the instrument does not need to exceed sediment concentrations of c=10-100 mg/l.

Measurements inside the sediment plume, however, are needed with high variation in sediment concentration, ranging from 10 mg/l to 10.000 mg/l. The rapid turbulent fluctuations need to be captured with high-frequency sampling of both sediment concentration and flow velocity, at the same time and location. This poses challenges, certainly for the determination of the turbulent fluxes of momentum and mass, see chapter 5.

The application of laser techniques (e.g. Particle Image Velocimetry, PIV) for simultaneous measurements of turbulent fluctuations of both flow velocity and sediment concentration has been shown to be successful (Breugem and Uijttewaal, 2007; Breugem, 2012). The PIV technique allows high temporal en spatial resolution. However, this technique is limited to flows with high translucency. Therefore, in turbid flows carrying relatively high concentrations of fine-grained sediments (>10-100 mg/l), acoustic techniques are often the methods of choice (Gratiot *et al.*, 2000; Sassi *et al.*, 2013).

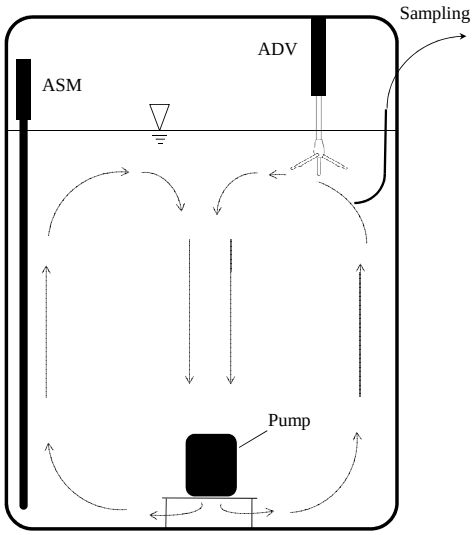

Figure 4.1: Setup of the mixing vessel during instrument calibration, with the ADV for backscatter measurements, a submersible pump for mixture homogenisation, an optical backscatter device (ASM) for sediment mixing monitoring and a sampling tube connected to a peristaltic pump (not shown). Arrows indicate circulation generated by the submersed pump.

A series of test experiments have been performed to analyse the response of the Acoustic Doppler Velocimeter or ADV (Lohrmann *et al.*, 1994) and Argus Surface Meter or ASM (Argus, 2007) to sediments in suspension. The mixing vessel with submersible pump is equipped with frames on which acoustic - ADV- and optical -ASM- backscatter instruments are installed as well as sampling equipment (Figure 4.1).

4.2 Acoustic measurements

4.2.1 Introduction

In the past, acoustic methods have been widely used for the determination of the flow velocity vector and sediment concentration at a point or along a profile. The sediment concentration measurements are based on the backscatter intensity of the returning acoustic signals (Hoitink and Hoekstra, 2005; Merckelbach and Ridderinkhof, 2006).

(a) (b)

Figure 4.2: Different types of probe for the ADV. (a) Field Probe; (b) Sidelooking Probe.

In present experiments, an Acoustic Doppler Velocimeter (ADV) has been used for the simultaneous measurement of flow velocity components and sediment concentration. The ADV was first described by Lohrmann *et al.* (1994) as a tool to obtain information on mean and turbulent properties of open-channel flows (figure 4.2).
Different authors have shown the capabilities of the ADV for detailed measurements of sediment concentration (Hosseini *et al.*, 2006; Nikora and Goring, 2002). The ADV is widely used as a tool to measure mean and fluctuating velocity components in both field work, e.g. Nikora and Goring (2002), Chanson *et al.* (2008) and Elçi *et al.* (2009), and laboratory experiments, e.g. García *et al.* (2005) and Salehi and Strom (2011). Due to its relatively high sampling rate (25-100 Hz), it is one of the preferred equipments for measurements of turbulent flows. Due to its sampling volume detached from the transducers, it is seen as a non-intrusive measurement instrument, although Poindexter *et al.* (2011) found that acoustic streaming can induce artificial currents in low-dynamic flow.

4.2.2 Flow velocity measurements

The flow velocity measurement by an ADV is based on the Doppler principle. The ADV emits acoustic pulse pairs towards a relatively small sampling volume (figure 4.3), of which the height can be varied by changing the instrument settings. The acoustic pulses are backscattered by microscopic impurities in the flow (sediments in the field, seeding material in the laboratory).

The backscattered acoustic pulses are captured by three or four receivers (beams), positioned at a 60°angle with the emitting direction (figures 4.2 and 4.3).
The pressure data registered by the receivers is then processed using the pulse-to-pulse coherent method (e.g. Zedel *et al.* (1996)). Unlike in other acoustic instruments recording velocity, the Doppler phase shift is used rather than the Doppler frequency shift. The Doppler phase shift is the difference between the pulse-to-pulse distances before and after scattering in the sampling volume (schematically shown in two dimensions in figure 4.3). The transducer emits a pulse pair with a given time interval towards the sampling volume. When the scatterers in the sampling volume are moving with the flow towards a receiver (receiver A) the Doppler effect will cause a compression of the signal, both leading to a frequency shift and to a reduced distance between the pulses. The opposite occurs when the scatterers are moving away fromt a receiver (receiver B). When the phase shift is negative in both receivers, the flow is directed upwards, when the phase shift is positive in both receivers, the flow is directed downwards. When the signs of both phase shifts is opposite, the flow is from left to right, or from right to left, like in figure 4.3. In reality, the ADV has at least three receivers so that all three components of the flow velocity can be determined. The phase shift is computed in the electronics by evaluating the autocorrelation of the pressure time series received, using the covariance method (see Rusello (2009)). The result is a velocity signal for the three spatial components aligned with the beams. A transformation matrix representing the geometry of the beams is used to transform the signals to series of the three carthesian velocity components u, v and w. The firmware available in the ADV allows a maximum sampling frequency of 25 Hz, with an internal ping sampling frequency up to 5000 Hz. The resolution of the echo intensity is 0.45 dB.

The accuracy on flow velocity measurements taken by the ADV instrument is reported by Nortek to be equal to 0.5%$\pm$1 mm/s. This level of accuracy can most probably only be achieved in case of sound deployment settings by the user.

Different parameters have to be defined before starting a recording in the Nortek ADV deployment software. A Nominal Velocity Range has to be defined to set bounds to the computed phase shift, which lies between -π and +π. In the present measurements, this setting has been set to $\pm$0.3 m/s in all recordings.

The next parameters to consider are related to the extent of the sampling

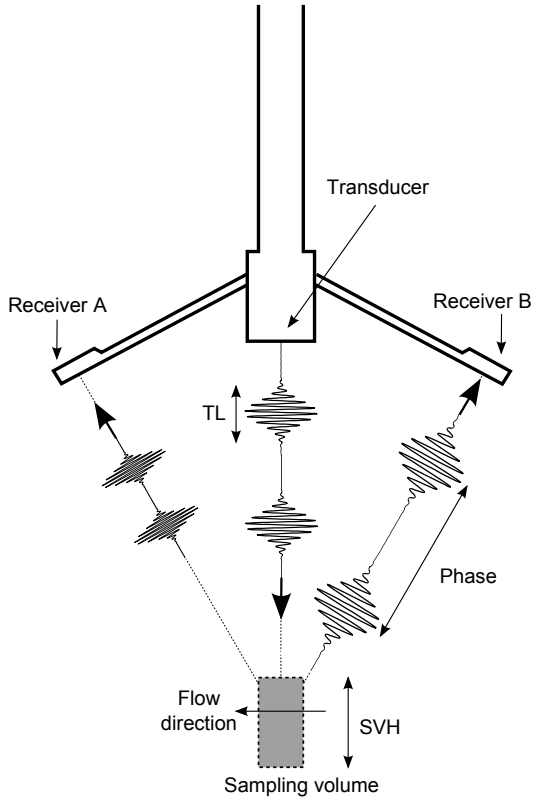

Figure 4.3: Working principle of the ADV, with a transducer emitting pulse pairs and receivers registering the backscattered pulses.

volume. The sampling volume is always cylindrical, with a diameter of 6 mm and is situated at a distance of 50 mm for the sidelooking probe (or 100 mm for the field probe). The height of the sampling volume (SVH) can be defined by the user, as well as the length of the pulses (or Transmit Length, TL). Considerations to make before choosing the SVH and TL are the following. Firstly, the SVH determines the volume of the sampling volume, which determines the number of scatterers in the sampling volume. TL determines how long the acoustic pulses will be in physical space, effectively limiting the sampling volume for low values of TL. In flows with limited scatterers, choosing a small sampling volume height and/or TL might lead to a weak signal amplitude, causing spikes in the flow velocity time series. On the other hand, choosing a high SVH and TL reduces the spatial accuracy of the measurement point. The measurement is indeed an average over the sampling volume. In case small turbulent length scales need to be taken into account, the sampling volume size should be put in relationship with the expected turbulent length scales. In the present measurements, scatterers are abundant, given the sediment in the plume. Here, another consideration has to be made related to the saturation of the amplitude signal. It is our goal to use the ADV not only for velocity measurements, but also for simultaneous measurements of c. As will be demonstrated below, the choice of SVH and TL determines the level of c at which saturation occurs and to which level of c the calibration is limited to.

In the sediment plume measurements, the SVH has been set at SVH=7.3 mm while the pulse length was set to TL=0.6 mm. It will be shown in chapter 5 that this setting results in an optimum extent of the calibration range for fine sediment concentration. An analysis of the expected length scales learns that the Taylor microscale will be between 1 and 10 mm for the studied flows, at laboratory scale. The pulse length setting TL=0.6 mm would therefore be small enough to capture the largest part of the turbulent kinetic energy present in the flow.

The method with which these optimum instrument settings were determined is described in the following section.

4.2.3 Calibration for suspended sediment: method

In this section, the method for the optimisation of the ADV deployment settings to obtain a widely applicable calibration function is described. A linear relationship between the fine sediment concentration and the logarithm of the

backscatter amplitude is widely accepted (Ha *et al.*, 2009; Salehi and Strom, 2011). The linear range can, however, be relatively limited. Therefore, it is investigated using acoustic theory whether a calibration curve including the start of the saturation range is valid and does not suffer from reduced accuracy.

The ADV emits single frequency acoustic waves, reflecting on the particles in the flow. Scattering in the Rayleigh regime (Rayleigh, 1945) produces a sufficiently strong backscatter signal if

$$k \cdot a > 0.05, \tag{4.1}$$

where k is the acoustic wavelength and a is the particle radius. The signals scattering off the fractions for which equation 4.1 is valid can be detected provided that for all fractions in the particle size distribution the following is true:

$$k \cdot a < 1. \tag{4.2}$$

The consequence is that single-frequency acoustics (as applied in the ADV) cannot be used for sediment concentration measurements when either the particle size distribution is strongly varying (in time or space) or the grain size distribution is relatively wide (Hanes, 2012). This is one of the arguments for the choice of china clay for the plume experiments, which consists mainly of the kaolin mineral. A second mineral was considered for the experiment for its inert behaviour avoiding flocculation: quartz powder. It was used in the validation process of the methods for calibration range optimisation and turbulent flux measurements. It was, however not selected for the remainder of the plume experiments due to the settling of the more coarse fractions of $d > 60\mu$m (figure 3.2), especially due to the longer run time in the plume in crossflow experiments.

A series of test experiments have been performed to analyse the response of the ADV signals to sediments in suspension. Two different probes for the 10 MHz Nortek Vectrino ADV have been used to carry out measurements in sediment suspensions: a sidelooking lab probe (SP) and the downlooking field probe (FP). Four different acoustic pulse settings of the ADV have been tested with the FP.

The calibration of the ADV for sediment concentration was performed inside the mixing tank described in section 3.3. The ADV was installed in the vessel with a sample intake pipe positioned near the ADV sampling volume. The ASM was monitoring the mixture homogeneity continuously. Both the

ADV FP probe and the SP probe were used to determine calibration curves. The FP probe has its sampling volume at 10 cm from the transducer, the SP probe at 5 cm. The acoustic backscatter signal is expected to saturate at a certain concentration, therefore the sediment concentration is varied between 1 mg/l up to 20 g/l in this case. The goal is to construct calibration curves at a variety of instrument settings using both probes and determine the optimal combination of probe and settings to extend the calibration range to the highest sediment concentration possible.

4.2.4 Acoustic sediment scattering theory

The ADV instrument emits pulse pairs to the sampling volume where particles scatter the acoustic wave. The portion scattered at a 30° angle arrives at four receivers. The volume backscatter at the instrument receivers, I, can be described by the sonar equation (Lohrmann *et al.*, 1994):

$$I = CS_f S_a \frac{e^{-2(\alpha_l+\alpha_r)R}}{R^2} \tag{4.3}$$

where C is the particle concentration, α_l is the water absorption, α_r is the attenuation of acoustic energy by suspended particles, R is the acoustic propagation path length, S_a describes the particle backscatter properties and S_f contains the instrument specific properties. For scattering at a wave number k of about $4.3 \cdot 10^4$ m^{-1} and a particle diameter of about 4 μm, Rayleigh scattering theory is valid since $k \cdot a < 1$, with a the particle radius. Using Rayleigh scattering theory, the volume backscatter intensity, B_r, can be written as (Hoitink and Hoekstra, 2005):

$$B_r = 10 \log_{10} I = 10 \log_{10} \left(\frac{3\phi(1+\cos^2\theta)k^4 a^3}{\rho_s} C \right) \tag{4.4}$$

with ρ_s the particle material density and ϕ a material parameter. The additional $1+\cos^2\theta$ factor stems from the instrument-specific angle θ between emitted waves and scattered waves traveling to the receivers. Rearranging equation (4.3) yields the following relation between the sediment concentration C and the acoustic signal received:

$$10 \log_{10} C = \frac{1}{2}(SNR + K) + \frac{20}{\ln(10)} \int \alpha_r \, dR - 10 \log_{10}(S_f S_a). \tag{4.5}$$

Here, the signal to noise ratio $SNR = 20\log_{10}(I/N)$, with N the noise level, is the expected echo intensity corrected with the instrument's inherent noise

levels. K contains the spherical spreading term and the acoustic attenuation in water, which are added to the output signal by the ADV and can thus be excluded from calculations. The derived expression is in line with the equations and coefficients found by Salehi and Strom (2011). The expression for the sediment attenuation coefficient α_r is used as defined by Hoitink and Hoekstra (2005) and is a linear function of sediment concentration. The integral of sediment attenuation can be linearised if it is assumed that the sediment concentration is uniform over the acoustic path.
Combining equation (4.3) without acoustic path loss terms (terms with R), and equation 4.4, the backscattering parameter S_a can be written as follows:

$$S_a = 3\phi(1 + \cos^2\theta)\frac{< a^2 f_b^2 >}{\rho_s < a^3 >} \tag{4.6}$$

with $f_b = 1.1\ k^2a^2$ the form function (Thorne and Hanes, 2002). The <> operator denotes averaging over the particle size distribution.
Equations (4.5) and (4.6) and the sediment attenuation expression by Hoitink and Hoekstra (2005) are applied to reproduce the echo levels (SNR) measured by the ADV. In case it can be shown that the non-linear part of the relation between sediment concentration and acoustic backscatter is dependent on the known equations only, the calibration beyond the linear region is justified. In that case, other factors such as multiple scattering are shown to be not relevant for the sediment concentration range studied, as will be shown below. The only remaining unknown constant in the equations, i.e. instrument parameter S_f, was fitted to the instrument output and set to $S_f = 7.85$. The actual speed of sound c_s, measured by the ADV, was used to compute the acoustic wave number $k = 2\pi f/c_s$ for each concentration level separately. The speed of sound increased by about 1.7% when measured at 20 g/l kaolin concentration (c_s = 1487 m s^{-1}) compared to clear tap water (c_s = 1462 m s^{-1}) at the same temperature. The full particle size distribution is used to compute the partial backscatter intensity, calculated as the backscatter emitted from a given class of sediment size. The total emitted backscatter is then computed as the integral over the full particle size distribution. The results are shown in figure 4.4. The SNR is computed directly from the equations, the backscatter amplitude (AMP, in counts) is derived from SNR and noise levels reported by the instrument: $AMP = N \cdot 10^{SNR/20}$, where N is the noise level (in counts). Overall, the Rayleigh scattering theory corresponds well to the signals in the ADV output, as does the sediment attenuation correction, with in both signals a saturation level around 10 g/l for the sidelooking lab probe (SP) with sampling volume at R = 5 cm from the emitter. The computed amplitude signal oscillates slightly due to the noise level in the equation to compute amplitude from SNR. The noise level

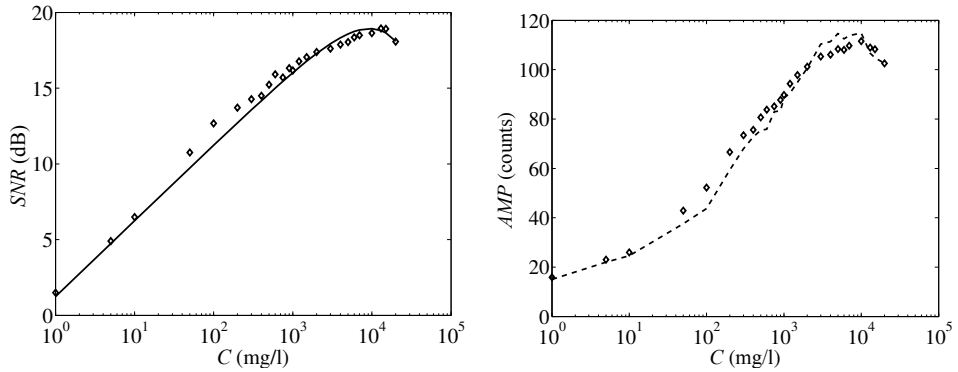

(a) (b)

Figure 4.4: Computed echo levels in SNR (a, full line) and Amplitude (b, dashed line) using full particle size distributions compared to measured levels using the SP probe (markers) in the mixing vessel experiment

is reported by the instrument as a rounded integer due to which the AMP curve is slightly oscillating.

It can thus be concluded that the saturation of the backscatter amplitude signal at higher sediment concentrations can be predicted using only the particle concentration as a variable. Therefore, the start of the saturation range can be included in the calibration range, provided the inversion of the acoustic equations does not induce an excessive error or noise amplification.

4.2.5 Calibration: results and optimisation

Varying the settings of the ADV pulse pre and post processing leads to a maximum extent of the range in which the signal can be calibrated against sediment concentration. The power level is set to LOW+ since Salehi and Strom (2009) found this leads to a calibration range for kaolin of an order of magnitude higher than for the High Power setting. A further reason to use a low power level is the instrument's acoustic streaming potentially inducing currents up to 2 cm s^{-1} when using the HIGH power level, rather than the LOW or LOW+ power level (Poindexter *et al.*, 2011). The low flow velocities studied in the test cases below make this consideration equally relevant.

Four combinations of different pulse Transmit Lengths (TL) and Sampling Volume Heights (SVH) have been tested using the FP probe. It appears that the SVH does neither influence the amplitude level, nor the saturation

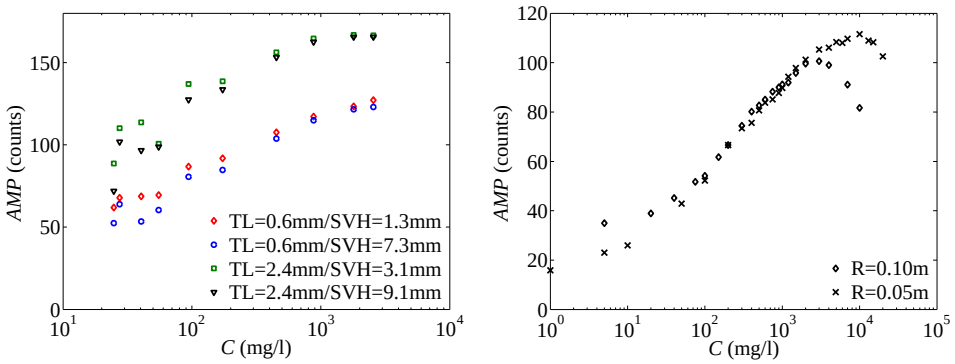

Figure 4.5: Amplitude versus kaolin sediment concentration curves as a function of (a) TL and SVH and (b) distance R between transmitter and receiver ($R = 0.10$ m for the FP and $R = 0.05$ m for the SP)

significantly. A longer pulse TL does increase the backscattered energy, and reduces the maximum sediment concentration at which the signal increases (Figure 4.5a). With the higher TL the amplitude signal saturates at a kaolin concentration of about 1 g/l, while with the lower TL at 2 g/l. Also for quartz powder the saturation point lies at a concentration a factor 2 or 3 higher with the shorter TL. Therefore, the shorter pulse TL of 0.6 mm was chosen to conduct the remainder of the experiments. The larger SVH was chosen due to the smaller noise variance in the amplitude signal, which is transformed to sediment concentration.

As expected from the dependency of the backscatter intensity on acoustic path length R in the sonar equation, the probe type has a significant influence on the saturation of the signal (Figure 4.5b). Since R is multiplied by the sediment attenuation in the exponential function of the sonar equation, the reduction of the signal starts at lower sediment concentration using a shorter R. From range tests in the mixing vessel, it can be observed that the calibration range can be extended further to 10 g/l in case the smaller SP probe ($R = 0.05$ m) is used rather than the FP probe ($R = 0.10$ m). This saturation point lies a factor 3 higher than what is found for most commonly used optical and acoustic field instrumentation, e.g. Fettweis *et al.* (2010), Elçi *et al.* (2009) and Hosseini *et al.* (2006).

Using the optimal instrument settings while measuring the amplitude level of increasing suspended sediment concentration and fitting a fourth order curve to $\log(C)$ yields a calibration curve spanning the range from 10 mg/l to 10 g/l for kaolin and from 10 mg/l to 3 g/l for quartz powder. Coefficients of deter-

mination of 0.99 and 0.98 respectively have been obtained for these fits (the kaolin curve is shown in figure 4.6). It must be pointed out that, using the law of propagation of errors, the uncertainty on the amplitude is transformed into an uncertainty on the sediment concentration as shown in equation 4.7, where for simplicity the case is shown with a first order relationship.

$$\sigma(C) = \left(\frac{\partial C}{\partial AMP}\right) \sigma(AMP) = p\, 10^{p(AMP)+q}\, \sigma(AMP) \qquad (4.7)$$

The raw backscatter signal of an acoustic wave (AMP_*) is Rayleigh distributed (Medwin and Blue, 2005). The variance introduced by this property is corrected for by means of the spectral correction described above, leading to a corrected backscatter intensity AMP. It can be seen that any remaining error in the amplitude signal is amplified with a factor equal to the coefficient p (equal to about 0.02 in a linear curve) times the sediment concentration itself. This can lead to significant errors in the higher end of the sediment concentration range. Since the amplitude shows lower relative variance levels for higher concentrations the effect described above is, however, partially cancelled out.
The variance existing on the amplitude signal measured in a uniform, still suspension is corrected for by means of the spectral correction described above. However, the spectral correction is performed using a constant reference spectrum for pink noise while there is some variation over the sediment concentration levels. It is estimated that this leaves about 10% of the variation in the amplitude signal. Application of equation 4.7 learns that the maximum errors on sediment concentration due to amplitude errors occur at higher concentrations and amount to about 1%. This is much smaller than the rms relative error on sediment concentration introduced by the calibration curve fit, which amounts to 24.6% on average.

4.2.6 Turbulence measurements

High-frequency measurements of flow velocity components can be obtained using the ADV. To derive turbulent information from the timeseries, a number of considerations are needed regarding measurement of turbulent length scales based on single-point observations.

Consider a Eulerian measurement of fluctuations $u'(t)$ at fixed point in space and an eddy with characteristic macro scales $\mathcal{U}$ and $\mathcal{L}$. The eddy is transported by the mean flow $\bar{u}$ across the measurement point. The definition of the total differential of a quantity leads to (Nieuwstadt (1998)):

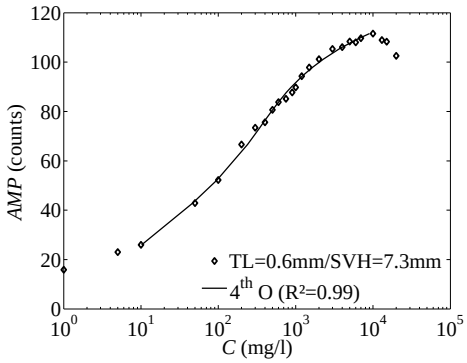

Figure 4.6: Calibration curve for transformation of the backscatter amplitude to sediment concentration. Measurements are shown by markers and are taken using TL=0.6 mm and SVH=7.3 mm. A fourth order fit is shown with a coefficient of determination (R^2) of 0.99.

$$\frac{\mathrm{d}}{\mathrm{d}t} = \frac{D}{Dt} - \bar{u}\frac{\mathrm{d}}{\mathrm{d}x} \tag{4.8}$$

Which means that the variation in time observed at a fixed point in space consists of two terms: the first term describes the change in time of the travelling eddy, the second term describes the change of observation due to the spatial structure passing by with velocity $\bar{u}$, the so-called advection term. Relative magnitudes of both terms can than be estimated as:

$$\frac{\mathrm{d}}{\mathrm{d}t} \approx \frac{\mathcal{U}}{\mathcal{L}} - \frac{\bar{u}}{\mathcal{L}} = \frac{\bar{u}}{\mathcal{L}}\left(\frac{\mathcal{U}}{\bar{u}} - 1\right) \tag{4.9}$$

The characteristic timescale of an eddy is here $\mathcal{L}/\mathcal{U}$. The ratio $\mathcal{U}/\bar{u}$ is the relative magnitude of turbulent to mean velocity scales. In most flows this ratio is small.

The Taylor hypothesis now assumes that the first term can be neglected, so that the change in spatial structure in a short time interval is small, also known as 'frozen turbulence'. Thus we can write:

$$\frac{\mathrm{d}}{\mathrm{d}t} = -\bar{u}\frac{\mathrm{d}}{\mathrm{d}x} \tag{4.10}$$

The measurements of fluctuations in an Euler reference frame can therefore be used to obtain information on the spatial structure of turbulence and not on the evolution in time of a turbulent structure. For that purpose observa-

tion must be executed in a Lagrangian (moving) reference frame.

The Taylor hypothesis can then be used for the determination of the length scale of local turbulent fluctuations, as shown by Lewis (1997). The length scales of the turbulent structures are determined by:

$$l = \bar{u}\ t_l \tag{4.11}$$

The time scales t_l present in the flow field can be obtained from spectral analysis of high-frequency velocity measurements. This is achieved by determining the autocorrelation of turbulent fluctuation signal u'(t) with itself,

$$R(\Delta t) = \overline{u'(t)u'(t+\Delta t)/u'(t)^2} \tag{4.12}$$

For any Δt with high autocorrelation R, a turbulent timescale $t_l = \Delta t$ can be associated with the turbulent flow studied. The corresponding length scales l, and equivalent wavelengths κ can then be found using equation 4.11. This information can then be used to construct a frequency spectrum for velocity components or scalars transported by the turbulent flow.

4.3 Optical methods

4.3.1 Introduction

The ASM instrument (Argus, 2007) combines 144 infrared backscatter sensors in one array and is often used to measure bed level changes and sediment concentration near the bed. The manufacturer indicates a detection range between 5 and 5000 mg/l for fine sediments (d_{50}=20 μm). Here, the instrument is applied for three purposes:

- to verify the homogeneous sediment concentration in the mixing tank;
- to monitor background sediment concentration in the flume;
- to record the plume sediment concentration in a vertical cross section.

In the following, the calibration for each of the 144 optical backscatter sensors in the ASM instrument is described.

4.3.2 Calibration for suspended sediment

During a number of calibration runs, the ASM instrument was mounted in the mixing vessel (figure 4.1). While keeping the sediments in a uniform suspension, the sediment concentration c was gradually increased from 5 mg/l to 10,000 mg/l. At each concentration level, the ASM recorded the reflectivity at 1 Hz during 300 seconds to obtain sufficient samples for averaging.

Water samples were taken from the mixing vessel and were analysed for suspended particulate matter by filtering, drying the filters and weighing the difference between a used and an empty filter. The sample sediment concentrations were linked to the ASM instrument backscatter intensity (reflectivity) for each sensor. It was found that the reflectivity signal from the ASM sensors reached a saturation point at about 1500 mg/l, which is considerably smaller than reported by the manufacturer for 20 μm fine sediments. Most likely, this can be explained the smaller particle sizes of the kaolin clay, causing higher turbidity for the same mass concentration (more particles per unit of volume).

For each sensor, a second order curve was fitted to the data. When plotting the calibration data in a linear scale, deviations from a linear relation between sediment concentration and ASM backscatter are not discovered. Applying a linear fit would lead to erratic concentration results in the lower range. When plotting the sediment concentration on a log-scale, and fitting a second order curve through the points, a calibration curve is found with a good fit for both lower and higher concentration ranges (figure 4.7).

For each of the 144 sensors, the coefficient of determination was calculated, according to:

$$R^2 = \frac{\sum_{j=1}^{n}(\hat{c_j} - \overline{c_j})^2}{\sum_{j=1}^{n}(c_j - \overline{c_j})^2} \tag{4.13}$$

where n is the number of concentration levels for which measurements were included (n=13), $\hat{c_j}$ is the estimated concentration at level j and c_j is the actual sediment concentration in the mixing tank, at level j.

The average coefficient of determination for the 144 sensors of R^2=0.99 shows that the sediment concentration can be accurately predicted from the ASM reflectivity signal.

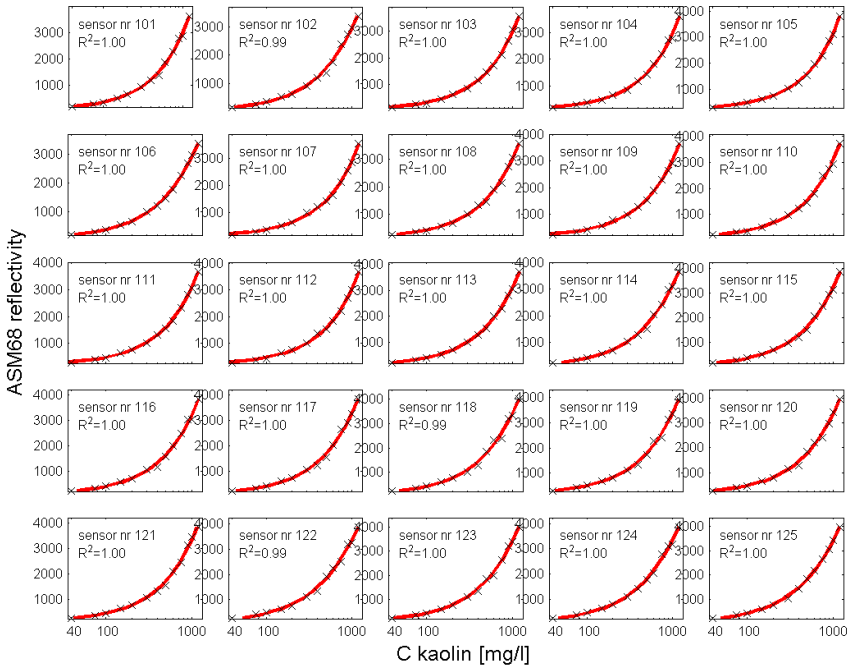

Figure 4.7: Calibration curves for a selection of the 144 sensors of the ASM instrument.

However, the limited upper bound of the calibration curves (1200 mg/l) requires a location in the plume at which the concentration has dropped to below this value. Therefore, the ASM instrument was positioned at 1.4 m downstream of the plume release point, or 22 to 41 pipe diameters, depending on the pipe. In some high-λ or low-F_Δ cases, the plume might have reached the flume bottom wall, or is already influenced by the flume sidewalls after this distance, which is a limitation. Nevertheless, the information on the two-dimensional profile of the sediment concentration can provide information on the structure of the plume.

4.4 Video imaging

4.4.1 Introduction

In addition to the detailed measurements of flow velocity and sediment concentration at a single point or line, a complete picture of the experimental plume is needed to determine the trajectory of the plume as well as its vertical extent. For this purpose, video imaging is used.

4.4.2 Method

Images were taken at high sampling frequency (5 Hz) of the plume's vertical outline. A background of diffuse white light is used to provide contrast with the plume edge. A minimum of 600 images per experiment have been used to compute fields of average light obstruction and its variance. The processing chain is designed to produce these fields on the plume symmetry plane at y=0. Obscuration α has been computed at each pixel as follows:

$$\alpha_{i,j} = \frac{B_{i,j} - I_{i,j}}{B_{i,j}} \tag{4.14}$$

where $B_{i,j}$ is the reference background light intensity, measured before the start of the experiment, $I_{i,j}$ is the light intensity measured during the plume experiment and i,j are the horizontal and vertical pixel indices. Images have been corrected for horizontal and vertical perspective deformation and for light refraction at an air-water interface, neglecting the intermediate refraction due to the 15 mm glass panels.

Light obscuration profiles are not used as a direct estimator of sediment concentration, which is complicated due to multiple scattering. The profiles are

used to determine the time-averaged plume trajectory and vertical extent as a function of horizontal distance. To this end, the images' pixel intensities have been averaged over time.

At each horizontal location x, the vertical position at which the light obscuration is maximal has been determined ($\bar{z}$). Connecting these points leads to a plume trajectory from the pipe to about 1 m downstream.

Assuming the average obscuration is a measure of the integrated, time-averaged concentration C over the y-direction, it can be shown that if a cross section of the plume has a Gaussian concentration profile, the obscuration profile's Gaussian half-width equals the 2D half-width. Let the 2D YZ-profile be a concentric Gauss profile with half-width equal to b_c in both the y and z directions:

$$C(y,z) = C_m \exp - \left[\frac{(z-z_0)^2 + (y-y_0)^2}{b_c^2} \right] \tag{4.15}$$

with C_m the maximum sediment concentration in the center of the profile. In this way, the concentration isolines are concentric circles. Assuming a linear relationship between C and light obstruction, a value of the obscuration α at level z is propertional to the laterally integrated sediment concentration:

$$\alpha(z) \propto \int_{-\infty}^{\infty} C(y,z) \ \mathrm{d}y \tag{4.16}$$

Solving the integral leads to:

$$\int_{-\infty}^{\infty} C(y,z) \ \mathrm{d}y = C_m b_c \sqrt{\pi} \ \exp\left(-z^2/b_c^2\right) \tag{4.17}$$

The vertical profile of the laterally integrated sediment concentration ($\sim \alpha(z)$), is indeed a gauss curve with the same (vertical) half-width b_c.

In this way, not only a time-averaged trajectory of the plume is obtained (figure 4.8) but also the vertical half-width. These parameters will be easily comparable with the numerical model to be developed.

Additionally, the standard deviation of the obscuration at each position gives the intermittency factor at the y=0 plane (figure 4.9). It can already clearly be observed that the intermittency (turbulent variations) in the lower section of the plume is more strongly developed compared to the upper part of the

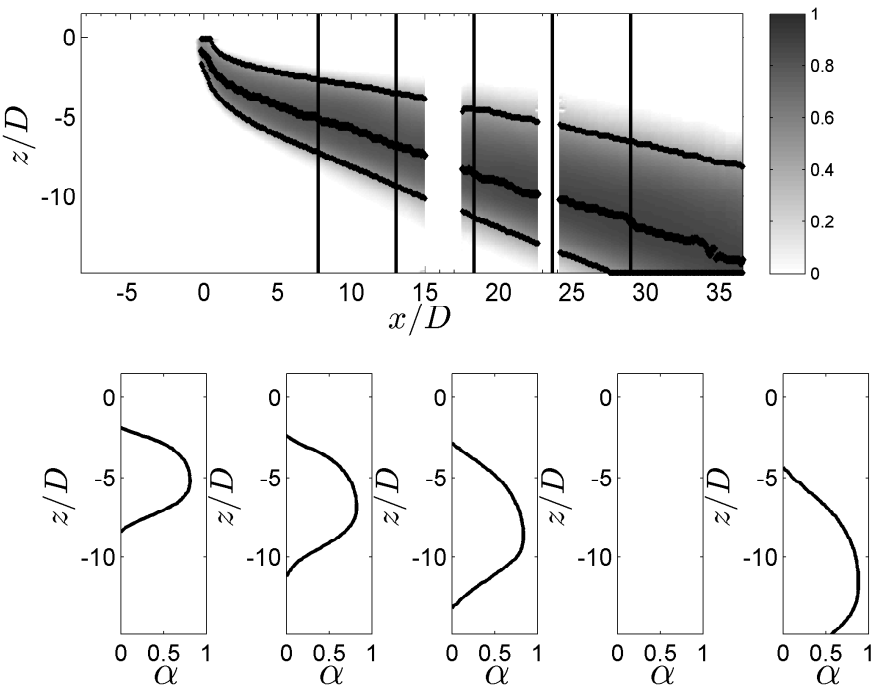

Figure 4.8: Interpretation of time-averaged obscuration images for trajectory and vertical extent of a plume.

plume (stable stratification).

In order to come to geometrically reliable results, corrections have to be made for the angle of perspective and for the refraction of light across the air-glass-water interface. These correction methods are described in the following sections.

4.4.3 Spatial calibration

Using a reference object held in the flume while taking images allows for the determination of the actual size of one pixel. This has been done for a location directly in front of the camera. The light penetrating the plume and reaching the camera is therefore not influenced by refraction at the air-glass-water interface and by perspective. At this location the reference pixel width $\Delta x_{p,ref}$ is valid. For locations away from the centre of the image, the increase in pixel size due to the perspective is taken into account. The apparent pixel size Δx_{ap} becomes:

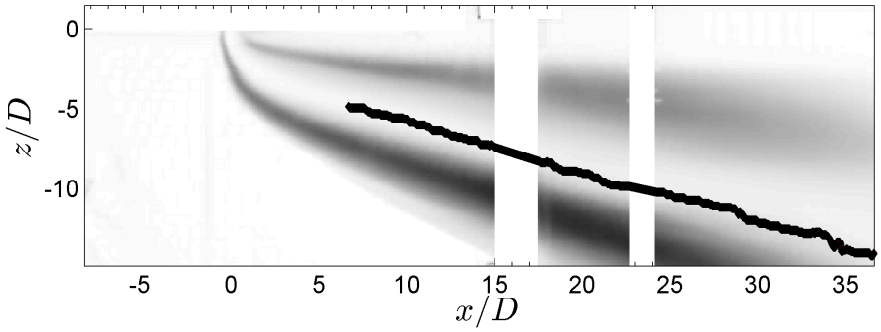

Figure 4.9: Pixel-per-pixel standard deviation of obscuration images.

$$\Delta x_{ap} = \left(\frac{1}{\cos\gamma_x}\right)^2 \Delta x_{p,ref} \tag{4.18}$$

where $\Delta x_{p,ref}$ is the reference pixel width and γ_x the angle between the frontal camera viewing direction (where Δx_{ap}=$\Delta x_{p,ref}$) and the actual viewing direction. The apparent pixel size is the pixel size at a location apparently observed, i.e. without correction for light refraction. A similar correction is made for the vertical apparent pixel size Δz_{ap}.

The actual apparent position x of the pixel in column i in the image can then be determined using:

$$x_{a,i} = \Delta x_{p,ref} \sum_{k=i(x_c)}^{i} \left(\frac{1}{\cos\gamma_{x,i}}\right)^2 \tag{4.19}$$

where $i(x_c)$ is the pixel column number at which $x = x_c$, with x_c the x-position of the camera. $i(x_c)$ is thus the column number in the center of the image.

The corrections for viewing angle and perspective are found to be no larger than 2 cm in the image section containing the plumes ($-0.03 < x < 1$), which is shown in figure 4.10.

4.4.4 Refraction correction

Apart from the correction for perspective and viewing angle, a coordinate correction for the refraction across the glass flume walls is needed.

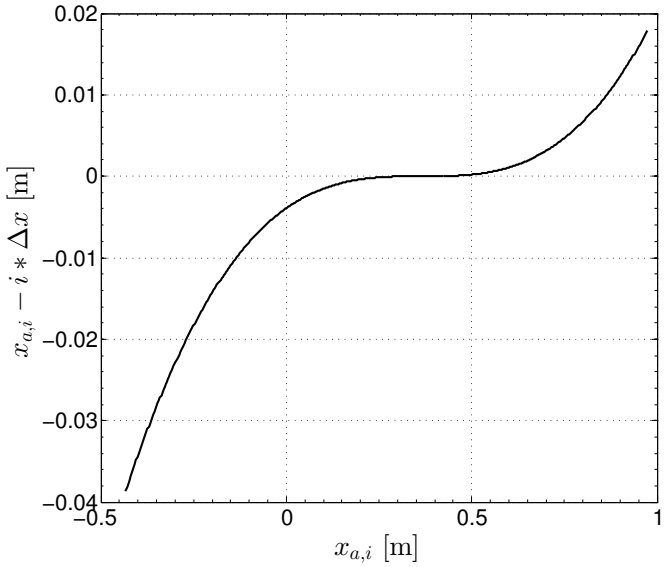

Figure 4.10: Correction for camera viewing angle and perspective.

The goal is to determine the vectorial difference between the apparent location on the $y = 0$-plane and the actual location. The basis is Snell's law, stating that

$$r_a \sin\gamma = r_w \sin\beta \tag{4.20}$$

where r_a and r_w are the refractive indices of respectively air and water, β is the angle between the incoming ray (between plume and glass) and the glass wall normal, and γ is the angle after refraction (between glass and camera). It implies the assumption that the thickness of the glass wall is small enough to neglect the refraction in two steps, namely first at the water-glass interface and second at the glass-air interface. The angle γ is known, as well as r_a and r_w. Therefore, the angle β can be determined.

It can then be shown that the vector difference between the apparent ray and the actual (refracted) ray between camera and $y = 0$-plane in the flume can be expressed as follows:

$$\overrightarrow{p_g p_w} - \overrightarrow{p_g p_{w,a}} = \left(\frac{\tan\beta}{\tan\gamma} - 1\right)\left(\frac{y_g}{y_c}\right)(x_a - x_c\ ,\ 0\ ,\ z_a - z_c) \tag{4.21}$$

where $\overrightarrow{p_g p_w}$ is the vector pointing from the viewed position in the plume p_w to the glass wall (p_g) and $\overrightarrow{p_g p_{w,a}}$ is the vector pointing from the apparently

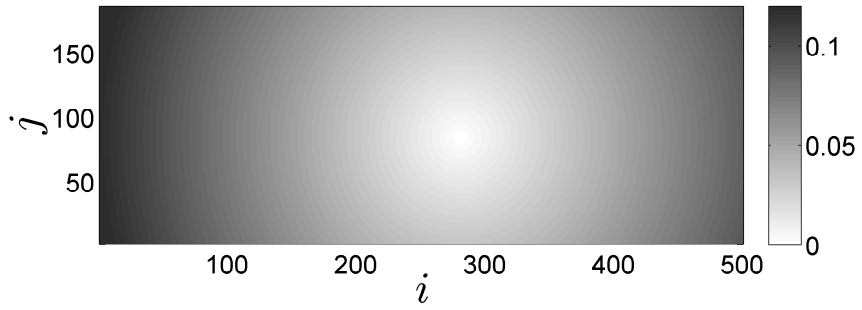

Figure 4.11: Correction for refraction of light across the glass walls of the flume.

viewed position in the plume ($p_{w,a}$) to the glass wall.

The corrections obtained in this way for the rows and columns of pixels used for the plume images are visualised as shown in figure 4.11.

Chapter 5

Turbulent flux measurements

The results presented in this chapter have been published in Decrop et al. *(2015a).*

5.1 Introduction

The analysis of turbulent sediment transport phenomena requires quantification of the different fluxes of momentum and sediment. In many environmental flows, turbulent fluxes play an important role in the associated transport processes, e.g. coastal sediment transport and plume dispersion (Fischer, 1979). Since turbulence is still not well-understood, no definitive turbulent diffusion model has been found. As a consequence, turbulence models still require calibration and validation, for which measurements of turbulent fluxes of momentum and sediments are needed (Lewis, 1997).

A number of difficulties are inherent to the quantification of turbulent fluxes of sediments. In order to determine the relevant correlations between velocity and sediment concentration, instantaneous measurements of both parameters are needed. Moreover, both measurements have to be conducted at exactly the same location. Additionally, the sampling frequency must be sufficiently high in order to resolve the relevant turbulent time scales, while the sampling volume has to be sufficiently small to resolve the relevant turbulent length scales.

The application of the Acoustic Doppler Velocimeter (ADV) for measurements of mean and fluctuating sediment concentration is still under debate

and different authors have attempted to determine range limits for sediment concentration calibration, background noise, influence of flocculation and grain size distribution (Zedel *et al.*, 1996; Ha *et al.*, 2009; Salehi and Strom, 2011).

This work aims to improve existing techniques and to develop additional methods to determine accurately the turbulent properties of water-sediment mixtures: Reynolds stresses, turbulent fluxes and turbulent intensity of sediment. The ADV's high sampling rate and its capabilities to measure both the velocity components and the sediment concentration simultaneously are exploited to develop procedures to obtain turbulent sediment flux information. This is achieved by means of carrying out the appropriate corrections for the high-frequency time series. This chapter describes methods to (i) optimise the extent of the calibration range for sediment concentration and (ii) to determine accurately the turbulent fluxes of sediment and momentum. The proposed methods are validated with measurements in a sediment plume test case.

In the following section, materials and methods used during the calibration of instruments and during the plume test case experiments are described. Subsequently, a chapter on basic acoustic scattering theory explores the validity of extending the calibration range for sediment concentration beyond the linear range. Next, a section describes the acoustic signal processing techniques used, followed by a chapter on the results obtained in test cases on a vertical, sediment-laden buoyant jet. Finally, conclusions are presented.

5.2 Experiments

5.2.1 Experimental method

An experiment has been set up in order to validate the calibration for sediment concentration and the techniques developed below to determine Reynolds stresses, turbulent intensity of flow velocity and sediment concentration as well as turbulent fluxes of sediment. Two types of vertically downward sediment plumes with constant outflow discharge and sediment concentration were released in still tap water at 12°C: a kaolin plume and a quartz powder-laden jet. The water used to prepare the sediment mixtures is the same tap water. To allow comparison of the measured flow parameters with plume measurements in the literature, a constant flow and concentration is impor-

tant. Also, the flow needs to be self-similar in order to scale the results and compare with measurements from literature taken in plumes of different dimensions and density difference. To comply with these criteria a dedicated installation was built. Figure 5.1 provides a sketch of the apparatus.

The water-sediment mixture is homogenised initially by mixing the sediment with water in high concentrations (order 100 g/l). Consequently, this mixture is added to tap water in the mixing vessel (Figure 5.1) until the experimental concentration is reached in the vessel. The mixture is kept in uniform suspension by a submersible pump (*Pump 1* in figure 5.1). A second pump (denoted as *Pump 2*) provides pressure to the mixture for transportation up to a constant-head tank located above the plume injection point. This tank consists of a smaller vessel constantly overflowing into a larger vessel. The overflowing mixture is channelled back to the mixing reservoir. From the smaller vessel, a pipe containing an orifice leads the mixture to the plume injection point. The constant head in the overflowing part ensures a constant discharge into the experimental flume.

The pipe diameter of 3.4 cm and pipe flow velocity of $W_0 = 0.12$ m/s lead to a turbulent pipe flow with Reynolds number of about 4100 (Pipe discharge Q_0 = 0.109 l/s). In the kaolin case, the clay concentration in the mixture was 5 g/l with a mixture excess density of $\Delta\rho = 3.1$ kg/m^3, equivalent to a reduced gravity $g' = g\Delta\rho/\rho = 0.039$ m/s^2. In the quartz powder case, a lower sediment concentration of 1 g/l was used ($\Delta\rho = 0.62$ kg/m^3, $g' = 0.0061$ m/s^2). The buoyant jet momentum length scale l_M ($=M_0^{3/4}B_0^{-1/2}$) determines the distance from the pipe where transition from initial jet behaviour to buoyancy driven plume behaviour occurs ($M_0 = Q_0W_0$ is the initial momentum of the plume, $B_0{=}g'Q_0$ is the initial buoyancy flux of the plume). Since measurements are taken at $z = 0.3$ m and the kaolin and quartz plumes had z/l_M values of 2.5 and 1.1 respectively, the kaolin case was in plume regime while the quartz case was still in jet flow regime.

The measurements of suspended sediment concentration and flow velocity components are decomposed using the Reynolds decomposition. The high-frequency signals are decomposed into a mean part (denoted by an overbar) and a fluctuating part (denoted with a prime), equal to the original signal minus the mean value. Radial profiles were taken point-wise from the axis of the plume towards the outer region. A minimum of $n = 3000$ samples was taken at each point, at a frequency of 25 Hz. When a normal distribution is assumed, a standard error on the measurement of the mean quantities is

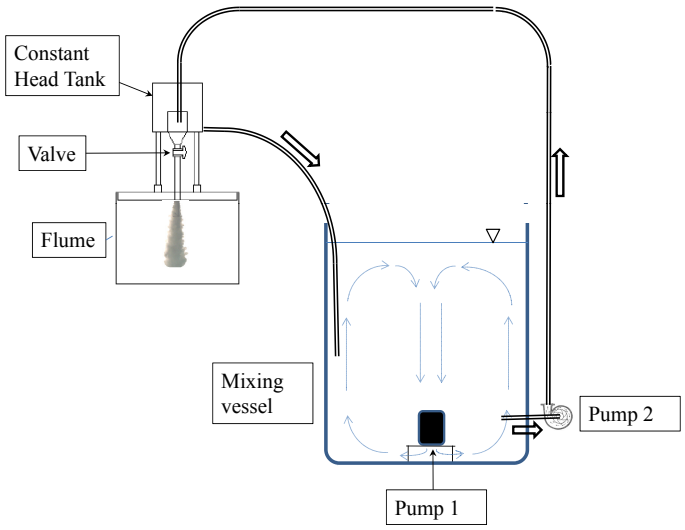

Figure 5.1: Setup of the vertical buoyant sediment plume experiment. Mixing vessel and constant head tank ensure constant plume flow properties.

obtained of $100/n^{1/2} \approx 2\%$. Since the run time was constrained by the limited mixing reservoir volume, a maximum of 7 points on the radial profile were taken. This number was considered sufficient for validation of the calibration and processing techniques.

5.3 Acoustic signal processing

Processing of ADV data is a critical step in producing reliable results due to different kinds of signal pollution. Chanson *et al.* (2008), Goring and Nikora (2002) and Wahl (2003) discuss the need for despiking of the ADV velocity output signals. Spikes in the velocity signals can be caused by wrong velocity range settings, wall reflections and lack of scatterers in the flow and should be filtered with techniques such as Phase Space Thresholding, Minimum Correlation Coefficient or Acceleration Limiting (Goring and Nikora, 2002). Doppler noise resulting from velocity shear and scatterers leaving and entering the sampling volume can be important in some cases and must be dealt with in an appropriate way (Lemmin *et al.*, 1999; Romagnoli *et al.*,

2012). Doppler noise can contribute to an overestimation of turbulence intensity and turbulent kinetic energy (Khorsandi *et al.*, 2012).

5.3.1 Flow velocity components

The pulse-to-pulse coherent Doppler technique (Veron and Melville, 1999) used by the ADV instrument is potentially prone to different kinds of error in the velocity output signals. To avoid deviations in the time-averaged velocity and (more importantly here) high-frequency velocity signals, these sources have to be identified and the errors corrected. A first source of error is the appearance of spikes in the velocity signal caused e.g. by a lack of tracer particles (per unit of instrument power) in the sampling volume or by a higher flow velocity compared to the flow velocity limits defined in the ADV settings. This type, however, can occur in the outer parts of the plume where the sediment concentration is low or temporarily vanishes, certainly given the choice for the LOW+ power level (i.e. one of the options in Nortek ADV settings) for increased sediment concentration calibration range. Using a combination of a minimum pulse correlation of 70%, a maximum acceleration of $0.1g$ and the Phase Space Thresholding technique (Goring and Nikora, 2002; Wahl, 2003), spikes are removed from the signal. No interpolation over deleted values is used since this would affect the rms velocity and Reynolds stresses. Moreover, it would affect the determination of the covariance between velocity and sediment concentration fluctuations for turbulent sediment flux computations.

A second source of error is Doppler noise. This kind of noise in the velocity output is inherent to acoustic instruments using the pulse-to-pulse technique and is considered to be white noise (Voulgaris and Trowbridge, 1998). It is generally agreed that predictions of Reynolds stresses with the ADV are accurate since the Doppler noise is cancelled out due to (i) the uniformity of the noise level over the beams and (ii) the structure of the matrix to transform beam velocities to XYZ velocities. Contrarily, it is assumed that Doppler noise enters the rms velocity and turbulent kinetic energy computations. Denoting the elements of the transformation matrix by a_{ij} and the number of beams by B, it can be shown that if the Doppler noise in a three beam ADV ($B = 3$) is equal in all beams, the resulting deviation in the Reynolds stress term is equal to

$$\frac{\overline{v'_* w'_*} - \overline{v'w'}}{\overline{V_d'^2}} = \sum_{j=1}^{B} a_{2,j}\, a_{3,j} \quad , \tag{5.1}$$

where $\overline{V_d'^2}$ is the Doppler noise variance and $\overline{v_*'w_*'}$ the uncorrected Reynolds stress (based on uncorrected horizontal and vertical velocity fluctuations v_*' and w_*').

Using the transformation matrix of a three beam ADV the right-hand side in equation (5.1), i.e. the deviation, is equal to zero. In this study, a side-looking probe (SP) with four beams ($B = 4$) is used and it was found that the right-hand side of equation 5.1 yields a non-zero value of 2.9. On the other hand, it can be shown that very small values are retrieved for the $\overline{u'v'}$, and $\overline{u'w'}$ terms (0.007 and -0.0169 respectively). When measuring Reynolds stresses using an ADV with SP, Doppler noise will thus be present in one of the three lateral components, depending on the orientation of the instrument's coordinate system in the flow. For the four-beam FP, equation 5.1 does yield values much smaller than one for all components of the lateral Reynolds stresses. It can thus be concluded that Doppler noise is cancelled out in all lateral Reynolds stress components when using a four-beam probe with orthogonal beams.

In a similar way, it can be shown that the deviation in the normal Reynolds stresses is equal to

$$\frac{\overline{u_{i*}'^2} - \overline{u_i'^2}}{\overline{V_d'^2}} = \sum_{j=1}^{B} a_{i,j}^2 \tag{5.2}$$

for i=1,...,3 corresponding to Carthesian velocity components u,v and w, respectively.
The right-hand side in equation 5.2 can be seen as an amplification factor α_i for the Doppler noise entering the normal components of the Reynolds stresses, $\overline{u_i'^2}$:

$$\sum_{j=1}^{B} a_{i,j}^2 = \alpha_i \tag{5.3}$$

For the two ADV's used in the presented experiments, the amplification factors α_u, α_v and α_w are presented in table 5.1. Both the FP and SP are four beam probes. The FP has a bistatic axis along the vertical velocity w, while the SP a bistatic axis along the v velocity component.

To correct for the Doppler noise in the normal stresses, Khorsandi *et al.* (2012) proposed to subtract the difference between the u and w variances ($\overline{u'^2} - \overline{w'^2}$) from the rms velocity in x-direction and ($\overline{v'^2} - \overline{w'^2}$) from the rms velocity in y-direction. In the type of flow studied in the present chapter,

Table 5.1: Amplification factors for Doppler noise in normal Reynolds stress terms (α_i) and average difference between spectral amplitude of non-bistatic axis velocity components and of spectral amplitude of the bistatic component: $S(i,j) = |E_i(f_N) - E_j(f_N)|$

	α_u	α_v	α_w	$S(u,w)$	$S(v,w)$	$S(u,v)$	$S(w,v)$
		[-]			$m^2\ s^{-1}$		
Field Probe	8.67	8.35	0.53	$1.99{\cdot}10^{-4}$	$1.75{\cdot}10^{-4}$	-	-
Sidelooking Probe	7.99	0.53	31.55	-	-	$3.99{\cdot}10^{-5}$	$8.86{\cdot}10^{-5}$

i.e. the vertical plume with anisotropic turbulence, this method would not be suitable since it would equalise the rms velocity in all three directions. Moreover, since in this work the aim is to produce estimates of turbulent sediment fluxes, a corrected time series is needed rather than a corrected rms value. Therefore, for each velocity component, the noise floor was detected as the spectral density function near the Nyquist frequency (equal to half the sampling frequency, i.e. $f_N = 12.5$ Hz).

It is known that frequencies in the physical velocity signal greater than f_N leak energy to the frequencies below f_N (aliasing). Yet, it cannot be verified whether these frequencies are physically present since sampling is done at twice the Nyquist frequency. It can be shown that for a spectrum with $E \propto f^{-5/3}$, energy leakage due to aliasing (E_a) is maximally equal to E at $f{=}f_N$, to $0.51E$ at $f{=}0.8f_N$ and to $0.35E$ at $f{=}0.7f_N$. To avoid excessive influence of aliasing, the noise floor level is not evaluated at the Nyquist frequency, but at a lower value. To further avoid influence of wiggles in the frequency spectrum, the average of the spectral density is computed from 70% to 80% of the Nyquist frequency.

In figure 5.2, the spectra of the three components are shown in grey. The spectrum with the lowest noise floor approaching the Nyquist frequency is the v (or y-velocity) spectrum, since this component lies along the bistatic axis of the sidelooking probe. The difference between u and v components on the one hand and between w and v components on the other hand is shown. These are not a constant (i.e. no white noise), so the spectrum obtained in this way is not the footprint of the Doppler noise. The level of the (white) Doppler noise spectral density is found near the Nyquist frequency where the spectrum flattens. It cannot be verified how large the influence of aliasing is on determining the noise floor level, except that the maximum deviation is around 40%, because only values of between 70 and 80% of f_N are used.

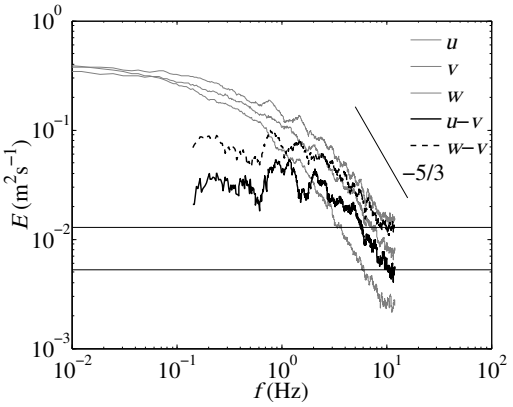

Figure 5.2: Frequency spectra of three velocity components (u,v,w), where the lowest noise floor stems from the v component; difference in frequency spectra of u and v ($|E_U(f) - E_V(f)|$, full line) and of w and v ($|E_W(f) - E_V(f)|$, dashed line) and the difference in Doppler noise floor between u/w and v (horizontal lines).

However, aliasing gradually reduces the slope of the spectrum and would therefore never produce a sharp shift to a fully flat spectrum over a range $0.7f_N < f < f_N$, as is observed in the measured spectra, especially of the v and w components. This shows that the noise floor correction is not falsely executed based on an aliasing-related flattening of the spectrum.

Following this procedure, the differences in noise floor $|E_U(f_N) - E_V(f_N)| = S_{u,v}$ and $|E_W(f_N) - E_V(f_N)| = S_{w,v}$ were determined for measurements in the mixing tank taken during calibration, at sediment concentrations ranging from 40 mg/l to 12 g/l, and showed fairly constant values in this range. The average values of $S_{u,v}$ and $S_{w,v}$ (table 5.1 for values of the FP and SP probes) are used to correct the frequency spectra of the velocity components for the plume measurements. The u and w velocity signals are decomposed using complex Fourier transforms, conserving the phase information. For each frequency in the spectrum, the amplitude is corrected with $S_{u,v}$ or $S_{w,v}$. Subsequently, the velocity time series are reconstructed using the phase information to obtain a corrected time series. Figure 5.3 depicts the spectra of uncorrected (black line) and corrected (grey line) time series of the vertical velocity component at radial distance from the axis $r/z = 0.14$. Here radial distance from the axis r is non-dimensionalised by the vertical distance z to the plume source. The applied spectral correction in this case, i.e. using the sidelooking probe, amounts to $S_{w,v} = 8.86 \cdot 10^{-5}$ m^2 s^{-1}.

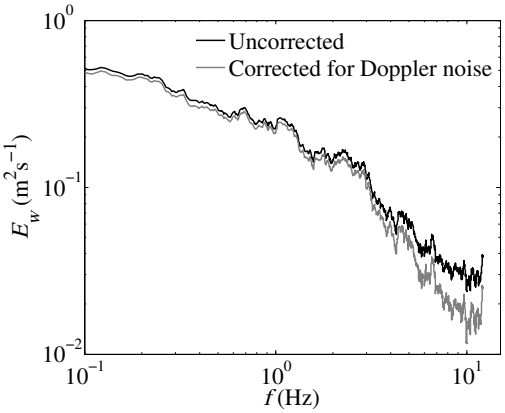

Figure 5.3: Frequency spectra of the vertical velocity component measured with the sidelooking probe, uncorrected and corrected for Doppler noise. Measured at $r/z = 0.14$

5.3.2 Turbulent sediment fluxes

In order to compute the turbulent sediment flux from the ADV output, noise free high-frequency time series of flow velocity and sediment concentration are necessary. In the previous section a noise-removal technique with conservation of phase information is introduced. A similar technique is used to remove noise from the suspended sediment concentration timeseries. In this case, the increase in signal variance is not caused by Doppler noise, but by background oscillations in the amplitude output. The raw signal of a backscattered acoustic wave with constant amplitude is Rayleigh distributed, i.e. the backscattered signal has a fluctuating amplitude. In order to measure only fluctuations caused by fluctuating sediment concentrations, the fluctuations caused by the acoustic scattering (noise) must be corrected for. Since the backscatter signal has a Rayleigh distribution (Medwin and Blue, 2005), the standard error in the uncorrected backscatter signal (AMP_*) can be approximated by $\sigma_{AMP_*} \approx \overline{AMP_*}/(2\sqrt{(n)})$, where n is the number of samples used for the average value $\overline{AMP_*}$. The noise is measured in still, uniform suspensions at a variety of sediment concentrations, where residual fluid movements were below 2 mm/s. The rms value of the fluctuating part, AMP'_{rms}, varies between 5 and 8% of the mean amplitude for the transmitted pulse length (TL) and sampling volume height (SVH) settings of 0.6 and 7.3 mm respectively. AMP'_{rms} was roughly twice as high for ADV settings where $TL > 0.5\ SVH$. The calibration measurements in the mixing tank using $TL = 0.6$ mm and $SVH = 7.3$ mm have also been analysed, showing similar values for AMP'_{rms} (i.e. between 3 and 9%) with exception

of the smallest concentrations. In particular, for C <50 mg/l it is found that $10\% < AMP'_{rms}/\overline{AMP_*} < 14\%$.

The noise shows a spectral footprint of pink noise, i.e. slightly higher spectral density towards the lower frequencies. The spectrum of background amplitude noise has been measured in concentrations ranging from 5 mg/l to 10 g/l (note that concentrations above 2 g/l have been measured in a smaller recipient, instead of a large tank, in order to limit the required sediment). Noise spectra are linear over the full frequency range considered (linearised spectrum is plotted in grey in figure 5.4a). The amplitude spectrum in all concentrations differs no more than 0.05 counts at $f = 12.5$ Hz and 1.0 counts at the minimum frequency. Consequently, it can be concluded that background noise levels in AMP are not dependent on sediment concentration. Therefore, all measured time series of AMP are decomposed into harmonic components using a Fourier Transform. The spectral amplitudes are corrected with the noise spectrum values (varying with frequency), as shown in figure 5.4a. Subsequently, the noise-free AMP time series are recomposed using corrected amplitude, original phase and frequency. Converting this AMP time series using the exponential calibration function yields a noise free sediment concentration time series. Frequency spectra of uncorrected (dashed line) and corrected (full line) sediment concentration time series are shown in figure 5.4b. It can be observed that the corrected signal for sediment concentration and AMP spectra follow the -5/3 turbulent cascade law closely, supporting the introduced procedure.

When the corrected time series of sediment concentration is used to compute turbulent sediment fluxes, the uncorrected turbulent sediment flux can be written as follows:

$$\overline{c'u_i*'} = \overline{c'\left[a_{1i}(V'_1 + V'_{d,1}) + a_{2i}(V'_2 + V'_{d,2}) + a_{3i}(V'_3 + V'_{d,3}) + a_{4i}(V'_4 + V'_{d,4})\right]} \tag{5.4}$$

or

$$\overline{c'u_i*'} = \overline{c'u'_i} + a_{1i}\overline{c'V'_{d,1}} + a_{2i}\overline{c'V'_{d,2}} + a_{3i}\overline{c'V'_{d,1}} + a_{4i}\overline{c'V'_{d,4}} \tag{5.5}$$

where u_i*' is the uncorrected turbulent velocity fluctuation, c' is the corrected signal of the sediment concentration fluctuations and $V'_{d,j}$ (j=1,2,3,4) the Doppler noise variance in the four beams of the ADV.
Since it can be assumed that the Doppler noise is uncorrelated with the sediment concentration fluctuations, the four last terms vanish and the correct turbulent fluxes $\overline{c'u'_i} = \overline{c'u_i*'}$ are found. This implies that the Doppler noise corrections do not necessarily have to be evaluated for turbulent fluxes.

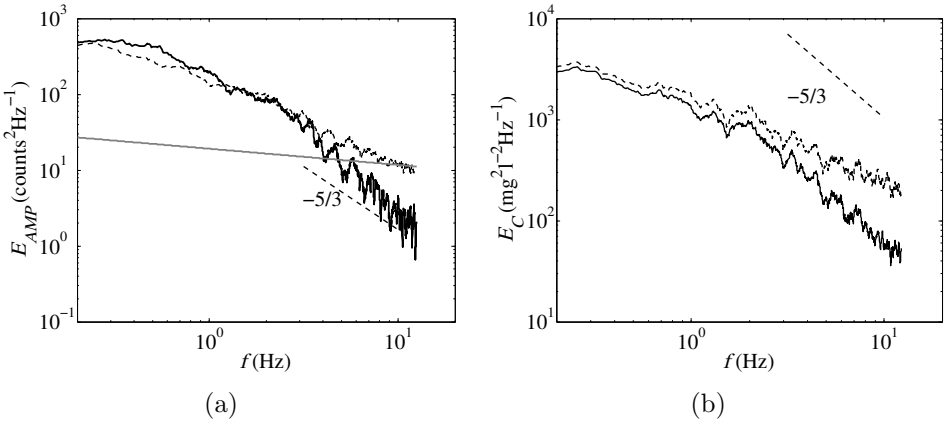

Figure 5.4: Backscatter amplitude and suspended sediment frequency spectra corrections: (a) Background AMP noise spectrum (grey line), uncorrected (dashed line) and corrected (full line) amplitude spectra; (b) Uncorrected and corrected spectra (dashed and full lines, resp.) of suspended sediment concentration fluctuations measured in the kaolin plume at $r/z = 0.19$.

Finally, the turbulent fluxes are computed by taking the covariance of the 25 Hz velocity and sediment concentration time series. The convergence of the mean and turbulent flow statistics have been determined by computing the mean and fluctuating sediment concentration and turbulent transports on 10%, 20%, etc of the length of the full 3000 sample time series. For the mean flow parameters, statistics converge after 50 to 60% of the 3000 samples. For the turbulent parameters, generally, 70 to 90% of the 3000 samples are needed for convergence.

5.4 Results

In this section the results of the turbulent flux determination is validated by comparing the present sediment plume and jet measurements with measurements reported in literature for two-fluid plume/jet cases.

5.4.1 Vertical sediment plume: mean flow properties

The self-similarity properties of plumes, along with the sharp gradients in flow velocity and sediment concentration result in test cases that are (i) challenging the developed techniques and (ii) practical to compare with results of earlier work (in two-fluid plumes). The quartz/kaolin plume measurements

were taken at a radial section at $z/D = 9$, where z is the vertical distance to the jet exit and D is the pipe diameter. Some authors suggest starting and maintained buoyant plumes need different penetration distances to reach similarity (e.g. Sangras *et al.*, 2002; Dai *et al.*, 1994a). Their work indicates that starting jets and plumes reach similarity after $z/D >$20-30, while steady round turbulent buoyant plumes need substantially longer distances, up to $z/D >$87 (Dai *et al.*, 1994a, 1995). The latter is contradictory to other publications, showing distances for self-similarity of $z/D >$12-22 for liquids (Papanicolaou and List, 1988; Westerweel *et al.*, 2009) and $z/D >$8-10 for gases (George Jr *et al.*, 1977; Shabbir and George, 1992). Note that in the work of Papanicolaou and List (1988), further in this paper referred to as PL88, and all other authors cited, buoyancy is introduced by considering fluids of different mass density or temperature, while the present work adopts sediment particles. Inlet conditions are also important for similarity installment, e.g. Reynolds number and whether or not turbulence is allowed to develop. The flow was released here from a pipe with a length of 17 diameters (or 57 diameters when smaller internal flow guiding pipes are considered), allowing for turbulence to develop (Doherty *et al.*, 2007).

Since present measurements are taken in a flume set up for future study of sediment plumes in a crossflow, the vertical distance at which measurements are taken is limited to nine pipe diameters to reduce the influence of the bottom of the flume. Yet, the radial sediment concentration profile found in the kaolin (plume regime) and quartz powder (jet regime) measurements shows the well-known Gaussian curve, here with concentration half-width $b_c/z = 0.116$ for the kaolin plume and $b_c/z = 0.105$ for the quartz laden jet (figure 5.5). The value of $b_c/z = 0.116$ is in the same range as values found for two-fluid plumes, like e.g. $b_c/z = 0.112$ (PL88) and $b_c/z = 0.120$ (Fischer, 1979). For the jet case, the value of $b_c/z = 0.105$ is equally in line with literature. The gaussian velocity half-width found in the plume case was $b_w/z = 0.119$, while for the jet is was $b_w/z = 0.102$. For two-fluid buoyant jets, larger concentration than velocity half-widths are generally accepted. This is explained by the standard value of the turbulent Schmidt number ($\mathrm{Sc_t} = \nu_t/D_t$=0.7, ν_t the turbulent eddy viscosity and D_t the turbulent mass diffusivity). Here, we find that concentration and velocity half-widths are nearly equal, suggesting a $\mathrm{Sc_t}$ number of around unity. This might be explained by the fact that in the current experiments the diffused mass consists of sediment particles. When applying the Boussinesq approximation for determining ν_t and D_t from turbulent fluxes and time-averaged gradients, $\mathrm{Sc_t}$ values of 0.9 to 1.4 are found. Especially at the center and outer fringes of the plume, the latter calculation

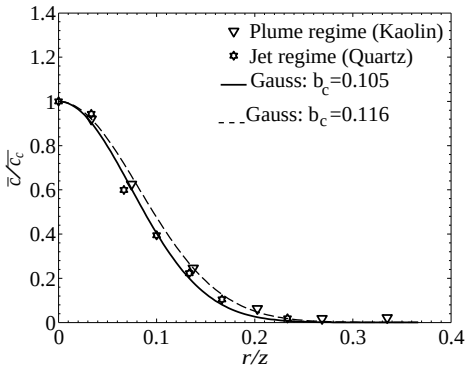

Figure 5.5: Radial profiles (at $z/D = 9$) of measured time-averaged sediment concentration and Gaussian fits. Both for the plume case with kaolin clay and for the jet regime case with quartz powder.

is very sensitive to near-zero gradients of sediment concentration and velocity.

To check for persistent spurious peaks in the sediment concentration series, the minimum and maximum values found at a radial profile are compared to PL88. The variations of both minima and maxima along the radial profile agree well with these data (figure 5.6), although the measured range is somewhat smaller between $r/z = 0.05$ and $r/z = 0.15$, both for the plume and jet cases.

5.4.2 Vertical sediment plume: turbulence properties

The main goal of this work is to obtain accurate measurements of turbulent diffusion of sediment particles, using the combined Doppler velocity and acoustic backscatter output of an ADV. Using the methods described above, the six components of the Reynolds stress tensor have been calculated and compared to two-fluid measurements of buoyant jets (Decrop *et al.*, 2012a). As shown above, calculations of both the lateral and the normal components of the Reynolds stress need corrections for Doppler noise when using four beam or sidelooking ADV instruments.

The rms radial velocity fluctuations u'_{rms} show a peak at $r/z = 0.07$ (figure 5.7a), which is in line with Shabbir and George (1992), but at greater distance from the axis than found by Dai *et al.* (1994a). In the kaolin case, the Reynolds stress component $\overline{u'w'}$, describing the lateral flux of vertical momentum, shows a peak value of $0.021\overline{w_c}^2$ at $r/z = 0.07$. As illustrated in figure 5.7b, the obtained value is in between the peaks reported by both ref-

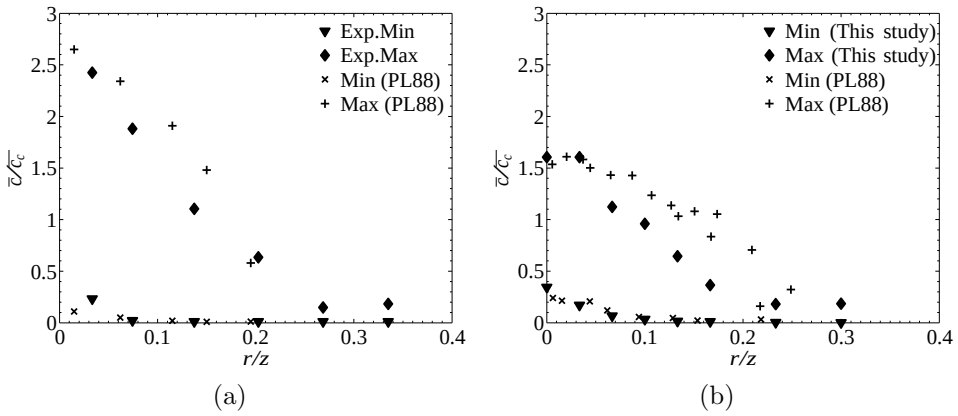

Figure 5.6: Radial profiles (at z/D = 9) of minimum and maximum observed sediment concentration in the kaolin plume case (a) and in the quartz powder jet case (b), compared to data obtained by Papanicolaou and List (1988)

erence works. It has to be noted that both authors used gaseous plumes, the first hot air, the latter sulphur hexafluoride. In the jet case, peak $\overline{u'w'}$ values measured (not shown) are within the range of those measured by Westerweel *et al.* (2009).

Root-mean-square sediment concentration fluctuations do not show a peak off the axis of the kaolin plume, whereas an off-centreline peak is observed both in the present quartz jet and in jet regime measurements by PL88 (figure 5.8). In both the kaolin plume and the quartz jet, the rms sediment concentration profiles correspond well with earlier work on two-liquid flows. In the plume case, the maximum value of $c'_{rms} = 0.35\ \overline{c_c}$ occurs at the axis. PL88 find almost identical behaviour at $z/l_M = 8.6$ and $z/l_M = 14.8$.

Both in the plume and jet cases, the radial turbulent flux of sediment ($\overline{c'u'}$) measured using the presented techniques are within 15% of previously reported values by PL88, Shabbir and George (1992) and Westerweel *et al.* (2009).

For the case with a quartz-laden jet, the peak value of the axial turbulent flux of suspended sediment amounts to $\overline{c'w'} = 0.038\overline{C_c}\overline{w_c}$, somewhat higher than values reported in literature (figure 5.9b). The inner and outer parts of the $\overline{c'w'}$ profile, however, correspond well with the profile by PL88. In the plume case, axial turbulent flux of suspended sediment measurements show a centreline (r/z=0) value for $\overline{c'w'}$ of 0.04 $\overline{C_c}\overline{w_c}$, again within the range

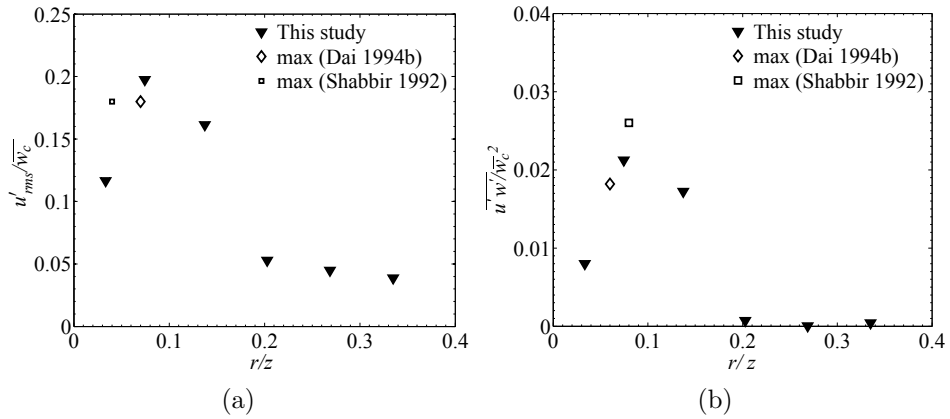

Figure 5.7: Radial profiles (z/D = 9) of rms values of radial velocity (a) and radial turbulent flux of axial momentum (b), compared to data obtained by Dai et al. *(1994b) and Shabbir and George (1992).*

found by other authors: Shabbir and George (1992) find a significantly higher peak value of 0.07, while PL88 and Antonia *et al.* (1980) find 0.049 and 0.30 respectively (figure 5.9a). The location of the peak value is found by other authors at $0.6 < r/z < 0.7$ which is near the location of the maximum value in the present measurements. Note that in the latter no clear peak is found, since the limited number of points along the cross section does not allow for an exact determination of the peak location. The full profile further away from the axis is compared to the measurements by PL88 in figure 5.9a and shows particularly good agreement.

5.5 Discussion

The results obtained using the methods above include the full Reynolds stress tensor and three components of turbulent sediment flux. The method avoids assumptions implicating isotropic turbulence by means of spectral noise corrections rather than bulk $\overline{u_i'^2}$ corrections. Yet, determining the Doppler noise floor in the velocity spectra of three velocity components and subsequently subtracting the $S(u,w)$ and $S(v,w)$ corrections, implies to a certain extent an assumption of isotropy at the Nyquist frequency scale. However, for the presented cases it can be shown that the length scale associated with the Nyquist frequency ($l = U/f_N$) is of the same order as the Kolmogorov length scale. At this scale, viscous dissipation occurs and the assumption of isotropic turbulent motions is justified. Moreover, in the present flows the energy in

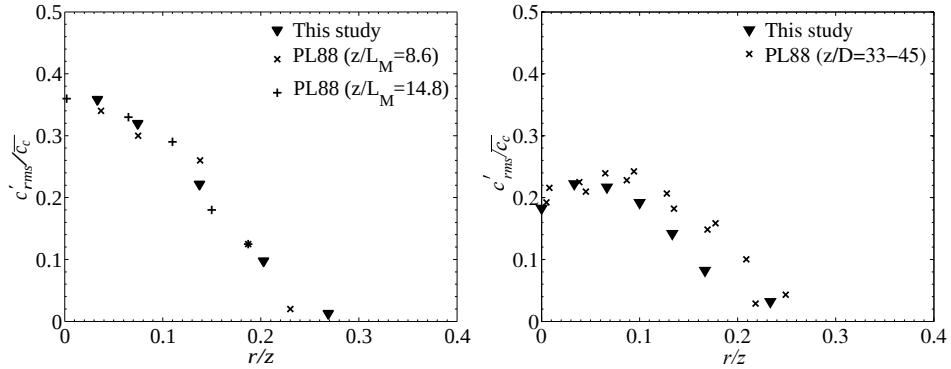

Figure 5.8: Radial profiles ($z/D = 9$) of rms turbulent fluctuations of sediment concentration in the kaolin plume regime (a) and in the quartz powder jet regime (b) , compared to data obtained by Papanicolaou and List (1988).

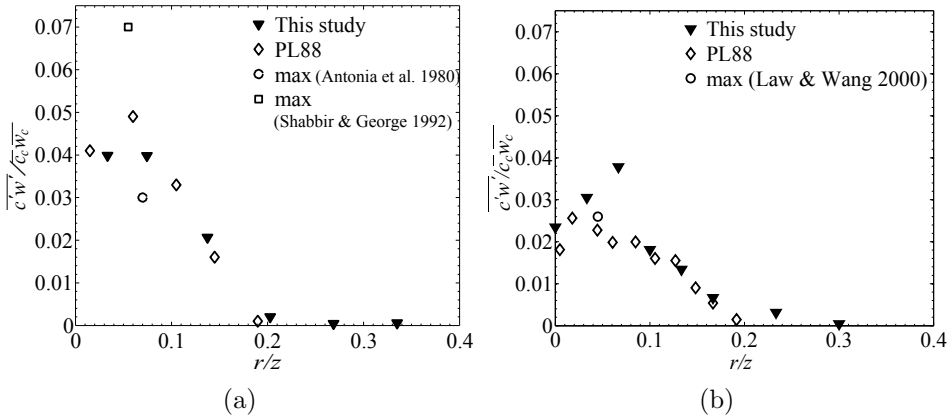

Figure 5.9: Radial profiles ($z/D = 9$) of vertical turbulent sediment flux in the kaolin plume regime (a) and in the quartz powder jet regime (b) , compared to data obtained by Papanicolaou and List (1988), Antonia et al. *(1980), Law and Wang (2000) and Shabbir and George (1992).*

these scales is a factor 20 to 100 smaller compared to the energy in the integral scales.

Another remark should be made about the remaining noise in the normal Reynolds stresses $\overline{u_i'^2}$. The corrections are based on $S(u,w)$ and $S(v,w)$, i.e. differences of noise floor elevations of non-bistatic axes with the noise floor of the bistatic axis. For both the FP and the SP bistatic axis an amplification factor of α=0.53 is found for Doppler noise entering $\overline{u_i'^2}$, a value 16 to 63 times smaller compared to the non-bistatic axes (Table 5.1). This implies that 0.53 times the noise variance is still present in $\overline{u_i'^2}$. However, by integrating the noise floor level over the frequency spectrum it can be estimated that the remaining noise variance is about $\sigma_N^2 = 3{\cdot}10^{-5}$ m^{2}s^{-2}. It should be verified that this value is not significant compared to the measured levels of $\overline{u_i'^2}$. In the present flows, $\overline{u_i'^2}$ is in the order of 10^{-2} m^{2}s^{-2}, from which it can be concluded that the applied correction methods remove a sufficiently high portion of the noise.

The impact of noise on Reynolds stress measurements can also be evaluated by computing a minimum detectable stress σ_R^2 (Williams and Simpson, 2004; Vermeulen *et al.*, 2011), which can be expressed in our notation as:

$$\sigma_{i,R}^2 = \mathrm{var}\left(\overline{u_i'^2}\right) = \frac{\sigma_N^4}{n}\alpha_i \tag{5.6}$$

with n the number of samples. The noise variance σ_N^2 can be estimated from integration of the noise floor level over the frequency spectrum. In terms of minimum detectable $u'_{i,rms}/\overline{w_c}$, values of $1{\cdot}10^{-5}$ for bistatic axes and values between $4{\cdot}10^{-5}$ and $9{\cdot}10^{-5}$ for non-bistatic axes are found. After correction of the non-bistatic axes stresses, the minimum detectable stress falls back to the value for bistatic axes. In the presented validation cases, the measured stresses are several orders of magnitude higher compared to the minimum detectable value.

Given the validity of Rayleigh scattering in a certain range of k and a, some comments on the applicaibility of the presented techniques are appropriate. Rayleigh scattering applies for $0.05 < k \cdot a < 1$, which implies a different validity range for different instruments with different acoustic wavelength. Given a speed of sound of 1500 ms^{-1} and fine sediments with grain size of order 10 microns, the presented methods are valid for instruments with acoustic frequency in the range 2.5 MHz $< f <$ 50 MHz. For fine sands in suspension with a grain size of 100 microns, the validity range is 250 kHz $< f <$ 5 MHz. Since validity depends on the grain size of the suspended

sediments, the question rises whether the methods are valid in case of a wide grain size distribution or flocculating sediments in a natural environment. In any case, for each expected sediment size class suspension, $0.05 < k \cdot a < 1$ should apply. Also, for single-frequency instruments, the combination of fine sediments and coarser sands could cause the problem that the backscatter of the smaller sediments is overshadowed by the backscatter of the sand grains, even for low sand fractions (Hanes, 2012). The same comments can be made for flocculating sediments. A flocculated suspension is likely to produce higher backscatter amplitude values. In any case, for each type of sediments in suspension a dedicated calibration should be performed linking backscatter values to sediment concentration. In dynamic (tidally influenced) natural waters, floc properties and grain size distributions can vary rapidly. In such cases, frequent sampling is needed for the adaptation of calibration curves and noise correction parameters.

5.6 Conclusions

A new procedure to obtain turbulent fluxes of momentum and fine sediments using ADV instruments was introduced and validated. The method involves the calibration range optimisation and spectral corrections for backscatter noise and Doppler noise.
The acoustic backscatter intensity has been calibrated to obtain kaolin clay and quartz powder sediment concentrations. The calibration range was maximized using optimal ADV settings of power level, transmitted pulse length and sampling volume height, resulting in a calibrated sediment concentration range of 10 mg/l to 10 g/l, or concentrations up to a factor 3 higher than previously reported for this type of fine sediment. It is shown that the calibration range can be extended into the start of the saturation range, since it can be predicted from acoustic theory.

Turbulent fluxes of sediment and momentum could be determined accurately by means of spectral corrections for Rayleigh backscatter noise and Doppler noise. Doppler noise corrections for the determination of turbulent velocity fluctuations are found to be necessary when using sidelooking or four-beam ADV instruments. The same applies for determination of both normal and lateral Reynolds stress components.

The mean and turbulent properties of the fine sediment plumes were very similar to the two-fluid cases drawn from the literature. Turbulent intensity of velocity and scalars were very close to these published data. This indicates

that multi-phase effects such as turbulence modulation are not important.

Noise-free, high-frequency sediment concentration series were obtained by a spectral correction for background Rayleigh scattering noise in the backscatter amplitude signal. Measured root-mean-square sediment concentration fluctuations and turbulent fluxes of suspended fine sediment in a negatively buoyant sediment plume show results consistent with observations in two-fluid cases described in literature. The results are consistent with the Gaussian shape of plume tracer concentration profiles.

In future work, it should be further examined how aliasing can influence the determination of the Doppler noise floor, for instance by means of measurements with equipment with a substantially higher sampling frequency.

In this work, the high shear stresses applied to the kaolin-sediment mixture are assumed to avoid formation of macroflocs. In future work, the application and modification of the presented techniques for dynamically flocculating sediments should be developed. The techniques presented in this chapter, however, are shown to work well in suspensions with both non-flocculating fine materials and high-shear flows with cohesive sediments.

Chapter 6

Laboratory experiments of sediment plumes in crossflow

A concise overview of the content presentent in this chapter has been published in Decrop et al. *(2012b)*

6.1 Introduction

In this chapter, the experiments with a physical plume model are described. The experiments have two objectives. Firstly, to generate a dataset covering a broad range of plume conditions, corresponding to the properly scaled range of conditions occuring in full-scale overflow dreding plumes. Secondly, to gain some insights in the behaviour of sediment plumes in crossflow, and the influence of some specific factors: a ship hull with stern and air bubbles.

In a first step, the dynamics of full-scale dredging plumes are captured in a number of characteristic dimensionless parameters. Exploiting the self-similar property of buoyant jets in crossflow, one can design a number of experiments in which the complete range of the full-scale characteristics is covered.

In principle, the complex geometry of a dredging vessel could be reproduced on a small scale and fitted in the laboratory flume. However, to avoid influence of the flume side walls, the model ship width would be limited to about 10% of the flume width, or 8 cm. For an undisturbed scaling, this would lead to a draft of 1 to 2 cm. Such a model would not produce a

turbulent wake, and would therefore not be a valid model for the full-scale situation.

Instead, a two-dimensional ship was introduced, represented by a schematic hull with a laterally uniform shape (see section 3.1). The draft of 5 cm produces a turbulent wake similar to a backward facing step (BFS), while the boundary layer thickness at the keel of the hull stays small compared to the plume release pipe diameter D.

In this way, the complex dynamics of plumes in crossflow, both with and without influence of a schematised hull can be measured in the experiments (and in a later stage simulated in the numerical model).

Measurements of a number of parameters are executed using the techniques developed in the previous chapters. Parameters include:

- Centerline trajectory $\bar{z}$,
- Top and bottom extent, vertical half-width b_c,
- Time-averaged sediment concentration C,
- Time-averaged flow velocity components U, V and W,
- Root-mean-squared turbulent velocity fluctuations u'_{rms}, v'_{rms}, w'_{rms},
- Turbulent kinetic energy k,
- Reynolds stresses (cross terms): $\overline{u'v'}$, $\overline{u'w'}$, $\overline{v'w'}$,
- Turbulent intensity of sediment concentration c'_{rms}/C,
- Turbulent sediment fluxes $\overline{c'u'}$, $\overline{c'v'}$, $\overline{c'w'}$,

The dataset containing these parameters for a wide range of plumes in crossflow cases will allow (i) an analysis of the dynamics of the plume in crossflow with influence of a hull and (ii) a thorough validation of a laboratory-scale numerical model.

6.2 Scaling

Using the Buckingham-π theorem or dimensional analysis, the important characteric dimensionless numbers in plume in crossflow dynamics can be identified. The important dimensionless numbers obtained include: pipe exit Reynolds number Re_p, the plume wake Reynolds number Re_w, the densimetric Froude number F_Δ, the jet-to-crossflow velocity ratio λ and the ratio of pipe diameter to keel clearance ζ_H.

$$Re_p = \frac{W_0 D}{\nu} \tag{6.1}$$

$$Re_w = \frac{U_0 D}{\nu} \tag{6.2}$$

$$F_\Delta = \frac{W_0}{\sqrt{g' D}} \tag{6.3}$$

with $g'=(\Delta\rho/\rho_w)g$, and $\Delta\rho=\rho_m - \rho_w$.

$$\lambda = \frac{W_0}{U_0} \tag{6.4}$$

$$\zeta_H = \frac{D}{H_k} \tag{6.5}$$

with H_k the depth below the keel.

The full dynamic scaling of the dredging plumes requires all of these dimensionless numbers to be equal in laboratory-scale and full-scale plumes. W_0 and D both appear in the numerator of Re_p, while W_0 appears in the numerator and D in the denominator of F_Δ. Therefore, the only solution for the scaling factors for these variables, and by consequence all other variables, is equal to one. Or in other words, the only scaling keeping both the Reynolds number and the Froude number equal in laboratory and prototype scale, is no scaling. To overcome this deadlock, it was chosen to keep the Froude number equal in both scales while varying the Reynolds number. By also keeping the velocity ratio constant, also the ratio of Re_p and Re_w is kept constant since

$$\lambda = \frac{Re_p}{Re_w}. \tag{6.6}$$

The main consequence of omitting the requirement of keeping the Reynolds numbers constant is the difference in turbulent properties. A higher Reynolds number will lead to smaller turbulent length and time scales, if the flow is turbulent at all. It will be assumed that the limitation of constant Reynolds

number can be omitted when both Reynolds numbers are higher than 4000 in all cases, so that both the pipe flow and the plume wake are turbulent.

The following procedure is used to develop a set of experimental runs covering the full range of prototype-scale values of D, g', W_0, U_0 and H. For each variable ϕ a scaling factor ξ_ϕ is defined so that ϕ_{LS}=$\xi_\phi\phi_{PS}$ and applied to the characteristic numbers. Variables with subscript PS are the prototype scale values, variables with subscript LS are the laboratory-scale values. Keeping the characteristic numbers F_Δ, λ and ζ_H constant in both scales, leads to:

$$\frac{(F_\Delta)_{LS}}{(F_\Delta)_{PS}} = \frac{\xi_{W_0}}{\sqrt{\xi_{g'}\xi_D}} = 1 \tag{6.7}$$

$$\frac{\lambda_{LS}}{\lambda_{PS}} = \frac{\xi_{W_0}}{\xi_{U_0}} = 1 \tag{6.8}$$

$$\frac{(\zeta_H)_{LS}}{(\zeta_H)_{PS}} = \frac{\xi_D}{\xi_H} = 1 \tag{6.9}$$

This is a system with 3 equations and 5 unknowns, which means that 2 variables can be varied when setting up a list of experimental conditions. Since the experimental facility is built with two possible pipe diameters D (3.4 cm and 6.5 cm) and three possible outflow discharges Q_0, D and W_0 are set beforehand, while the other variables follow from equations 6.7-6.9.

In this way an experimental program is defined corresponding to the following prototype-scale limits. These limits (MIN/MAX) are in line with the range of these parameters found in real-life overflow dredging plumes. For completeness, the bounds for the laboratory scale are also listed (LS).

	F_Δ [-]	λ [-]	D [m]	U_0 [m/s]	W_0 [m/s]	ρ_m [kg/m^3]
MIN PS	0.24	0.11	1.26	0.67	0.5	1026
MAX PS	9.15	3.00	3.61	4.6	2.0	1221
MIN LS	0.24	0.11	0.034	0.065	0.11	1003
MAX LS	9.15	3.00	0.060	0.32	0.30	1031

Table 6.1: Overview of dredging plume parameters covered (MIN/MAX) in prototype scale (PS) and laboratory scale (LS) test conditions.

A total of 33 different runs with a sediment plume in crossflow have been executed. The densimetric Froude number varied between 0.24 and 9.15, while

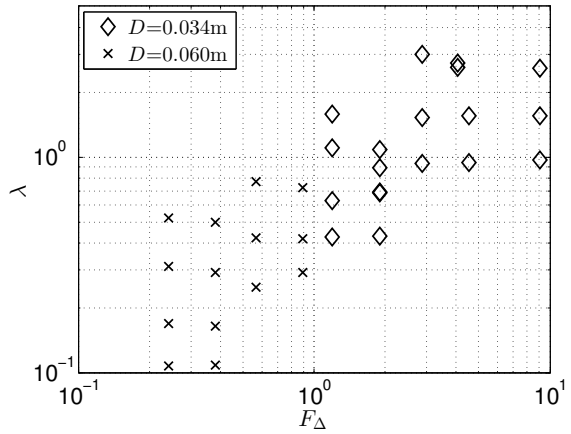

Figure 6.1: Overview of main plume parameters F_Δ and λ for the total of 33 different experimental sediment plume runs.

the velocity ratio varied between 0.11 and 3 (figure 6.1). The runs with smaller W_0 were executed using the wider pipe with D=0.065 m, resulting in a smaller W_0 than the D=0.034m pipe for a given Q_0.

6.3 Reproducibility and setup validation

In order to validate the reproducibility and stationary character of the experiments, some experiments were executed twice (Decrop *et al.*, 2013). The centerline of the plumes was identified by detecting the position of the maximum mean turbidity using video imaging.

The 17,000 l water tanks need to be drained and cleaned after each plume run due to fine sediments causing permanent turbidity and deposits. For this reason, only a limited number of test runs are executed. An example of a validation run repeating a run executed on an earlier day is described below.

In run with number 11, the outflow velocity W_0 was equal to 0.29 m/s while the background flow velocity U_0 was equal to 0.11 m/s. The overflow pipe used was the D=0.034m pipe and the overflow sediment concentration C_0 was equal to 25 g/l. Several weeks after the first execution of this run, it was repeated to compare the resulting trajectory. The obtained centerline deviations were within 0.2 pipe diameters, or about 0.7 cm (Figure 6.2).

The outflow conditions and the mean and turbulent variation of sediment

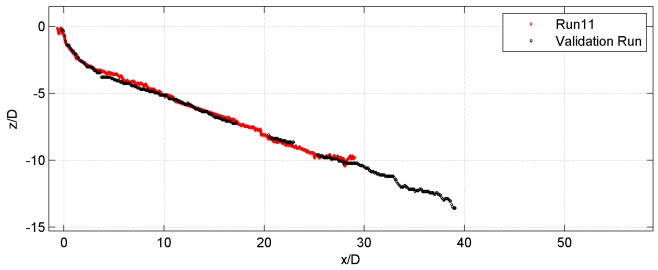

Figure 6.2: Validation of the laboratory conditions by executing a validation run with exactly the same parameters as a previous run. Centerline trajectory of the plumes are shown.

concentration have been validated by executing an experiment without background flow. The results of the mean and turbulent fluctuations of sediment concentration and flow velocity in the flow have been compared to vertical buoyant jet measurements by other authors. The radial profiles in the plume compared well to the well-known self-similar flow of vertical buoyant jets (chapter 5).

Further, the plume trajectories have been compared to a Langrangian model for buoyant jets in cross flows based on the theory by Lee and Chu (2003) and to asymptotic solutions for trajectories by Fischer (1979). It was shown that for plumes not influenced by the hull boundary layer, the plume trajectories corresponded well with both the Lagrangian and the asymptotic solutions Decrop *et al.* (2012b).

6.4 Results

6.4.1 Centerline trajectory

As expected, the trajectory of the plumes was mainly influenced by the parameter pair (F_Δ , λ). When using the Richardson number,

$$Ri = F_\Delta^{-2} = \frac{g'D}{W_0^2} \tag{6.10}$$

and the inverse of the velocity ratio ($1/\lambda = U_0/W_0$), the following graphical representation of the influence of both parameters can be observed (figure 6.3). A higher sediment concentration (or higher $\Delta\rho$ or higher Ri or lower F_Δ) leads to a lower plume trajectory. A higher crossflow-to-jet velocity ratio

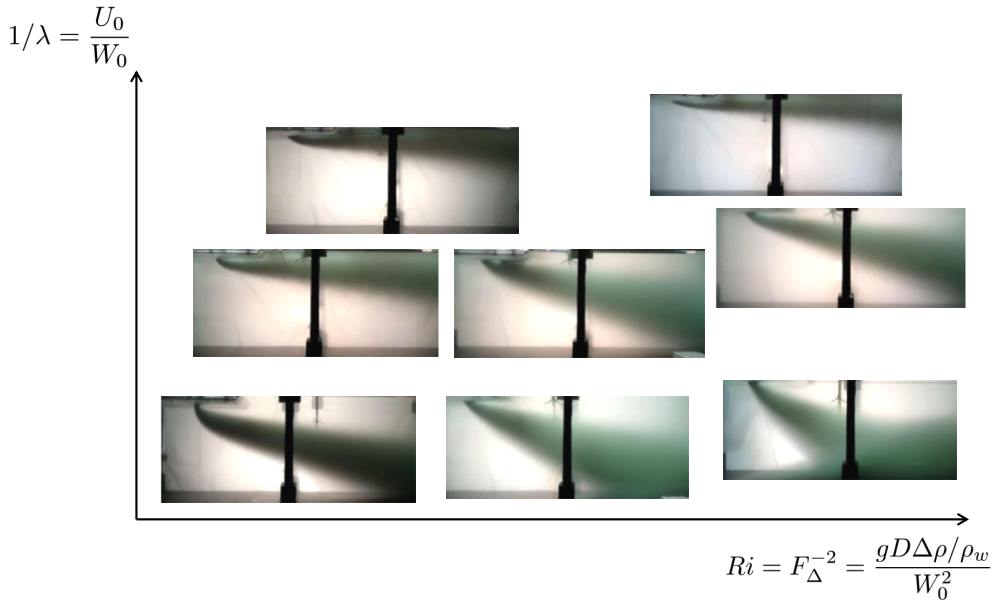

Figure 6.3: Dependency of the plume trajectories on Ri and $1/\lambda$=U_0/W_0.

$1/\lambda$ leads to a higher plume trajectory.

Two plumes are compared with equal, relatively high, Froude number F_Δ=4.5, but with different velocity ratio's (figure 6.4). Due to the relatively high outflow velocity W_0, the plumes start vertically before the crossflow-induced turbulence can mix enough horizontal momentum in the plume to start bending over. Indeed, the theory by Fischer (1979) states that z_M, the height at which crossflow momentum starts to take over, is equal to

$$z_M = \frac{\sqrt{M_0}}{U_0} = \sqrt{D\pi/4}\frac{W_0}{U_0} \propto \lambda. \tag{6.11}$$

Thus, when the pipe diameter is constant, λ is also proportional to the height at which the crossflow starts to dominate over initial pipe exit momentum. Indeed, it can be observed that in the case with higher λ, the plume starts to bend over at greater distance from the pipe exit (figure 6.4a).

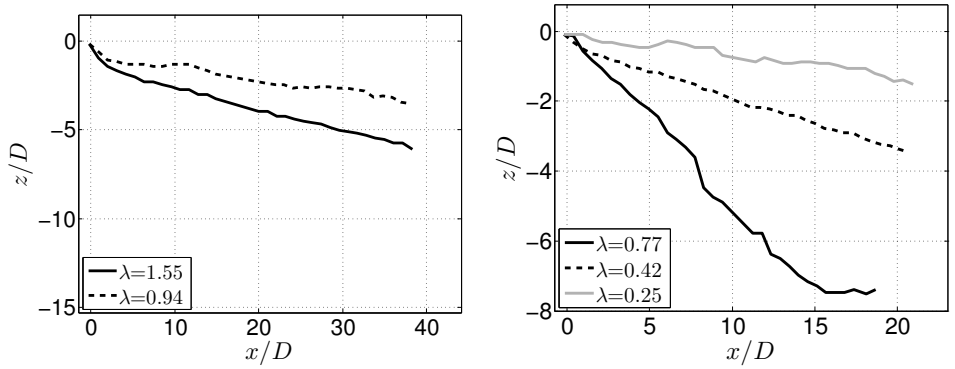

(a) (b)

Figure 6.4: Dependency of high-F_Δ plume trajectories on λ (a). Dependency of low-F_Δ plume trajectories on λ (b).

When now three plumes are compared with relatively low Froude number F_Δ=0.6 (and D=0.065 m) the velocity ratio is equally determining the height of the plume trajectory. However, in this case the initial momentum is very weak, and the crossflow influences the plume trajectory almost immediately after the pipe exit (figure 6.4b). The plume with λ=0.77 reaches the bottom of the flume after x/D=15.

The influence of the Froude number is evaluated by comparing plume trajectories with equal velocity ratio and different F_Δ (figure 6.5). As expected, three plumes with equal and relatively high λ have a similar initial plume trajectory in the momentum-dominated near field (λ=1.55 in figure 6.5a). At a certain depth, the plume bends over and the crossflow momentum and buoyancy dominate, leading to a trajectory with almost a linear rate of descent.

For a constant and relatively low λ, the influence of F_Δ is shown in figure 6.5b (for λ=0.3). Here, the crossflow velocity is more than three times as high as the pipe exit velocity. Yet, with high-density sediment mixture (50 g/l) and outflow velocity of 0.03 m/s (giving F_Δ=0.24), the plume still has a low trajectory due to the domination of the buoyancy. The combination of a low jet-to-crossflow velocity ratio and a higher Froude number (low sediment concentration) leads to the highest trajectory, i.e. very close to the hull wall. In the plume with F_Δ=0.90 in figure 6.5b, the trajectory is clearly influenced by the stern section of the schematised hull (situated at x/D=5.3). It can indeed be observed that the trajectory is ascending in the stretch

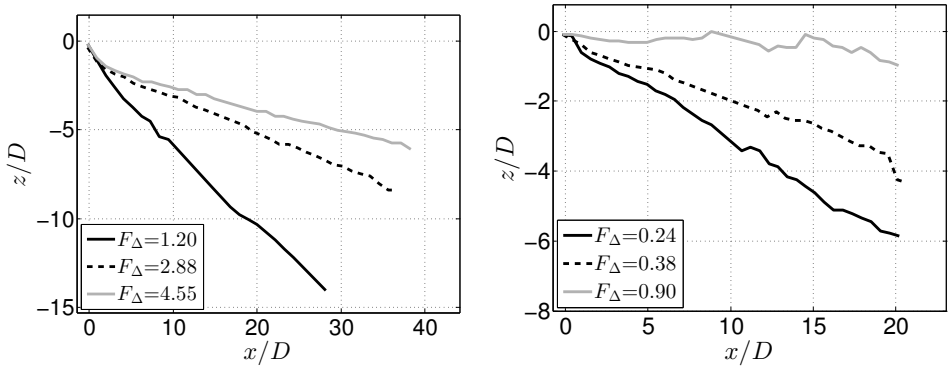

(a) (b)

Figure 6.5: Dependency of high-λ plume trajectories on F_Δ (a). Dependency of low-λ plume trajectories on F_Δ (b).

5.3> x/D >9. Stern influence can equally be observed for λ=0.94 in figure 6.4a and for λ=0.25 in figure 6.4b. This indicates that a higher sediment concentration in the overflow could lead to a reduced sediment dispersion. The influence of the stern section will be further analysed by comparing the trajectories with integral laws and a Lagrangian model solution (in section 6.5).

6.4.2 ADV measurements

6.4.2.1 Introduction

In the following section, the results of the ADV measurements are presented. These consist of point location data such as frequency spectra of u_i' and c'. On the other hand, limited cross sectional profiles of the plumes are recorded at a distance of x=0.5m from the plume release point. The ADV instrument, however, is observing in a single point. To overcome this limitation partial cross sectional profiles of the plumes are captured on a grid. On the one hand, the run time is limited due to the limited capacity of the mixing vessel. During this limited run time, a minimum number of 3000 ADV-samples (at 25 Hz) has to be recorded to ensure converging statistics for the turbulent properties. Using 2 ADV's, the measurement grid could contain only 12 points. In order not to overlook certain smaller features of the time-averaged plume cross section, only a quadrant was covered at each run. Assuming the symmetry of the plume over the $y = 0$-plane, only data has been recorded at

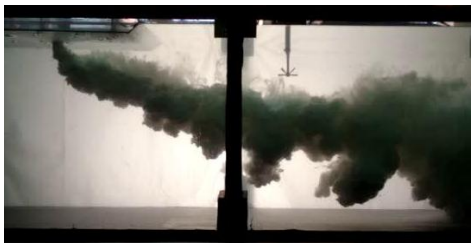

Figure 6.6: Instantaneous image of a plume with U_0=0.11 m/s, W_0=0.30 m/s and C_0=25g/l.

$y > 0$. The limited extent of the ADV profiles reduces to a certain extent the possibility to analyse the full cross sectional properties of sediment plumes in a crossflow. However, the gathered data will mainly serve for comparison with the LES model developed later in this study.

6.4.2.2 Sediment concentration

The high-frequency time series of sediment concentration show a highly intermittent course, certainly at the lower fringes of the plume, where an instable stratification induces convective boils (figure 6.6). At the upper extent of the plume this behaviour is not observed. This can be explained by the stable stratification at which any vertical turbulent motions are damped by the work done by the water-sediment mixture (with $\rho_m > \rho_w$) penetrating into clear water with lower density ρ_w above.

At locations with a more continuous time series of sediment concentration (in the core of the plume), turbulent energy cascade can be visualised. This is done using a fast-Fourier transform and plotting the power spectral density of the concentration signal at each frequency available according to the Nyquist criterion. For a f=25 Hz sampling rate, the maximum oscillation detectable is at $f/2$=12.5 Hz. An example is given in figure 6.7. The integral turbulent scales have a frequency of 0.1 to 1 Hz. Then there is no sharp transition to a -5/3 power law for the cascade of turbulent kinetic energy towards the viscous dissipation scales. The spectrum shows a gradual evolution towards a short region in which the -5/3 power law is found. In the vertical plume experiments in chapter 5, a more pronounced transition was found, towards a more extended -5/3 power law. A possible explanation could be found in the strong intrusion of weakly-turbulent background flow. Also, in the plume in crossflow, the Reynolds number is higher, which leads to smaller turbulent scales with higher frequency. The maximum frequency of 12.5 Hz is possible

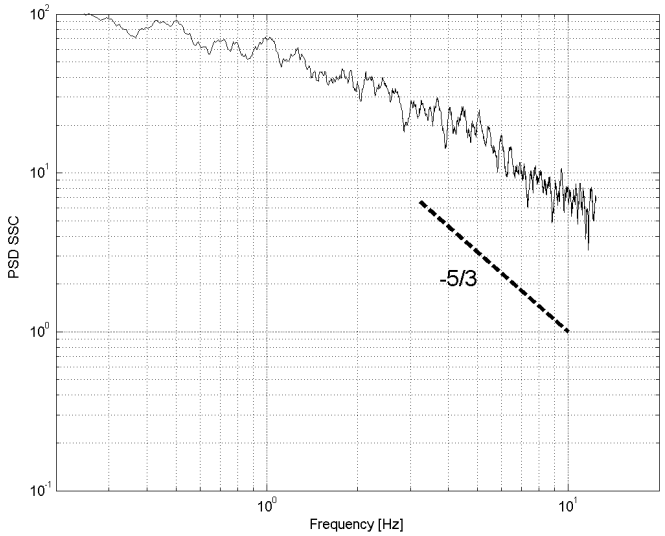

Figure 6.7: Frequency spectrum of the sediment concentration signal in the core of a plume with C_0=20g/l at x/D=7.7, where dilution C/C_0 is about 5%.

leading to aliasing. An effect due to which energy of the higher frequencies not sampled is leaking towards the lower frequencies.

The cross-sectional profiles are available for one quadrant per run. Nevertheless, the structure of the flow and sediment distribution can be visualised. In figure 6.8 and following, the profiles are shown at a lower-right quadrant of a plume with W_0=0.08 m/s, U_0=0.19 m/s and C_0=50 g/l, resulting in F_Δ=0.57 and λ=0.43. In figure 6.8a, the time-averaged sediment concentration (dilution) C/C_0 is shown. In each profile, the time-averaged velocity vectors in the YZ-plane are shown. The signature of a counter-rotating vortex pair (Diez *et al.*, 2005) can be clearly observed. Since only the $y > 0$ part is shown, only one vortex of the pair appears in the measurement.

The profile of c'_{rms} (or the turbulent intensity of sediment concentration) is similar to the C-profile. c'_{rms} varies in this particular profile between 0.01 and 0.05 times C_0. This range is roughly the same as for the concentration C/C_0, which indicates the root-mean-squared fluctuations of c have the same magnitude as time-averaged sediment concentration C. This indicates the highly intermittent character of the concentration signal. This is most pronounced in the lower left area in the profile, corresponding to the lower part of the plume near the symmetry plane. There, c'_{rms}/C_0 is almost twice as high as

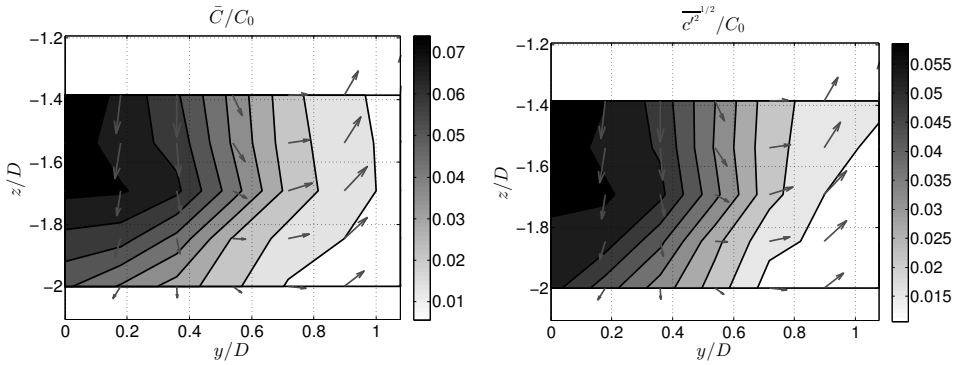

Figure 6.8: (a) Time-averaged profile of C in the lower-right quadrant of the cross sectional profile taken at x/D=7.7. (b) Profile of the root-mean-squared fluctuations of sediment concentration. The time-averaged velocity vectors in the YZ-plane are showing one of the two counter-rotating vortices.

C/C_0. As mentioned above, this can be explained by the convective circulations passing by the observation points in the lower part of the plume. Also, meandering of the plume in horizontal and vertical planes can amplify the intermittent character of the concentration signal. Meandering of the plume in the flume has been observed in some cases. The amplitude of the meandering is amplified when the distance of the plume edges to the flume walls becomes smaller. For the ADV measurements at x=0.5 m this horizontal undulation of the centerline is not yet developed. For the ASM measurements at greater distance (x=1.4 m), the larger plume width induces undulations which causes the cross sectional profile to become more uniform. The typical double concentration peak tends to become less pronounced. Therefore, the ASM dataset will not be used for comparison with the numerical model.

Below, an example is given for a horizontal profile of sediment concentration measured by the ASM. The profile is drawn for the z-level at which the maximum concentration occurs. Again, only the $y > 0$ half is measured, and mirrored in figure 6.9.The concentration peaks amount to about 1.5% of the initial concentration C_0. In this case, the typical double concentration peak is found.

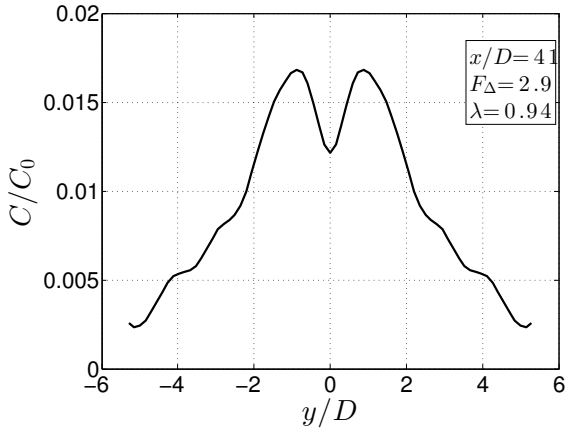

Figure 6.9: Horizontal sediment concentration profile across the concentration maxima at x/D=41, measured by the ASM instrument.

6.4.2.3 Flow velocity components

As for other turbulent flow statistics presented in this section, the streamwise flow velocity u was time averaged over a minimum of 3000 samples at 25 Hz. The resulting time-averaged flow velocity cross section is shown in 6.10. When comparing with figure 6.8, it can be observed that the lowest values of U occur in the center of the plume, where C is high. In an article by de Wit *et al.* (2014b), it was found that buoyant jets in crossflows can overtake the crossflow. In the present measurements, this was not found. Possibly, the present ADV measurements were taken shortly after the start of the buoyancy-dominated region of the plume, due to which the required acceleration did not take effect yet.

Towards the lateral extremity of the plume, the velocity reaches a maximum value of 1.04 times U_0, the initial crossflow velocity upstream of the plume. This indicates that the plume itself forms an obstruction for the flow and a local acceleration is needed for the flow to curl around the plume. It can also be observed that the counter-rotating vortex pair (CRVP, in the YZ plane) is associated with streamwise velocity (in x direction). The CRVP is visualised by taking the velocity vectors in the YZ-plane and subtracting the mean vertical velocity W (corresponding with the rate of descent of the plume). Locations where the CRVP vectors point downward roughly correspond with areas where U/U_0 <1. Likewise, locations where the CRVP vectors point upwards, correspond with areas where U/U_0 >1. The latter area is the zone of lateral mixing with the crossflow.

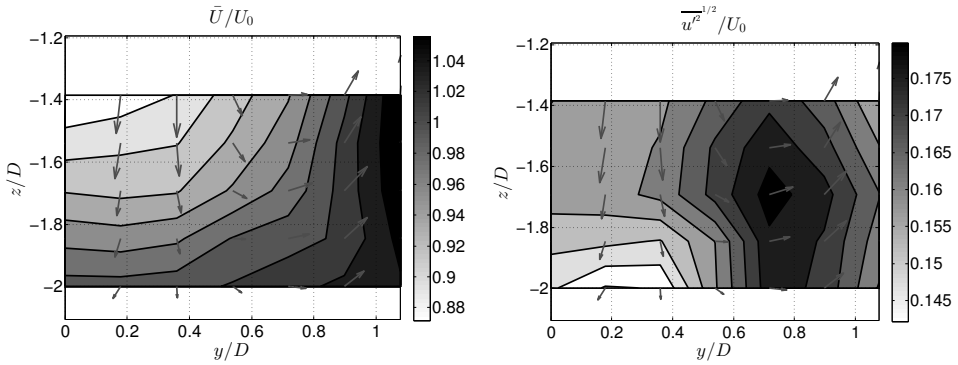

Figure 6.10: (a) Time-averaged profile of U in the lower-right quadrant of the cross sectional profile taken at x/D=7.7. (b) Profile of the root-mean-squared fluctuations of u. The time-averaged velocity vectors in the YZ-plane are showing one of the two counter-rotating vortices.

The zone of strong mixing at the lateral edge of the plume is visualised by plotting u'_{rms} (figure 6.10). It can be seen that the zone of maximal u'_{rms} occurs where the lateral gradient in streamwise velocity ($\partial U/\partial y$) is highest. In these zones, the turbulent intensity u'_{rms}/U_0 has values up to 0.17. Areas with low u'_{rms} correspond with areas where the isocontours of U are horizontal (i.e. where $\partial U/\partial y$ is small).

6.4.2.4 Reynolds stresses

The zones of strong mixing of momentum can also be identified by computing the Reynolds stress. The three cross components, $\overline{u'v'}$, $\overline{u'w'}$, $\overline{v'w'}$ are computed by calculating the covariance of the fluctuating part of u' and v' for $\overline{u'v'}$, and so on for the other two components.

The $\overline{u'v'}$ component of the Reynolds stress tensor indicates the rate of turbulent diffusion of streamwise velocity in the lateral direction. The result for the presented case of ADV measurements in shown in figure 6.11a. It can be observed that $\overline{u'v'}$ is negative throughout the profile. This fits the theory in the sense that at this particular location, the crossflow velocity is higher outside the plume compared to within the plume. Streamwise u-momentum will be mixed inbound the plume. Where y >0 (measured part), that direction corresponds with a negative y-direction (from right to left in figure 6.11). Indeed, the lateral diffusion of streamwise momentum is negative in

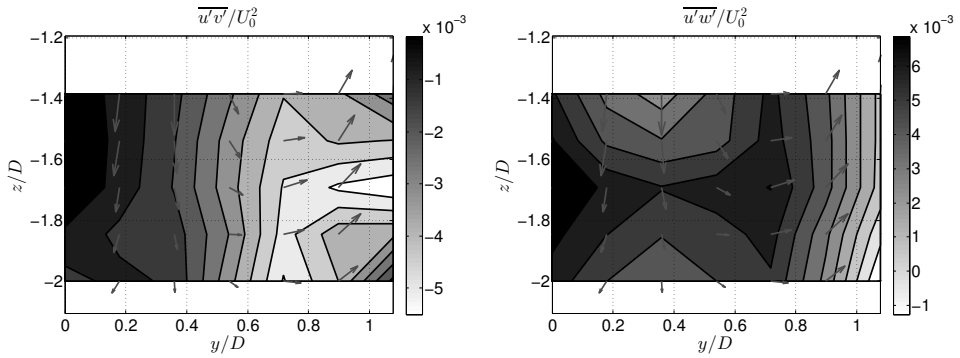

(a) (b)

Figure 6.11: Reynolds stress component $\overline{u'v'}$ (a) and $\overline{u'w'}$ (b). The time-averaged velocity vectors in the YZ-plane are showing one of the two counter-rotating vortices.

the measurements. The strongest stress occurs again in the zone where the lateral gradient of U is highest, with values of $\overline{u'v'}/U_0^2$ up to $5{\cdot}10^{-3}$.

A similar interpretation can be given to the $\overline{u'w'}$ component shown in figure 6.11b. The absolute values of $\overline{u'w'}$ and $\overline{u'v'}$ are of the same size. Throughout the cross section, it can be observed that $\overline{u'w'} > 0$. This can be interpreted as streamwise momentum being mixed upwards. Since the studied section for this case is situated in the lower part of the plume, this means a strong turbulent influx of ambient water occurs at the lower (upstream) part of the plume.

6.4.2.5 Turbulent sediment fluxes

Using the spectral correction method described in chapter 5, high-frequency time-series of sediment concentration are available as well. When taking the covariance of the 25 Hz sediment concentration and velocity component signal, a turbulent flux of sediments in the direction of the chosen velocity component is obtained. In figure 6.12, the lateral and vertical components are shown. Lateral component $\overline{c'v'}$ (figure 6.12a) has positive values on the right half of the profile, while negative values at the left side of the profile. This implies that a turbulent sediment flux towards the center of the plume occurs close to the symmetry plane. To the contrary, a turbulent sediment flux outbound the plume is taking place at the outer parts of the plume. This is not surprising since the plume is widening along its course, which has to be the result of outbound turbulent sediment mixing towards the lateral

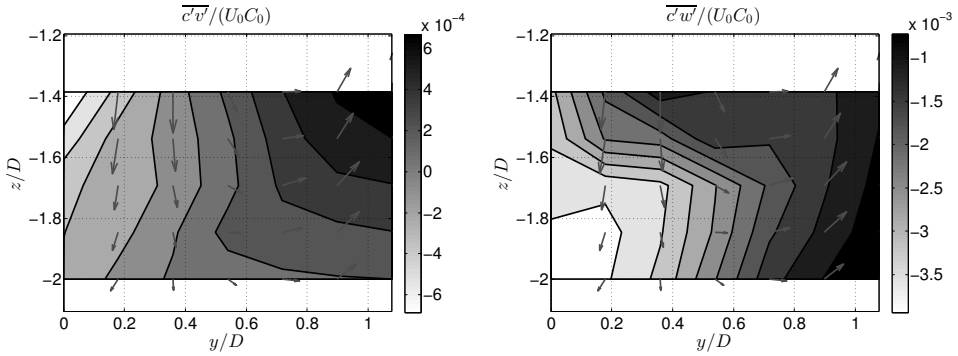

Figure 6.12: Turbulent sediment fluxes: the lateral component $\overline{c'v'}$ (a) and the vertical component $\overline{c'w'}$ (b). The time-averaged velocity vectors in the YZ-plane are showing one of the two counter-rotating vortices.

ends of the plume.

The vertical component of the turbulent sediment flux is negative throughout the profile (again, for the lower part of the plume). A downward turbulent sediment flux is thus observed, away from the lower fringes of the plume. The strongest downward flux is observed near the symmetry plane. This can be related with the qualitative observation of strong convective circulations at the bottom of the plume (figure 6.6).

6.5 Analysis

6.5.1 Influence of the wall step

The influence of a stern section of the schematised ship hull (i.e. the wall step) can be determined when comparing the plume trajectories with integral laws (Fischer, 1979) or the Lagrangian model for buoyant jets in crossflow by Lee and Chu (2003). A plume with trajectory far from the flow expansion and turbulent mixing induced by the wall step would be expected to adhere closely to a prediction of a standard buoyant jet in crossflow.

In figure 6.13a-b, it can be observed that a plume with centerline and upper extent sufficiently away from the wall step is not influenced by it. Which can be concluded from the tight fit with the buoyant jet in crossflow predictions.

In a plume with upper extent slightly higher (figure 6.13c) the influence of the stern cannot be seen for the centerline, but the upper extent is clearly drawn in the flow expansion region behind the stern (located at x/D=4.9). In a plume with much stronger crossflow (λ=0.17) a trajectory close to the hull is found. It can here be seen in figure 6.13d that the plume is completely drawn upward by the stern section. Centerline, upper and lower extents are located significantly higher than predicted by a simple buoyant jet in crossflow model. In general, the Lagrangian model seems to be closer to the (start of the) plume trajectory compared to the integral model by Fischer (1979). This does not mean either of both is more accurate. The central streamline of the plume might be more close to the integral solutions of Fischer (1979).

Over the full set of experimental runs, a pattern is found for the relation between the main plume parameters (λ,F_Δ) and the influence of a wall step section on the plume. The influence is divided in a mild influence (only the top fringes of the plume are lifted) or a severe influence (the full plume trajectory is altered). The result is shown in figure 6.14a. For each value of F_Δ, a certain range of values for λ can typically be associated with overflow dredging plumes. Clearly, plumes with λ in the lower part of the range for a given F_Δ are affected by the stern. A second order polynomial was fitted to the data points, approximately separating the regions of influence and of no influence of the stern.

The asymptotic (integral) solutions from Fischer (1979) show that for large ξ, the horizontal and vertical distance can be scaled by, respectively:

$$\xi = x\ z_{_M}^{-2} z_{_B} (C_3/C_1)^4 \tag{6.12}$$

and

$$\zeta = \bar{z}\ z_{_M}^{-3/2} z_{_B}^{1/2} C_1^{-3} C_3^2 \tag{6.13}$$

with $\bar{z}$ the mean trajectory elevation, C_1=1.8, C_2=1.44, C_3=1.8 and C_4=1.1, determined by Wright (1977).

When all experimental plume trajectories are plotted using these self-similar coordinates, they should collapse in case they are not influenced by external factors. In figure 6.14b, the self-similar trajectories are plotted. Plume trajectories uninfluenced by the stern are plotted in thin black lines, it can be seen that these plumes show relatively good self-similarity. A number of plume trajectories are above the self-similar group (drawn in thick black lines). These are the plumes influenced by the stern. In grey are the plumes of which only the upper fringes seem to be in fluenced. It is observed that those

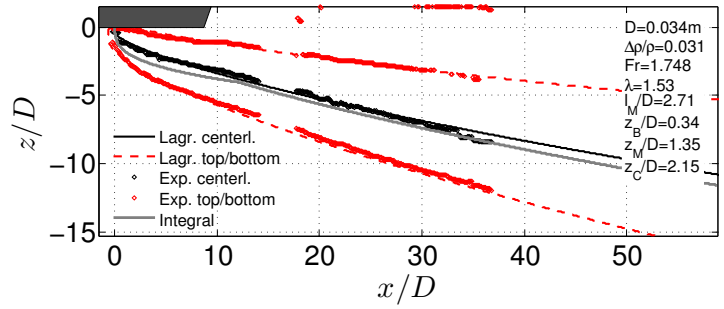

(a)

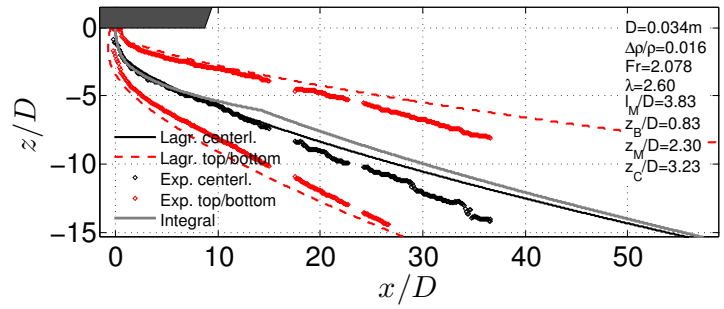

(b)

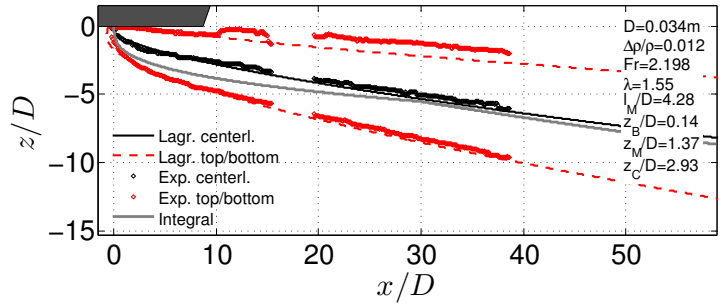

(c)

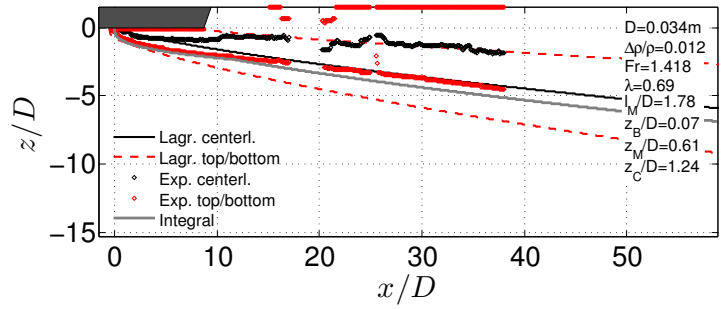

(a)

Figure 6.13: Comparison of experimental results with Lagrangian model (Lee and Chu, 2003) and integral laws (Fischer, 1979). Experimental centerlines in black markers, experimental upper and lower extents in red markers. Lagrangian model centerlines and extents in black, resp. red line. Integral laws in grey line.

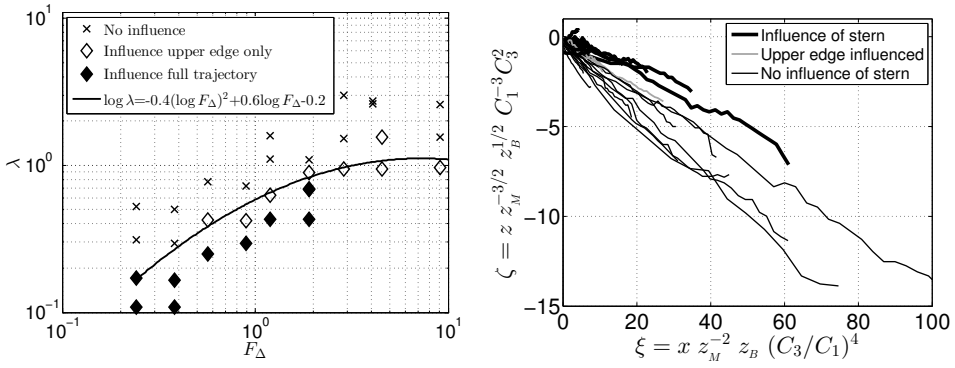

(a) (b)

Figure 6.14: (a) Overview of the relation between main plume parameters (λ,F_Δ) and the influence of a wall step section on the top fringes of the plume or on the full plume trajectory. (b) Non-dimensionalised trajectories of all observed sediment plumes in crossflow, with plumes of which the full trajectory is influenced by the stern drawn in red, plumes of which only the upper fringes are influenced in blue and plumes not influenced by the stern in black.

are in between the self-similar group and the heavily in fluenced plumes. A drawback of this method is that the plumes with large z_M and small z_B have very small maximum value of the scaled horizontal dimension, ξ. Moreover, the present non-dimensionalisation is only valid for plumes with $z_M < z_B$. The full asymptotic solutions by Fischer (1979) are given in table 6.2.

In figure 6.15, these asymptotic solutions (ζ) are compared with the non-dimensionalised measured trajectories, $\widehat{\zeta}$. It can now be confirmed that the experimental plume trajectories with no influence of the stern are in line with the theoretical solutions. The trajectories of plumes with influence of the wall step are significantly off these theoretical solutions. It can also be seen that the plumes that were qualitatively classified as plumes of which only the top edge was influenced by the stern, have actually also a mean trajectory which is slightly influenced by the stern (grey diamonds in figure 6.15).

Finally, it is investigated which is the critical distance $|\bar{z}|$ between plume centerline height and the hull wall (z=0) at the x-position of the wall step (x_{ws}). Also, the distance $|\bar{z}_t|$ between the plume's top edge and the hull wall at that position could be of importance. This critical distance for influence of the wall step on the plume trajectory and upper edge can be found by plotting the values of $|\bar{z}(x = x_{ws})|$ and $|\bar{z}_t(x = x_{ws})|$ for each plume and

Table 6.2: Dimensionless distances and asymptotic solutions for the buoyant jet in crossflow, according to Fischer (1979).

	$z_M > z_B$	$z_M < z_B$
Horizontal distance ξ	$x\ z_M^{-1}(C_1/C_2)^6$	$x\ z_B z_M^{-2}(C_3/C_1)^4$
Vertical distance ζ	$-\bar{z}\ z_M^{-1}C_1^2(C_2)^{-3}$	$-\bar{z}\ z_M^{-3/2}z_B^{1/2}C_1^{-3}C_3^2$
κ	$(C_4/C_1)(C_2/C_1)$	$(C_4/C_3)(C_3/C_1)^{1/3}$
Critical ξ, ξ_c	$\kappa^{1/2}(z_B/z_M)^2$	$\kappa^{-3}(z_M/z_B)$
Solution for $\xi << 1$	$\xi^{1/2}$	$\xi^{1/2}$
Solution for $1 << \xi << \xi_c$	$\xi^{1/3}$	$\xi^{3/4}$
Solution for $\xi_c << \xi$	$\kappa(z_B/z_M)^{1/3}\xi^{2/3}$	$\kappa(z_B/z_M)^{1/6}\xi^{2/3}$

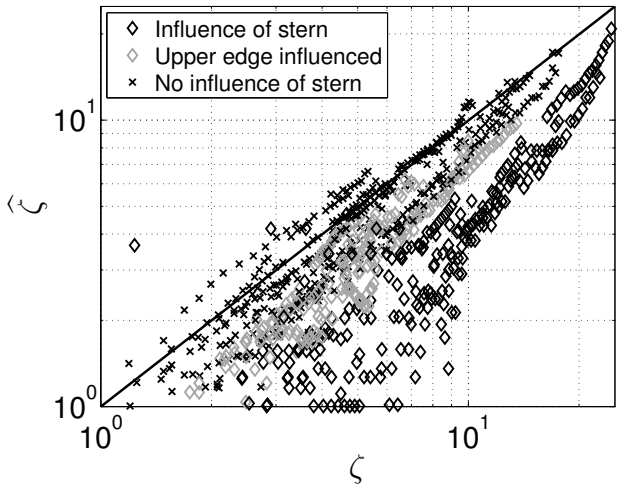

Figure 6.15: Self-similarity solutions ζ of all observed sediment plumes in crossflow compared with non-dimensionalised measured plume trajectories $\widehat{\zeta}$. Plumes of which the full trajectory is influenced by the stern drawn in black diamonds, plumes of which only the upper fringes are influenced in grey diamonds and plumes not influenced by the stern in black crosses.

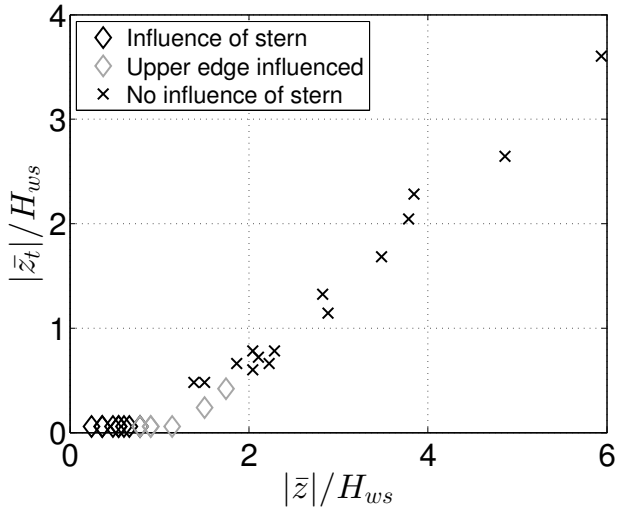

Figure 6.16: Scatter plot of $|\bar{z}(x = x_{ws})|$ and $|\bar{z}_t(x = x_{ws})|$ for each plume, with indications of wall step influence.

using the same marker code for wall step influence as above. The result is shown in figure 6.16. It can clearly be seen that the plumes of which the complete trajectory is influenced by the wall step have a value of $|\bar{z}|$ smaller than the wall step height H_{ws}, which can be seen as the draft of a dredging vessel. So the trajectory is influenced if

$$|\bar{z}(x = x_{ws})| < H_{ws} \tag{6.14}$$

Also, for plumes of which the top edge only is influenced by the wall step, roughly the following is valid:

$$H_{ws} < |\bar{z}| < 2H_{ws} \tag{6.15}$$

and also

$$0 < |\bar{z}_t| < 0.5H_{ws} \tag{6.16}$$

The above discussions have demonstrated that a buoyant jet in crossflow containing fine sediments is closely following the expected buoyant jet trajectories in case no external influences are present. The influence of the stern of a schematised hull is clearly seen to deviate the plume trajectories and/or vertical edge towards the water surface.

6.5.2 Classification of buoyant sediment plumes

The present experimental plume trajectories can be used to derive a simple law for the fast prediction of the class to which the plume belongs. Three classes can be defined: density currents, passive (horizontal) plumes and transitional plumes.

Based on the two main characteristic numbers of buoyant jets or plumes in crossflow -Richardson number Ri ($=F_{\Delta}^{-2}$) and the inverse of the velocity ratio- a classification is developed for the behavior of buoyant jets released shortly upstream a backward-facing step (stern). The classification is performed based on the angle of the plume axis in the bent plume regime, relatively far from the source. A plume showing no vertical momentum for x/D >30 is categorized as horizontal plumes. Plumes having a slope of 1/5 or more after this distance are categorized as density currents. Intermediate cases are labeled in transitional regime.

When all 33 experiments are added to a diagram, an exponential function can be fitted forming the boundary between plume regimes (figure 6.17). A density current is found under the condition $1/\lambda < \lambda_1(Ri)$, while a horizontal plume is found in case $1/\lambda > \lambda_2(Ri)$, with

$$\lambda_1 = a_1 Ri^{\frac{b_1}{\log(10)}} \tag{6.17}$$

$$\lambda_2 = a_2 Ri^{\frac{b_2}{\log(10)}} \tag{6.18}$$

where, a_1=1.14, b_1=0.64, a_2=2.26 and b_2=0.81.

It is clear that the coefficients will be in turn a function of the distance between plume exit pipe and stern, which was in these experiments equal to 4.9 or 9.4 pipe diameters. In dredging vessel construction an overflow pipe at large distance from the stern seems to be advantageous for overflow plume containment, since it gives more time for the plume to descend, before reaching the uplifting effect of the stern section. This effect will be investigated in more detail using the CFD model, of which the developement is described in the next chapters.

6.5.3 Influence of air bubbles

A number of tests have been executed in which air bubble have been injected in the overflow pipe. The tests are qualitative since the diameter of the air

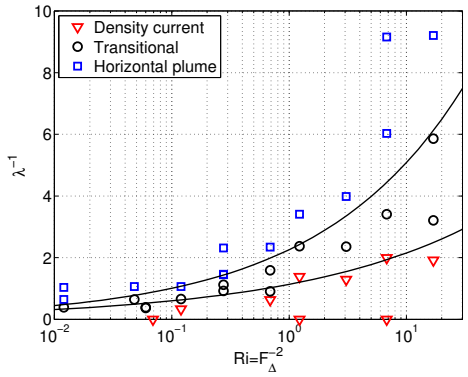

Figure 6.17: Classification of plumes in crossflow, released shortly upstream of a backward-facing step (wall step). Plumes are classified as density currents for $1/\lambda < \lambda_1(Ri)$ *(red line), while horizontal plumes are found for* $1/\lambda > \lambda_2(Ri)$ *(blue line).*

bubbles is hard to control in a laboratory. Moreover, the air bubble diameter can never be brought to scale with the prototype situation. Using the air bubble rising velocity (w_b) diagram by Chanson (1996), a 1/50 scaling of bubbles with w_b=0.2 m/s in the full-scale flow, results in an air bubble diameter of 0.1 mm in equivalent lab conditions. This objective is very hard to meet in the present laboratory flows. In the overflow plume setup, air bubbles are generated by sending compressed air through an injection needle inserted in the overflow shaft. This produced air bubbles in the plume between 0.5 and 3 mm. The analysis of the effect of these bubbles will be thus qualitatively since the bubbles are too large compared with the pipe diameter and plume length scales.

A simple way to evaluate the effect of the presence of air bubbles in the laboratory plume, is to perform two experiments with identical plume input parameter, once without and once with air bubbles injected. Two cases are shown in figure 6.18.
It seems the air bubbles have an influence in the early stages of the plume, where the net mixture density is lowered by the air bubbles fraction. This results in an upward deviation of the plume with bubbles, roughly through $0< x/D <5$. For $x/D >5$, the trajectories of plumes with and without bubbles have a parallel course, at the same rate of descent. This suggests the air bubbles do work by buoyancy in the first stages of the plume, without disrupting the amount of mixing. Different mixing would result in a different dilution, buoyancy and rate of descent in the downstream part.

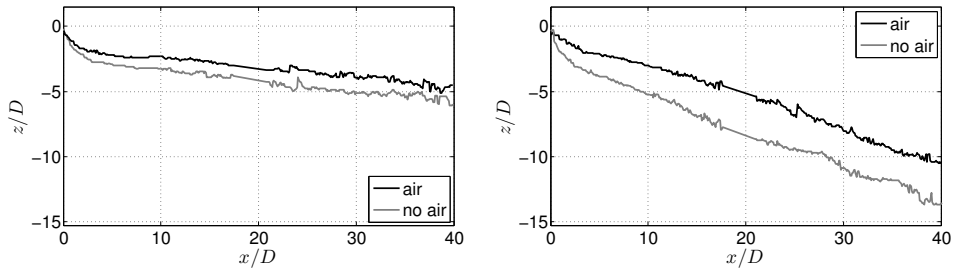

Figure 6.18: Two cases for qualitative analysis of the influence of air bubbles in a sediment plume in crossflow. For both cases, λ=3, while in the case in (a) F_Δ=9.1 and for the case in (b) F_Δ=4.1.

When observing the obscuration of the plumes in the images taken from the case shown in figure 6.18a, another influence of the air bubbles can be seen (figure 6.19). In figure 6.19a, the plume without air produces vertical profiles of obscuration with a shape similar to a Gauss curve. The obscuration goes to zero both below and above the plume. In figure 6.19b, the plume with air is shown. It can be observed that the vertical profile of obscuration α has a different shape. The value of α above the plume is not going to α=0. Instead, a higher value is found above the plume, indicating an increased sediment concentration above the plume. Below the plume, α goes to zero here as well. The air bubbles caused a fraction of the sediment to tear off from the main plume. A likely explanation is the entrainment of fine sediments in the wake of rising air bubbles. Another possible mechanism is the adherence of sediment particles to the interface between air and water. However, this would likely cause the sediment to be transported all the way to the surface.

It can thus be concluded that the air bubbles in an overflow plume potentially have two effects. Firstly, the reduced excess mass density $\Delta\rho = \rho_m - \rho_w$ causing a higher trajectory. Secondly, a surface plume generated by sediment transported in air bubble wakes. In the numerical simulation of the air bubble phase, this will have to be taken into account.

6.6 Conclusions

The set of laboratory experiments conducted in this stage of the research had a twofold objective. Regarding the first objective -generating a dataset

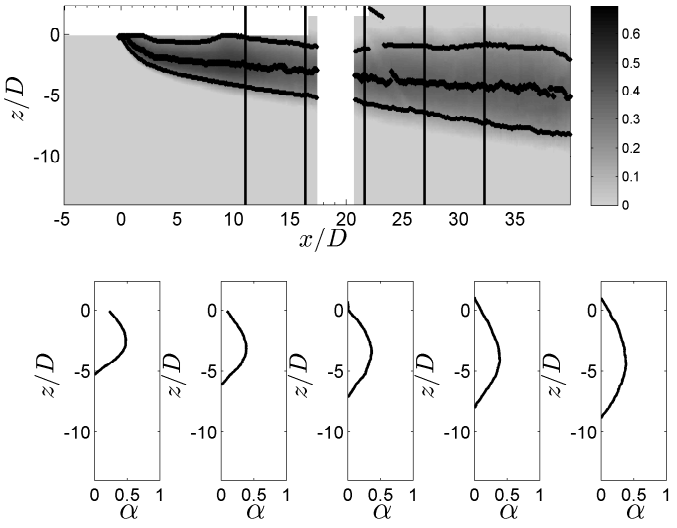

(a)

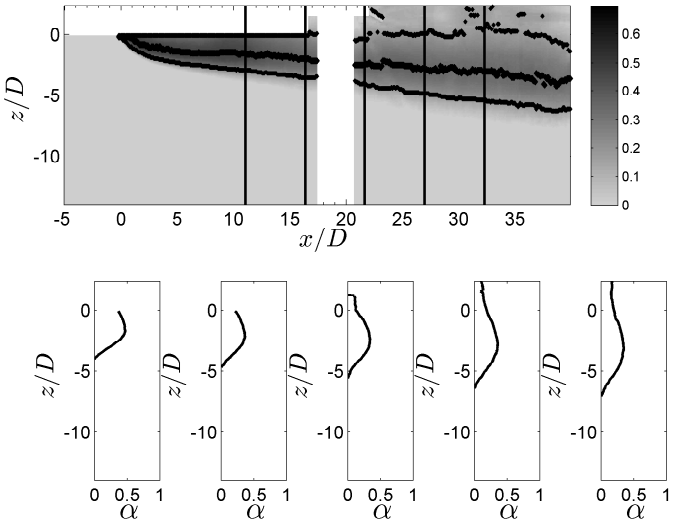

(b)

Figure 6.19: Imaging results for the case in figure 6.18a. In (a), the plume without air bubbles is visualised, in (b) the plume with air bubbles. Both in the grey scale map and in the profile plots below, the light obscuration α is plotted.

for comparison with the numerical model, a set of 33 plumes with different conditions have been monitored. Observed parameters include plume trajectory, plume width and a complete set of time-averaged flow variables as well as turbulence properties. For the measurements of Reynolds stresses and turbulent sediment mass fluxes, a newly developed technique for ADV data processing was applied.

Regarding the second objective -gaining insight in the plume behaviour, a number of general patterns have been described:

- Fine sediment plumes in crossflow without external influences other than the wall boundary layer along the hull have trajectories corresponding to those found in literature for the buoyant jet in crossflow. Neither the settling velocity of the fine sediment particles, nor the possibly different turbulent Schmidt number for particles did not have an influence on the plume trajectory.
- The classification of plumes based on the most important dimensionless numbers λ and F_Δ.
- The influence of the stern section of a ship hull on the plume behaviour.
- The potential influence of air bubbles in the released water-sediment mixture through the reduced excess mass density of the plume, as well as through entrainment of sediment in the wake of the rising bubbles.

The insights gained can be incorporated in the setup of a large-eddy simulation model of the plume in crossflow with equal dimensions and geometry compared to the experimental plumes (see next chapter). The dataset obtained will be expoited for the validation and performance assessment of the developed model.

Chapter 7

LES model at laboratory scale

With exception of section 7.4, this chapter has been published in Decrop et al. *(2015b)*

7.1 Introduction

The objective of the work described in this chapter is to develop a numerical model capable of accurately predicting the mean trajectory and the turbulent dispersion of a negatively buoyant sediment plume in a crossflow. To be able to validate the numerical model thoroughly, a model is made with the same geometry as the laboratory experiments described in previous chapters. In this work the equations are solved using Ansys Fluent, release 14.5.

In a first step, the vertical plume experiments are reproduced by the numerical model. Next, experiments of a plume in crossflow are simulated. Both the flow fields with and without the influence of a vessel stern are analysed. The latter is in this chapter schematised as a wall step. To this end, a Large-Eddy Simulation (LES) approach is selected. This approach allows the resolution of the larger turbulent motions, but requires a higher processor cost compared to steady-state (Reynolds-Averaged Navier-Stokes, RANS) or unsteady RANS (URANS). Yet, it was intended to set up a model with acceptable process times to enable later upscaling of the model to prototype scale, including realistic dredging vessel geometry and propeller action.

As mentioned in section 2.4.4, many types of turbulent structures occur in plumes in crossflow. Some of the large-scale structures have a steady nature

and can also be solved with a RANS model. Therefore, one could wonder why a more time-consuming LES model is used in that case. Many of the larger turbulent structures are only resolved in a time-domain model, for example buoyancy bursts referred to as cauliflowers and sediment entrained in wake vortices (observed by Smith and Mungal (1998)). This makes the use of a RANS model with an isotropic turbulence model less suited. The influence of the geometry of the surrounding walls on these structures can therefore ideally be studied using time-domain solutions. Also, in the future, the study of pulsed plumes using the presented model would require time-domain resolution in any case (Coussement *et al.*, 2012; Hsu and Huang, 2012). Another main argument to make use of LES is the interaction of individual large eddies with three specific flow features present in the prototype-scale cases: flow expansion behind the stern, air bubbles and propeller jets.

Frequency analysis of the turbulent fluctuations of velocity and tracer concentration is possible using LES results. Experiments in the past show both -5/3 and -3 exponential spectral energy cascade laws (Dai *et al.*, 1994a).

In order to set up an LES model of good quality, two requirements are specified. The first one is to ensure that the percentage of resolved turbulent kinetic energy (TKE) is sufficient. Pope (2004) defined a criterion for the minimum amount of turbulence to be resolved in an LES model. The idea of complete LES was defined by Pope (2004) as an LES simulation in which solution-adapted gridding is applied in order to ensure that at each time and at each location the criterion is met. The second requirement is that the time-averaged result of the LES simulation should be grid-independent. The flow fields obtained by the numerical simulations presented in this work are evaluated using both quality requirements.

In the following section (7.2), the governing equations as implemented in the Ansys Fluent code and the sub-gridscale models selected for the development of the plume model are presented, as well as the discretisation of the equations on unstructured grids. In section 7.3 the boundary conditions along the edges of the domain are described. In section 7.4, a number of benchmark cases are simulated and compared with data from the literature. In section 7.5.1, the simulation of an experimental run of a vertical plume is described. In order to manage the large number of relevant processes in a near-field overflow plume, complexity is added in a step-wise manner: firstly crossflow is added to the vertical plume, and the results are described and analysed in section 7.5.2. Secondly, the effect of a schematised ship hull on the plume dispersion

is studied by adding a wall step to the flow (section 7.5.3). Finally, the results are discussed and conclusions are drawn in section 7.6.

7.2 Governing equations

7.2.1 Water-sediment mixture

Two-phase flows can be classified as dense or dispersed flows (Crowe, 1982). In a dilute two-phase flow, the particle motion is determined by the surface and body forces acting on the particle. In dense two-phase flows, the forces acting on particles due to interparticle collisions are also important. An important dimensionless number in fluid-particle interaction is the Stokes number, defined as

$$\mathrm{St} = \frac{\tau_p}{\tau_f} = \frac{\rho_s d^2 U}{18 \mu L} \tag{7.1}$$

where τ_p and τ_f are the particle response time and characteristic time-scale of the fluid turbulent motions. U is a characteristic fluid velocity and L a characteristic turbulent length scale. For particles with very small diameter (order of magnitude 10^{-5} m), it is clear that the Stokes number will be very small ($\mathrm{St} \ll 1$). This implies that the particles will be nearly in equilibrium with the fluid velocity and that the relative velocity will be small.

In two-phase flows, a number of coupling mechanisms between fluid and particles can occur. One-way coupling indicates that the fluid velocity has an influence on the particle trajectory, but that the presence of the particles has negligible effect on the fluid phase. In two-way interaction, the particles have an effect on the properties of the fluid flow. In $\mathrm{St} \gg 1$ flows, the particles might be much larger than the fluid turbulent scales and the particle wakes might increase the turbulent fluctuations of the fluid velocity. In $\mathrm{St} \ll 1$ flows, on the other hand, the particles which are much smaller than the fluid turbulent scales might damp the fluid velocity fluctuations. The effect of particles on the velocity turbulence is called turbulent modulation.

Elghobashi (1994) presented a map in which the volume concentration limits are given for the different coupling modes. The limit between one-way coupling and two-way coupling was defined at a volume concentration $\phi = 10^{-6}$. When the volume concentration is higher than $\phi = 10^{-3}$, additional effects play a role. When $\phi = 10^{-2}$, the average interparticle distance is about 8 particle diameters and particle-particle collisions are more likely to occur. At this

stage, three-way coupling occurs. Finally, when the Stokes number is large enough, particles are also influenced by other particles' wakes, in which case four-way interaction occurs.

In the near-field of dredging plumes, the volume concentration of fine sediment is typically of the order 1 to 10%, or ϕ=10^{-2} to 10^{-1}. This would be clearly in the four-way interaction region. However, since the particle Reynolds number (equation 7.2 in which U_r is the relative velocity) is smaller than one, the flow around the particles will be in Stokes regime and there will be no wake to influence other particles. For coarse sand, this might be the case, but the sand fraction is only a minor fraction in the overflow plume. The four-way interaction can therefore not be expected.

$$\mathrm{Re_s} = \frac{U_r d}{\nu} \tag{7.2}$$

Given the relatively small particle-fluid density ratio ρ_s/ρ_w, and given the small Stokes numbers, the particle inertia will be damped very quickly in accelarating or decelerating flows. The probability of particle-particle collisions will therefore also be small. This makes that the most probable regime for fine-sediment flows is the two-way interaction. According to Crowe (1982), LES of two-way coupled flows might impose difficulties since the turbulence modulation or turbulence damping might require some modifications to the subgrid-scale turbulence model.

The dispersed (particulate) fraction can now be treated according to different methods. Either a Lagrangian approach is followed in which a force balance determines the individual trajectories of the particles. This allows for more complex fluid-particle interactions to be implemented at the level of single particles, but is prohibitive when the number of particles is extremely large, such as in highly-concentrated fine sediment flows. The other method often used is the two-fluid model (Spalding, 1981). This method implies a volume averaging (or Favre averaging) of the properties of the particulate phase. This requires that the number of particles in each computational cell is high enough to guarantee a constant value for the averaged property in a stationary turbulent flow. In the currently presented modelling work, the two-fluid approach is followed since the number of fine sediment particles in highly-concentrated flow will always be very high, unless micrometer-size computational cells are used.

For the two-fluid model, two sets of momentum equations need to be solved. This is required when the relative velocity of the particles is large. For small $\mathrm{Re_s}$, however, another approach can be adopted. The mixture model approach was described by Ishii and Hibiki (2006), in which one set of momentum and continuity equations is solved for the mixture only rather than for each phase separately. This approach has been used in the present modelling work. The Navier-Stokes equations are written for the mixture and are in conservative form. For LES, the equations are filtered in space with a filter size equal to the grid size. The mixture continuity equation reads:

$$\frac{\partial}{\partial t}\left(\rho_m\right) + \nabla \cdot \left(\rho_m \overrightarrow{u_m}\right) = 0 \tag{7.3}$$

where ρ_m is the mixture mass density, $\overrightarrow{u_m}$ is the mass averaged velocity vector of the water-sediment mixture.

$$\overrightarrow{u_m} = \frac{1}{\rho_m}\left[(1-\phi)\rho_m \overrightarrow{u_w} + \phi\rho_s \overrightarrow{u_s}\right] \tag{7.4}$$

where ϕ is the sediment volume concentration, ρ_w and ρ_s are the mass density of water and sediment, respectively and $\overrightarrow{u_w}$ and $\overrightarrow{u_s}$ are the velocity vector of sea water and sediment, respectively. The momentum equation for the mixture reads:

$$\frac{\partial}{\partial t}\left(\rho_m \overrightarrow{u_m}\right) + \nabla \cdot \left(\rho_m \overrightarrow{u_m}\overrightarrow{u_m}\right) = -\nabla p - \nabla \cdot \tau + \rho_m \overrightarrow{g} + \overrightarrow{F_D} + \nabla \cdot \overrightarrow{D} \tag{7.5}$$

where p is the pressure, τ is the shear stress tensor, $\overrightarrow{g}$ is the gravitational acceleration vector, $\overrightarrow{F_D}$ is a momentum source from air bubble drag and $\overrightarrow{D}$ is a drift flux (see equation 7.17).

In LES modeling, the large scales of turbulent eddies are resolved on the model grid. The effect of the remaining smaller scales of turbulent motions, i.e. smaller than the grid size, is included in a sub-grid scale eddy viscosity. To this end, the Navier-Stokes equations are filtered with a spatial filter so that only the small scales are filtered away and the larger turbulent motions are allowed to develop in the model results. The filter can be defined as follows

$$\widehat{\phi}(\overrightarrow{x}) = \int \phi(\overrightarrow{y}) G(\overrightarrow{x}, \overrightarrow{y}) \mathrm{d}\overrightarrow{y} \tag{7.6}$$

where ϕ can be any scalar or vector field and G is the filter function. In the current modelling, the top-hat filter has been used: $G(\overrightarrow{x}, \overrightarrow{y}) = 1/V$ for all $\overrightarrow{y}$ inside a grid cell and $G(\overrightarrow{x}, \overrightarrow{y}) = 0$ otherwise, where V is the grid cell volume. Effectively, the finite volume discretisation and corresponding grid cells are used as an implicit filter.

The complex dynamics of a plume in a crossflow such as formed below the keel of a TSHD, include time-varying turbulent phenomena similar to a cylinder wake vortex street and Kelvin-Helmholtz instabilities (Fric and Roshko, 1994; Kelso *et al.*, 1996; Lim *et al.*, 2001). In order to capture the effect of these flow features on the sediment dispersion, a time domain model is needed which can resolve the main turbulent motions.

The filtered equations result in a stress term for the contributions of the sub-grid scale (SGS) turbulent motions, the sub-grid stress τ_{SGS}. In equation 7.5, τ is the sum of the molecular (τ_m) and the turbulent shear stress τ_{SGS}. The molecular shear stress τ_m is modelled using the Boussinesq approximation:

$$\tau_m = \mu_m \left(\nabla \overrightarrow{u_m} + \nabla \overrightarrow{u_m}^T \right) \tag{7.7}$$

where u_i is the instantaneous velocity vector, μ_m is the molecular dynamic viscosity of the mixture. Einstein's formula for the apparent viscosity of a dilute mixture reads (Einstein, 1906):

$$\mu_m = \mu_w (1 - \phi)^{-2.5} \tag{7.8}$$

With ϕ the particle volume concentration (m^3 solids per m^3 of mixture) and μ_w the molecular dynamic viscosity of the liquid phase. Using a first order Taylor expansion around ϕ=0, it can be shown that this equation can be linearised to $\mu_m = \mu_w(1 + 2.5\phi)$ for $\phi < 0.1$.

In order to explain the appearance of the subgrid-scale stress tensor, the filtered Navier-Stokes equations are written in Einstein notation, and for a fluid with zero viscosity and in zero gravity:

$$\frac{\widehat{\partial \rho u_i}}{\partial t} + \frac{\widehat{\partial \rho u_i u_j}}{\partial x_j} = -\frac{\widehat{\partial p}}{\partial x_i} \tag{7.9}$$

where the $\widehat{...}$ notation indicates spatial filtering of a variable (equation 7.6). This can now be written as

$$\frac{\partial \widehat{\rho u_i}}{\partial t} + \frac{\partial \widehat{\rho u_i u_j}}{\partial x_j} = -\frac{\partial \widehat{p}}{\partial x_i} + \left(\frac{\partial \widehat{\rho u_i u_j}}{\partial x_j} - \widehat{\frac{\partial \rho u_i u_j}{\partial x_j}} \right) \tag{7.10}$$

where the term between brackets is the commutation error due to the assumption that the filtered gradient of $u_i u_j$ is equal to the gradient of the filtered $u_i u_j$. In LES, this term is usually neglected. It is not certain what the implications are of omitting the commutation term.

This equation cannot be used in this form, since the correlations between the instantaneous velocity components are unknown. Therefore the Navier-Stokes equations are written in the form:

$$\frac{\partial \widehat{\rho u_i}}{\partial t} + \frac{\partial \widehat{\rho} \widehat{u_i} \widehat{u_j}}{\partial x_j} = -\frac{\partial \widehat{p}}{\partial x_i} - \frac{\partial}{\partial x_j} \left(\widehat{\rho u_i u_j} - \widehat{\rho} \widehat{u_i} \widehat{u_j} \right) \tag{7.11}$$

The SGS stress tensor τ_{SGS} can thus be written as:

$$\tau_{SGS} = \widehat{\rho u_i u_j} - \widehat{\rho} \widehat{u_i} \widehat{u_j} \tag{7.12}$$

The first term on the right-hand side is unknown, so τ_{SGS} has to be modelled. The deviatoric part of the SGS stress term is assumed isotropic and the Boussinesq approximation is used (Hinze, 1975):

$$\tau_{i,j} - \tau_{k,k} \delta_{i,j} = -2 \mu_t \widehat{S_{i,j}} \tag{7.13}$$

with $\widehat{S_{i,j}}$ the resolved rate-of-strain tensor. The isotropic SGS viscosity μ_t has to be modelled. For this purpose, the model by Smagorinsky (1963) is used:

$$\mu_t = \rho (C_s \Delta)^2 |\widehat{S}| \tag{7.14}$$

with C_s the Smagorinsky coefficient, Δ the grid filter width (equal to the cubic root of cell volume) and $|\widehat{S}|$ the modulus of the rate-of-strain tensor. In case the length scale $C_s \Delta$ is larger than the distance to a wall d_w, it is replaced by κd_w, where κ is the von Kármán constant.

Although this model has proven to be suitable for a wide range of flows, a universal value for C_s does not exist. For this reason Germano *et al.* (1991) defined an identity with which a dynamic value for C_s can be determined based on filtering operations on two levels, a method later modified by Lilly (1992). More precisely, when the equations are filtered for a second time,

using a so-called 'test-filter' $\tilde{\Delta}$ (here equal to 2Δ), a stress tensor is found for the scales smaller than the test filter width (sub-test scale, STS):

$$T_{STS} = \widetilde{\widehat{\rho u_i u_j}} - \tilde{\widehat{\rho}}\tilde{\widehat{u}}_i\tilde{\widehat{u}}_j \tag{7.15}$$

Where $\tilde{(...)}$ denotes the test-filtering of a variables. Subtracting the test-filtered SGS stress from T_{STS}-stresses yields the Germano identity:

$$T_{STS} - \widetilde{\tau_{SGS}} = \widetilde{\widehat{\rho}\widehat{u}_i\widehat{u}_j} - \tilde{\widehat{\rho}}\tilde{\widehat{u}}_i\tilde{\widehat{u}}_j = L \tag{7.16}$$

In which L can be seen as the stress related to the resolved turbulent motions between grid-filter and test-filter scales. L is known and both stress terms on the left-hand side can be written in similar fashion (eq. 7.13), allowing to isolate and solve for C_s.

In this form, some two-way interaction effects are captured. First, the change in molecular viscosity due to sediment particles, secondly, the turbulence destruction due to vertical density gradients caused by varying sediment concentration. The test-filtering operation has the property that the reduction of resolved turbulent fluctuations (due to density gradients) is also fed in the subgrid turbulent viscosity.

Since the momentum equation for the mixture is derived from summing the momentum equations for water and sediment, a drift velocity advection term arises with the drift flux $\overrightarrow{D}$:

$$\overrightarrow{D} = (1-\phi)\rho_w\overrightarrow{u_{dr,w}}\overrightarrow{u_{dr,w}} + \phi\rho_s\overrightarrow{u_{dr,s}}\overrightarrow{u_{dr,s}} \tag{7.17}$$

where velocities with subscript 'dr' are drift velocities of water and sediment phases, defined as the difference between phase velocities $\overrightarrow{u_w}$ and $\overrightarrow{u_s}$ on the one hand and the mixture velocity on the other hand. This term expresses the momentum exchange due to sub-grid scale diffusion of sediment particles to adjacent grid cells.

The slip velocity is defined as $\overrightarrow{u_{sw}} = \overrightarrow{u_s} - \overrightarrow{u_w}$ and is calculated by the expression by Manninen *et al.* (1996) in addition to an extra term for gradient diffusion of the particulate phase:

$$\overrightarrow{u_{sw}} = \frac{(\rho_s - \rho_m)d_s^2}{18\mu_w}\overrightarrow{a} - \frac{\nu_t}{\mathrm{Sc_t}}\left(\frac{\nabla\phi}{\phi} - \frac{\nabla(1-\phi)}{1-\phi}\right) \tag{7.18}$$

where $\overrightarrow{a}$ is the acceleration vector, d_s is (one of)the diameter(s) of sediment particles (fractions) and $\mathrm{Sc_t}$ is the turbulent Schmidt number for the SGS sediment diffusion, which is derived in a similar way as C_s, from the difference between grid-filtered and test-filtered SGS sediment fluxes, according to the procedure below. The second term on the right-hand side is the drift velocity (for sediment and for water), which can be seen as the mean fluctuations of the fluid velocity at the location of the particle, $\overline{u'_{f_p}}$ (Breugem, 2012). The drift velocity can be written as the turbulent flux divided by the concentration, in which the turbulent flux can be modelled by the Boussinesq approximation with an eddy diffusivity (Viollet and Simonin, 1994).

The turbulent eddy viscosity ν_t is varying in time and space and is determined using the Germano identity. Similarly, the turbulent Schmidt number has to be considered neither constant in time nor uniform in space. A similar procedure as used in the Germano method is used to find the optimal local value of Sc_t (Lilly, 1992). The grid-filtered, $\widehat{(...)}$, and test-filtered, $\widetilde{(...)}$, scalar transport equations yield sub-grid and sub-test turbulent sediment fluxes. The difference between both yields a turbulent sediment flux associated with the window of turbulent scales between the grid filter and test filter lengths:

$$P_i = \widetilde{\widehat{\phi}\widehat{u}_i} - \tilde{\widehat{\phi}}\tilde{\widehat{u}}_i = F_{STS} - \widetilde{F_{SGS}} \tag{7.19}$$

P_i is known and the SGS fluxes can be written in the form:

$$F_{SGS} = \frac{2(C_s\Delta)^2}{Sc_t}|\widehat{S}|\frac{\partial\widehat{c}}{\partial x_j} \tag{7.20}$$

The STS flux F_{STS} is written in the same form, but Δ, $|\widehat{S}|$ and $\widehat{\phi}$ have been test-filtered.

$$F_{STS} = \frac{2(C_s\widetilde{\Delta})^2}{Sc_t}\widetilde{|\widehat{S}|}\frac{\partial\widetilde{\widehat{c}}}{\partial x_j} \tag{7.21}$$

Therefore, a solution for Sc_t can be found at every time-step at every cell in the domain. Clipping of Sc_t is needed since the test-filtering procedure can give rise to unrealistic values of Sc_t, as well as instabilities in case of Sc_t close to or below zero (Kim, 2004). For locations away from a sediment bed, values of $Sc_t \gg 1$ are unphysical since it would mean the diffusion of momentum would be many times larger than the diffusion of particles. This is unlikely since (i) both diffusion fluxes are the result of the same vortices

and (ii) the small Stokes numbers in the flow studied here. A range of about $0.5 \leq Sc_t \leq 2$ was found by Cellino (1998) and Cellino and Graf (2000) in sand transport experiments in an open channel (away from the sand bed). The same range of Sc_t produced a good behaviour in the model used in this work.

Finally, a transport equation for the sediment phase is needed. The SGS diffusion of sediment particles is already included in the slip velocity formulation (eq. 7.18). The dispersed phase transport equation has therefore only the time derivative and advection terms and is written as:

$$\frac{\partial}{\partial t}\left(\rho_s \phi\right) + \nabla \cdot \left(\rho_s \phi \overrightarrow{u_m}\right) = -\nabla \cdot \left(\rho_s \phi \overrightarrow{u_{dr,s}}\right) \tag{7.22}$$

In the following, the $\widehat{(...)}$ notation for grid-filtered LES results will be omitted.

7.2.2 Air bubbles

The air bubble volume fraction is tracked using a Lagrangian discrete phase model. In this model, the bubbles' trajectories are governed by a force balance including drag force, gravity force, virtual mass force and pressure gradient forces in the fluid phase. The acceleration of the air bubbles is thus determined from Newton's second law:

$$\rho_a \left(\frac{\mathrm{d}\overrightarrow{u_a}}{\mathrm{d}t}\right) = \overrightarrow{F_D} + \overrightarrow{F_g} + \overrightarrow{F_v} + \overrightarrow{F_p} \tag{7.23}$$

Where the following forces (per unit volume of fluid) appear in the RHS: $\overrightarrow{F_D}$ is the drag force and $\overrightarrow{F_g}$ is the gravitational force. In bubbly flows a virtual mass force $\overrightarrow{F_v}$ and the pressure gradient force $\overrightarrow{F_p}$ should be taken into account (Bel F'Dhila and Simonin, 1992). The virtual mass force $\overrightarrow{F_v}$ accounts for added mass associated with the air bubble, like liquid in the wake of a rising bubble. The added mass of this liquid should be taken into account when the acceleration of the bubble is computed. $\overrightarrow{F_v}$ is defined as (Odar and Hamilton, 1964),

$$\overrightarrow{F_v} = \frac{1}{2}\rho_m \frac{\mathrm{d}}{\mathrm{d}t}\left(\overrightarrow{u_m} - \overrightarrow{u_a}\right) \tag{7.24}$$

The local pressure gradient gives rise to a pressure gradient force $\overrightarrow{F_p}$, defined as follows

$$\overrightarrow{F_p} = \rho_m U_a \nabla U_m \tag{7.25}$$

where U_a and U_m are the air bubble and mixture velocity magnitude, respectively.

Additional forces on particles to consider in multi-phase flow are the Saffman lift force (Saffman, 1965) and the Basset history force (Odar and Hamilton, 1964). The saffman lift force arises when a particle in a shear flow experiences a gradient in the relative velocity and thus in the pressure. Since the Saffman lift force is much smaller than the buoyancy of the bubbles, this force is not taken into account. The Basset force is experienced by a particle when the time needed for the boundary layer to develop is lagging behind oscillations in the relative velocity. In order to compute this force, the particle history needs to be integrated to determine the state of the boundary layer. This makes the computation of the Basset history force rather complicated and time-consuming. The Basset force is therefore not be taken into account here.

In equation 7.5, $\overrightarrow{F_D}$ is accounted for as a momentum transfer between air bubbles and the continuous phase, i.e. the water-sediment mixture:

$$\overrightarrow{F_D} = \frac{18\mu_m C_D \mathrm{Re_a}}{24\, {d_a}^2} (\overrightarrow{u_a} - \overrightarrow{u_m}) \tag{7.26}$$

$$C_D = K_1 + \frac{K_2}{\mathrm{Re_a}} + \frac{K_3}{{\mathrm{Re_a}}^2} \tag{7.27}$$

$$\mathrm{Re_a} = \frac{\rho_m d_a U_a}{\mu_m} \tag{7.28}$$

where C_D is the air bubble drag coefficient, $\mathrm{Re_a}$ is the air bubble Reynolds number, d_a is the air bubble diameter and $\overrightarrow{u_a}$ is the air bubble velocity vector. The coefficients K_1, K_2 and K_3 are $\mathrm{Re_a}$-dependent and have been determined by Morsi and Alexander (1972). These coefficients, however, were determined for spherical particles while air bubbles become non-sperical for d_a >1 mm. Although the air bubbles are expected to stay relatively small due to the large Reynolds number of the plunging jet in the overflow and in the plume, a significant fraction might be larger than 1 mm. It will be assumed though, that the spherical formulation will be accurate enough. This assumption is further supported by the work of Tomiyama *et al.* (1998). They found that the drag coefficient of bubbles rising in a contaminated fluid (e.g. fine sediment) is higher compared to bubbles in a clean fluid. This indicates that

bubbles in a contaminated fluid behave more like a rigid sphere (less deformation) than bubbles in a clean fluid. The assumption of spherical bubbles is therefore plausible.

Through action-reaction (Newton's third law), F_D causes a rising bubble to exert an upward force per unit of volume on the continuous phase. This approach is preferred over the use of a uniform bubble rise velocity for each size class since it allows non- equilibrium behaviour, which is relevant in the dynamic environment near the exit of an overflow shaft.

Discrete random walk model

For a discrete phase, sub-grid scale turbulent dispersion of air bubbles cannot be dealt with using a diffusivity based on shear, as for the continuous phase. In LES, an important part of the turbulent motions are resolved in the model. However, in models with relatively coarse grid a significant part of the turbulent kinetic energy is included in the sub-grid scale turbulence model. To account for the dispersion of air bubbles due to the sub-grid scale turbulence, a discrete random walk model is used.
The random walk model is based on a Gaussian distribution of the random velocity fluctuations u' and on a time scale τ_e. For each interaction of an air bubble with a sub-grid eddy, a velocity fluctuation is determined

$$u' = \gamma \, u'_{rms} \tag{7.29}$$

where γ is a random number with a normal distribution. Since the sub-grid model is isotropic, the other components of the velocity fluctuations are set equal to each other, u'=v'=w'=$\gamma\sqrt{2k_{SGS}/3}$.

Next, the characteristic life-time of an eddy τ_e is computed from the sub-grid turbulent kinetic energy k_{sgs}. The particle eddy crossing time is determined from

$$\tau_{cr} = -\tau_p \ln\left[1 - \left(\frac{l}{\tau_p \left(U_m - U_a\right)}\right)\right] \tag{7.30}$$

where τ_p is the particle relaxation time and l is a turbulence length scale.

It is assumed a particle interacts with an eddy over time t=$\min(\tau_{cr}, \tau_e)$. Over this time, the random velocity fluctuation u' is applied on the particle, after which a next value for γ is randomly selected.

The sub-grid air bubble diffusivity is given by $\nu_t/\mathrm{Sc_a}$, where $\mathrm{Sc_a}$ is a Schmidt number for air bubbles. It is defined as :

$$\mathrm{Sc_a} = \int_0^\infty \frac{u_p'(t)u_p'(t-\tau)}{\overline{u_p'^2}}\mathrm{d}\tau \tag{7.31}$$

where τ is a dummy variable.
Coalescence after bubble collision is included in the model, bubble breakup is not. Coalescence of air bubbles and the related dynamic bubble size distribution are important to obtain the correct behaviour of surface plumes generated by air bubbles. It is indeed nearly impossible to determine a suitable bubble size distribution a priori for each location in complex flows such as an overflow plume.

In large-scale simulations, tracking the path of each individual air bubble is prohibitive. Instead, a number of bubbles with the same properties are collected into a parcel. Subsequently, the position and properties of each parcel are tracked. In a typical dredge plume simulation, at any time between 10^4 and 10^5 parcels are tracked until escaped through the water surface.

To account for coalescence, the model by O'Rourke (1981) has been used. It determines for each air bubble parcel in a computational cell a statistical probability of collision with another bubble parcel. For each time step, an expected number of collisions is determined for each cell. Once it has been determined two parcels will collide, the outcome of the collision is determined. The outcome can be bouncing or coalescence. Whether either of both will occur is determined by a function of the collisional Weber number $We_c{=}\rho_w U_r^2 \overline{d_a}/\sigma$, where U_r is the relative velocity of the collision pair, $\overline{d_a}$ is the mean (bubble pair) diameter and σ is the surface tension. When the outcome of this function is smaller than a certain threshold, coalescence will be the outcome of the collision. In the other case bouncing is the outcome. After coalescence or bouncing, a new velocity vector is determined for the resulting coalesced bubble or the bounced bubble pair. More details can be found in the manual of Ansys Fluent 14.5 or in O'Rourke (1981).

7.3 Boundary conditions

The flow field is forced by means of a prescribed velocity at the upstream end of the laboratory flume and at the inlet of the overflow release pipe. The inner wall of the laboratory plume release pipe was defined with a Nikuradse

roughness height of 10 μm. Lateral walls in the model are defined with a free slip condition, and are located at sufficient distance from the simulated jet or plume. This is the best option since the width of a flume or wind tunnel used in cases described in literature is often unknown. The wall in which the plume exit pipe is mounted is modelled with a no-slip condition. The wall shear stress τ_w is determined from the laminar stress-strain relationship $\overline{u_1}/u_* = u_* y/\nu$, with $u_* = (\tau_w/\rho_m)^{1/2}$ and $\overline{u_1}$ the velocity in the first grid cell near the wall. The LES model was not equipped with detached eddy simulation (DES) regions near the wall. It is therefore advisable to enhance the development of the boundary layer by providing a velocity profile at the pipe inlet. Separate RANS simulations were performed from which profiles of velocity, turbulent kinetic energy k and dissipation rate ε were extracted. The velocity profile is used to prescribe the mean velocity component normal to the boundary.

The RANS pipe flow solution provides turbulence parameters k and ε, which are applied to superimpose an unsteady component to the mean flow at the inlet boundary of the LES simulation. An LES simulation is capable of resolving vortices, but needs some agitation of the flow field for the development of turbulent structures. At the pipe inlet, the mean velocity profile is modulated with a 2D representation of vortices passing by the boundary plane. This method is called the vortex method (Mathey *et al.*, 2006). Based on a mixing length hypothesis, a local vortex size s is calculated from k and ε:

$$s = c_\sigma \frac{k^{3/2}}{2\varepsilon} \tag{7.32}$$

with $c_\sigma = 0.16$.

The vortex size distribution is subsequently capped to a minimum value equal to the local grid cell size to avoid attempts to generate vortices in the subgrid-scale range.

7.4 Benchmark validation cases

7.4.1 The jet in crossflow

Two cases reported in literature are simulated using the LES model. One case with a high and one case with a low jet-to-crossflow velocity ratio λ.

In low-λ cases, the flow has other distinct features, such as the effect of the cross flow on the flow inside the exit pipe (Andreopoulos, 1985; Walters and Leylek, 2000). In high-λ the correct rate of turbulent mixing of the crossflow into the plume will be of greater importance.

In the following sections, simulation results of both the high-λ and a low-λ case will be discussed.

7.4.1.1 High velocity ratio

The nitrogen jet in air crossflow measured by Su and Mungal (2004) has a velocity ratio of λ=5.7. Even though the experiments were executed in a wind tunnel with higher velocities and a narrower jet exit pipe compared to our experiments, the pipe Reynolds number Re_p=5000 is similar to our experimental cases (2210< Re_p <9960). Using Particle Image Velocimetry (PIV), Su and Mungal (2004) obtained mean and turbulent scalar fields which can be compared with our results of C, c'_{rms} and $\overline{c'u'_i}$. In the data of Su and Mungal (2004), c is a concentration of acetone vapour, with which the nitrogen jet was seeded. In our results c stands for the (sediment) particle concentration. The initial sediment concentration was defined so that the jet-to-ambient density ratio is the equal in model and experiment.

A LES simulation with the formulation as described above is performed, using exactly the same geometry and pipe Reynolds number. In the pipe, the average cell size was 0.6 mm, whereas the smallest cells in the pipe wall boundary layer had a wall-normal size of 0.25 mm, or 0.022 times the pipe diameter. The first cell in the boundary layer of the flat conduct wall had a wall-normal size of 1 mm, or 9% of the pipe diameter of 11 mm. The tetrahedral cells in the plume region had cell sizes ($V^{1/3}$) of 0.5 mm nearest to the jet exit, gradually increasing to 4 mm at x/D=10.

Streamlines

The time-averaged streamlines in the symmetry plane are plotted and compared to the streamlines reported by Su and Mungal (2004) in figure 7.1. The pattern of the streamlines is very similar. The crossflow streamline approach the jet in a parallel way until the pressure gradient of the jet as an obstacle in the flow is felt. Above z/D=-6, the streamlines go slightly upward before being entrained in the turbulent jet, whereas below that elevation they move

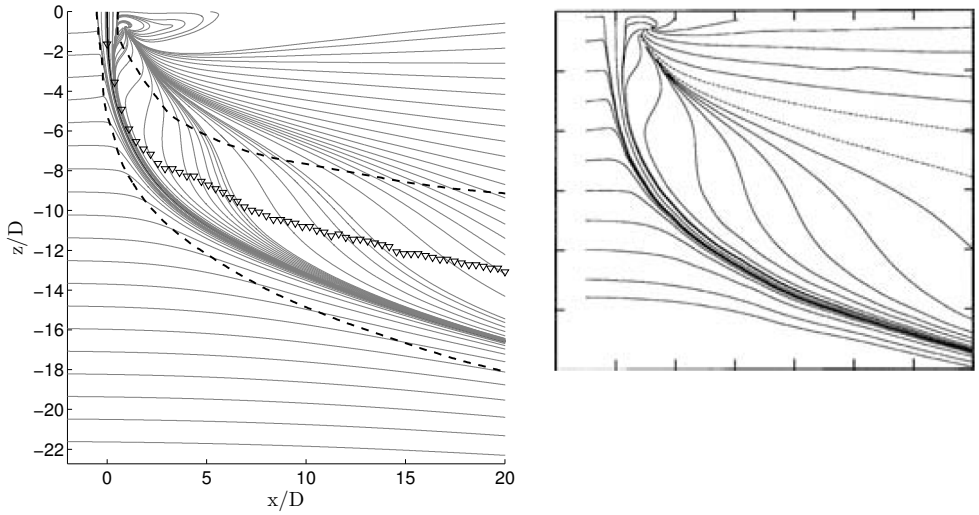

(a) (b)

Figure 7.1: Simulated (a) and measured (b) streamlines of the experimental case by Su and Mungal (2004). In (a), the top and bottom extent of the jet are indicated in dashed lines, the concentration-based centerline is shown in triangles. In (a), the lower extent of the figure does not correspond to the wind tunnel wall.

downward before entering the jet. This effect is also seen in the model results.

In the symmetry plane, the crossflow streamlines do not move at any location downstream of central streamline, which is the streamline originating from the centre of the pipe. This can both be seen in the model and in the experiments by Su and Mungal (2004). At about z/D=-1 and x/D=1, a stagnation point is found in the streamlines. From that point onwards, all streamlines downstream of the central streamline originate from this node. The stagnation point can be related to the crossflow-wake of the jet shortly after exiting from the pipe. Part of the streamlines originating from the stagnation point stay in the wake of the plume (above the plume). The other part flows towards the downstream end of the central streamline, some of which through a trajectory starting in the direction opposite to the crossflow.

All the above described features of the streamline pattern can be found in both the simulated and the measured streamlines.

Mean concentration

First, horizontal and vertical profiles of C are compared with the measurements by Su and Mungal (2004). In Su and Mungal (2004), a passive tracer was used while here very small particles were considered. Therefore the diffusion model should converge to the behaviour of the passive scalar. Horizontal profiles are shown in figure 7.2, at $z/\lambda D$=0.1, 0.5 and 1.0. The normalisation using λD is chosen in analogy with the presentation of the results by Su and Mungal (2004). The concentration peaks are simulated very accurately at all z-levels. The shape of the profile is almost identical to the measurements for $z/\lambda D$=0.1 and 0.5, while at $z/\lambda D$=1.0 a small shift $\Delta x/D$=0.2 is observed. The maximum sediment concentration is very close to the initial concentration C_0 up to $z/\lambda D$=0.5. At greater distance from the wall, at $z/\lambda D$=1, C/C_0 peaks at about 0.4.

Secondly, the vertical profiles of C/C_0 are compared with the measurements at x/D=2.85, 5.7, 8.55 and 14.25. The results are shown in figure 7.3. The maximum relative concentration decreases from 0.25 to 0.06 between x/D=2.85 and x/D=14.25. The model predicts the position of the peaks in a satisfactory way. At x/D=2.85 and x/D=14.25, the peak concentration is fairly close tot the experiments. At the x locations in between, the concentration is underpredicted, possibly because the jet is wider in the simulations. This cannot be confirmed since no information on width or lateral profiles is available from the experiments. The vertical extent of the plume is fairly close to the experimental one, but slightly underpredicted at $x/D \leq$8.55. At x/D=14.25, the vertical extent in the simulations corresponds with the experiments.

Concentration fluctuations

Again, the horizontal profiles are compared first. Horizontal profiles of c'_{rms}/C_0 are shown in figure 7.4, at $z/\lambda D$=0.1, 0.5 and 1.0. The development of concentration fluctuations as a function of the distance from the wall corresponds well with the observations by Su and Mungal (2004). Shortly after leaving the pipe ($z/\lambda D$=0.1), two small peaks develop in the shear layers at the outer fringes of the jet. The fluctuations have the highest intensity at distance of $z/\lambda D$=0.5 from the pipe. Here, the simulated fluctuations are about 40% higher compared to the experiments, but the double-peak structure is observed both in experiment and in simulations.

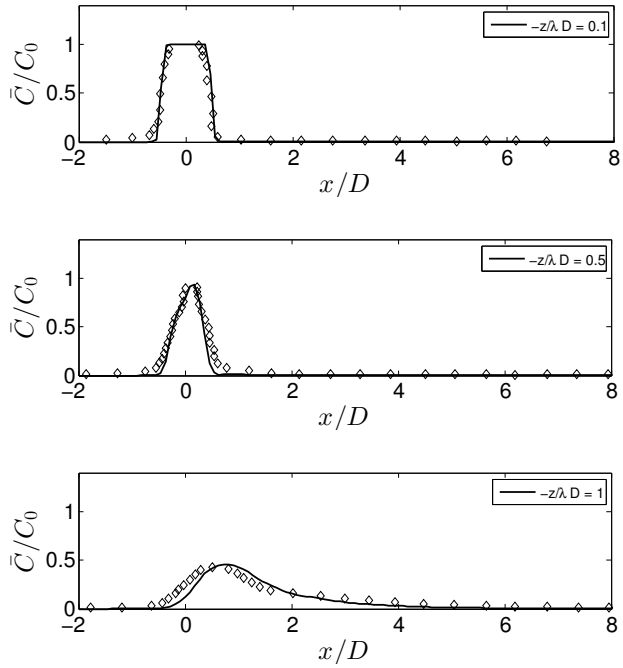

Figure 7.2: Simulations (full line) and measurements (circles) of the experimental case by Su and Mungal (2004). Wall-parallel profiles of dilution C/C_0 at the symmetry plane $y = 0$, at $z/\lambda D$=0.1, 0.5 and 1.0.

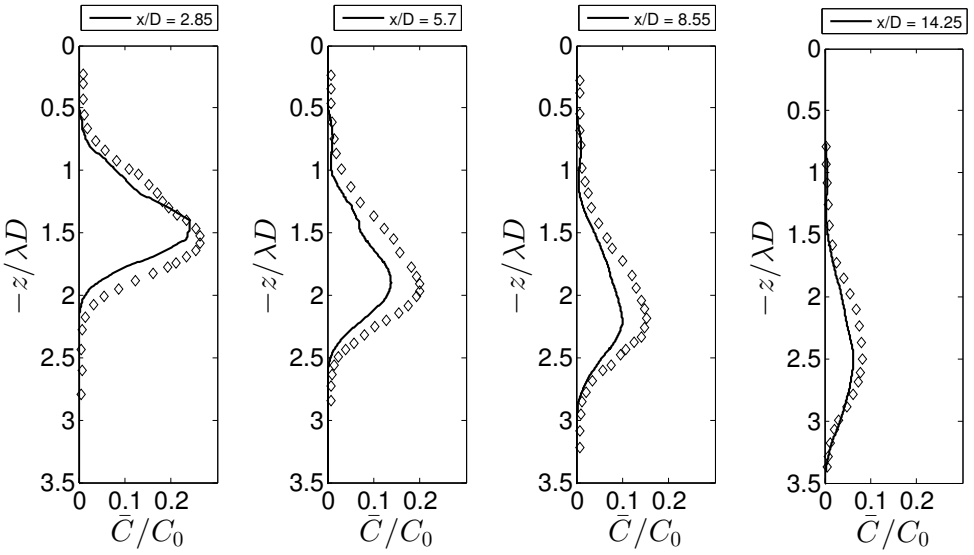

Figure 7.3: Simulations (full line) and measurements (circles) of the experimental case by Su and Mungal (2004). Wall-normal profiles of dilution C/C_0 at the symmetry plane $y = 0$, at x/D=2.85, 5.7, 8.55 and 14.25.

Using a 10 million cell DNS model, Muppidi and Mahesh (2007) and Muppidi and Mahesh (2008) simulated exactly the same transverse jet setup as measured by Su and Mungal (2004). They also obtained higher c'_{rms} values compared to Su and Mungal (2004). At horizontal profiles on the symmetry plane, at $0.1 \leq z/\lambda D \leq 1$ below the jet exit wall, Su and Mungal (2004) found values of c'_{rms}/C_0 around 0.16, while Muppidi and Mahesh (2008) found peak values between 0.24 and 0.30 in their DNS simulations. These values are very similar to the present LES model.

A portion of the tracer/sediment is stripped of the main jet towards the downstream end, visible as a slight increase of c'_{rms} around x/D=1. This effect is present both in the simulations and in the experiment, and is associated with the start of a secondary plume. At $z/\lambda D$=1.0, the double peak has disappeared and a streamwise profile is found with the higher c'_{rms} value at the upstream end of the plume ($x/D \approx 0$). Further downstream, a long tail is found in the wake of the plume, extending to x/D=6 in experiment and simulation.

Subsequently, the vertical profiles of c'_{rms}/C_0 are compared with the measure-

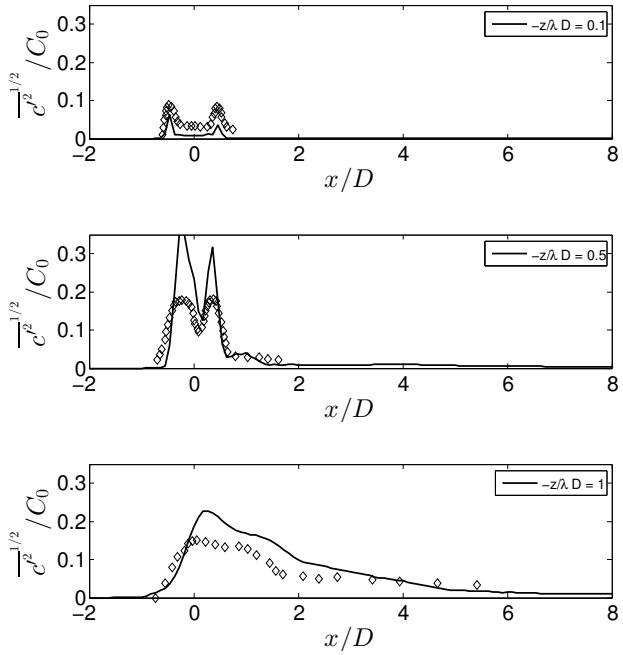

Figure 7.4: Simulations (full line) and measurements (circles) of the experimental case by Su and Mungal (2004). Wall-parallel profiles of concentration fluctuations c'_{rms}/C_0 at the symmetry plane $y = 0$, at $z/\lambda D$=0.1, 0.5 and 1.0.

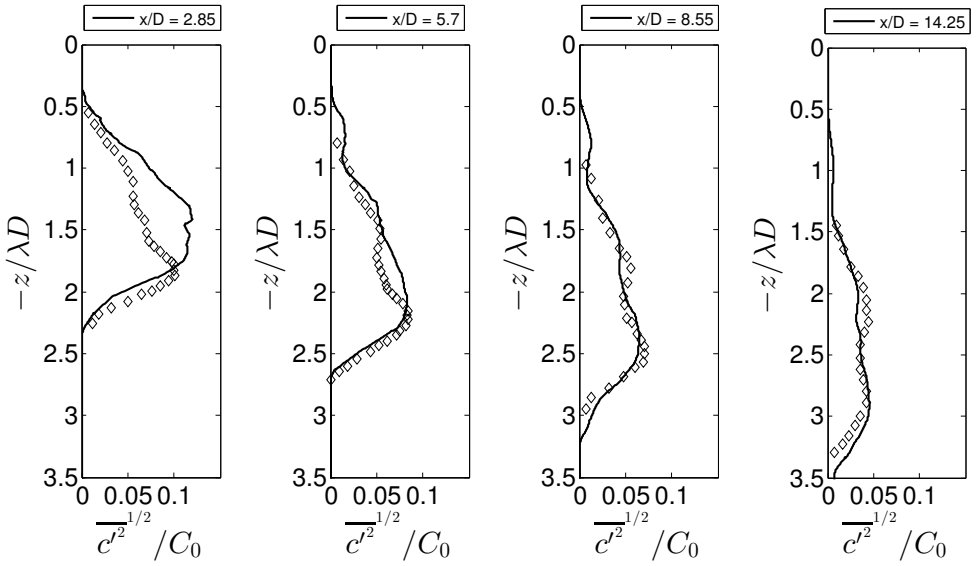

Figure 7.5: Simulations (full line) and measurements (circles) of the experimental case by Su and Mungal (2004). Wall-normal profiles of dilution c'_{rms}/C_0 at the symmetry plane $y = 0$, at x/D=2.85, 5.7, 8.55 and 14.25.

ments at x/D=2.85, 5.7, 8.55 and 14.25. The results are shown in figure 7.5. Overall, the vertical profiles of the turbulent fluctuations of concentration correspond well with the experimental observations. Apart from the nearest profile at x/D=2.85, c'_{rms}/C_0 is higher in lower (upstream) end of the plume. This is caused by the stronger shear at the upstream end, where the crossflow meets the plume. Above the plume (downstream side, $z/\lambda D \sim$1) weak fluctuations are present. These can be associated with small packets of sediment torn off from the main plume. These clouds have a much lower average concentration (figure 7.3) and this phenomenon is similar to what is called a surface plume in the context of dredging plumes. Even in this case with relatively weak crossflow, a secondary surface plume forms.

Turbulent mass fluxes

The horizontal profiles of the turbulent mass flux $\overline{c'u'}/C_0U_0$ are shown in figure 7.6, at $z/\lambda D$=0.1, 0.5 and 1.0. The general pattern is very similar. At short distance below the pipe ($z/\lambda D$=0.1), no correlations between c' and u' are found, while slightly further ($z/\lambda D$=0.5), the turbulent flux is at its maximum of the three shown positions. Here a negative correlation is

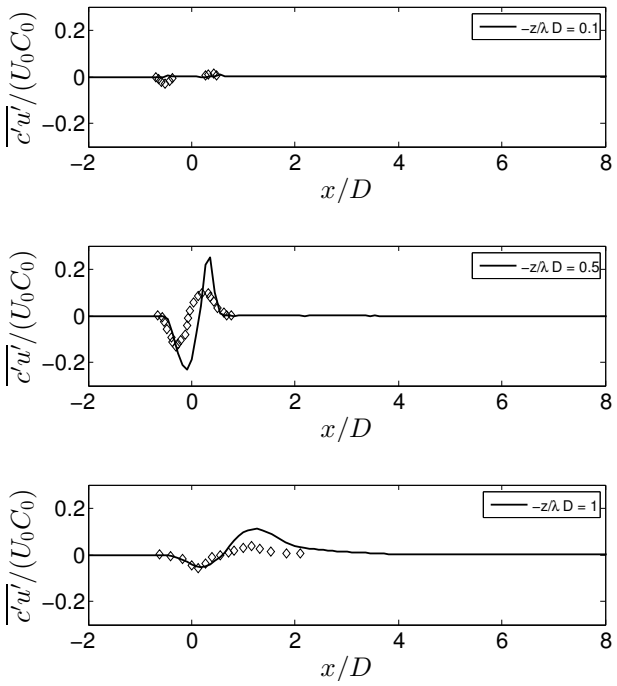

Figure 7.6: Simulations (full line) and measurements (circles) of the experimental case by Su and Mungal (2004). Wall-parallel profiles of the turbulent mass flux $\overline{c'u'}/C_0U_0$ at the symmetry plane $y = 0$, at $z/\lambda D$=0.1, 0.5 and 1.0.

found between c' and u' at the upstream end, indicating a turbulent flux of sediment in the $-x$ direction. This is logical since the spreading of the jet at the upstream end is in opposite direction of the main crossflow. At the downstream end of the plume (which is still quite vertical here), a turbulent flux in positive x direction is found, both in the simulations and in the observations by Su and Mungal (2004). The location of the zero-crossing of $\overline{c'u'}$ is slightly different. At $z/\lambda D$=1.0, the upstream (negative) peak corresponds well with the experiments as well as the zero-crossing. The downstream peak is smaller in the experimental observations.

7.4.1.2 Low velocity ratio

Andreopoulos (1985) also performed measurements in a jet in crossflow, but at lower jet-to-crossflow velocity ratios of λ=0.5, 1 and 2. Since the previous case had a relatively high λ of 5.7, a simulation was executed of the low-λ case of λ=0.5. The experiments by Andreopoulos (1985) were also performed in a wind tunnel, like the experiments by Su and Mungal (2004) in the previous

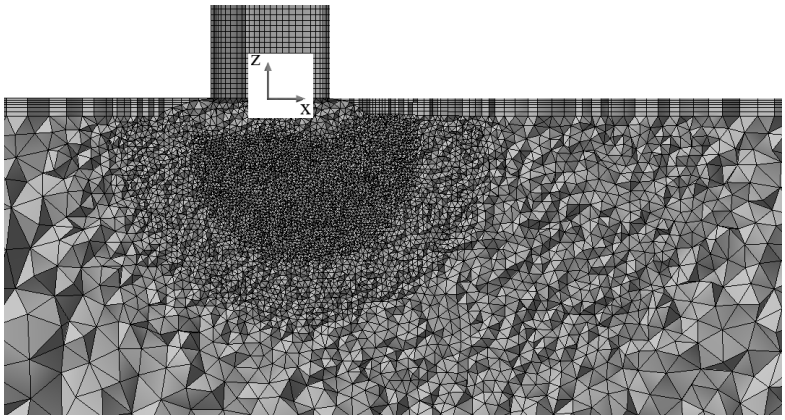

Figure 7.7: Detail of a slice through the unstructured grid used for the simulation of the experimental case by Andreopoulos (1985).

section. The pipe Reynolds number was $\mathrm{Re_p}$=20,500, which means the jet wake Reynolds number $\mathrm{Re_w}=U_0D/\nu$ is 10,250 for λ=0.5. Consequently, both the pipe flow and the jet wake are fully turbulent. The inner pipe diameter was 50 mm, the crossflow velocity was 13.9 m/s and the jet velocity was 6.95 m/s.

In the LES simulation, the dimensions of the domain were identical to the wind tunnel setup of Andreopoulos (1985). The pipe was discretised using a mesh with wall-normal size of the first cell near the wall of 0.4 mm, or 0.8% of the pipe diameter (see figure 7.7 for a slice of the unstructured mesh at y=0). For cells further away from the flat wall (which is the boundary at z=0), a growth rate was adopted of 1.3 leading to a second cell of 0.52 mm, a third cell of 0.68 mm and so on for the first 6 cells. The rest of the interior of the pipe was discretised with cells of about 2 mm or $0.05D$ in the wall-normal direction. The boundary layer of the flat wall had a first cell thickness of 0.5 mm and a growth rate of 1.2 was adopted for the first 6 cells. The plume region had cell sizes of 0.9 mm near the exit, gradually increasing to 8 mm at x/D=5.

The simulated mean streamwise velocity component has been compared with the experiment at vertical (flat wall-normal) profiles at y=0 and at x/D=2, 4, 6 and 10 (figure 7.8). At the outer flow below the jet, the streamwise velocity goes to the initial crossflow velocity U/U_0=1. The height at which U starts to differ from U_0 is in agreement with the experiments. At x/D=2, the streamwise velocity profile is almost identical. Further downstream, it seems the lateral mixing of the crossflow towards the symmetry plane was stronger

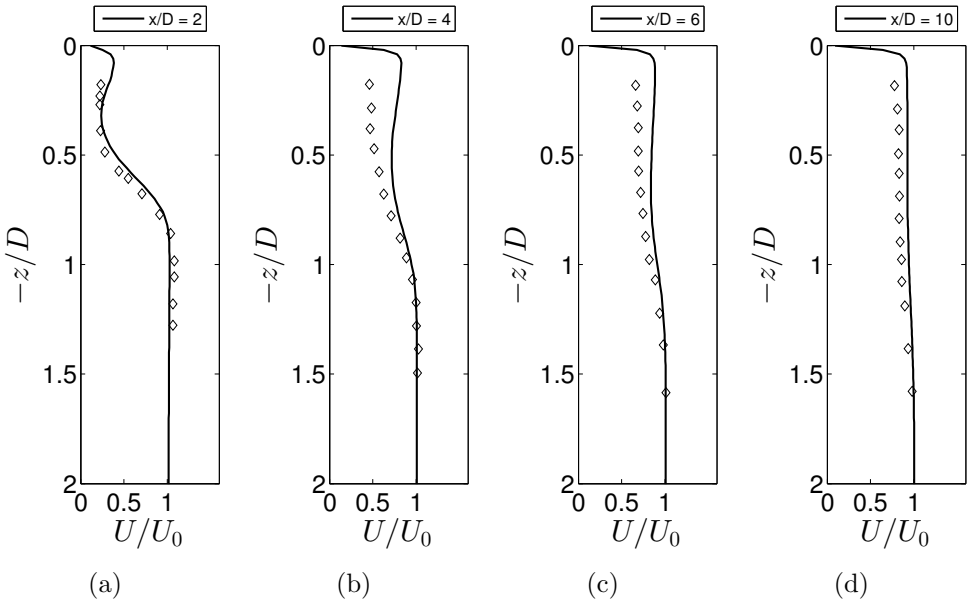

Figure 7.8: Simulations (full line) and measurements (circles) of the experimental case by Andreopoulos (1985). Wall-normal profiles of mean streamwise velocity U/U_0 at the symmetry plane $y = 0$ and at x/D=2, 4, 6 and 10.

in the model compared to the measurements. As a result, the streamwise velocity at the symmetry plane was slightly higher in the simulations.

The simulated mean vertical velocity component has been compared with the experiment at vertical (wall-normal) profiles at y=0 and at x/D=0.5, 1, 2 and 4 (figure 7.9). For all profiles, the vertical velocity is in good agreement with the experiments. Generally speaking, a vertical velocity component towards the wall ($-W > 0$) occurs at the symmetry plane. This corresponds to the counter-rotating vortex pair (CRVP), typically occuring in a jet in crossflow. The CRVP be will discussed in detail further in this manuscript, but is also visualised in the vector field in figure 7.11. The strongest vertical component of W/U_0=0.6 is found at smallest distance from the exit pipe, at x/D=0.5. After four pipe diameters, the vertical component has disappeared from the flow field.

Finally, the resolved turbulent kinetic energy (TKE) k_{res} has been compared with the experiment at vertical (wall-normal) profiles at y=0 and at x/D=2, 4, 6 and 10. (figure 7.9). At x/D=2, the onset of turbulence is simulated well near $-z/D$=1, but k_{res} is higher near the flat wall. Further away from

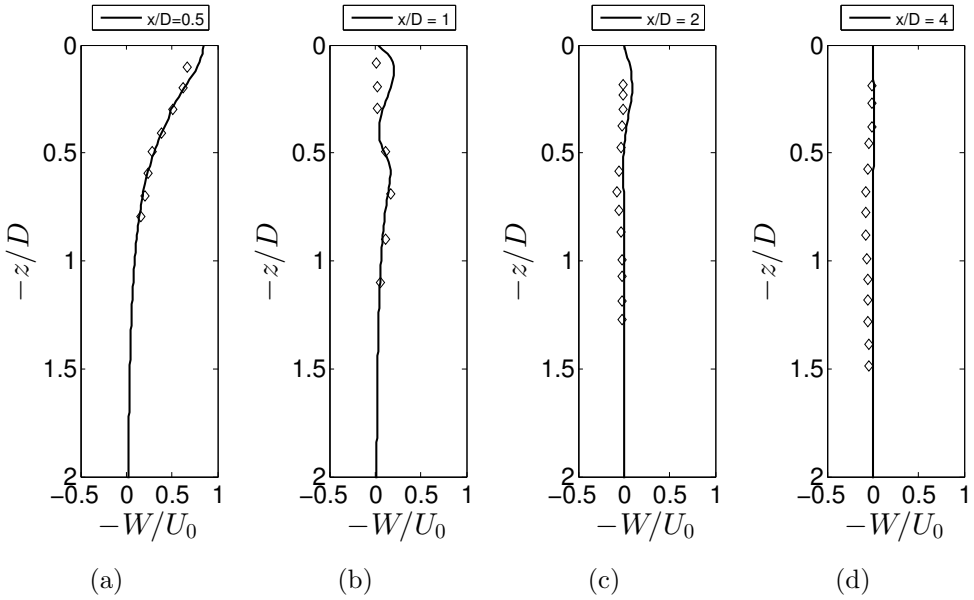

Figure 7.9: Simulations (full line) and measurements (circles) of the experimental case by Andreopoulos (1985). Wall-normal profiles of mean vertical velocity W/U_0 at the symmetry plane $y = 0$ and at x/D=0.5, 1, 2 and 4.

the exit pipe, the resolved kinetic energy is lower than the observed one, possibly due to decreasing grid resolution with increasing distance from the pipe.

When the resolved TKE is compared with the subgrid-scale TKE k_{sgs}, it can be seen that for the high resolution part at x/D=2, k_{sgs} is two orders of magnitude smaller than the resolved TKE, k_{res} (figure 7.11). Here k_{sgs} is computed with the method according to Coussement *et al.* (2012). The subgrid-scale part is therefore much smaller than the resolved part. However, at x/D=10, k_{sgs} is less than one order of magnitude smaller than the resolved TKE, k_{res}. This means that a much larger part of the effect of the turbulent fluctuations is not present in the resolved turbulent field. Hence the smaller values of k_{res} compared to the experiments at $x/D \geq$6. The analysis of the fraction of the TKE resolved on the mesh, and whether a given fraction is sufficiently high to be called a LES, is given in (Pope, 2004). This is further discussed in section 7.5.2.2.3.

7.4.2 Wall-impinging sediment-laden jet

In the near-field of overflow plumes, a plume impinging on the sea bed can occur when the water depth is limited or when the cross flow is weak. After

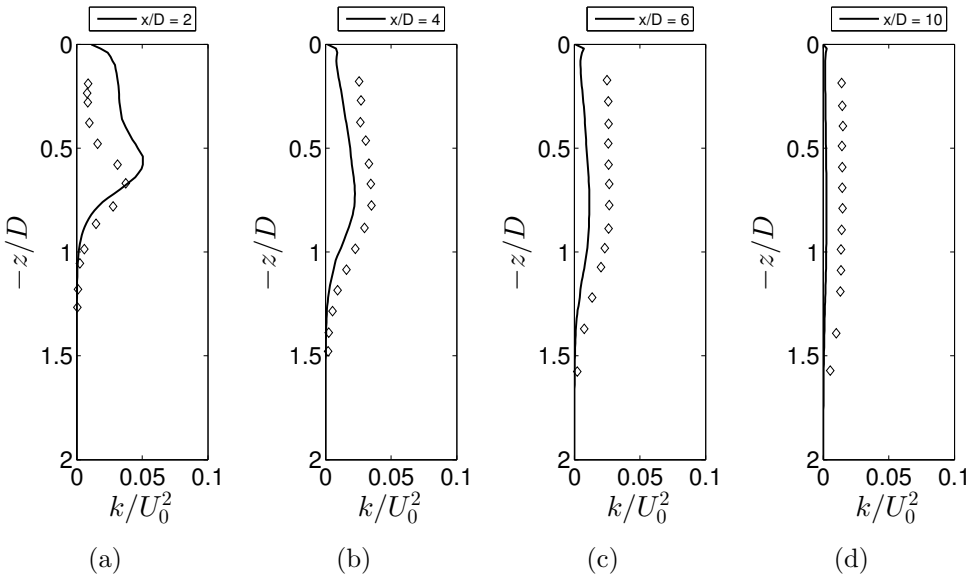

Figure 7.10: Simulations (full line) and measurements (circles) of the experimental case by Andreopoulos (1985). Wall-normal profiles of the resolved turbulent kinetic energy k_{res}/U_0^2 at the symmetry plane $y = 0$ and at x/D=2, 4, 6 and 10.

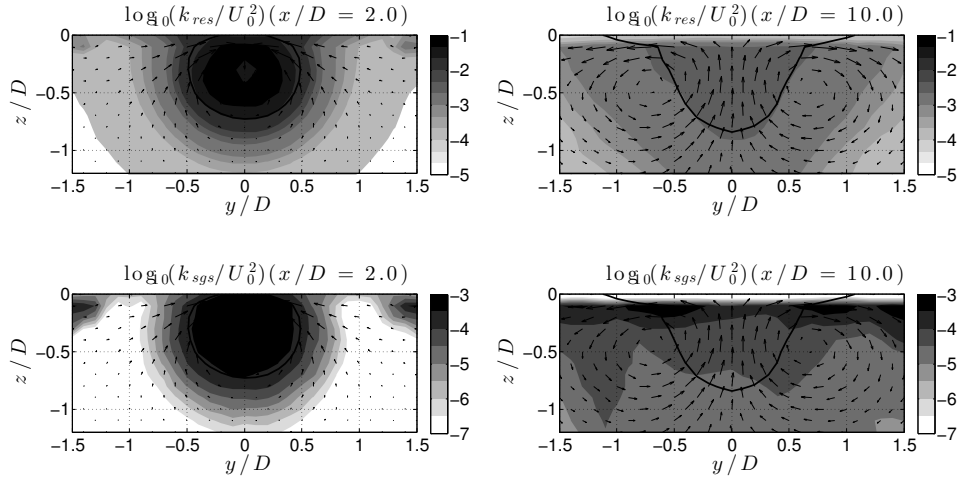

Figure 7.11: Resolved and subgrid-scale TKE at two different distances from the pipe, x/D=2 and x/D=10. The vectors show the (V,W) velocity field, which is the 3D velocity field projected on the constant-x planes. The full black line connects the points at which C/C_{max}=0.4.

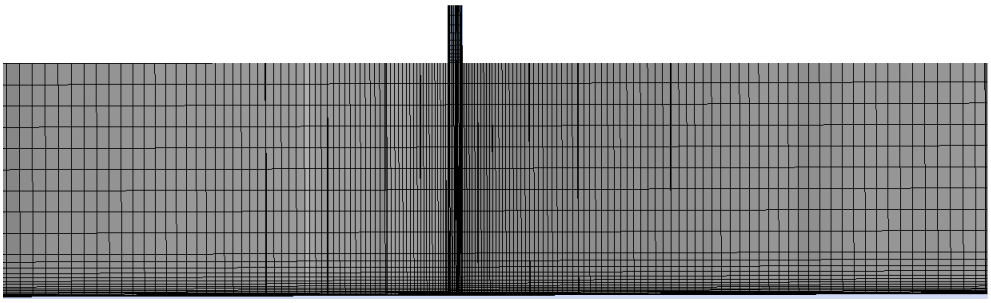

Figure 7.12: Vertical slice through the mesh used to solve the experimental wall-impinging sediment jet by Chowdhury and Testik (2014).

the plume touchdown the sediment will spread out in the shape of a pancake. In the validation case described in this section, a similar situation has been simulated.

In a recent article, Chowdhury and Testik (2014) describe experiments with a particle-laden axisymmetric jet impinging on a flat surface. The result is a density current of which the time-evolution of the outer contours have the shape of concentric circles. Two series of experiments were executed with different water depths. Water-sediment mixtures were discharged in a large tank (3.6 x 3.6 m) through a D=2.54 cm pipe. For validation of the present LES model, case two was selected. In this case, the distance between the discharge pipe and the bottom was 0.4 m, the sediment concentration was 69 g/l and the densymetric Froude number was equal to F_Δ=12.6. The exit velocity of the fluid mud was W_0=0.91 m/s. This means the jet reaches the bottom wall after less than one second after which the flow is first in a so-called wall jet phase. At greater distance from the touchdown point, the flow behaves as a density current.

A hexahedral mesh was designed with refinements in the pipe, the descending jet region and the density current region near the bottom wall (figure 7.12). In these zones, the mesh size was around 1 mm. The inlet boundary condition at the pipe was defined in this case as a uniform velocity over the cross section of the pipe, given the laboratory setup with a very short pipe. Given the relatively high velocity at the jet exit and the small grid cells a time step as small as 1 ms was needed to keep the CFL number smaller than one at all locations.

A global overview of the time-evolution of the LES solution is given in figure 7.13. In the first few seconds, the radial spreading is in a wall-jet mode, with

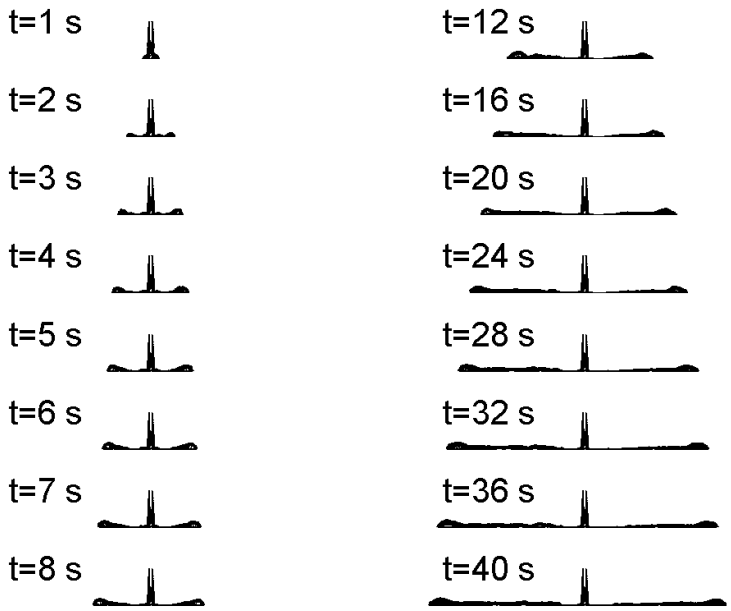

Figure 7.13: LES result of the time evolution of the sediment contours of a wall-impinging fluid mud jet and density current.

supercritical flow. After some distance of radial spreading, the velocity has decreased and it is known that in some cases an internal hydraulic jump can occur (Wilkinson and Wood, 1971). At this point, the flow transforms to a regular density current, driven by the excess mass density of the fluid mud. In the present simulations, this happens between 8 and 12 s after the start of the jet flow. In figure 7.14, a more detailed view of the distribution of the concentration of the fluid mud is shown. It can be observed that at a radial position $x/D \approx 10$, the flow thickness starts to increase rapidly, indicating an internal hydraulic jump.

Chowdhury and Testik (2014) fitted relationships for the time-evolution of the radial spreading. They found that in the wall-jet phase, the radial spreading evolved as $r \sim t^{0.5}$. Subsequently, in the density current phase the spreading evolved with $r \sim t^{0.8}$. The fits by Chowdhury and Testik (2014) are compared with the present LES solution. In figure 7.15, the fit for the wall-jet phase is shown in full line, the fit for the density current phase is shown in the dashed line. The LES model solution for every second is plotted

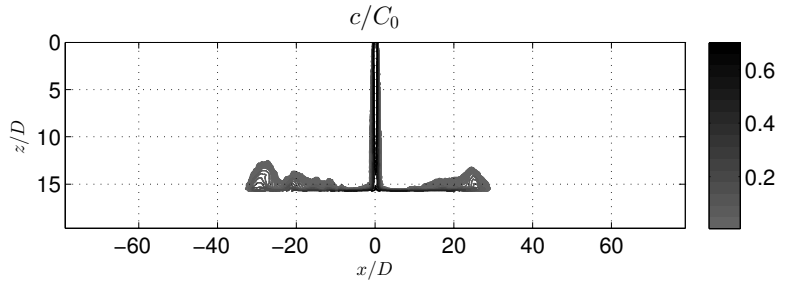

Figure 7.14: Detail of the sediment distribution of the wall-impinging fluid mud jet after 12 seconds, shortly after the transformation of the outer fringes from wall-jet to density current.

with markers. It can be seen that the wall-jet phase is modelled properly, and that the transition to a density current phase occurs at the correct time (after 20 s). The transition to density current phase in terms of spreading rate occurs thus about 10 s later than the start of the formation of an internal hydraulic jump.

7.4.3 Air bubble plumes

Air bubbles will be an important aspect to take into account for the full-scale simulations. However, air bubbles are very difficult to measure in the field since they occur mainly underneath the dredging vessel and cannot be sampled or measured with acoustic or optical instruments. They cannot be distinguished from sediment particles with the common instrumentation. Air bubbles can therefore also complicate sediment concentration measurements, see section 8.6.1. The only option to validate the capability of the model in its current form is to draw results from experimental bubble plume cases in literature. Such cases are, however, rare: only one set of experiments of a water-bubble plume in crossflow have been found in which the trajectories of both the liquid plume and the gas plume are observed (Zhang, 2012; Zhang and Zhu, 2013).

In Zhang and Zhu (2013), an experiment is described in a flume filled with tap water at 20°C. The flume had a water depth of 65 cm and a circular nozzle with diameter D=2.2 cm was situated at 12 cm above the bottom wall. From the nozzle a water-air mixture is released in different air-water ratios. All combinations of water discharge of 0, 1, 3 and 5 l/min and air flow rates of 1, 3 and 5 l/min were studied. In dredging plumes, the air fraction is of

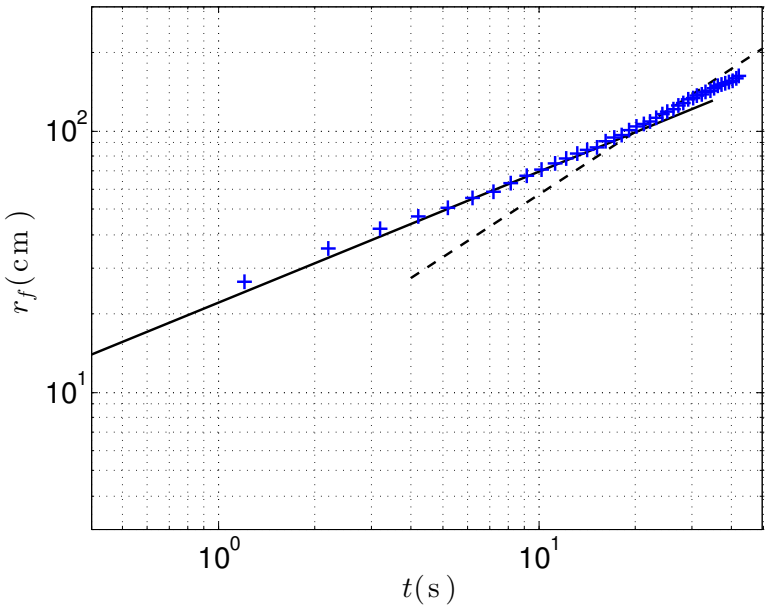

Figure 7.15: Radial spreading of the outer fringes (r_f) as a function of time. Markers represent model results, lines represent the fits by Chowdhury and Testik (2014).

the order of magnitude of 10%. The case with air flow rate of 1 l/min and water flow rate of 5 l/min comes therefore closest to the dredging plume case.

In the experiments, the plume is ejected upwards, so the air separates from the plume at the upstream end and in the same direction as the plume trajectory (upwards). In dredging plumes, the plume is ejected downwards, so the air separates in the opposite direction of the plume direction. Also in dredging plumes the air separates from the plume in the wake of the plume, on the downstream end. Nevertheless, this experimental case forms a good test for the multi-phase model consisting of a water phase and a sediment phase in a mixture model, and an additional air bubble phase solved using a Lagrangian discrete phase model (section 7.2.2).

An unstructured grid was designed taking into account similar refinement strategies as used in the previous test cases. The refinement near the flat wall (in which the exit pipe is mounted) was not needed here since the plume is released 12 cm above the bottom. A uniform flow velocity of 0.2 m/s was defined at the upstream boundary, while a constant pressure condition was applied at the downstream boundary. A uniform and constant flow velocity, sediment and air concentration was defined at the inlet of the release pipe.

The length of the pipe, as well as the conditions in the pipe are unknown. A relatively short pipe of 30 cm was used to avoid excessive air bubble coalescence before the release.

Also, no information about the air bubble diameter at the pipe exit is available. The only information about bubble diameter is available at a distance of $80D$, where the average bubble diameter was d_a=1.77 mm. Since coalescence is more likely than bubble breakup for small bubbles, the initial bubble diameter was defined as smaller compared to the measured d_a at distance $80D$. Two tests were done in which the air bubble dispersion was compared with the experiment, one with initial bubble diameter $d_{a,0}$=0.5 mm and one with $d_{a,0}$=1 mm. The results for the air bubble diameter distribution are shown in figure 7.16. It was found that if $d_{a,0}$=0.5 mm (figure 7.16a) too many small bubbles were advected with the plume, in which case the turbulent entrainment of ambient water into the plume prevented the small bubbles to leave the plume. Only a minor fraction of larger (coalesced) bubbles could escape through the entrainment flux and form a secondary bubble plume. When $d_{a,0}$=1 mm (figure 7.16b) the correct behaviour was found, with the majority of the bubbles forming a separate bubble plume with steeper trajectory. The larger bubbles rise faster and are found on the top of the plume, while the smaller bubbles rise less fast and are between the water plume and the plume of the larger bubbles. This was also observed by Zhang and Zhu (2013).

In the end $d_{a,0}$=1 mm was used. At the water surface, a zero-flux boundary condition was used for the water and sediment phases, while air bubbles were allowed to escape.

Zhang and Zhu (2013) determined average trajectories of air bubble and water (with tracer), based on video imaging. The best way to compare the model results with the trajectories by Zhang and Zhu (2013) is therefore to integrate bubble and tracer concentrations over the lateral dimension (into the image) and search for the maxima. The same method will be used to compare simulated plume trajectories with our video imaging (equations 7.33-7.34). In figure 7.17, the simulated plumes are compared with the plumes observed by Zhang and Zhu (2013). The simulated tracer plume follows very closely the experimental plume trajectory. The bubble plume separates from the main plume at the correct location and the rising angle is also very similar. A small fraction of bubbles escapes more slowly from the main plume. These are the smaller fractions that can also be found between the main plume and the bubble plume (also observed by Zhang and Zhu (2013)).

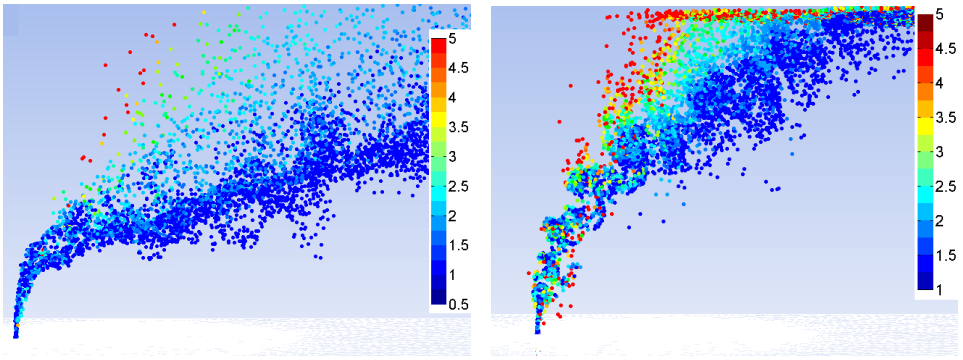

(a) (b)

Figure 7.16: Bubble size distributions in the simulated air bubble plumes (in mm), with initial air bubble diameter $d_{a,0}$=0.5 mm (a) and $d_{a,0}$=1 mm (b).

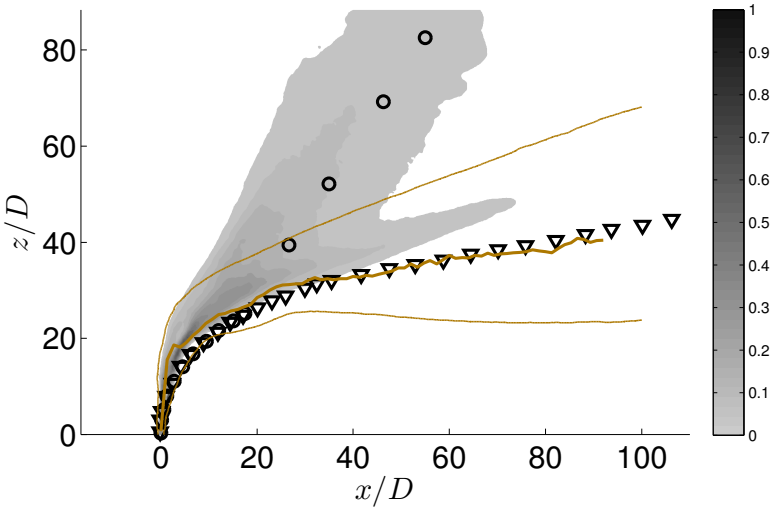

Figure 7.17: LES simulation of separating water and bubble plumes in a crossflow, compared to experimental observations by Zhang and Zhu (2013). Simulated volume fraction of air is shown in the grey scale. The simulated mean trajectory of the water (tracer) plume is shown in wide line, the top and bottom extent of the tracer plume in thin lines. The experimental bubble plume trajectory is shown by black circles, the experimental tracer plume by black triangles.

Table 7.1: Overview of experimental cases of sediment plumes which are also simulated using the presented LES model. Case V is a vertical plume in still environment, cases with letter 'A' did not have a wall step, cases with letter 'B' did. All cases except A1 have been executed experimentally as well.

Case	λ	F_Δ	$\Delta\rho$ [kg/m^3]	D [m]	W_0 [m/s]	U_0 [m/s]	Wall Step
V	∞	9.09	3.11	0.034	0.293	0.0	n/a
A0	2.58	9.09	3.11	0.034	0.293	0.113	No
B0	2.58	9.09	3.11	0.034	0.293	0.113	Yes
A1	1.10	1.20	31.13	0.034	0.122	0.110	No
B1	1.10	1.20	31.13	0.034	0.122	0.110	Yes
B2	0.17	0.24	31.13	0.065	0.034	0.199	Yes
B3	2.72	4.07	15.57	0.034	0.293	0.108	Yes

In general, the behaviour of the Lagrangian discrete bubble model is satisfactory, with the coalescence model leading to a plausible bubble size distribution.

7.5 Experimental validation cases

In this section, a number of experimental cases executed in this research are compared with the LES model results. The cases comprise a vertical plume case, plumes in crossflow cases and cases with a plume in crossflow and a wall step. The latter refers to the schematised hull and stern as used in the laboratory experiments, explained in chapter 3. In the LES model runs described in this section, exactly the same geometry as in the experiments is implemented. In table 7.1, an overview is given of the experimental cases simulated for validation and analysis purposes.

7.5.1 Vertical plume

7.5.1.1 Introduction

The goal of the presented LES model is to simulate accurately the mean flow and major turbulent structures in a negatively buoyant sediment plume, with different crossflow to pipe flow velocity ratios. As mentioned above, the model validation was executed stepwise, starting with a vertical plume and introducing crossflow and the wall step consecutively.

The model settings and grid requirements were tested against measurements in a vertical plume of $\Delta\rho/\rho = 3.1 \cdot 10^{-3}$ and $F_\Delta = 9.09$ (case 'V' in table 7.1). Measurements of mean flow properties and turbulent fluxes were used to compare with LES model results, in order to verify the appropriateness of settings for the numerical schemes, boundary conditions and SGS models. An unstructured grid was used with cell size of $\sqrt[3]{V}/D \approx 0.03$ in the near field (with V the cell volume), and gradually increasing with radial coordinate r and vertical coordinate z. Gaussian half-widths of axial velocity (b_w) and of concentration (b_c) were nearly equal in the measurements ($b_w = 0.119$ and $b_c = 0.116$).

Laboratory measurements of turbulent fluxes of momentum and sediment concentration in a vertical turbidity plume have been executed by Decrop *et al.* (2015a), using a new technique to obtain turbulent sediment fluxes from acoustic measurements. In this chapter, these measurements are compared with turbulent statistics obtained from LES simulations. A Reynolds decomposition has been executed on both measurements and model results. Time-averaged sediment concentration is denoted as C. Radial, tangential and axial time-averaged velocity components are written as U, V and W, respectively. Turbulent fluctuations of radial (u'), tangential (v') and axial (w') velocity components as well as sediment concentration (c') are denoted with a prime.

7.5.1.2 Model validation

The results of the LES simulations are compared with measurements of the mean flow characteristics in figure 7.18. The simulations show a good fit with the gaussian profiles over the radial direction as well as a self-similar behaviour at $z/D \geq 8$ for velocity and sediment concentration.

Since calculations of resolved TKE (k_{res}) and SGS TKE (k_{SGS}) show that more than 95% of the total TKE is resolved in the model, Reynolds stresses resolved on the model grid will be considered as total Reynolds stresses ($\overline{u_i' u_j'}$).

Figure 7.19 shows measurements and simulation results of RMS sediment concentration fluctuations $c'_{rms} = \sqrt{\overline{c'^2}}$ and the $\overline{u'w'}$ Reynolds stress component, indicating lateral turbulent diffusion of axial momentum. Again, the sediment flow was not yet fully developed at $z/D = 4$, where an axial dip in c'_{rms} related to the region of flow development was still observed. At greater distance from the pipe a gaussian-like profile for c'_{rms} was observed in model and measurements, consistent with measurements in literature for

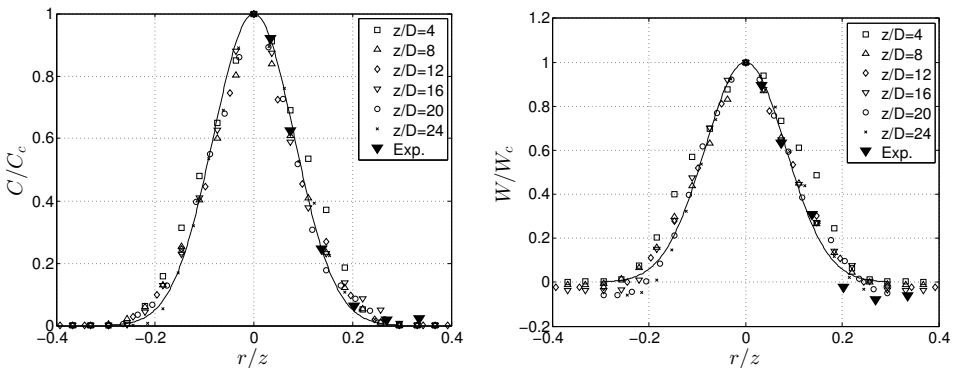

(a) (b)

Figure 7.18: Radial profiles of (a) time-averaged sediment concentration C and (b) time-averaged axial velocity W. Case V model results are shown at different distances from the pipe (open markers). Experimental data in filled triangles, full line represents Gauss profile.

two-fluid plumes (Papanicolaou and List, 1988; Dai *et al.*, 1995). The axial peak values of c'_{rms}/C_c=0.35 found in measurements and model are consistent (figure 7.19a). These results compare well with observations in single-phase plumes, where a value of 0.36 was found at the axis by Papanicolaou and List (1988). Radial Reynolds stresses show a peak value at $r/z = 0.07$, both in model and measurements (figure 7.19b). Dai *et al.* (1995) find a peak of $\overline{u'w'}/W_c^2$=0.026 at $r/z = 0.08$, with W_c the time-averaged axial velocity at the centerline. Peak values found in our measurements (0.022) are in the same range compared to LES model results (0.020-0.026) and results by Dai *et al.* (1995). The stress profile showing two peaks with opposite sign indicates that vertical momentum is transported away from the plume axis at all radial positions.

7.5.2 Plume in crossflow

7.5.2.1 Model setup

7.5.2.1.1 Introduction

In a next step, crossflow was added to the setup and one experimental case (case A0) of a negatively buoyant plume in crossflow was simulated with the LES model settings obtained from the previous step. For the remainder of the text, the cartesian coordinate system as shown in figure 3.1 is used.

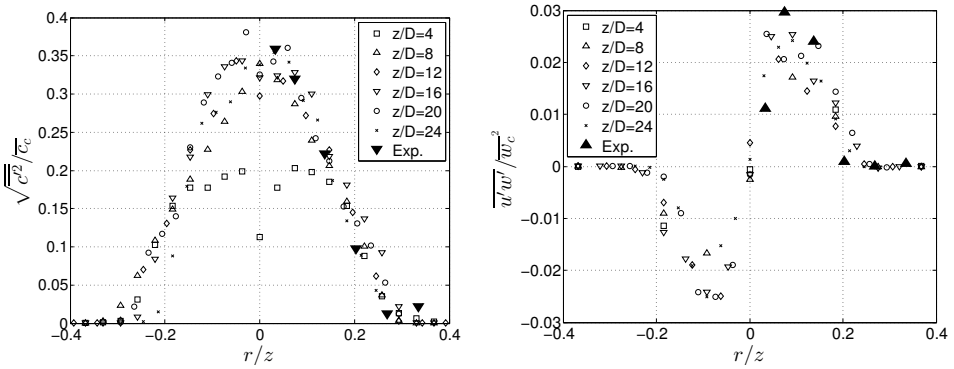

(a) (b)

Figure 7.19: Radial profiles of (a) RMS sediment concentration fluctuations and (b) Reynolds stress component $\overline{u'w'}$. Case V simulation results are shown at different distances from the pipe (open markers) and experimental data at $z/D = 9$ (filled triangles).

The dimensions of the model domain equalled experimental flume dimensions, while a wall step was not yet added at this point. The free surface was modelled as a rigid lid with free slip and zero flux boundary condition. The water depth H was 0.53 m or H/D=15.6, while the cross flow velocity boundary condition was defined as measured in the experiment before plume release, with a uniform value of U_0=0.11±0.002 m/s.

Measurements of plume trajectories (chapter 6), also described in Decrop *et al.* (2012b), show that fine sediment plumes follow the exponential integral laws for the different momentum- and buoyancy-dominated regimes (Fischer, 1979). Integral laws omit the internal turbulent structure of the plume, and consider an average vertical level $\bar{z}$. Different types of trajectories can be used for comparison. Here, the maximum value of the horizontally integrated and time-averaged dilution S_y was determined at every streamwise position for the construction of a mean trajectory:

$$S_y(x_i, z) = \frac{1}{C_0 D} \int_{-B/2}^{+B/2} C(x_i, y, z) dy \tag{7.33}$$

$$\bar{z}(x_i) = z(max(S_y(x_i, z))) \tag{7.34}$$

where B is the width of the flume.

Since measurements of the trajectory were taken using lateral sediment obscuration images, the vertical position $\bar{z}$ at which S_y is maximal is chosen

for comparison with measurements. In order to determine the upstream and downstream extent of the plume, the vertical position was determined at which the light obscuration reduced to half of the centerline maximum.

The time-step was set at 0.06 dimensionless time units t_* ($=tU_0/D$), corresponding to a maximum flow Courant number of 2, at the finest grid cells located near the jet exit (for which $\sqrt[3]{V}/D \approx 0.03$, with V the grid cell volume). The simulation was run for 470 dimensionless time units, which is considered sufficient for flow statistics to converge (Muppidi and Mahesh, 2007). Time series of the evolution of the statistical properties of the flow were examined (mean and fluctuating velocity and sediment concentration, Reynolds stress components and turbulent sediment flux). The results showed stabilised statistics after about two-thirds of the simulation.

The first point of the grid near the wall of the pipe was located at $y_1^+ = 4$. This means the first grid cell is located in the viscous sublayer and the velocity profile is resolved in the following cells in the direction normal to the wall.

7.5.2.1.2 Model grids

The equations are solved on unstructured grids with tetrahedral cells in the plume domain and prism shaped cells in the release pipe, using the commercial code Ansys Fluent 14.5. A short section of pipe with length of $12D$ was included in the model domain to reduce the influence of the inflow boundary condition on the plume solution. At the pipe wall and near the plume release point, the grid resolution is about 3% of the pipe diameter. Near the walls of the hull, the wall-normal cell height is 2.5% of the boundary layer thickness, the wall-parallel grid size is 8% of the boundary layer thickness near the release point and downstream of it, gradually increasing to 25% further upstream. This is coarser than the stringent grid resolution requirements for wall-resolved LES. In this work it will be verified whether these relaxed grid properties can lead to good results in case the bulk of the plume is not located in the boundary layer. In order to optimise the model grid, a coarse base grid (away from the walls) is used for a RANS solution of a plume. Based on minimum strain rate and sediment concentration gradients, consecutive grid adaptations are executed. In this way, the grid is moderately refined in areas where either high gradients or high strain rates are found. The grid is most refined where both quantities have high values.

Typically, this procedure refines the grid not only in the volume occupied by the plume, but also in the region where the upstream crossflow starts to

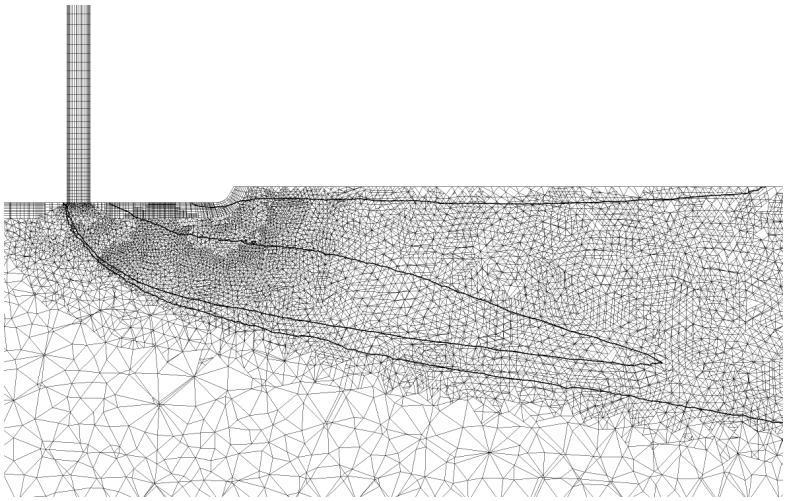

Figure 7.20: Symmetry plane slice of the unstructured grid with RANS flow dependent adaptations. Contour lines of C/C_0 at values 1% and 10% shown in full black lines.

feel the obstacle of the dense plume and the flow experiences strain due to curvature. The same applies for the wake of the plume, exhibiting lateral momentum fluxes above the plume. Refinement in this area is important for resolution of eddies capable of entraining plume material towards the water surface. As an alternative for refinement based on RANS calculations, a dynamic grid adaptation directly in the LES simulation was tested. Based on sediment concentration gradients the grid is refined and coarsened as a function of gradient thersholds, but the method proved unstable due to the highly dynamic character of the sediment clouds. An example of a step-wise refined grid (sliced along symmetry plane y=0) based on a RANS solution is shown in figure 7.20. The position of the plume is indicated by 0.01 and 0.1 contour lines of the time-averaged dilution C/C_0 (time-averaged concentration and velocity components are written in capitals).

A posteriori checks are made of the turbulent flow field Taylor microscale in relation to the grid size. The smallest values are found near the pipe exit. Surprisingly, not in the plume itself but in the zone where the crossflow diverges before encountering the first part of the jet shortly after release. Typical values for the Taylor microscale are found there of 5 to 10 mm, while the grid cell size (Δ) in the area nearest to the exit is about 1 mm, or Δ/D=0.03. The ability of the mesh and solver to resolve at least 80% of the turbulent kinetic energy (Pope criterion) is checked as well.

7.5.2.2 Results and validation

7.5.2.2.1 Introduction

In this section, the results of an experimental plume in crossflow case will be compared with the LES model results. After validation of this case, the next step in adding complexity to the flow can be taken: the addition of a ship hull stern.

7.5.2.2.2 Comparison with experiments

The trajectories obtained using the laterally integrated concentration (S_y) show good agreement with the measurements for case A0, as can be observed in figure 7.21a. The measured centreline is based on maximum time-averaged obscuration (bold full line), while the downstream and upstream half-widths are defined by the points where the obscuration is equal to half the centreline maximum. Modelled centrelines are determined by maximum S_y and are indicated by circles. Modelled (halfwidth-based) downstream and upstream extents are indicated by diamonds. For each point along the central streamline, the modelled downstream and upstream extent of the plume is determined by finding the locations where S_y reduces to 0.25 times the centreline value, along a line perpendicular to the central streamline (perpendiculars shown in thin lines).

In figure 7.21a, the first part of the modeled plume centerline is located somewhat higher than the experimental one. This might be caused by the difference in horizontal averaging method and internal sediment distribution in the plume. The measured average upstream and downstream extents of the plume (obscuration half-width) correspond well with the modelled edges of the plume. At $x/D > 30$, the downstream extent of the plume evolves rather horizontally in the experiment, while a mild slope was found in the model results. Overall, the time-averaged position of the plume is reproduced in a satisfactory way with the LES model.

The trajectory of the modelled plume can be analysed further by comparing with integral laws discussed higher (figure 7.21b). When the plume is in the MDFF regime, it follows from integral analysis that

$$z/z_M \propto c_m (x/z_M)^{1/3}. \tag{7.35}$$

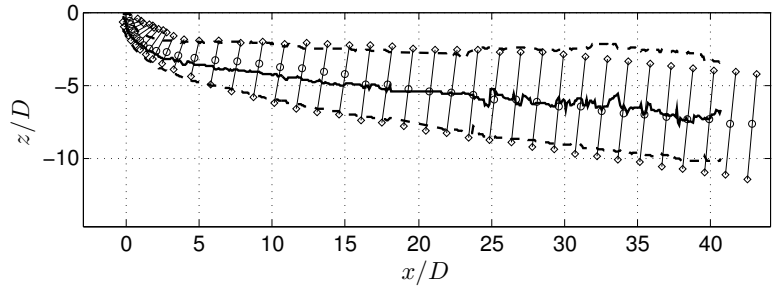

(a)

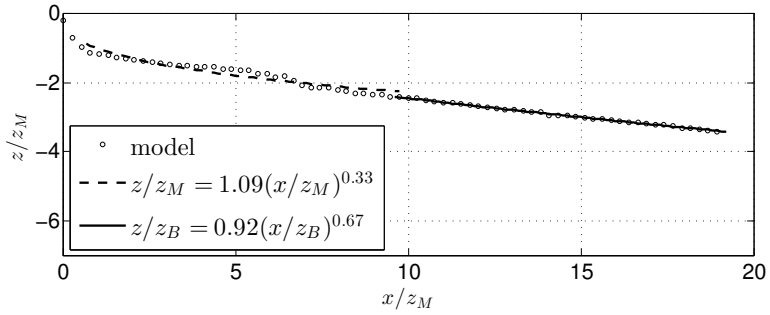

(b)

Figure 7.21: Simulation case A0: (a) Modelled centreline (∘) and plume edges (⋄), which are connected by a line perpendicular to the central streamline. Experimental centreline in thick line, experimental plume edges in dashed lines. In (b), the modelled centreline (∘) is shown with integral law fits, coefficients shown in the legend.

When the simulated centerline was fitted to the exponential function, a proportionality coefficient of $c_m = 1.09$ was obtained. For the exponential function of the BDFF integral law,

$$z/z_M \propto c_b(x/z_M)^{2/3}, \tag{7.36}$$

a coefficient of $c_b = 0.92$ was found. A plume in MDFF regime moves to a BDFF regime when the vertical distance becomes larger than $z_C = (M_0^2/U_0B_0)^{1/3}$. In this case, z_C/z_M=2.4, so the plume transforms theoretically from the MDFF to the BDMM regime at z/z_M=-2.4. The simulated trajectories follow relatively closely the integral laws for two-fluid plumes. The coefficients c_m and c_b are 10 to 20% lower compared to values found in literature for two-fluid plumes (Wright, 1977; Fischer, 1979).

In order to study the discrepancies between different options to define the plume trajectory, two methods are plotted in combination with streamlines at the symmetry plane y=0 (figure 7.22). The central streamline, originating from the pipe axis, is drawn in black full line, streamlines originating from the crossflow are drawn in grey. Contours at which S_y reduces to 0.1 are drawn in dashed lines. The central streamline is located closer to the lower S_y=0.1 contour. The streamlines at the wake side are characterised by a node downstream of the pipe exit. From the node, streamlines propagate downstream and intrude deeply into the downstream half of the plume, which is due to the secondary flow related to the counter-rotating vortex pair (CRVP), as will be demonstrated in section 7.5.2.2.5 below. Streamlines originating from the crossflow upstream are intruding the upstream part of the plume and approach asymptotically the central streamline. The plume trajectory defined by local S_y-maxima (i.e. the definition adopted in equations 7.33-7.34 ; indicated by triangles) is shown to divert significantly from the central streamline, especially in the MDFF regime, where strong bending of the plume occurs. Drawn in circles, the trajectory defined by the points of maximum C at the symmetry plane, however, aligns much closer to the central streamline. It appears the methods for trajectory definition differ most up to $x/D \approx$15, or in the MDFF regime. Therefore, the comparison with observed plume trajectories is most sensitive to the choice of trajectory definition method in this region .

Turbulent statistics related to sediment concentration exhibited self-similar properties, statistics of flow velocity did not. Normalising the turbulent statistics as in eq. 7.42-7.43 yields self-similar behaviour of the turbulent sediment fluxes $\overline{c'u_i'}$ (e.g. $\overline{c'v'}$ in figure 7.23a), but does not for the Reynolds

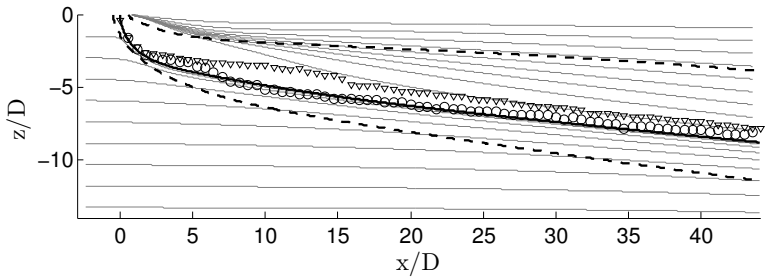

Figure 7.22: Model results of Case A0 with crossflow. Symmetry plane streamlines are drawn in grey, except for the central streamline, in full black line. Dashed lines are the contours at which S_y reduces to 0.1. The plume trajectory defined by points of local maximum S_y, i.e. $\bar{z}(x)$, is shown (triangles) as well as the trajectory defined by symmetry plane maxima of C (circles)

stress components (e.g. w'_{rms} in figure 7.23b). The latter are therefore driven by the uniform crossflow rather than the buoyancy (or sediment concentration). Time-averaged velocity components do not show self-similar properties in the far field either.

7.5.2.2.3 Turbulence resolution

The turbulence resolution M (Pope, 2004) is an indicator of the capability of the grid and numerical scheme to resolve a substantial part of the turbulent motions. It is defined by equation 7.37, while Pope (2004) states that a 'complete' LES simulation has a turbulence resolution lower than 0.2 at all times and at all locations.

$$M(x,y,z,t) = \frac{k_{SGS}(x,y,z,t)}{k_{SGS}(x,y,z,t) + k_{res}(x,y,z,t)} \tag{7.37}$$

where k_{SGS} is the turbulent kinetic energy (TKE) of the sub-grid turbulent motions captured by the sub-grid model and k_{res} is the TKE of the resolved scales. k can be determined by the sum of the squares of the fluctuating velocity parts, indirectly found by subtracting the square of the mean flow velocity components from the mean of the square of the instantaneous velocity components (it can be shown that $\overline{u'^2} = \overline{u^2} - \overline{U}^2$):

$$k_{res} = \frac{1}{2}\left((\overline{u^2} - \overline{U}^2) + (\overline{v^2} - \overline{V}^2) + (\overline{w^2} - \overline{W}^2)\right) \tag{7.38}$$

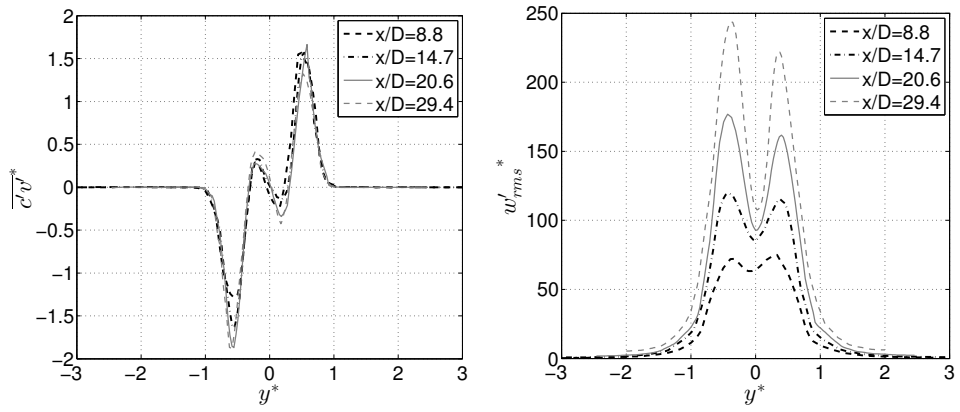

(a) (b)

Figure 7.23: Case B1: Horizontal profiles at elevation of max(C) at different distances from the pipe in the self-similar region. (a) lateral turbulent sediment flux $\overline{c'v'}^*$; (b) Vertical velocity fluctuations $w'_{rms}{}^*$.

Here, the Reynolds decomposition is used for the velocity components. The value of k_{SGS} at each location cannot be found directly from the velocity statistics. The expression used by Coussement *et al.* (2012) is applied:

$$k_{SGS} \approx \overline{\tau_{ii}} \approx \frac{\overline{\nu_t^2}}{(f_s \Delta)^2} \tag{7.39}$$

where τ_{ii} are the normal components of the Reynolds stresses, ν_t is the turbulent eddy viscosity from the SGS model, Δ is the filter size and f_s is a turbulence similarity parameter,

$$f_s = \sqrt{2/3} \frac{A}{\pi K_0^{3/2}} \tag{7.40}$$

with A=0.44 and K_0=1.4.
The turbulence resolution M was calculated a posteriori to verify the completeness of the LES calculation, using k_{SGS} and k_{res}. In figure 7.24, the resolved turbulent kinetic energy is shown in normalised form (k_{res}/U_0^2), as well as the turbulence resolution M. Local maxima of sediment concentration and curl of the YZ-planar velocity field are indicated with '+' and 'x' markers, respectively. The vectors of mean velocity in an YZ-plane normal to the crossflow direction are also shown to indicate the location of the counter-rotating vortex pair. The time- and space-averaged vertical velocity has been subtracted from these vectors. Contours of constant k_{res} follow the shape of the sediment concentration contours, apart from the zone above the plume

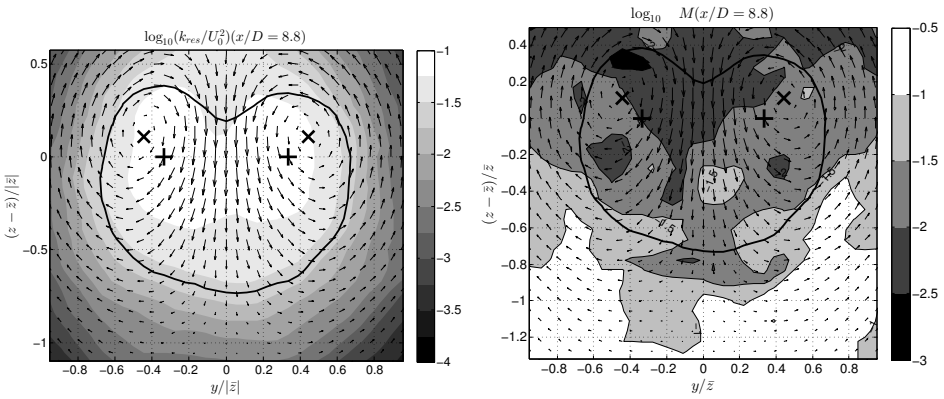

(a) (b)

Figure 7.24: Case B1: Vertical profile of (a) $log_{10}(k_{res}/U_0^2)$ and (b) $log_{10}M$, at $x/D = 8.8$. The full black line connects the points where C has been reduced to a factor $\exp(-1)$ times the local maximum. The '+'-signs indicate local maxima of sediment concentration, the 'x'-markers indicate local maxima of the curl of the velocity field projected on the vertical plane (vectors).

where the wake of the upstream (higher) part of the plume produces an increase in TKE. The SGS turbulent kinetic energy (equation 7.39) was about two orders of magnitude smaller compared to the resolved TKE, hence the value of M is well below 0.1 throughout the main part of the plume cross-section.

Within the $C_{max}/\exp(1)$-contour this lead to a turbulence resolution between 10^{-2} and $3{\cdot}10^{-2}$ from the plume release point up to $x/D = 10$. Further downstream M was between $3 \cdot 10^{-3}$ and $1 \cdot 10^{-2}$. Higher values occur below the plume, where the grid cells are larger, but where the strain rate is above zero due to crossflow streamline divergence in the approach to the plume. Therefore, within the plume at least 97% of the TKE was resolved, at the outer fringes at least 90%.

7.5.2.2.4 Turbulence frequency spectrum

The accurate simulation of turbulent motions is related to the energy transfer from energy-containing scales through the inertial range to the dissipative turbulent scales. The solution of LES models is generally limited to the inertial subrange. The well-known energy cascade concept shows the Kolmogorov's energy spectrum with a -5/3 power law for the energy distribu-

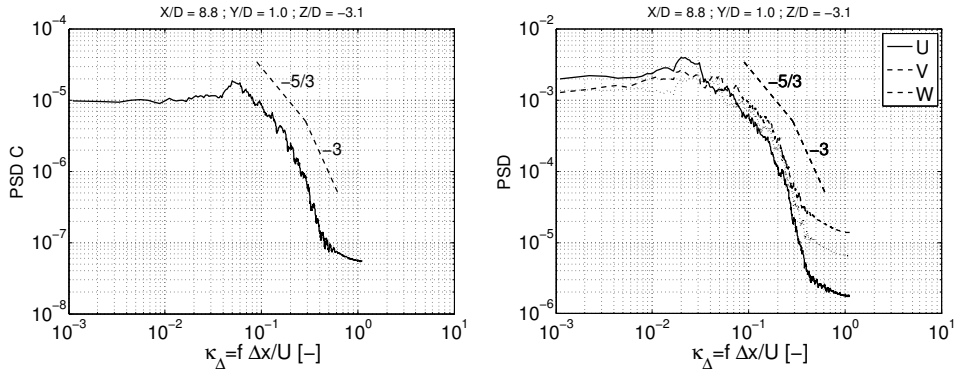

Figure 7.25: Power spectral density of sediment concentration fluctuations (a) and velocity component fluctuations (b), shown as a function of the grid-normalised Strouhal number κ_Δ.

tion along turbulent wavelengths (Kolmogorov, 1941) in the inertial subrange (figure 2.3). The energy associated with a wavelength is in essence energy contained in the motions of eddies of the corresponding size. For the present simulations, the frequency spectrum is drawn as a function of a dimensionless Strouhal number κ_Δ, which is the frequency normalised by the mean flow and grid cell size $U/\Delta x$ (the frequency with which the mean flow passes grid cells). The Strouhal number κ_Δ can be seen as the number of resolved eddies per unit of distance equal to the grid cell size. The spectra of both the sediment concentration fluctuations and velocity fluctuations show that in terms of a characteristic number-of-grid-cells-per-vortex length-scale $l/\Delta x$, vortices with size $5< l/\Delta x <20$ are resolved. They transfer energy in a way the -5/3 power law predicts (Figure 7.25), both from the sediment concentration fluctuations and from velocity fluctuations. Smaller eddies with size $2< l/\Delta x <5$ exchange energy following a -3 power law, in the so-called inertial-diffusive subrange. This behaviour has been observed earlier in the region close to the dissipative range in buoyant (two-fluid) plumes, in experiments by Dai *et al.* (1994a) and LES simulations by Zhou *et al.* (2001).

7.5.2.2.5 Counter-Rotating Vortex Pair

In the time-averaged flow field, the typical counter-rotating vortex pair (CRVP) is found, shown in figure 7.26a by the vectors of the time-averaged flow field projected on a YZ-plane and in a reference frame moving with the spatially averaged vertical velocity. Effectively, the mean vertical velocity has been

subtracted, hence the upward pointing vectors at both lateral sides of the plume. The 'x' markers show the positions of the local concentration maxima, while the '+' markers show the approximate position of the center of the counter-rotating vortices.

In order to compare the results with data from other work and to evaluate the self-similarity of different quantities, the self-similar form of C can be written (eq. 7.41) as given by e.g. Diez *et al.* (2005). In the following, self-similar forms of $\overline{c'w'}$, w'_{rms} and c'_{rms} are also used (eq. 7.42-7.44).

$$C^* = \frac{C}{C_0}\frac{U_0}{B_0}\bar{z}^2 g \tag{7.41}$$

$$\overline{c'w'}^* = \frac{\overline{c'w'}}{C_0 U_0}\frac{U_0}{B_0}\bar{z}^2 g = \frac{\overline{c'w'}}{C_0 B_0}\bar{z}^2 g \tag{7.42}$$

$$w'_{rms}{}^* = \frac{w'_{rms}}{U_0}\frac{U_0}{B_0}\bar{z}^2 g = \frac{w'_{rms}}{B_0}\bar{z}^2 g \tag{7.43}$$

$$c'_{rms}{}^* = \frac{c'_{rms}}{C_0}\frac{U_0}{B_0}\bar{z}^2 g \tag{7.44}$$

Self-similar forms $u'_{rms}{}^*$ and $v'_{rms}{}^*$ are written in the same fashion as $w'_{rms}{}^*$.

As suggested by Diez *et al.* (2005), the lateral and vertical coordinates are nondimensionalised as follows:

$$y^* = y/|\bar{z}| \tag{7.45}$$

$$z^* = (z - \bar{z})/|\bar{z}| \tag{7.46}$$

where $\bar{z}$ is the level of the concentration maxima. The absolute value is used to obtain positive coordinates for locations above the concentration maxima and vice versa.

As shown in figure 7.26a, the contours of the sediment concentration in C^*-form exhibit the well-known kidney shaped profile. The image is very similar to the PIV measurements taken by Diez *et al.* (2005) on a buoyant jet of water containing potassium salt. Even though the source-to-crossflow velocity ratio was more than 20 times larger compared to the present work, the self-similar YZ-profile is almost identical. The plume cross section resulting from their measurements extended from dimensionless height z^*= -0.5 to 0.2 and laterally in the range $y^*=\pm 0.45$. These values are somewhat larger in this case, probably because the lower source-to-crossflow velocity ratio induces a shorter section of the plume dominated by initial vertical momentum, leading

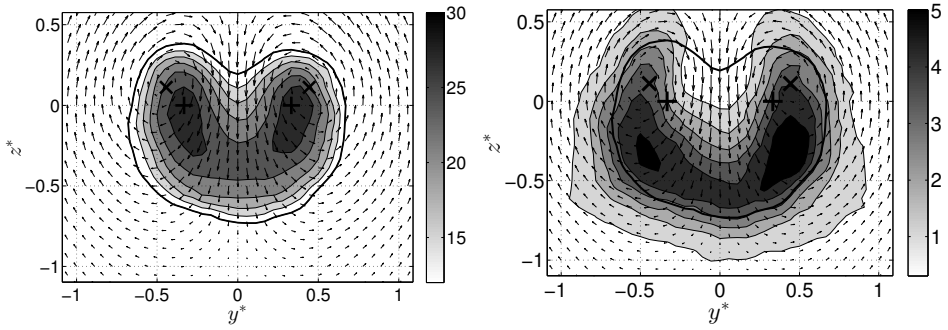

(a) (b)

Figure 7.26: Case B1: Profile in a plane normal to the crossflow (X/D=8.8). Profiles of (a) time-averaged normalised sediment concentration C^* and (b) normalised vertical turbulent sediment flux $\overline{c'w'}^*$. The full black line connects the points where C has been reduced to a factor $\exp(-1)$ times the local maximum. The '+'-signs indicate local maxima of sediment concentration, the 'x'-markers indicate local maxima of the curl of the velocity field projected on the vertical plane (vectors).

to a lower $|\bar{z}|$ value. The source-to-crossflow density ratio, however, was close to the currently simulated case. Also, the self-similar form of the dimensionless concentration includes a factor $|\bar{z}|^2$, due to which the peak values of C^* are lower in the current case. In terms of self-similarity, the peak values of C^* were equal to 30 within a range from 8 to 30 pipe diameters downstream of the source.

The centers of CRVP in the simulation results are located further from the centerplane than the concentration maxima, as found in the PIV data in Diez *et al.* (2005). The CRVP centers ('x') and concentration maxima ('+') are found at the same height in Diez *et al.* (2005), while the latter are located more upstream than the former in this case. This is possibly due to the different turbulent diffusion properties of small particles compared to miscible liquids. Increased vertical strain ($\partial w/\partial z$) due to the wall step has an influence on this internal structure of the plume. Particularly in case only one side of the plume is affected by the wall step.

The initiation and vorticity source of the CRVP has been the subject of a number of previous studies (Andreopoulos, 1985; Sykes *et al.*, 1986; Kelso *et al.*, 1996; Walters and Leylek, 2000; Lim *et al.*, 2001; Cortelezzi and Karagozian, 2001; Peterson and Plesniak, 2004; Cambonie and Aider, 2014).

Different theories have been postulated in the past about the CRVP-initiating mechanism. Using dye injections throughout the circumference of the pipe boundary layer, Kelso *et al.* (1996) showed that CRVP vorticity at least partly originates from secondary currents and related vorticity (ω_z) inside the pipe. Peterson and Plesniak (2004) found that secondary currents with the same sense of rotation as the CRVP indeed strengthen the CRVP. Yet, when in-pipe secondary currents with opposing sense of rotation are introduced, the CRVP is weakened but still present. This feature has been examined in the flow field of the present LES calculations. 3D streamlines of the time-averaged flow have been plotted in black in figure 7.27a, starting in the pipe boundary layer at elevation z/D=3 at different points along the pipe circumference. It can be seen in figure 7.27a that the observations of Kelso *et al.* (1996) are reproduced by the model, since the streamlines divert towards the downstream end of the pipe before leaving the exit. The flow folds after exiting the pipe, leading to converging and twisting streamlines. It is shown clearly that the black streamlines (originating from the pipe boundary layer) twist and converge, while streamlines from the crossflow at y/D=0.15 and -3< z/D <-1 (in rainbow colormap, red nearest to the flat wall) bend and curl around the streamlines from the pipe. The crossflow streamlines are fully taking part in CRVP circulation, while it is clear the streamlines originating from the pipe boundary layer are at the center of the CRVP. Figure 7.27b shows the in-pipe vorticity ω_z (at the z/D=0.1 plane) as well as planar, time-averaged streamlines. It can be observed that secondary currents with the same sense of rotation as the CRVP are present. However, many authors agree that the vorticity source of the CRVP is not limited to the in-pipe vorticity of low-λ jets (Kelso *et al.*, 1996; Walters and Leylek, 2000; Cambonie and Aider, 2014). Amongst other reasons, Walters and Leylek (2000) dismiss the shearing between crossflow and jet as a source of CRVP vorticity because the jet in their case is largely located inside the crossflow boundary layer. It is interesting to mention that for the simulation case of the streamline plot in figure 7.27a, a free slip flat wall was also tested, displaying nearly the same behaviour as a case with a δ/D=0.32 boundary layer at the flat wall, where δ is the wall boundary layer thickness. Therefore, unlike the flows in Walters and Leylek (2000), the boundary layer at the flat wall is relatively thin, resulting in only a minor influence of the boundary layer on CRVP strength. For this reason -and given the observation of crossflow streamlines curling around the CRVP center (figure 7.27a)- in thin δ/D crossflows the shearing between jet and crossflow is likely to contribute to CRVP vorticity.

Interesting to further discuss are the YZ-profiles of $\overline{c'w'}$, v'_{rms} and c'_{rms} (figures 7.26b and 7.28). The vertical turbulent sediment flux $\overline{c'w'}^*$ at the x/D=8.8-

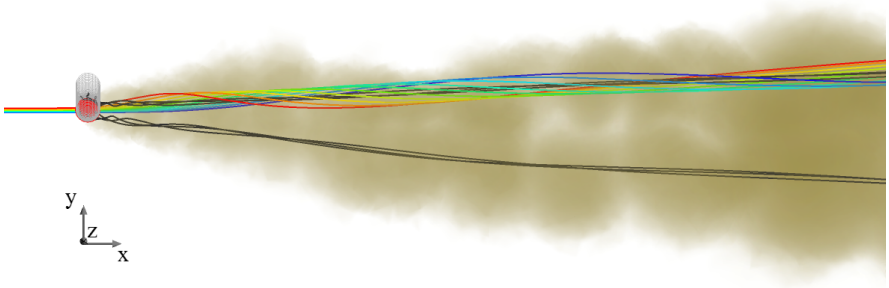

(a)

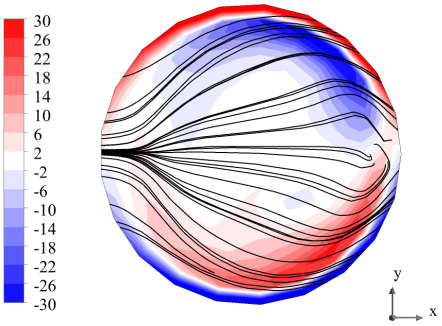

(b)

Figure 7.27: Case A1, time-averaged streamlines: (a) Top view, looking down in z-direction, view point slightly tilted towards $-y$ to show the colour order of approaching crossflow streamlines. Black lines originate from the pipe boundary layer at elevation z/D=3. Coloured streamlines originate from the crossflow at y/D=0.15 and -3< z/D <-1, with the red streamline nearest to the flat wall. (b) In-pipe vorticity ω_z (s^{-1}) in colourscale, shown at a slice perpendicular to the pipe axis (z/D=0.1, indicated in red in (a)). Planar, time-averaged streamlines are shown in black.

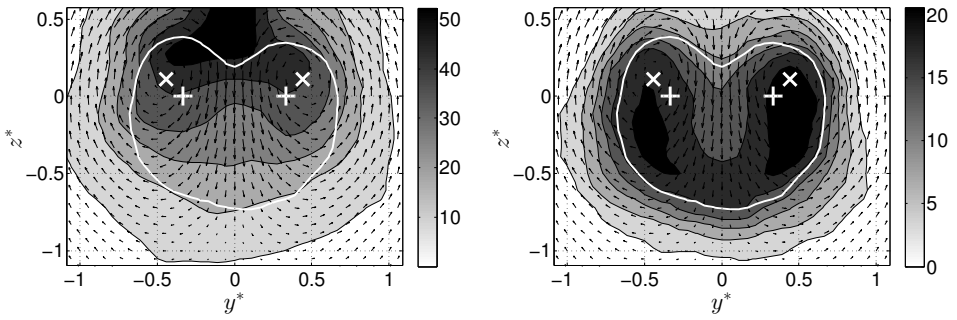

Figure 7.28: YZ-plane contours of turbulent quantities in case B1 (x/D=8.8): (a) Lateral normal Reynolds stress component ${v'_{rms}}^*$,(b) Turbulent fluctuations ${c'_{rms}}^*$. The full white line connects the points where C has been reduced to a factor $\exp(-1)$ *times the local maximum. The '+'-signs indicate local maxima of sediment concentration, the 'x'-markers indicate local maxima of the curl of the velocity field projected on the vertical plane (vectors).*

plane is shown in figure 7.26b. Its value is positive throughout the plume while the strongest values are found in the upstream part of the plume, where the vertical sediment concentration gradient is unstable. The high $\overline{c'w'}$ value at the upstream part of the plume's circumference reflects the exchange due to leading edge vortices (see paragraph 7.5.4.1).
The first profile in figure 7.28a is marked by two types of flow features generating a fluctuating lateral velocity component:
(i) the large $\partial U/\partial y$-gradient between the streamwise velocity maxima associated with the CRVP centers, and (ii) the turbulent wake formed behind the plume itself. The wake behind the plume as it exits the pipe (z/D=-2-0) has a Reynolds number of Re_w=$U_0 D/\nu$=3500. The wake is thus turbulent, which can be seen by the increase in v'_{rms} above the centerline of the plume.
The profile in figure 7.28b shows the turbulent fluctuations of the sediment concentration. Peak values of ${c'_{rms}}^*$ were equal to about 20, the turbulent intensity of sediment concentration is therefore quite high, locally up to 80%. This can be explained by the intermittent character of the sediment concentration time series at a location where sediment-laden convection cells are advected by the mean flow.

7.5.3 Plume in crossflow with ship hull

7.5.3.1 Introduction

Since plumes released from floating offshore structures or dredging vessels experience streamline divergence downstream of the edge of the structure (i.e. stern of a vessel), the effect of a wall step on a plume is studied. The impact of wall step-associated turbulence on the trajectory and structure of the sediment plume is studied. A number of experiments have been executed at a variety of release and crossflow conditions. The densimetric Froude number F_Δ varied between 0.24 and 9.1, while the velocity ratio λ was in the range 0.17 to 2.72 (table 7.1). The horizontal distance of the pipe axis to the wall step is $x_{ws}/D = 7.06$ (figure 7.29), while the height of the wall step (or vessel draft) H_d/D=0.88. The water depth downstream of the wall step was H=0.53 m, or H/D=15.6. The mean horizontal flow velocity without plume was measured at $17H_d$ downstream of the wall step and was equal to 0.113±0.002 m/s. Since the under keel clearance (i.e. under the schematised hull) is only 50 cm, the velocity boundary condition is taken as $0.113 \cdot 0.53/0.50 = 0.120$ m/s. For better comparison between cases with and without hull, U_0 values given in table 7.1 refer to the velocity downstream of the hull stern.

7.5.3.2 Sensitivity analysis

7.5.3.2.1 Introduction

In section 7.5.2.2, it was shown that the model with the chosen grid resolution, SGS turbulence model, time step and advection scheme performed well. The choices made there, need to be assessed for their influence on the results. The aim of this section is also to verify whether smaller grid resolution and time step do not change the time-averaged results significantly. Both refinements would ultimately result in DNS simulations in which the turbulence is much better represented, so only the time-averaged results are analysed.

7.5.3.2.2 Grid resolution

The simulated experiment 'case B1' has been revisited with a refined numerical mesh. In the zone in which the plume is located, in addition to zones with significant strain rate, each tetrahedral grid cell has been replaced by four grid cells. The average grid refinement factor is thus equal to $4^{1/3} = 1.6$ resulting in four times as many cells in the zones with sediment and strain.

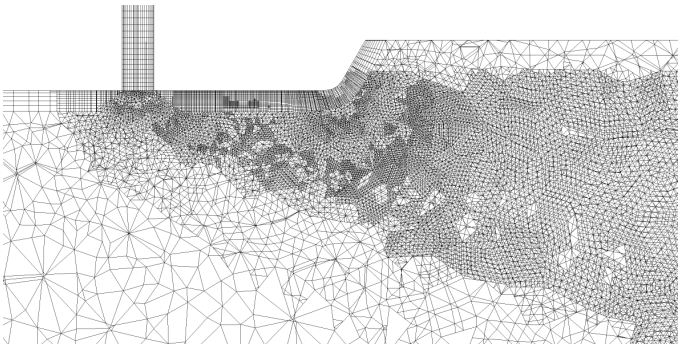

Figure 7.29: Slice at $y = 0$ of the tetrahedral mesh used for the grid refinement analysis of case B1. Zoom on $x/D < 12$.

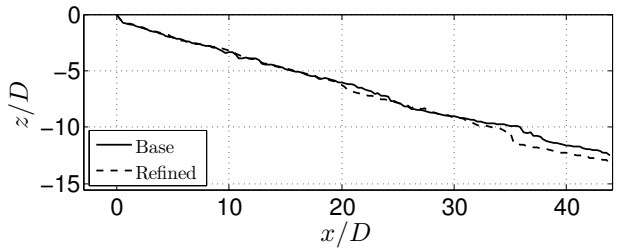

Figure 7.30: Comparison of the trajectory of a plume simulation case with regular grid resolution ('Base') and the trajectory of a case with a refined grid with four times as many grid cells in the plume zone ('Refined').

For the complete domain, the number of cells increased from 1.6 million to 2.9 million. A $y = 0$-slice of the refined unstructured mesh is shown in figure 7.29. In this figure, the tetrahedral grid cells are sliced, due to which some individual cells appear smaller than in reality. In order to keep the CFL number at the same level, the time step was decreased from 20 ms to 12.5 ms.

In figure 7.30, the trajectories of the simulations with the original grid ('Base') and refined grid ('Refined') are shown. It can be seen that, apart from small differences, the base case with 1.6 million cells results in the same trajectory as the refined simulation with 2.9 million cells. It can thus be concluded that a higher resolution for the remainder of the simulations at laboratory scale is not needed.

Further, the horizontal and vertical profiles of the time-averaged sediment concentration are compared (figure 7.31). The time-averaged concentration is compared rather than the flucuating part, since it is natural that more turbulent motions and thus more turbulent fluctuations would be obtained

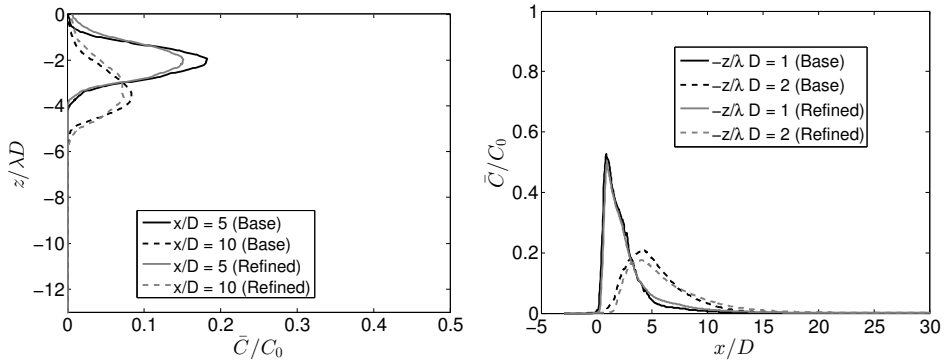

(a) (b)

Figure 7.31: Comparison of the vertical (a) and horizontal (b) profiles of C/C_0 from the reference simulation and the refined simulation.

with a finer mesh. The time-averaged concentration relative to the source concentration, $\bar{C}/C_0$, is compared at x/D=5 and x/D=10 (figure 7.31a). As was observed in the previous paragraph, the concentration maxima or plumes centerlines are located at the same vertical level. The values of $\bar{C}/C_0$ are slightly lower in the refined case, about 10% at the concentration peak. The vertical profiles of C/C_0 at vertical distances $z/\lambda D$=-1 and $z/\lambda D$=-2 from the source are compared (figure 7.31b). At $z/\lambda D$=-1, almost no difference can be found, while at $z/\lambda D$=-2, the refined case has again a peak concentration of about 10% lower than the reference case. The width of the horizontal and vertical distributions of C/C_0 is the same in reference and refined cases.

Also, the turbulent fluctuations of sediment concentration have been analysed in the reference simulation and in the refined simulation (figure 7.32). It can be observed that the correspondence of the simulation results with the experimental results is comparable in the reference simulation and in the refined simulation.

7.5.3.2.3 The subgrid turbulence model

The SGS turbulence model selected for the plume simulations presented above, is the Dynamic Smagorinsky-Lilly model described in section 7.2 (Lilly, 1992). The advantage of this model is its coefficient varying in time and space. Other SGS turbulence models considered are Wall Modelled LES (WMLES), Wall-Adapted Local Eddy-viscosity (WALE) and a 1-equation

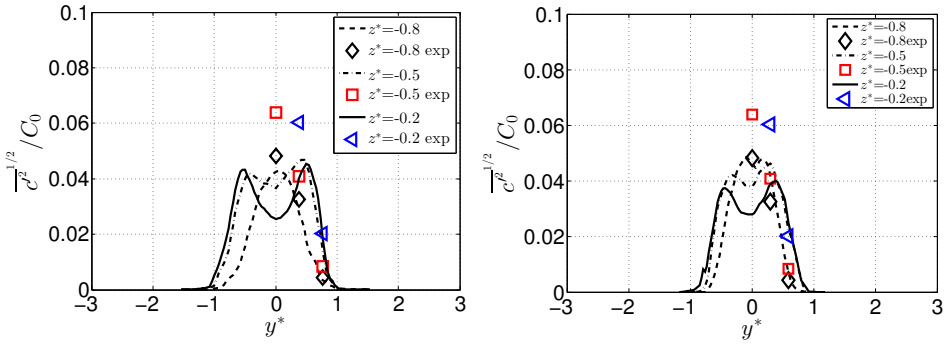

(a) (b)

Figure 7.32: Comparison of the reference simulation (a) and refined simulation (b) with the experimental results.

transport of k model.

Since resolving the turbulence in the wall boundary layer using LES is only possible for limited Reynolds numbers, a number of hybrid turbulence model were developed, which are combinations of RANS and LES. Such an example is WMLES where in the inner boundary layer, a RANS solution is deployed while in the outer boundary layer a modified LES formulation is used. Different weighting functions take care of the transitions between the modes. This model was tested at the laboratory-scale cases presented here, but was found to perform not as good as the Dynamic Smagorinsky model. A likely explanation is the lack of a time- and space-varying turbulence length scale such as in the Dynamic Smagorinsky model. The advantage of WMLES - an adapted solution for the boundary layer- is not that advantageous in a plume simulation where the largest part of turbulence is generated by free shear flow. The boundary layer thickness has the same order of magnitude as the pipe diameter and is therefore in this case not that important in the plume behaviour. Also, remind that in the experimental setup, the hull is located at x/D <9, after which the free water surface starts and no wall boundary layer is present. The simulations with Dynamic Smagorinsky do not solve the boundary layer turbulence either and have no separate solution for the boundary layer shear. The nature of the Dynamic Smagorinsky makes that the eddy viscosity goes to zero at the wall, as it should be, but the boundary layer velocity profile will not be entirely correct. Yet, the plume simulations show a good behaviour.

Simulations of the same case (B0, see tabel 7.1) have been simulated with all

four SGS models, the trajectories are shown in figure 7.33. The trajectories are similar, but differences are present. Different cross sectional structures of the plume can result in different trajectories, without a significantly different average plume height. The WMLES result shows two jumps in the trajectory that are associated with changing internal structure of the plume. In the phase of bending over, the WMLES result has the CRVP structure, as expected for a plume in crossflow of this λ. After x/D=2, the structure changes to a more uniform cross sectional distribution of C, which is different from the expected behaviour.

Another hybrid model is the WALE model, proposed by Nicoud and Ducros (1999). It combines a turbulent length scale with a strain rate to determine the eddy viscosity, as the Smagorinsky-Lilly model. The strain rate is modified to give the correct wall-asymptotic behaviour. For this model to be usefull for real industrial flows, a dynamic version is needed, in which the length scale coefficient (Smagorinsky Coefficient) is varying in time and space (Nicoud and Ducros, 1999). This dynamic version of the WALE model is not available in the Fluent code (v14.5). As for the WMLES model, the internal cross sectional structure of the plume was not as expected. The trajectory is situated about $1D$ lower compared to the Dynamic Smagorinsky. The WALE model trajectory was very similar to the last SGS model in the comparison, i.e. the 1-equation k.

The 1-equation for the transport of k is a SGS model in which the production, dissipation and transport of turbulent kinetic energy is determined (Kim and Menon, 1997). The local SGS turbulent kinetic energy is used to determine the eddy viscosity. Also for this SGS model, the counter-rotating vortex pair was simulated correctly, but the kidney-shaped cross-sectional profile for C was not. The average trajectory was also slightly lower than for Dynamic Smagorinsky and the measured trajectory.

Kim *et al.* (2004) performed a number of validation cases using the Dynamic Smagorinsky model. A high-Re 'flow past cylinder' case with Dynamic Smagorinsky showed good agreement for drag coefficient C_D, but failed to determine the laminar-turbulent transition location. Channel flow simulations at Re=3300 showed highly accurate results for profiles of mean flow and turbulence statistics near the wall. In these cases, the grid resolution was high enough to resolve the turbulent motion in the boundary layer.

Overall, it can be concluded that the solution of the average trajectory is fairly sensitive to the SGS turbulence model. The internal structure of the

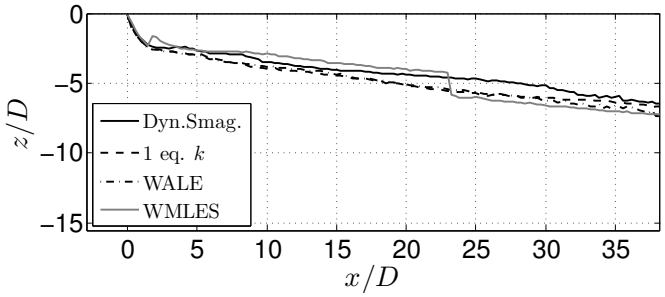

Figure 7.33: Comparison of mean trajectories from simulations with the same boundary conditions, but using four different subgrid-scale turbulence models.

sediment concentration is very sensitive, and only the Dynamic Smagorinsky model yields the expected kidney-shaped concentration profile.

7.5.3.2.4 Time step - CFL number

In this paragraph, it will be verified whether the time step is not limiting the accuracy of the solution. In the reference simulations, the CFL number is kept below 1 throughout the domain, except for a small zone at the pipe exit. The time-averaged solution should be independent of the time step. Given the typical grid resolution used for the plume in crossflow simulations at laboratory scale, the results with the reference time step and the results using half the time step are compared. The CFL number was thus effectively halved. Time-averaging of the sediment concentration is done over twice the number of time steps compared to the reference case.

In figure 7.34a, the vertical profiles of C/C_0 at x/D=5 and x/D=10 are shown. It can be observed that the profiles are almost identical. Likewise, the horizontal profiles at vertical distances $z/\lambda D$=-1 and $z/\lambda D$=-2 from the source are compared (figure 7.34b). Also here, no significant difference between the simulation with time step of 20 ms and a time step of 10 ms is observed. The level at which the sediment concentration is maximal has been compared for each horizontal distance from the pipe, x/D. Also here, the differences between the lines from the simulations with time step of 20 ms and 10 ms are very small. It can be concluded that the time-averaged solutions of the LES equations are independent of the chosen time step.

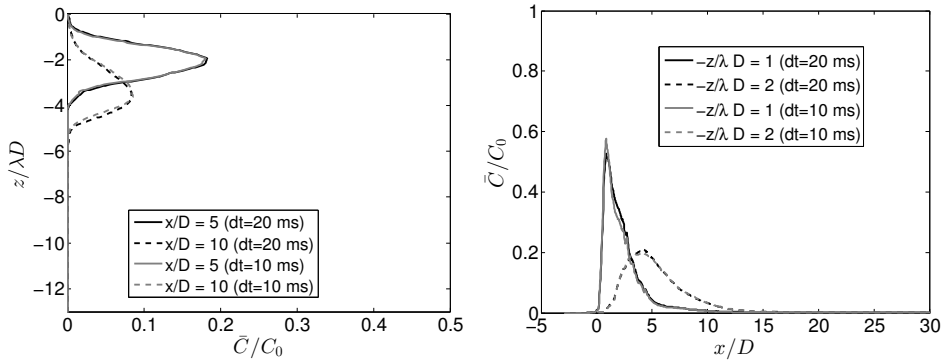

(a) (b)

Figure 7.34: Comparison of the vertical (a) and horizontal (b) profiles of C/C_0 from the reference simulation and from the simulation with half the time step.

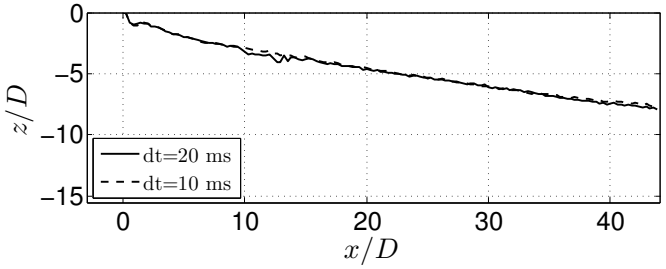

Figure 7.35: Comparison of the level of maximum concentration C of a reference plume simulation case with time step 20 ms and a test case with half the time step, 10 ms.

Case	Rmse T	Bias T	Rmse Up	Bias Up	Rmse Low	Bias Low
A0	0.60	-0.57	0.58	-0.49	0.28	-0.14
B0	0.25	0.00	0.20	0.04	0.21	0.14
B1	0.51	0.44	0.61	0.54	0.37	0.36
B2	0.12	-0.10	0.16	0.13	0.26	-0.20
B3	0.21	-0.08	0.31	0.21	0.30	0.06

Table 7.2: Overview of root-mean-squared errors and bias of simulated trajectories (T) and downstream (Up) and upstream (Low) edges of the plume. Values normalised by the pipe diameter.

7.5.3.3 Model validation against experimental data

The simulated plume trajectory for the experimental case B0 (with same boundary conditions as the reference case without wall step, A0) matches the measured trajectory closely in the MDFF regime, in the downstream part (BDFF) the simulated trajectory has a slightly more upstream position than observed (figure 7.36). In figure 7.36a, the simulated trajectory and plume edges are compared with the observed ones in the same way as for case A0 in figure 7.21a. The half-width on the downstream and more upstream edges of the plume agrees well with the simulated edge of the plume. The upward vertical diffusion due to the wall step is locally visible near x/D=7 to 10. Both in measured and simulated plume edges, a local positive slope of the time-averaged downstream edge of the plume is observed. Beyond the influence of the step, the downstream edge of the plumes resumes its buoyancy driven negative slope. The slight deviation in trajectory in the downstream part of the model result is probably due to wall effects in the experiment becoming more important when the plume widens. In the MDFF and BDFF regimes, the plume closely follows the exponential power laws (figure 7.36b). The fitted coefficients are lower compared to a plume without wall step, indicating a slightly higher plume trajectory. This might be caused by increased mixing due to the step, resulting in reduced (negative) buoyancy compared to a case without step.

Plumes with a total of five different combinations of F_Δ and λ have been simulated with the identical model settings. Trajectories and plume edges compared well with data from the measured plumes (table 7.2). The average (over all cases) RMS error on the trajectory and plume edge heights amounted to 0.34 pipe diameters. The average absolute value of the bias was 0.23 pipe diameters.

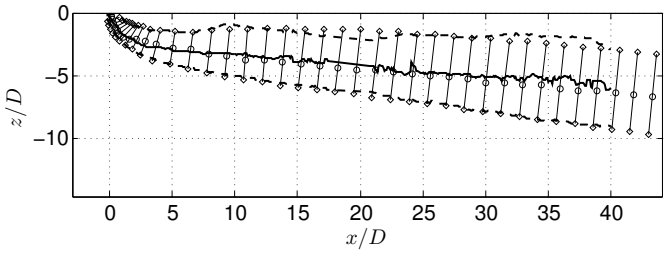

(a)

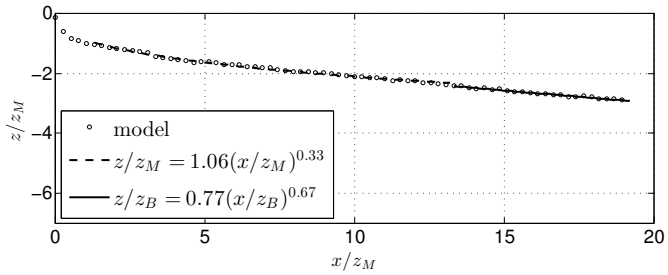

(b)

Figure 7.36: Simulation case B0: (a) Modelled centreline (∘) and plume edges (⋄), which are connected by a line perpendicular to the central streamline. Experimental centreline in thick line, experimental plume edges in dashed lines. In (b), the modelled centreline (∘) is shown with integral law fits, with coefficients shown in the legend.

Measurements of mixture velocity and sediment concentration were taken using an Acoustic Doppler Velocimeter (Lohrmann *et al.*, 1994) at point locations in the x/D=14.7-plane (see chapter 6). Measurements have been processed for the determination of Reynolds stress components as well as turbulent sediment fluxes as well. Since the resolved part of the turbulence amounts to 95 to 99% of the total, the resolved Reynolds stresses and turbulent sediment fluxes can be compared with the total stresses from the experimental data.

The normal components of the Reynolds stresses are shown in figure 7.37a-b. Simulated Reynolds stresses are in relatively good agreement with the measurements. Note that all measurements are taken below the level of maximum concentration in this case (i.e. z^* <0). Simulated peak values differ about 10% from the measurements. The deviations on the turbulent intensity of concentration c'_{rms}/C_0 shown in figure 7.37c are somewhat higher, about 20 to 50 % of the centreline values.

Comparison with point measurements is highly sensitive to slight differences in position of the plume as well as to the shape of the internal turbulent structure. However, the measurements at the outside of the plume indicate that the width of the turbulent structure is accurate (figure 7.37a-c).

Simulated values of C^* (case B1) are compared with observations in figure 7.37d. The lateral extent of the plume was simulated quite accurately, with values of C^* <2.5 at y^*=0.77. Concentrations in the center of the plume coincide well with the measurements, while it was overestimated on the symmetry plane at the lowest part of the measurements (at z^*=-0.2).

Cross components of the Reynolds stresses show more complex patterns compared to the normal components (figure 7.38a), changing sign two times across a lateral profile. Measured values exhibit roughly the same profile shape and are in the same range as the model results. However, peak values of $\overline{u'w'}$ at the centerplane are overestimated (figure 7.38a). Values of $\overline{u'w'}$ are mainly positive at the centerplane (where U-momentum is mixed upwards), while they become negative towards the outer edge of the plume (where negative W-momentum is mixed in crossflow direction). This is not the case for the lowest fringes of the plume (here at relative vertical coordinate of z^*=-0.8), where the centerplane value is negative. At this location, the flow is dominated by convection cells (see figure 7.39 in 7.5.4.1) torn off from the plume by gravity, adding to the diffusion of positive U-momentum in negative z direction. The resulting negative values of $\overline{u'w'}$ are therefore

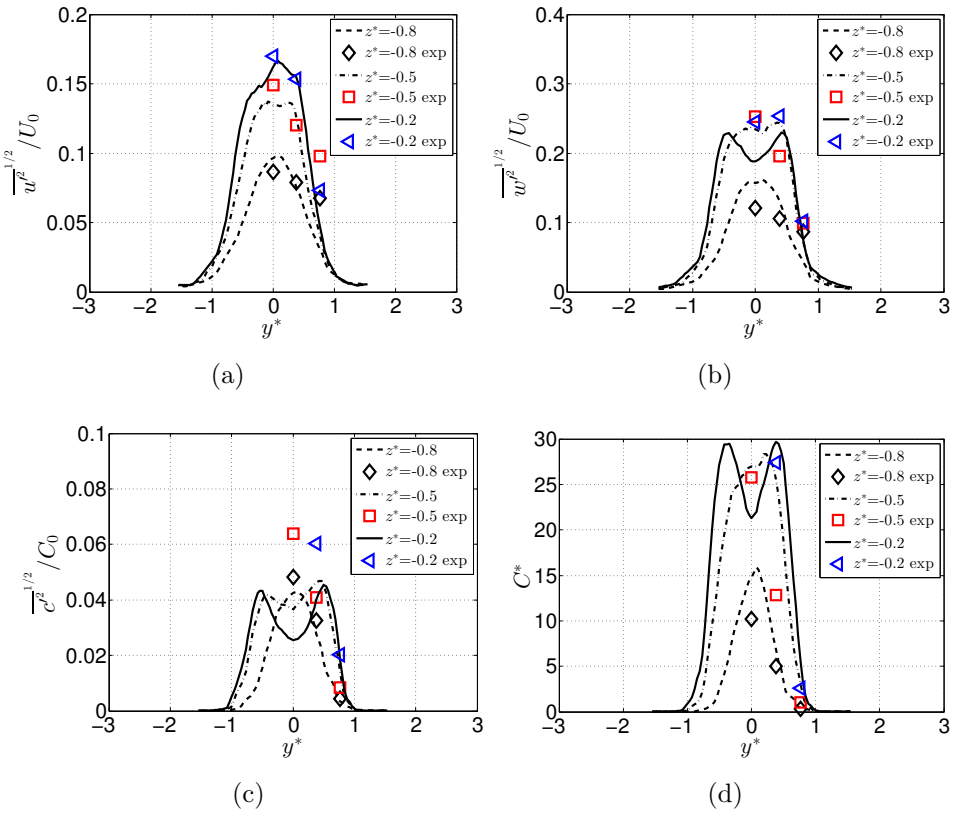

Figure 7.37: Simulation Case B1: Root-mean-square turbulent fluctuations of (a) horizontal velocity, (b) vertical velocity and (c) sediment concentration at x/D=14.7 in experiment and LES model. Panel (d) shows the average sediment concentration in self-preserving form. Markers indicate measurements, model results are shown with lines.

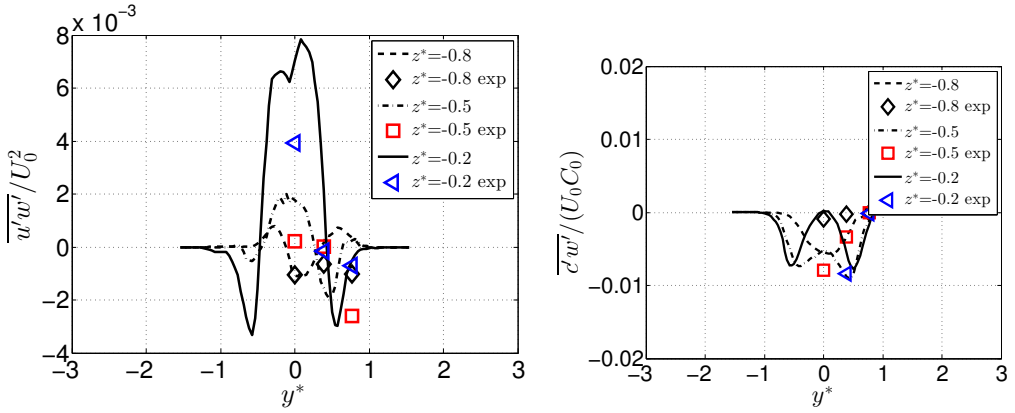

(a) (b)

Figure 7.38: Simulation Case B1: Turbulent momentum and sediment mass fluxes at x/D=14.7 in experiment and LES model: (a) $\overline{u'w'}$ Reynolds stress component and (b) Vertical turbulent sediment flux $\overline{c'w'}$.

more pronounced compared to the tiny upstream notch in $\overline{u'w'}$ profiles in Su and Mungal (2004). At x/D=14.2, those authors find maximal $\overline{u'w'}/U_0^2$ values on the wake side of the central streamline of about 0.02. At x/D=14.7, we find in our measurements a value of 0.004 and in the LES simulations a value equal to 0.007. The lower values in our sediment plume case can be explained by turbulence damping in the stable density gradient on the downstream side (wake side) of the plume.

The vertical turbulent sediment flux $\overline{c'w'}$ (figure 7.38b) is calculated from the measurements as the covariance of w' and c' timeseries, while from model results it is determined from $\overline{c'w'}$=$\overline{cw} - \bar{c}\bar{w}$. The quantity is calculated by the model within the range found in the experiments, but the profile shapes differ: a single-peak lateral profile for measurements at z^*=-0.5 while a double peak was found with the LES model. As shown in paragraph 7.5.2.2.5, $\overline{c'w'}$ has also a double-peak structure related to the CRVP and vertical sediment concentration gradients. From figure 7.38b it appears that the lateral $\overline{c'w'}$ profile does not have a double peak at z^*=-0.8 while it does at z^*=-0.5 and above.

In general, the model is capable of computing accurately the mean trajectory and height of the sediment plumes. The profiles of normal Reynolds stresses are close to the measurements, while Reynolds shear stresses and turbulent

sediment fluxes are in the good order of magnitude and the profiles' shapes are represented well.

7.5.4 Discussion

7.5.4.1 Effect of a wall step on the instantaneous flow field

When the instantaneous quantities are examined, a number of other turbulent structures are found in the simulation results. The downstream side of the plume is rather smooth, while the upstream fringes are dented with a wavy surface, both with and without wall step, as shown in figure 7.39. Figure 7.39b shows the case with wall step, which clearly induces sediment clouds to be drawn towards the wall. The Q-invariant is the difference between the moduli of the vorticity tensor and of the strain rate tensor, see Hunt *et al.* (1988); Kolář (2007). It is computed and shown in figure 7.40, where it can be seen that three different structures not present in mean flow fields of the plume are found: convection cells initiated by the leading edge vortices, plume wake vortices and wall step wake vortices.

The convection cells appear at the leading edge of the plume (figure 7.39) and originate from internal waves caused by Kelvin-Helmholtz instabilities near the pipe exit and around the symmetry plane. These instabilities have the shape of a horseshoe vortex and are referred to as leading-edge vortices in literature on jets in crossflows (Cambonie and Aider, 2014). They are, however, no static horseshoe vortex but originate from shearing between plume and crossflow. In figure 7.40, these vortices can be recognised as rib-like coherent structures on the upstream fringes of the plume. The colouring indicates the vertical vorticity ω_z, it can be observed that the wake vortices do not have the property of a von Kármán vortex street, in which vortices have alternating vertical vorticity. Here, two or more subsequent wake vortices have a ω_z value with equal sign, followed by a number of upright vortices with opposite ω_z-sign. In theory, no source of ω_z is present, and therefore the sum of the vertical vorticity over all the wake vortices should equal to zero. Vortices with opposite sign of ω_z should therefore appear one by one, or two by two, so that the number of $\omega_z > 0$ vortices equals the number of $\omega_z < 0$ vortices.

Next, streamlines with approach at different lateral distance from the pipe are analysed (figure 7.41) in relation with the different structures. An iso surface is plotted at ω_z=$\pm$0.5 s^{-1} (red and blue). Here, ω_z is used to identify the structures in order to focus on the vertically oriented wake vortices and their

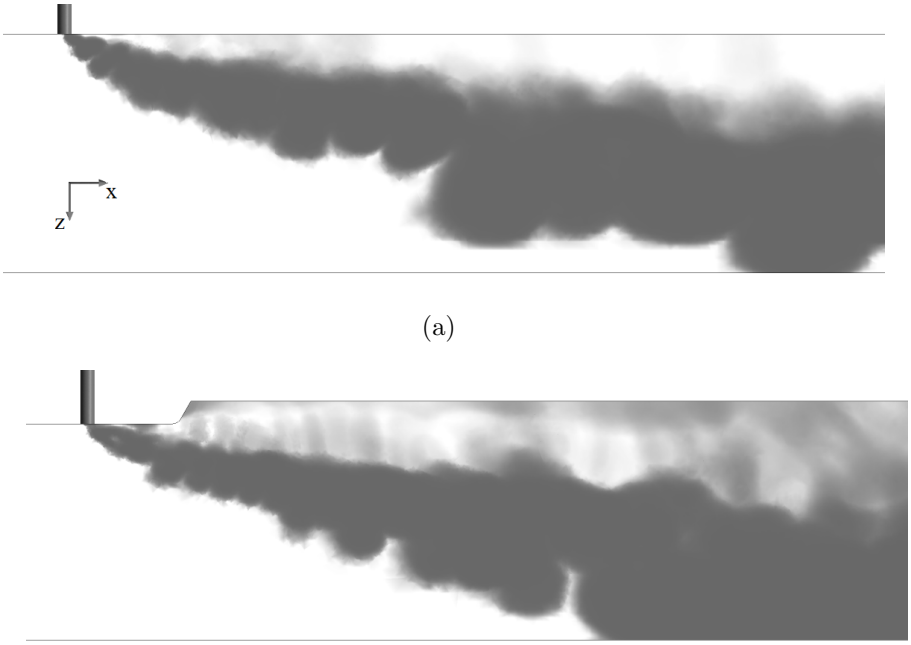

(a)

(b)

Figure 7.39: Instantaneous sediment concentration, transparent for $C < 10^{-7}$, opaque for $C > 5 \cdot 10^{-2}$. Case A1 without wall step (a) and Case B1 with (b) wall step, illustrating the effect of the wall step on sediment drawn into the wake vortices.

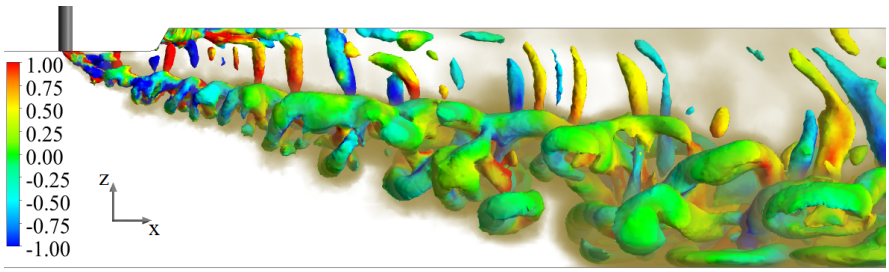

Figure 7.40: Case B1: Isosurface at Q invariant equal to $0.05s^{-2}$, showing different types of turbulent structures in the solution. Colouring by ω_z. Brown transparent shades indicate the instantaneous sediment concentration field.

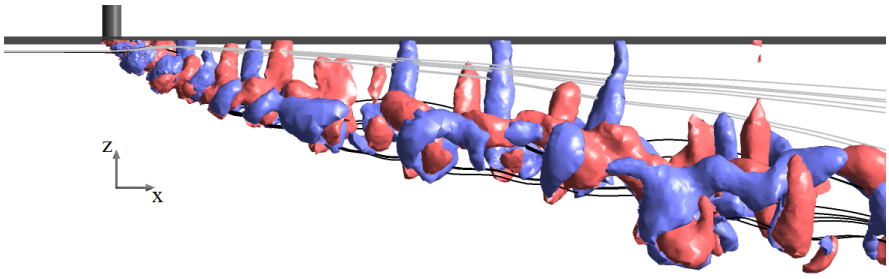

Figure 7.41: Case A1: Isosurfaces of vertical vorticity ω_z equal to -0.5 s^{-1} (blue) and +0.5 s^{-1} (red). Streamlines originating close to the flat wall and at distance 0.5< $|y|/D$ <0.8 from the symmetry plane (black) and at distance 1.0< $|y|/D$ <1.3 from the symmetry plane (grey).

rotation direction. In the wake of the plume, the upright, tube-like structures are appearing. Note that they can reach the wall due to the free-slip treatment at the water surface downstream of the jet release point. Positive and negative vertical vorticity structures alternate. However, Kelso *et al.* (1996) found that these vortices can also appear in pairs of equal ω_z-sign, forming mushroom-like structures. In figure 7.41, streamlines originate at short distance below the flat wall. Streamlines in black originate at 0.5< $|y|/D$ <0.8 while the grey streamlines at 1.0< $|y|/D$ <1.3, so at greater lateral distance from the pipe. It can be observed that the streamlines passing at small distance from the pipe exit are drawn in the CRVP circulation. The streamlines approaching at distance greater than one pipe diameter from the symmetry plane are bent around the plume and participate in the vortex street in the wake of the plume.

As such, the cylindrical wake vortex cores have the potential to influence the sediment distribution. These cores can also be clearly identified in figure 7.42, where the Q invariant at the centerplane is shown. Figure 7.42a shows case A0, without wall step, while figure 7.42b shows the same plume with wall step (Case B0). The circular structures at the upstream end of the plume have a vorticity vector in Y-direction and can be identified as the convection cells discussed above. The vertical structures above the plume have a vertically oriented vorticity vector and are linked with vortices in the wake. Note that these features were also present in the experiment, causing the plumes to meander in some cases. The relation between the presence of wake vortices and sediment-laden patches is analysed. When the Q invariant contours are plotted at a horizontal plane at z/D=1, combined with sediment concentration at the same plane (figure 7.43), the correlation between both

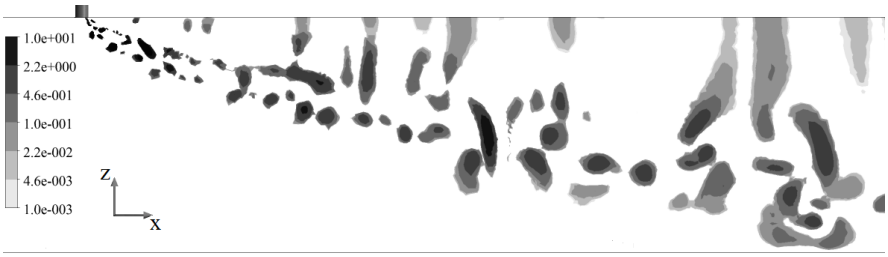

(a)

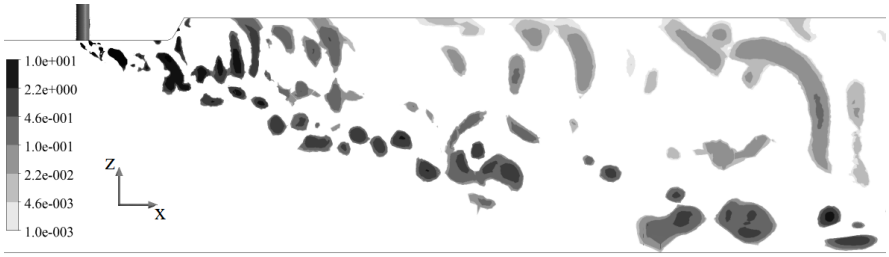

(b)

Figure 7.42: Q invariant (s^{-2}) at the centerplane, in a plume simulation without (a) and with (b) backward facing step, and equal settings otherwise.

becomes clear. The vortices draw sediment from the plume due to secondary currents in the meandering flow field caused by the wake vortex street. In figure 7.42b it can be observed that the Q invariant of the wake vortices first increase and than decreases downstream of the wall step. In the case without wall step the swirls are advected downstream, but stay relatively strong. The reattachment of the streamlines behind the hull stern seems to stretch the swirls up to the surface, thereby experiencing an increase in Q invariant in the core. Further downstream these vortices break up. This effect is causing more sediment to be lifted above the plume.

7.5.4.2 Effect of a wall step on the mean flow

Four plumes with different λ and F_Δ have been simulated with and without wall step (cases B0-B3 in table 7.1). The influence of a wall step on the main trajectory of the plume depends largely on the distance of the plume's centreline from the wall when approaching the wall step ($\overline{z}(x_{ws})$). As was found in the analysis of the experimental data in section 6.5.1. In general, the trajectory of the plume is significantly drawn towards the wall step if

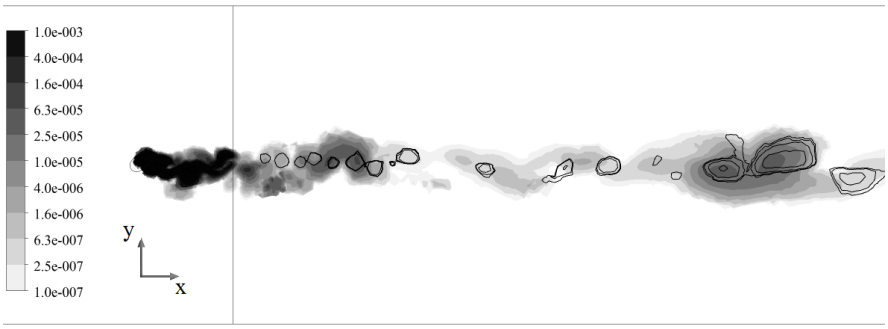

Figure 7.43: Isolines of Q invariant (s^{-2}) and sediment volume concentration c, shading at a horizontal plane located at z=-D in Case B1.

$$|\overline{z}(x_{ws})| < H_{ws}. \tag{7.47}$$

An example of this behaviour is given in figure 7.44. Compared to cases without step, the plume trajectory begins to deviate just downstream of the wall step. It keeps shifting away from the results of the case without wall step over a streamwise distance of about $8H_{ws}$. Further downstream, the plumes in both cases follow parallel trajectories in the far field. It seems the interaction between a wall step and the CRVP structure is determining the behaviour.

In figure 7.45, contour bands of ω_x are drawn at two planes with normal along the crossflow direction (for case B2). This case has a very low jet-to-crossflow velocity ratio (λ=0.17), causing a plume close to the flat wall and higher influence of the wall step. The contours are drawn at vertical planes up- and downstream of the wall step (indicated in yellow). Lines indicate where the different planes and walls intersect with the z=0 plane (blue lines), and with the symmetry plane (red lines). Here, ω_x is the x-component of the curl of the time-averaged velocity field, indicating the position and extent of the CRVP. The smaller values of ω_x are blanked to remove weaker circulations and bring foreward the CRVP signature. In this way, the position of the time-averaged CRVP can be clearly seen. It can be seen that upstream of the wall step the CRVP is located near the wall, having a compact shape. Downstream of the wall step the shape of the CRVP has been stretched towards the water surface by flow expansion in the wake of the wall step. The arrows indicate the rotational direction of the CRVP. It can be seen that, downstream of the wall step, the stretched CRVP induces transport towards the water surface. In a laterally uniform wall step step flow without plume, reattachment of the

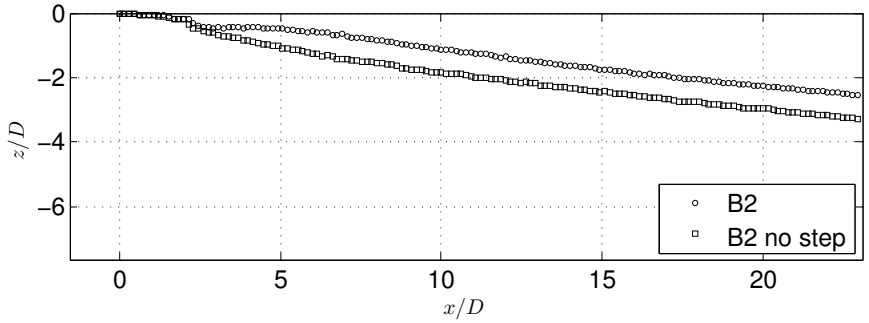

Figure 7.44: Trajectories of simulations of plumes in relatively strong cross flow. One case with wall step (B2), and exactly the same plume without wall step.

streamlines is expected at about 7 times the step height downstream of the step, due to turbulent diffusion of momentum. The present analysis shows that in the wall step wake, apart from turbulent diffusion, also the CRVP plays a role in the sediment transport towards the water surface.

As shown higher in this chapter (figure 7.36a), also plumes with trajectory further from the wall (high λ and/or low F_Δ) are influenced by the wall step, approximately in case

$$|\overline{z}(x_{ws}) + b_t(x_{ws})| < H_{ws}. \tag{7.48}$$

Where $b_t(x_{ws})$ is the half-width of the plume on the wake side of the trajectory ($S_y(\bar{z} + b_t)$=$0.5S_y(\bar{z})$). The downstream fringes of the plume are thus experiencing wall step induced mixing if they are within a distance H_{ws} from the wall at the position of the wall step. In figure 7.46, the centreplane particle concentration at small distance from the flat wall (z/D=-0.3 below release pipe) is shown for cases with and without wall step.

The wall step Reynolds number $Re_b = U_0 H_{ws}/\nu$ is based on the value of U_0, while the wake of the plume causes a drop in the centerplane streamwise velocity U at the wall step. However, depending on the jet wake Reynolds number Re_w ($=U_0 D/\nu$) and λ, the streamwise length of the wake is about $3D$ to $5D$. Note that this is shorter than for a cylinder wake. Indeed, the flow on the lee side of the jet exit is in essence not a wake, see Kelso *et al.* (1996). The wall step Reynolds number Re_b should therefore be representative for the flow with interaction between plume and wall step. With Re_b between 2530 and 5500, all step wakes in the study are turbulent. For the studied cases, the wall step modifies the turbulent structure of the flow at about 15 to 16 times the step height downstream of the step. However, streamline

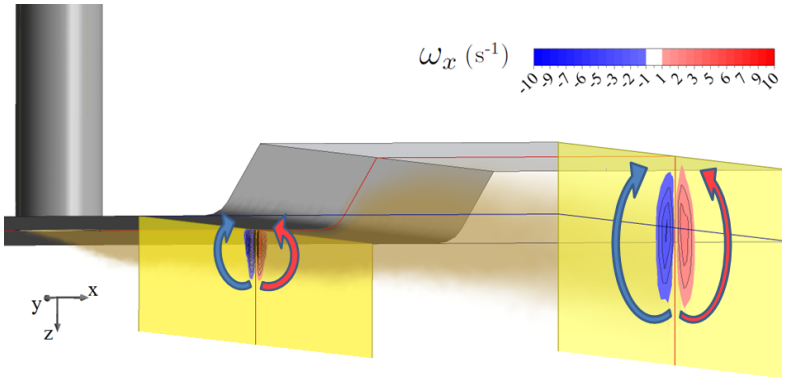

Figure 7.45: Case B2: Contour bands of ω_x (s^{-1}) of the time-averaged velocity field, upstream (left contours) and downstream (right contours) of the wall step. The ω_x contours are plotted on planes normal to the cross flow direction and represent the location of the time-averaged CRVP. Arrows indicate the rotational direction of the vortex pairs. Lines indicate where the different planes and walls intersect with the z=0 plane (blue lines), and with the symmetry plane (red lines). Brown shades indicate the extent of the time-averaged sediment plume.

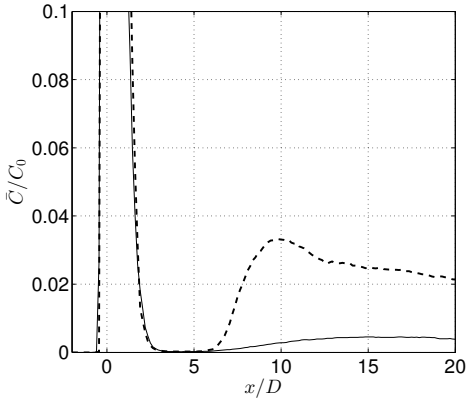

Figure 7.46: Horizontal profiles of centreplane particle concentration at $z/D = -0.3$. Case without step (A0) shown in full line, case with step (B0) shown in dashed line.

reattachment at the centerplane occurs at a distance of 4 to 5 step heights, which is relatively close compared to undisturbed wall step wakes (Armaly *et al.*, 1983; Kaltenbach, 2004). This might be explained by the secondary flow induced by the CRVP interacting with the wall step wake. In regions above the plume, the flow approaches the wall step under an angle with the centerplane. The study by Kaltenbach (2004) shows that the streamline reattachment length downstream of a wall step at a 50° angle with the main flow (rather than the typical 90°) reduces to 5.5 step heights, which further supports this assumption. Additionally, the flow is pushed towards the wall since the CRVP secondary flow adds a vertical component to the flow near the wall step.

In figure 7.47a, the $\overline{u'w'}$ Reynolds stress component along a horizontal line at $z/D = 0.3$ and $y = 0$ is plotted, for two cases with and without wall step. For both cases, $\lambda = 2.58$ and $F_\Delta = 9.09$. The dashed line shows the Reynolds stress for the case with wall step, the full line for the case without. The peaks associated with the exit are not shown due to reduced x-axis limits, to bring foreward the scales in the wake. The hidden peaks amount to $|\overline{u'w'}|/U_0^2 \approx 0.1$, which corresponds well with vertical plume measurements by Dai *et al.* (1995). Note that the wall downstream of the wall step is the free surface and modelled with a free slip condition, hence the asymptote to zero. It can be seen that between $x/D = 6$ and x/D=16 a jump in $\overline{u'w'}$ from negative to substantially positive is caused by the wall step. This indicates induction of vertical diffusion of horizontal momentum, which affects the vertical diffusion of sediment in the plume passing by underneath. In the present case, without wall step, the sediment concentration amounts to about $C/C_0 = 5{\cdot}10^{-3}$ at $z/D = 0.3$. Albeit a relatively small value, it can be important in plume dispersion. However, when a wall step is present, the value of C/C_0 at $z/\lambda D$=0.1 in the wall step wake peaks at $3.5{\cdot}10^{-2}$, a factor 7 higher (figure 7.46). The strong increase (factor 25 larger) in upward sediment diffusion is also reflected in the $\overline{c'w'}$ term (figure 7.47b). The c'_{rms} term peak value (not shown) displays a fivefold increase at $z/D = 0.3$.

7.5.4.3 Behaviour of the subgrid-scale model

The Smagorinsky coefficient should not be a constant, as reflected in the dynamic procedure by Germano *et al.* (1991), applied in this work. The dynamic Smagorinsky coefficient should be dependent on the local ratio of the filter width Δ to the Kolmogorov scale η (Meyers and Sagaut, 2006). Also, the Smagorinsky coefficient C_s should be a function of the relative

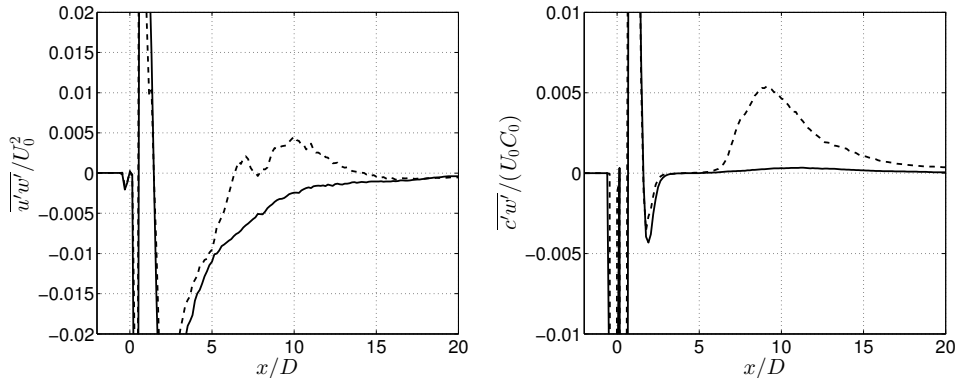

Figure 7.47: Impact of a wall step on the $\overline{u'w'}$ (a) and $\overline{c'w'}$ (b) in the wake of the plume. Profiles along the x direction at z/D = -0.3 and y=0. Case A0 without step (full line) is compared with case B0 with step (dashed line).

importance of the subgrid dissipation to the total dissipation. This so-called subgrid activity (Celik *et al.*, 2005) is thus defined as follows

$$s = \frac{\varepsilon_t}{\varepsilon} = \frac{\varepsilon_t}{\varepsilon_t + \varepsilon_\mu} \tag{7.49}$$

where ε_t is the subgrid-scale turbulent dissipation, ε_μ is the viscous dissipation and ε is the total dissipation.

Celik *et al.* (2005) showed that, by expressing ε_t in terms of the turbulent viscosity ν_t and substituting in the Smagorinsky formulation for ν_t, it can be shown that

$$s \cong \frac{\nu_t}{\nu_t + \nu} \tag{7.50}$$

where ν is the molecular diffusion.

For infinite Reynolds numbers, s=1 corresponds to an LES, while s=0 to a DNS.
Meyers and Sagaut (2006) determined a theoretical solution for the evolution of C_s with the subgrid activity. It shows that the Smagorinsky coefficient should go to zero when s goes to zero. It also showed that when s goes to 1, C_s goes to a value of about 0.17. Hence the limiter of $C_s \leq 0.17$ applied in the currently presented simulations.

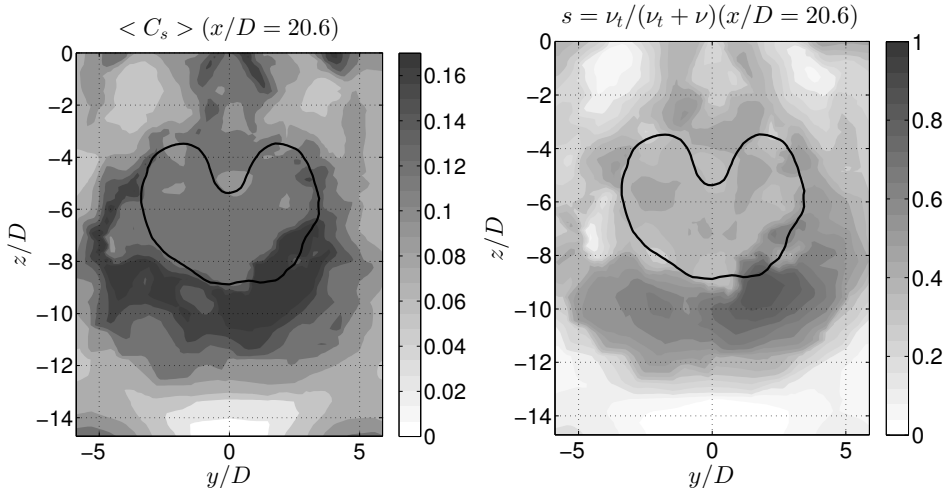

Figure 7.48: C_s and s at x/D=20.6 in a plume in crossflow simulation, contour of C/C_{max}=0.4 shown in black.

In figure 7.48, both the dynamic value of C_s and the subgrid activity s are shown, from a simulation of a sediment plume in crossflow. A vertical cross section of the plume is shown at x/D=20.6. The contour where C/C_{max}=0.4 is shown in black. C_s ranges from 0 to 0.17, while s ranges from 0 to 0.9. Both C_s and s have higher values just below the main plume. This can be explained by the fact that the mesh is less refined in that region, while still a certain amount of strain is present. Also, near the wake of the plume itself, an increases value of C_s and s can be found (-1< y/D <1 and -2< z/D <0).

Also the ratio of grid filter width Δ to Kolmogorov length scale η should be related to C_s. The (simulated) Kolmogorov scales are plotted in figure 7.49. In this simulation, the Kolmogorov length scale at which viscous dissipation begins is about 1 mm inside the plume. Time and velocity scales are t_η=1 s and u_η1 mm/s respectively. This indicates the Kolmogorov turbulent scales are small and have relatively small rotational velocity. The ratio Δ/η is shown in figure 7.50a. The shape of the profile is not as similar to the profile of C_s, compared to the profile of s. However, the main pattern is found back, more specifically the increased values below the plume. Values of Δ/η between 5 and 10 are found, indicating that the grid size is 1 to 4 times higher than in a DNS. It must be noted that η is computed based on the dissipation, which is also simulated and thus not exact.

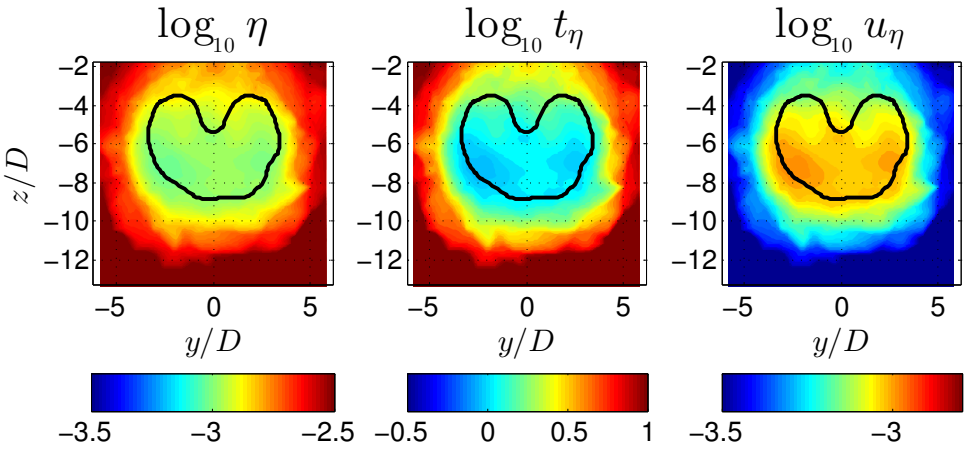

Figure 7.49: Computed Kolmogorov length, time and velocity scales.

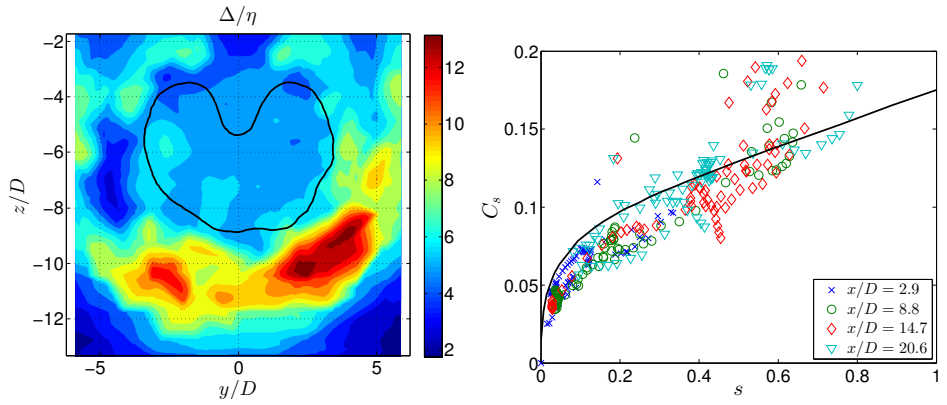

Figure 7.50: (a): Ratio Δ/η at x/D=20.6 in a plume in crossflow simulation, contour of C/C_{max}=0.4 shown in black. In figure (b), a scatter plot of C_s and s at different x/D is shown. The theoretical solution from Meyers and Sagaut (2006) is shown by the black line.

When the subgrid activity s is plotted against C_s for the current LES simulations (figure 7.50b), it can indeed be found that C_s goes to zero for s going to zero using the dynamic procedure by Germano *et al.* (1991). The theoretical derivation of the relation between C_s and s as found by Meyers and Sagaut (2006) is shown in black. The currently presented simulations show a behaviour very similar to that theoretical solution. It can be seen that for increasing distance from the pipe (x/D), the subgrid activity s increases. This is logical since the grid cell size is increasing with increasing distance x. For the analysed section close to the plume release (x/D=2.9), s ranges from 0.01 to 0.4.

7.5.4.4 LES compared to RANS

Since it is anticipated that the interaction between an individual eddy and the stern can be important in the generation of surface plumes, LES has been used. In order to verify whether a large difference is effectively found between both approaches for turbulence modelling, a comparison is made between LES results for case B1 and a RANS solution. The RANS solution has been executed on the same grid, with a realiseable k-ε model and the mixture model with drift flux term for the sediment. The turbulent Schmidt number was set to Sc_t=1, in line with the findings from the experiments.

Qualitatively, the RANS-plume (figure 7.51a) can be compared with figure 7.39b, and with the time-averaged LES-plume in figure 7.51b. The RANS plume seems to be located somewhat higher compared to the time-averaged LES-plume. Also, a difference can be observed between the secondary plumes, above the main plume and formed due to wake vortices of the plume itself and the wall step. It can be seen that the secondary plume in the RANS case is more concentrated compared to the LES case. This is possibly related to the turbulence destruction due to the work done by eddies taking more dense plume material upward. This is explicitly solved in the LES model, while it has to be modelled with a buoyancy destruction term in the k-ε model.

When comparing horizontal and vertical profiles of the time-averaged sediment concentration, it can be confirmed that the RANS plume is located higher and that the surface concentration is higher in the RANS case (figure 7.52a). The horizontal profiles in figure 7.52b are more comparable, but again the increased value for C/C_0 in the RANS solution surface plume can be seen at $z/\lambda D$=-2 and 5< x/D <10.

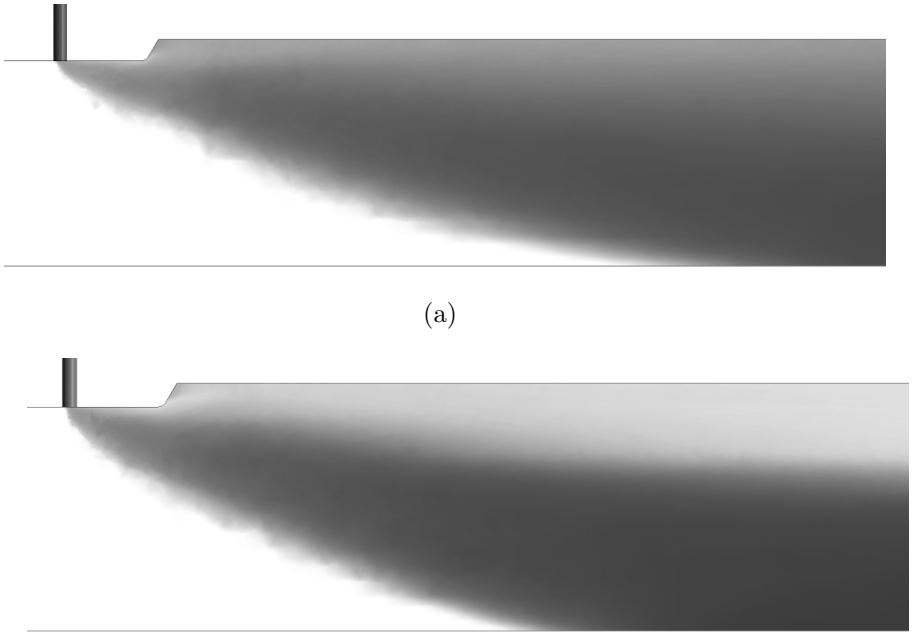

(a)

(b)

Figure 7.51: Time-averaged sediment concentration, transparent for $C < 10^{-7}$, opaque for $C > 5 \cdot 10^{-2}$. Case B1 with RANS solution (a) and with LES solution (b).

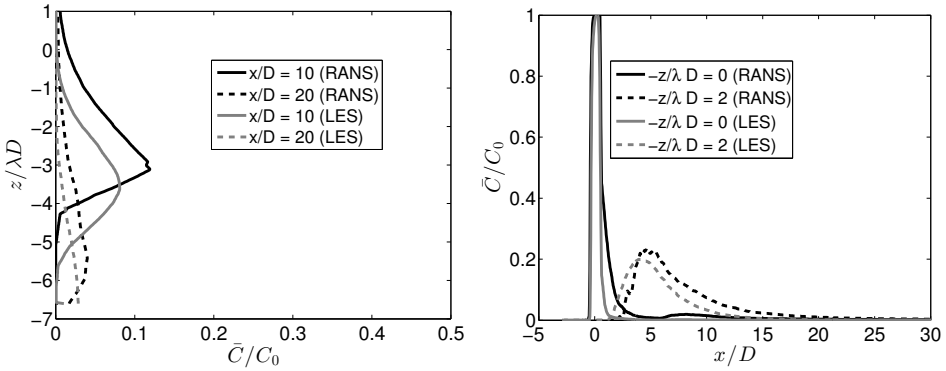

(a) (b)

Figure 7.52: Comparison of the vertical (a) and horizontal (b) profiles of C/C_0 from the RANS and LES simulations.

7.6 Conclusions on lab-scale LES model

The multiphase LES model with a mixture model approach for the dispersed phase has been validated against experiments by the author and by other authors. The objective was to develop a numerical model capable of simulating the plume trajectory and turbulent dispersion properly in time and in three spatial dimensions. The LES model was designed to execute simulations with acceptable processing times so that the upscaling from laboratory to prototype scale (chapter 8) becomes possible, as well as implementation of a realistic dredging vessel geometry. The LES model proved to be rather complete in resolving turbulent structures. Up to 97 % of the turbulent kinetic energy was resolved on the numerical mesh. A sound turbulent energy cascade with -5/3 law was found for turbulent structures between 5 and 20 grid cells large. Even though LES has limitations in the vicinity of walls, the correct behaviour was found in terms of well-known turbulent structures.

The multiphase aspect of the water-sediment mixture was characterised by a small relative velocity, due to the small particle Stokes number. A vertical plume case showed that the velocity and concentration profile widths are roughly equal, showing the bulk turbulent Schmidt number (often used in RANS simulations) was around one, which is a generally accepted value.

The influence of the wake of the schematised vessel's hull from which the plume was released was investigated. The outer fringes of a plume being torn off by the mechanisms described in this chapter might have a dilution factor of 100 or higher compared to the source concentration C_0. Therefore buoyancy no longer does any work in moving these clouds away from the release elevation, they are advected by the ambient flow. In practical plume dispersion situations such as dredging plumes and exhaust plumes this is often an adverse effect. In the case of dredging plumes, these turbidity patches no longer take part in the convective descent towards the sea bed, but are being transported through estuaries or regional seas in large passive plumes. In the far field part of dreding plumes, small particle concentrations can be harmful for environmentally sensitive areas. It is therefore of great importance to include in a modelling effort the instantaneous turbulent structures with potential to create secondary plumes, in turn giving rise to long-range passive plumes. In this chapter, it was shown that the vertical distance between plume and vessel stern is determining the amount of particles drawn towards the surface. The horizontal distance between the overflow pipe and the stern of the dredging vessel will therefore have an impact on the amount

of turbidity generated in many cases. While studying environmental impacts of plumes, these considerations need to be taken into account.

The simulation of the behaviour of a third phase (air bubbles) was validated by comparison with laboratory experiments by (Zhang, 2012; Zhang and Zhu, 2013). It was shown that the Lagrangian approach including coalescence reproduces the air bubble plume in a crossflow with reasonable accuracy.

In general, it can be concluded that an LES model with a number of cells that can be handled in practical situations is able to resolve the important turbulent structures. It is shown that two-phase LES with sediment transport can produce results with similar accuracy compared to DNS simulations which use a number of cells one or two orders of magnitude larger. Plume trajectories as well as the upper and lower extent of the plume is proved to be modelled accurately by the LES model. The major turbulent structures responsible for the dispersion of the particulate material are simulated correcly and the turbulent fluxes are of reasonable accuracy.

The consequence is that the presented type of LES simulations can be upscaled and used for practical environmental impact assessment studies, provided the upscaling operation does not cause violation of the LES completeness criterium. This will be further investigated in more detail in the next chapter.

Chapter 8

LES model at prototype scale

A condensed version of sections 8.3 and 8.6 in this chapter have been published in Decrop et al. *(2014).*

8.1 Introduction

After the CFD model on laboratory scale was validated, the challenge remains of demonstrating that the model stays accurate when the Reynolds number of the plume is increased with a factor 100. It will be the goal to keep the same accuracy in a full-scale simulation with a similar number of grid cells compared to the laboratory-scale model.

In this chapter on the prototype-scale CFD simulations, first a validation of the Reynolds independency is executed (section 8.2) as well as a validation against some relevant benchmark cases (section 8.4). Later, the geometry of an actual TSHD is implemented in the model domain and the propeller jets are included (section 8.3).

The prototype-scale model will then be validated by comparison with in situ measurements in an overflow plume at sea, collected during this research project(section 8.6).

Afterwards, a sensitivity study of the boundary conditions acting on the overflow plume is executed (section 8.7).

8.2 Validation of LES upscaling

Even though many ship design optimization studies are executed on towing tank scale, many authors agree that simulations of ship hydrodynamics should be carried out at full scale since scale effects are unavoidable (Visonneau *et al.*, 2006; Zorn *et al.*, 2006). Naturally, a step in reaching a validated model of a full-scale dredging plume simulation is the upsizing from laboratory scale ($\mathrm{Re_p} \approx 10^4$) to prototype scale ($\mathrm{Re_p} \approx 10^6$).

Two methods will be used to verify the accuracy and soundness of the LES results after migration to a prototype scale. First it will be checked whether the plume trajectories coincide after applying the proper scaling, as defined by Fischer (1979), see also table 6.2.

Secondly, the completeness of the LES after upscaling will be verified using Pope's criterion (Pope, 2004). The so-called turbulence resolution M (eq. 7.37) has to be maintained at levels of at least 0.8.

8.2.1 Dynamic scaling

Obviously, no experimental data is available for comparison with the high-Reynolds number flow. After resizing the laboratory scale model to prototype dimensions, while keeping identical geometry and number of grid points, the performance can be evaluated by dynamic scaling of the trajectories. When applying the appropriate similarity laws for buoyant plumes, the trajectories of plumes of different Reynolds number should coincide, given the fact that they own dynamically equivalent properties, namely the densimetric Froude number F_Δ and the velocity ratio λ. The scaling of the horizontal and vertical coordinates can be done using the characteristic length scales for buoyant jets: l_M, z_M, z_B and z_C. The scaling is done according to the equations used for the comparison of the experimental plumes (eq's 6.12-6.13).

For the mean flow properties and turbulence statistics to converge, a sufficiently long period of time needs to be simulated. The small-scale simulations were simulated for about 500 dimensionless time units $t_* = t(U_0/D)$. Cross-flow velocity U_0 (here the vector sum of ambient currents and vessel speed) increased by about a factor 10 in the prototype simulations. Pipe diameter D roughly by a factor 100. This means the simulation time should be increased with a factor 10 to obtain t_*=500. The velocity scales increase by a

factor 10 and the grid size by a factor 100. This implies that the time step can be increased by a factor 10 to keep the same CFL number. Thus, both the simulation time and the time step should be increased by a factor 10, by consequence the number of time steps to compute stays the same. In the full-scale simulations time-averaged flow properties U_i and C converged after about 5000 time steps, while the Reynolds stresses take the most time steps to converge, about 8000.

8.2.2 Self-similarity of scaled plume trajectories

In this work, the question is answered whether succesfull laboratory-scale LES simulations can be upscaled to prototype-scale LES in an accurate way without increasing the number of cells drastically. The plume in crossflow case is well suited to study the validity of upscaled LES simulations, since appropriate scaling laws can be invoked to compare small scale and prototype scale simulations.

After simulation of dynamically equivalent plumes with a two orders of magnitude increase in Reynolds number compared to the experiment, the scaled trajectories were compared (figure 8.1). The laterally integrated sediment concentration S_y (eq. 7.33) is shown in grey color scale for the large-scale simulations at $\mathrm{Re_p}$=1.9 x 10^6 (top) and $\mathrm{Re_p}$=4.5 x 10^6 (lower panel). The green line represents the large-scale simulated trajectory based on S_y. The red circles show the trajectory of the small-scale plumes, the red diamonds the top and bottom extent. It can be seen that both the top and bottom extent of the large-scale plume as well as the trajectory correspond well with the small-scale experiments ($\mathrm{Re_p}$=4,000 (top) and $\mathrm{Re_p}$=12,000 (lower panel)).

The accuracy of the LES simulations with the Dynamic Smagorinsky subgrid-scale model can therefore be considered as Reynolds-independent for the plume trajectories.

8.2.3 Turbulent Structure

Since the LES method is selected to resolve individual large eddies which are important for the mixing behaviour of the plumes, also the turbulent structure should be preserved in the large-Reynolds simulations. In figure 8.2, the internal structure of C is shown for simulations at $\mathrm{Re_p}$=4,000 and at $\mathrm{Re_p}$=1.9 x 10^6. It can be observed that the structure with a double peak has

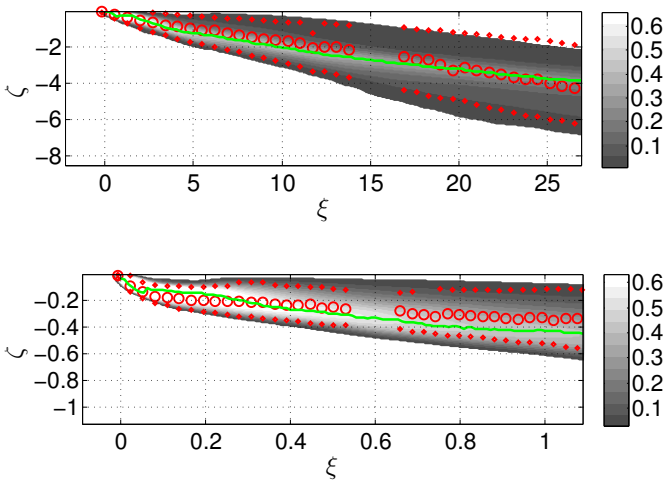

Figure 8.1: Comparison of scaled experimental plume trajectories at $\mathrm{Re_p}$*=4,000 (top panel) and* $\mathrm{Re_p}$*=12,000 (lower panel) with large-scale LES simulations at* $\mathrm{Re_p}$*=1.9 x* 10^6 *(top) and* $\mathrm{Re_p}$*=4.5 x* 10^6 *(lower panel). Large-scale simulations presented in grey color scale of* S_y *and centerline in green. Small-scale experimental trajectories in red circles and upper and lower extent in red diamonds.*

the same shape. The peak values of the self-similar variables differ, however, with a factor 2.

8.2.4 Turbulence resolution

Due to the increase in grid cell size and the higher Reynolds number, the percentage of resolved turbulent kinetic energy drops. In the small-scale simulations, the turbulence resolution M was between 0.90 and 0.99. In the large-scale simulations M drops to 0.8 to 0.9. Especially near the point where the crossflow meets the plume, M is lower. However, it was found that the resolved turbulent motions still accounted for more than 80% of the total TKE at all locations in the domain, which is considered sufficient. In figure 8.3, the average resolved TKE is compared with the average subgrid-scale TKE, as a function of the distance from the plume exit. The TKE is normalised with the square of the crossflow velocity U_0. The TKE is in general an order of magnitude lower at x=30D downstream of the pipe compared to x=2D. At all locations, the resolved TKE k_{res} is two orders of magnitude higher than the subgrid-scale TKE k_{sgs}.

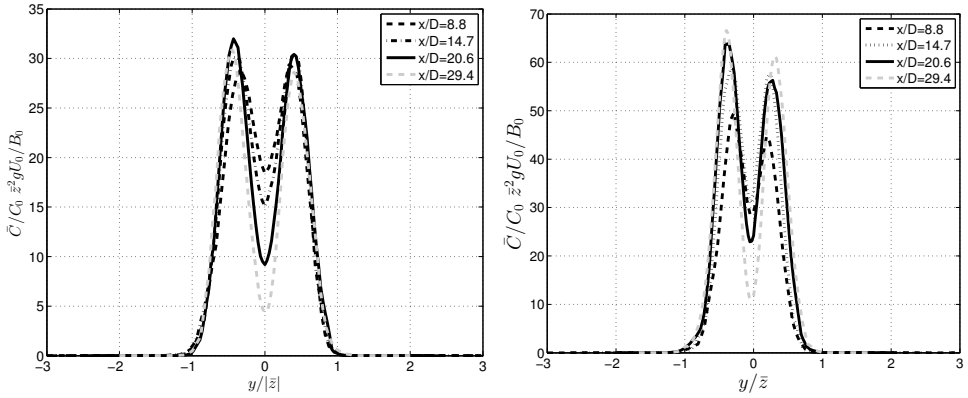

(a) (b)

Figure 8.2: Internal structure of C in small-scale LES at $\mathrm{Re_p}$*=4,000 (a) and at large-scale LES simulations at* $\mathrm{Re_p}$*=1.9 x 10^6 (b).*

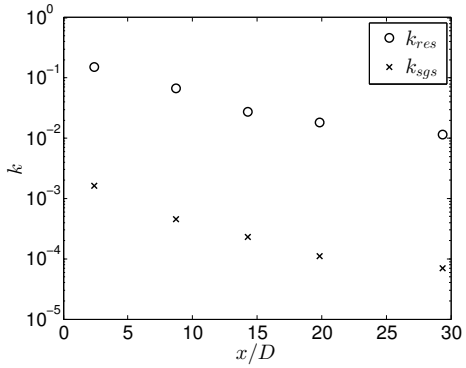

Figure 8.3: Normalised TKE k/U_0^2 *as a function of the distance from the pipe. Comparison of the resolved scales (*k_{res}*) and the subgrid scales (*k_{sgs}*).*

The spectral footprint of the resolved turbulence (not shown) still shows a region in which the turbulent energy decays with the -5/3 power law. In the range of scales corresponding with 5 to 30 grid cells, this law is found for the 3 velocity components U, V, W and for the sediment concentration C.

8.2.5 Conclusion

After scaling the grid of the experimental-scale simulations to a prototype scale, using the appropriate horizontal and vertical scale factors, the LES simulations were carried out again. In this operation the Reynolds number increased approximately two orders of magnitude. It was shown that the scaled trajectories still coincide well with the measured trajectories and that the turbulence resolution and turbulence frequency spectra are still sound.

8.3 Realistic TSHD Model setup

8.3.1 Introduction

After veryfying the LES model accuracy after upscaling, the next step can be taken. In this section, the setup of the LES model for realistic cases is described. A real-world dredging vessel geometry will be implemented in the grid and the jets resulting from the propellers are incorporated. The effect of air bubbles is taken into account through the discrete phase model.

8.3.2 Model formulation

The LES model formulation adopted is exactly the same as for the small-scale simulations and for the upscaling tests, see section 7.2. An additional feature is foreseen to account for the propeller jets: an actuator disk with a spatially varying pressure jump.

8.3.3 Model domain and numerical solution

The LES model at prototype scale was built using identical formulations and numerical settings as used for the validated laboratory-scale model, with the addition of a realistic TSHD vessel geometry, actuator disks for the propellers and air bubble transport.

The model equations are solved using the Ansys Fluent 14.5 code, on an unstructured grid in which specific refinements are foreseen for regions of high strain (near ship walls, overflow wall, flow approaching bow, propeller jets) and expected high sediment concentration. The advantage of using this software over other options is the availability of unstructured grids. This type of grids allow following the shape of a ship hull accurately. Detailed views of the geometry of the vessel and the unstructured surface mesh are shown in figure 8.4. The propellers, propeller shafts and rudders have been removed from the geometry.

Unstructured grids also allow refinements in regions of interest or regions of strong gradients. The regions of high concentration are obtained from initial steady-state RANS calculations. An example of a slice of the grid along the symmetry plane is given in figure 8.5.

The coordinate system origin is located where the axis of the overflow shaft crosses the plane of the vessel keel. The x-coordinate is positive along the vessel symmetry plane towards the stern; the z-coordinate is pointing to zenith. The domain for the main simulations extends from 0.5 ship lengths (L_s) in front of the bow to $3L_s$ downstream of the overflow shaft. Laterally, the domain extends 1.2 ship lengths at either side. An overflow shaft section with a length of 5 pipe diameters is included in the computational domain. Inside the shaft mesh, local refinements are foreseen near the wall to resolve the pipe flow velocity profile starting from a first cell in the log layer at $y^+ = y_n u_*/\nu$=300-2000, depending on the case. Here, y_n is the wall-normal distance from the wall, u_* is the shear velocity and ν is the kinematic viscosity of the sea water. Away from the wall, a mesh size of $D/20$ is used in the overflow shaft, where D is the overflow shaft diameter. Below the keel of the vessel, in the first two pipe diameters from the overflow exit, the mesh resolution increases from $D/20$ to $D/10$. At a distance of $4D$ from the exit, the resolution is $D/4$. In this way, a sufficient representation is obtained of the hull boundary layer velocity profile -which determines the crossflow attack on the plume directly after the exit. Wall y^+-values between 80 and 9000 are obtained at the hull, depending on the location and case. These are all in the log layer and can thus be approximated by the logarithmic law-of-the-wall.

The surface meshing at the hull of the vessel is based on triangles with maximum edge size of $L_s/100$, where a curvature refining algorithm forces refinements at locations where the hull shape is curved. For example, the areas near the fins and propeller shaft at the stern, the surface mesh is refined to a size of $L_s/400$ (25 cm). The curved area near the bulbous bow has

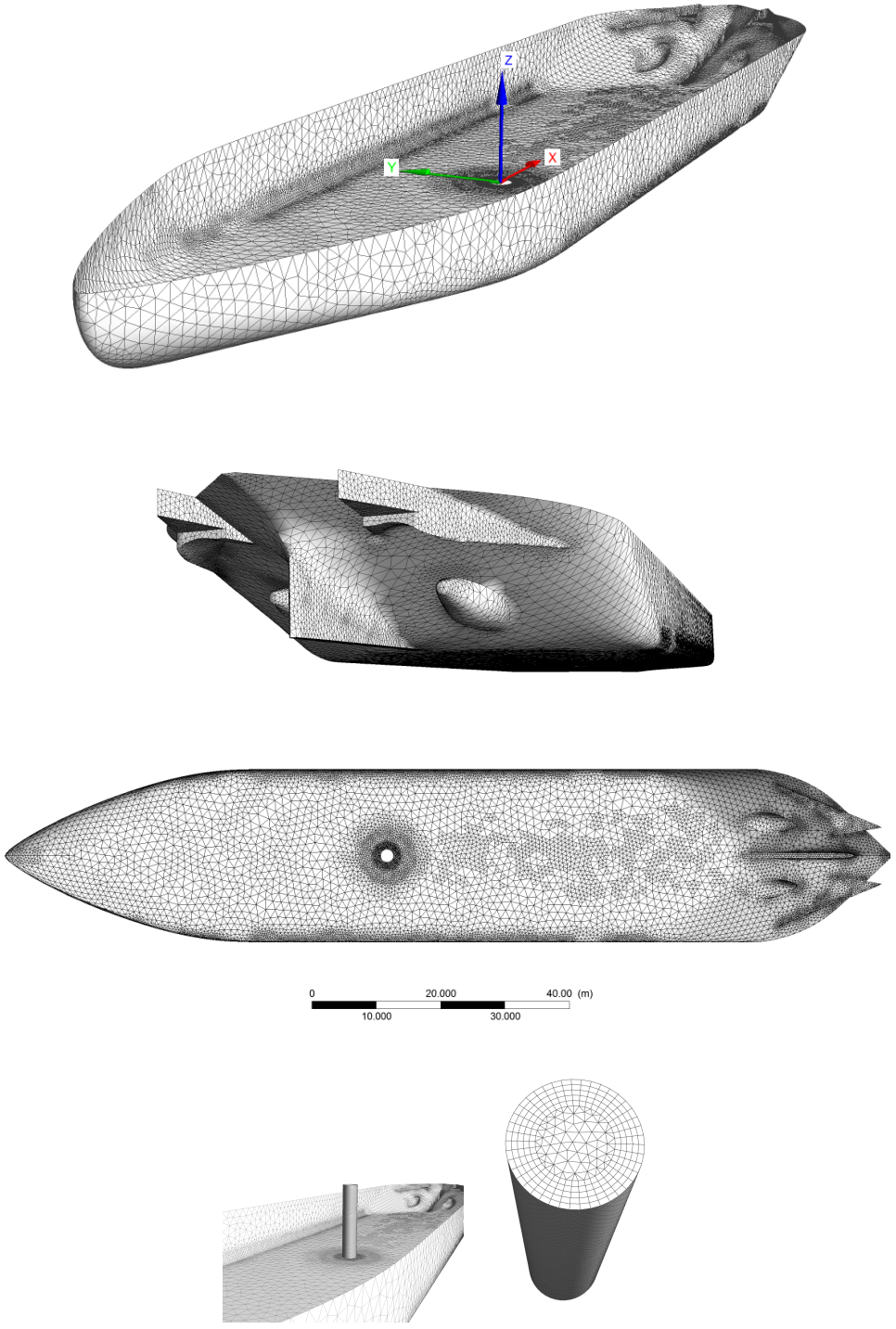

Figure 8.4: Detailed perspective views of the surface mesh forming the TSHD geometry (part below the water surface and overflow shaft). The origin of the coordinate system is located at the plume exit.

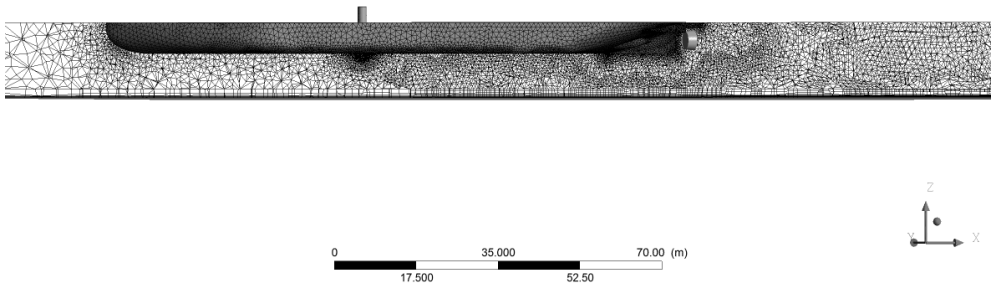

Figure 8.5: Example of an unstructured mesh with realistic TSHD geometry. A slice through the mesh at symmetry plane $y = 0$ is shown. The vessel hull surface mesh is visible with the bow at the left and stern at the right. Local refinements are included at the bow, plume exit, at hull curvature regions upstream of the propeller intake and in zones to be occupied by the plume.

a surface mesh of about $L_s/200$. At increasing distance from the hull, the mesh size is gradually increased with a growth rate of 1.2, to reach a size of about $1D$ at a distance of 30 m from the hull. Near the sea bed, grid layers with increasing thickness are placed parallel to the bed in order to represent the boundary layer at the sea bed. The first layer above the seabed has a thickness of 0.2 m, five layers are defined with wall-normal mesh size growth rate of 1.6, leading to a boundary layer mesh with a thickness of about 3 m. This is not sufficient to resolve ambient turbulence at the sea boundary. It is assumed, however, that the highly concentrated sediment jet disturbs the seabed boundary layer to a large extent. The turbulence generated by the plume in a strong crossflow is much stronger compared to the seabed turbulence.

The collection of mesh resolution rules described above results in an initial mesh, which is relatively coarse away from the vessel. The grid is further refined based on the location of areas where plume material or increased strain rates occur. To obtain these areas, a RANS simulation is performed on the coarse grid. Subsequently, zones in which sediment concentration, strain rate or turbulent kinetic energy are pronounced, the grid is refined. Setting a very low sediment concentration threshold for the definition of the refinement area, combined with a minimum strain rate criterion ensures that even in the time-dependent LES simulations, all zones where turbulent structures of the plume are located are within the refined zone. Additionally, the strain rate criterion allows for additional refinements where the ship-induced

flow velocity gradients are important.

For the spatial discretisation of the integral form of the equations to solve, the finite volume method is used. The finite volume method is the most commonly used method for unstructured grid CFD problems (Versteeg and Malalasekera, 2007). The momentum equations are discretised using the Bounded Central Differencing Scheme (Kim, 2004), while the sediment volume fraction transport equation was discretised using the QUICK scheme (Leonard and Mokhtari, 1990). The pressure-velocity coupling was handled with the PISO algorithm with two pressure correction steps (Issa, 1986).

Time was advanced with a second order implicit scheme and a timestep of 200 milliseconds. The maximum Courant number is found near the plume exit, with a value of about 1.9. This seems rather high for LES calculations, however, at a few meter away from the overflow exit, the Courant number drops rapidly to values below 0.5. At each model run, the simulation was carried out with stationary background flow for a time span equal to the time needed for the flow to travel through the complete length of the model domain (700 m), after which turbulence statistics were reset. Afterwards the model was run for twice that time, while collecting statistics for turbulent quantities. It was found that the time-averaged quantities of the turbulent flow reached equilibrium before the end of the simulation time.

8.3.4 Boundary conditions

The issue of the moving vessel in a static coordinate system is addressed as follows. Since both the current and the dredging vessel have a velocity relative to the sea bed, one would have to use a dynamic mesh in which the vessel moves through the grid and coordinate system of the numerical model. This method is not preferred here since the combination with the internal boundary conditions for the propeller-induced pressure jump could lead to unnecessary interpolation errors. Therefore, the vessel is considered stationary, while the current imposed at the model boundary is the relative velocity of sea water to dredging vessel. This is equal to the vector of the current velocity minus the vector of the vessel velocity. In this way, however, the boundary condition at the sea bed would generate an unrealistic boundary layer because the relative velocity of the flowing water to the sea bed is no longer consistent. To compensate for the unrealistic flow velocity over the sea bed, the sea bed has been defined as a moving wall with a velocity vector equal to the opposite of the vessel velocity vector. In this way, the flow velocity of the vessel relatively to the water is correct, and the flow velocity

of the sea water relatively to the sea bed is also correct, while the model grid can be kept static.
Apart from the moving bottom approach, the boundary conditions are applied in the same way as for the small-scale model. See section 7.3 for a description. The lateral sea boundaries are modelled here as open boundaries with prescribed velocity or as a pressure outlet.

8.3.5 Air bubbles

The initial air bubble concentration at the overflow exit is difficult to measure in the field. An empirical formulation by Ervine (1998) was used to estimate the air bubble concentration resulting from a surface-impinging jet in a shaft. See section 2.5.2 for an analysis of bubble entrainment in typical overflow shafts. It was found that values between 5 and 15% by volume can occur in overflow shaft air entrainment. Fixed values for air bubble volume concentration and initial air bubble diameter were determined in the present work, based on model validation exercises using field data (in section 8.6 below).

Air bubbles generated by the bow wave of the sailing ship were not taken into account. It was shown by Carrica *et al.* (1999) that ship-generated air bubbles mainly occur near the sidewalls of the vessel, and above the level of the keel. These bubbles can therefore be assumed as not of any influence on the behaviour of the plume while it is below the keel of the vessel. When a surface plume develops and interacts with ship-generated air bubbles in the wake of the vessel, the latter bubbles might be of influence. Carrica *et al.* (1999) show, however, that the mean air bubble diameter in the wake (near the level of the keel) is about 50 microns, for which the rising bubbles are in the Stokes regime. This means that the bubbles have a rising velocity of the order of magnitude of 5 mm/s and the bubble wakes do not generate turbulence. This leads us to the assumption that the ship-generated bubbles do not affect the trajectory or turbulent dispersion of a dredging plume.

In large-scale simulations, tracking the path of each individual air bubble is prohibitive. Instead, a number of bubbles with the same properties are collected into a parcel. Subsequently, the position and properties of each parcel are tracked. In a typical dredge plume simulation, at any time between 10^4 and 10^5 parcels are tracked until escaped through the water surface or downstream open boundary.

8.3.6 Approach for propeller jets

The source of momentum and turbulent energy ejected by the two propellers of a TSHD is modelled using the concept of an actuator disk, e.g. Hough and Ordway (1964). Over a disk-shaped internal boundary condition, a pressure jump is imposed. The pressure jump p_d is a function of the propeller power P , disk surface area A_d and the axial velocity at the disk, u_d:

$$p_d = \frac{P}{A_d u_d} \tag{8.1}$$

The propeller velocity is also a function of the power, so that the pressure jump can be derived from the propeller power only. Assuming the approach velocity is small compared to u_d, it can be written as:

$$u_d = \left(\frac{P}{2\rho_m A_d} \right)^{1/3} \tag{8.2}$$

For the engine power while trailing (P, 60% of the full power), a typical average value of the axial propeller jet velocity of 4.3 m/s is found for propellers with radius of 2.1 m. A radially varying profile of axial and tangential velocity components is applied considering the findings of Lam *et al.* (2006, 2010). See section 2.6 for a description. The correct propagation and spreading of the propeller jets in our model will be validated using data of the same authors (in section 8.4.2). In the cone-shaped volume in which the propeller jets are expected to occur, a grid refinement is applied in order to improve the determination of the strong velocity gradients and turbulence intensity related to these jets.

8.3.7 Initial conditions

A separate RANS simulation is performed to provide adequate initial conditions to start the LES model with a realistic flow field. The LES model is run for a minimum of 2000 time steps of 0.25 seconds. Afterwards, the turbulence statistics and running averaging procedure are reset and the actual computation starts.

8.3.8 Assumptions

8.3.8.1 Turbulence generated by suction head and ladder

Two objects in the flow field induce turbulence potentially of influence on the plume dispersion. The suction head is located near the sea bed and is typi-

cally two to four meters high. The ladder and hydraulic pipes transporting the pumped mixture towards the hopper are also located in the water column. These structures have a complex shape and are difficult to implement in a numerical grid in a proper way. They are, however, located next to the dredging vessel and therefore at a lateral distance of about 20 m from the plume leaving the overflow shaft. Any turbulence induced by these structures would therefore only meet the plume at some distance behind the stern, order of magnitude 100 m. It will be assumed that this turbulence has decayed sufficiently after this distance and no suction head and ladder geometry will be included in the numerical grid.

8.3.8.2 Zero-flux boundary condition at the bed

In the currently presented near-field model, the increase in sediment concentration on top of the natural concentration is calculated. It is not needed and not feasible to compute the natural sediment concentration in a model that only covers the direct vicinity of a dredging vessel. For that reason, no bed boundary condition for sediment is implemented. The grid cell layers near the bed are very fine and the density currents near the bed can be solved while all the sediment stays in the model domain.

In extremely shallow water, with very limited keel clearance, the jet leaving the overflow shaft would induce a local increase in bottom shear stress. For these cases, some additional sediment could be eroded from the seabed. It is however assumed that the erosion rates at the relatively small surface area below the jet would be many orders of magnitudes smaller compared to the sediment flux through the overflow. Moreover, in case the sea bed would consist of pure mud, this rate could be substantial, but in that case the overflow will most likely not be used. The overflow will only be used if fine sediments are a minor fraction of the sediment to be dredged. In that case, the majority of any sediment that would be eroded below the plume exit in the case of shallow water would be the coarser fraction, which will settle relatively fast further downstream.

8.3.8.3 Flocculation

Both the formation of flocs and the effect of flocculation are time-dependent. In the simulation of near-field sediment plumes, the time-scales are relatively short. At a sailing speed of 2 knots in still water, the plume has reached a distance of 100 m behind the vessel in about 2 minutes. This is a very

short time for the formation of flocs, certainly given the very high strain rates and turbulent intensity associated with the mixing in the plume and the propeller jets. Even though unlikely, in the case that large flocs would have been formed, the effect of increased settling velocity would be limited, given the short time-scales. For example, if a macrofloc with settling velocity of 5 mm/s exists during a 2 minute period, it would have settled 60 cm in a still settling column. In the turbulent environment, such a floc would not have the time to reach an equilibrium settling velocity. Therefore, it can be assumed that flocculation effects on the near-field plume can be neglected.

The near-field models presented in this work will typically provide source terms for the far-field models of a dredging site. In any such far-field models, covering the complete environmental system studied, the flocculation will have to be taken into account.

8.4 Benchmark validation cases

8.4.1 introduction

A number of additional processes will be added in the LES model of the full-scale TSHD prototype simulations. First, air bubble entrainment in the overflow shaft and in the resulting plume needs to be taken into account. Secondly, the generation and spreading of two propeller jets will be implemented in the LES model. And thridly, in the case of multiple overflows, the merging of different plumes needs to be simulated correctly. The simulation accuracy of these processes cannot be verified by comparison with field data. Therefore, a number of benchmark cases are drawn from the literature in order to compare our model performance to these experimental cases.

An air bubble plume case has been described in section 7.4.3, since it was simulated at laboratory scale due to the difficult scaling of air bubbles. Propeller jet verification and merging plumes test cases are simulated on prototype scale and will be covered in this section.

8.4.2 Propeller jet validation

In the concise literature review on propeller jets measurements (section 2.6) both the radial and axial distributions of axial and tangential velocity are

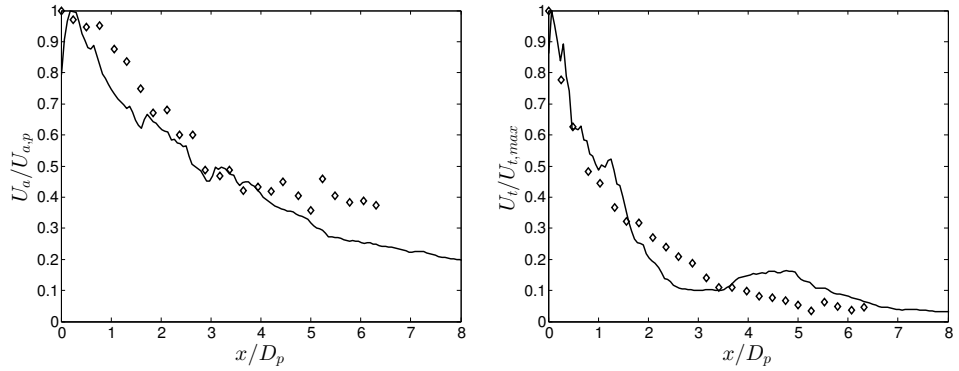

(a) (b)

Figure 8.6: Numerical simulation results (lines) compared to laboratory-scale measurements by Lam et al. *(2011), for the axial component (a) and the tangential component (b).*

shown. The radial velocity profiles at the location of the propeller have been used to define the pressure jump distribution for the actuator disk internal boundary condition. In this section, the simulated axial decay of axial and tangential velocity are compared with the measurements by Lam *et al.* (2011). The simulations are done at prototype scale, using the same propeller diameter (D_p=4.2 m) as for the full overflow plume simulations. The mesh size definitions were identical to the full simulations.

At a number of positions along the axis of a propeller jet, Lam *et al.* (2011) performed velocity measurements on a grid across the jet. For each distance x/D_p, the maximum value of a velocity component in a cross section of the jet was determined. In this discussion on propeller jets, x refers to the streamwise distance from the propeller, rather than from the overflow pipe. The axial component shown in figure 8.6a decays to about 50% of the initial value after about 3 propeller diameters (x/D_p=3). Afterwards a slower decay takes place. This pattern was correctly simulated by the LES model. In the model results, the point at which the axial velocity reduced to 50% was also found after x/D_p=3. At greater distance, however, the decay slows down, but continues at x/D_p >4 while in the measurements it seems the velocity stays fairly constant, which is in a way surprising for a jet. Possibly the flume in which the measurements were done had a width limiting the jet spreading.

In figure 8.6b, the decay of the tangential velocity U_t is shown. At x/D_p=3, the tangential component has rapidly decayed to only 15% of the initial value.

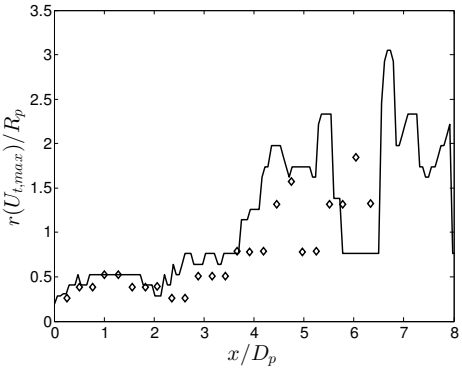

Figure 8.7: Numerical simulation results (black line) of the streamwise evolution of the position at which the maximium value of U_t occurs. Markers indicate laboratory-scale measurements by Lam et al. *(2011).*

In the numerical result, the very fast decay in the range $0< x/D_p <2$ is also found. The decay is following the measurements quite closely until x/D_p=1.5, after which the decay in the model is faster. In the range $2.5< x/D_p <6.5$, the decay in the model is first slower and then catches up with the measurements. Both in the model and in the measurements, about 5% of the initial tangential velocity U_t at the the propeller is found at x/D_p=6.5.

In Lam *et al.* (2011), a further analysis is given of the streamwise evolution of the position r/R_p at which the maximum tangential velocity occurs, where R_p=$D_P/2$. In figure 8.7 the comparison of the experimental data with a full-scale LES simulation is given. The maximum U_t at $0< x/D_p <2$ occurs at r/R_p=0.5, or in between the propeller axis and the tip of the blades. Only after $x/D_p >$2.5, the rotational flow begins to spread, with $U_{t,max}$ occurring at $r/R_p \sim$1.5 and at x/D_p=5. The same phenomenon has been reproduced with the LES model. For $x/D_p >$4-5, the tangential component becomes very weak, and the determination of the maximum value across the propeller jet becomes unstable due to small variations in the time-averaged flow field. The range of values found in experiment and model solution, however, corresponds well.

It is expected that the propeller jets induce an important amount of mixing in the overflow plume. Therefore, a sufficiently high portion of the turbulent kinetic energy k needs to be resolved on the numerical grid. For a standard simulation case with a TSHD geometry and two propellers, the mean streamwise velocity is shown at a cross section at a distance from the overflow of 100 m, or at a distance x/D_p=5 from the propeller (figure 8.8, top panel).

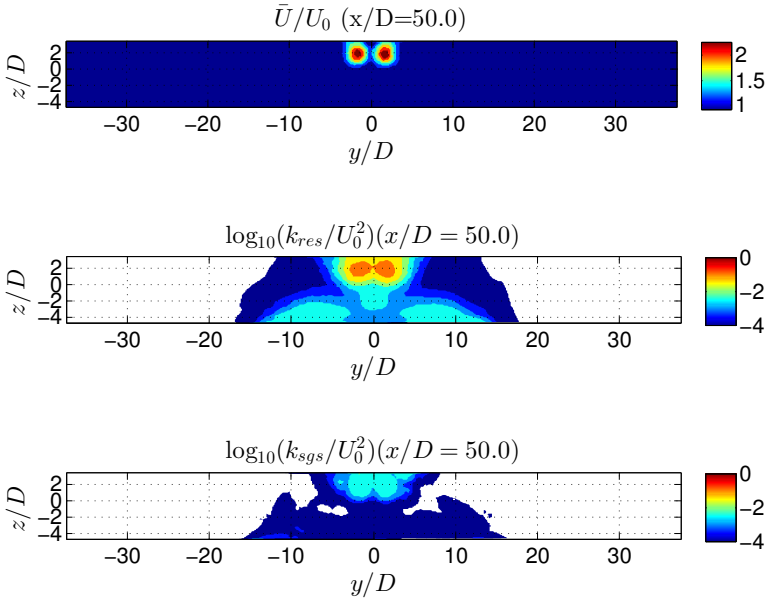

Figure 8.8: LES model results at a cross section at x/D_p=5. Results of mean streamwise velocity U/U_0 (top) and turbulent kinetic energy in the resolved scales, k_{res} (middle) and in the subgrid scales, k_{sgs} (lower panel).

The resolved k_{res} and subgrid-scale k_{sgs} turbulent kinetic energy has been determined at the same cross section (figure 8.8, middle and lower panel). The signature of the two propellers can clearly be seen at z/D=2 and y/D=$\pm$2. It can be observed that the resolved turbulent kinetic energy k_{res} is 1.5 orders of magnitude larger than k_{sgs}. In the propeller jet, k_{res} is also two orders of magnitude higher compared to the surroundings and in the rest of the plume.

It can be concluded that the flow pattern induced by the propellers of the dredging vessel are represented in a sound way in the LES model. The modification of the streamlines and the additional turbulence generated due to the propellers should provide the correct effects on the near-field plume.

8.4.3 Coalescing plumes validation

One final validation case has been defined for the verification of the LES model performance. Some TSHD's have multiple overflow shafts, resulting in two or more superimposed plumes. The coalescence of multiple plumes has been studied by Kaye and Linden (2004) in a laboratory study. Two vertical

plumes with distance Δx_0 between both pipe axes have been released, and the axial distance at which both plumes have been merged is recorded. Two plumes are considered as merged when the double peak in concentration is transformed to a single peak. The interesting aspect about this data set is the inclusion of different density ratios between the plumes. This can occur in a multiple dredging plume where different surface concentrations at different locations in the hopper lead to a different C_0. Kaye and Linden (2004) express the initial plume density ratio, or initial buoyancy ratio as:

$$\beta = \frac{\Delta\rho_1}{\Delta\rho_2} \tag{8.3}$$

where $\Delta\rho_i$, i=1,2 is the mass density difference between the plume and surrounding fluid. In terms of sediment concentration this can simply be expressed as

$$\beta = \frac{C_{0,1}}{C_{0,2}}. \tag{8.4}$$

Simulations have been carried out using a grid with dredging vessel and sediment plumes, but with large water depth of 100 m to provide sufficient distance to the bottom. In this way the coalescing plumes can be studied without influence of the bottom. Four different simulations with different β have been carried out.

After allowing some spin-up time, the simulations were run for 15000 time steps of 0.2 s, at which point the time-averaged statistics had converged. An example is given for β=5 in figure 8.9. Turbulent entrainment attracts surrounding water towards the plumes, resulting in the typical spreading of vertical plumes (Fischer, 1979; Kaye, 2008). The entrainment of surrounding water into the plume results in a pressure drop. This results in turn in both plumes attracting each other, leading to a faster touching of the edges of the plumes than one would expect from simple plume spreading.

The distance from the source at which the plumes have coalesced was found by Kaye and Linden (2004) to be dependent on the buoyancy ratio β. When one of the plumes has a lower relative mass density, the pressure gradient causes a higher acceleration compared to a plume with $\Delta\rho$ as high as the other plume. The four simulations carried out using the LES model had values of β=0.1, 0.2, 0.5 and 1.0. The time-averaged concentration field was integrated over the y coordinate (S_y) to eliminate any twisting of the plumes from the result. At the location at which a horizontal profile of S_y exhibits no longer a double peak but a single peak, the plumes are considered to have

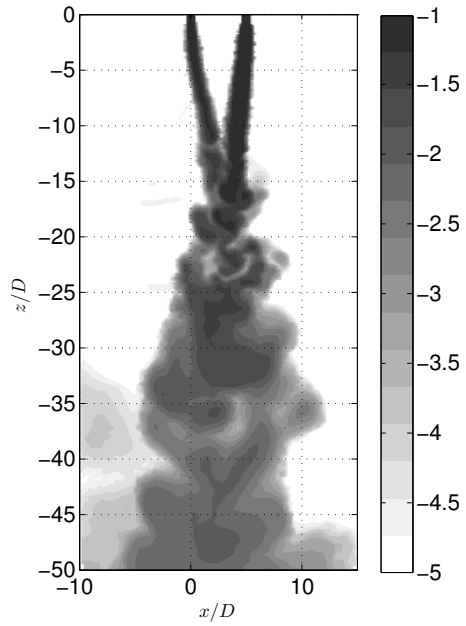

Figure 8.9: LES simulation of two coalescing plumes with initial buoyancy ratio β=5. The logarithm of C/C_0 is shown in greyscale.

merged. This is the same method as used by Kaye and Linden (2004). In figure 8.10, the evolution of the coalescing plumes' profiles are shown for the four cases.

When the distance from release to plume merging (z_m) is plotted for all cases as a function of β, it is found that the plumes merge at varying distances between $z_m/\Delta x_0$=2.5 and $z_m/\Delta x_0$=4 (figure 8.11). The smaller values are found for the cases with low β, and vice versa. The same was found by Kaye and Linden (2004), of which the results are also plotted in figure 8.11. The LES results oscillate slightly around the experimental findings, but are in general close to or within the range of uncertainty on the experimental results.

8.5 Sensitivity analysis model parameters

8.5.1 Sub-grid scale turbulence model

For the applications with large Reynolds number, the subgrid-scale (SGS) model will be more active and will account for a larger fraction of the total dissipation. It is therefore advisable to assess the sensitivity of the model

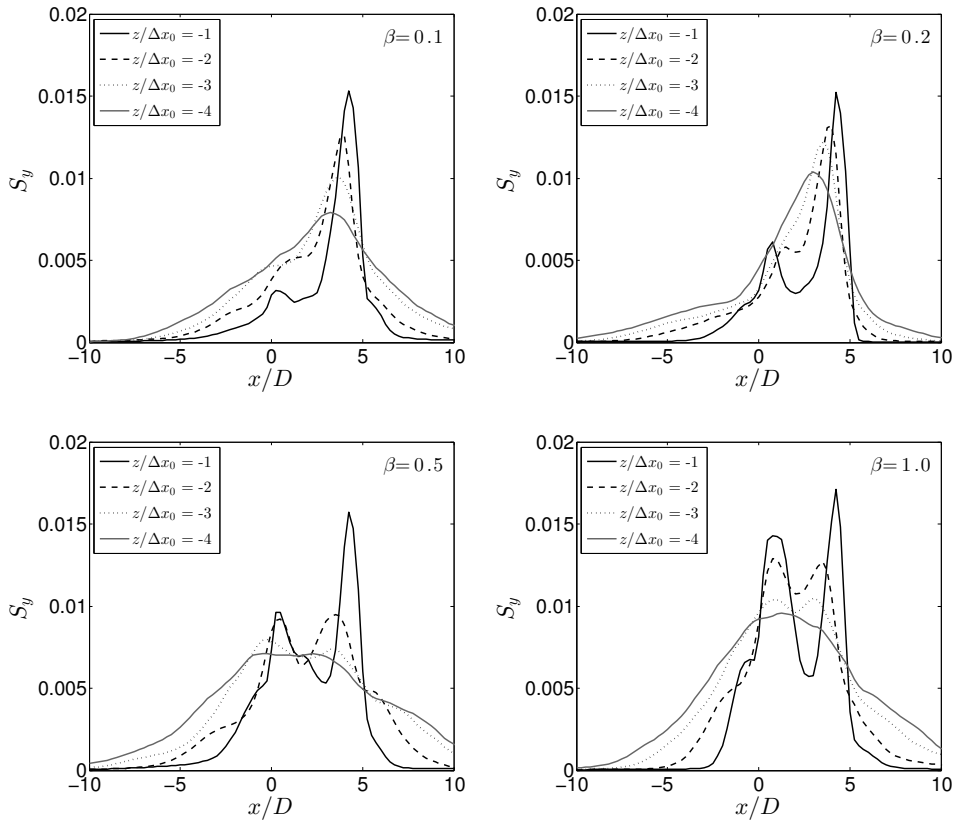

Figure 8.10: LES model results of merging plumes with different β. The horizontal profiles of S_y are shown at different distances from the source, all the plumes are coalesced at $z/\Delta x_0$=-4.

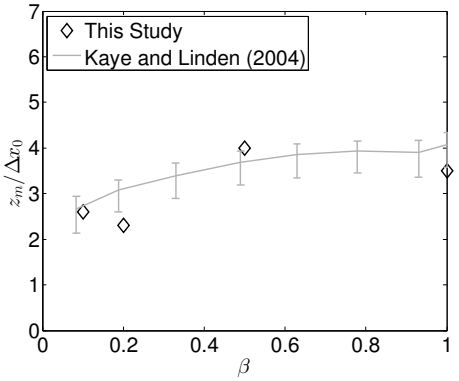

Figure 8.11: Results of plume coalescence case with four different values of β, compared to the experimental results of Kaye and Linden (2004).

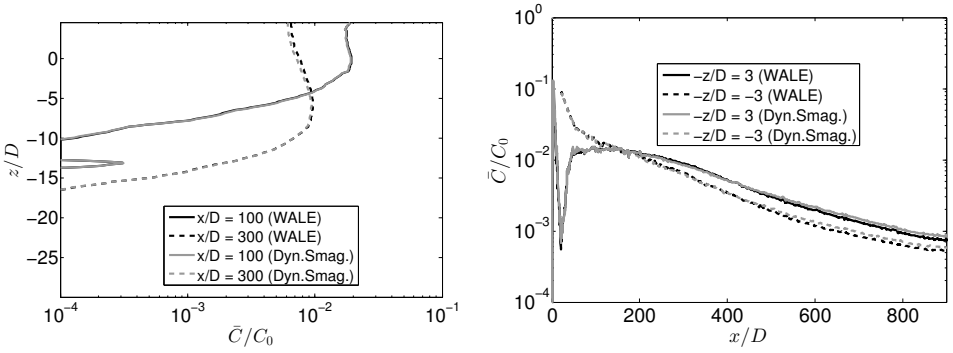

(a) (b)

Figure 8.12: Comparison of full-scale LES results with the dynamic Smagorinsky and WALE subgrid-scale turbulence models. (a) vertical profiles (b) horizontal profiles at the y=0-symmetry plane.

results to the choice of the subgrid-scale model. The simulation of a base case with W_0=3.2 m/s, U_0=1.5 m/s, C_0=20 g/l and D=1.1 m has been executed with the dynamic procedure of the Smagorinsky subgrid model and with the WALE subgrid model. The vertical profile of C/C_0 has been compared at distances of x/D=100 and 300 downstream of the overflow shaft. In this case about 80 m and 250 m behind the stern of the vessel. It was found that the results with both subgrid models are very close to each other (figure 8.12a). A difference of 9% was found in the surface plume at x/D=300, which is marginal. Otherwise, the results are almost identical. Horizontal profiles at $-z/D$=-3 (close to the surface) and at $-z/D$=3 (6m below the surface) have also been plotted for both subgrid models (figure 8.12b). Also in this case, differences in sediment concentration of maximum 10% have been found along the plume.

The main differences between both SGS models is the near-wall treatment and the varying coefficient C_s in the dynamic Smagorinsky procedure. It was also discussed earlier for the lab-scale simulations (section 7.5.4.3) that the coefficient C_s should be dependent on the subgrid activity s (Meyers and Sagaut, 2006). In a very large Reynolds application, s is either very small (away from the ship in uniform conditions) or very high (in the plume, near the ship). For another case with a plume that spreads throughout the water column, this can be nicely illustrated (W_0=1.9 m/s, U_0=1.0 m/s, C_0=55 g/l and D=2.0 m). Also for this case, the C/C_0 profiles are almost identical for both SGS models. In figure 8.13 (top panel), the subgrid activity s is shown. It is indeed either close to zero or close to one. In the lower panel, C_s is

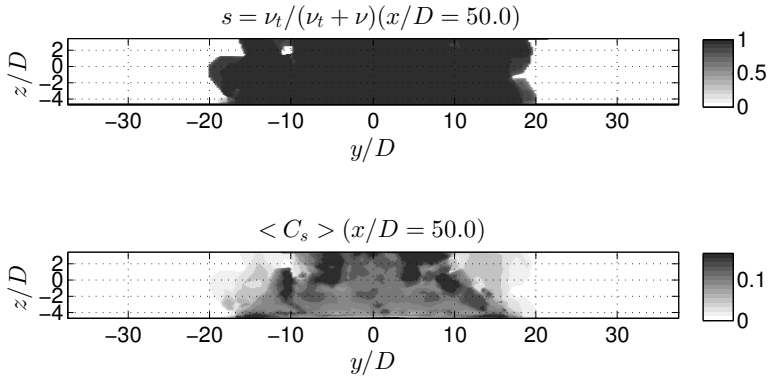

Figure 8.13: Full-scale LES simulation using the dynamic procedure for the Smagorinsky SGS model: subgrid activity s and dynamic Smagorinsky coefficient C_s.

shown. It can be observed that the largest part of the plume area has a C_s value close to the standard value of 0.1. The effect of highly varying values of C_s in the small-scale simulations is not as strong in the high-Reynolds cases. The difference in approach for near-wall eddy viscosity (at the ship hull) does not seem to have a significant effect either.

8.5.2 The choice of advection scheme

A similar analysis can be made based on two identical plume simulation cases, of which one uses the Bounded Central Differencing scheme and the other a very simple second order upwind scheme. It is investigated what the impact is of a more advanced advection scheme on a large-scale LES simulation.

Interestingly, the differences are not that large (figure 8.14). In a plume in deep water which is pushed to the surface, the differences are marginal (figure 8.14a). Also interesting is that in a case with more dense plume in shallow water, the differences are more pronounced (figure 8.14b). Here, the surface plume ($C/C_0 \sim 10^{-3}$) has to separate from the main density current ($C/C_0 \sim 10^{-2}$). The way this happens is influenced by the advection scheme, be it not drastically. The differences are of the order of a factor 1.5, but the general pattern stays the same.

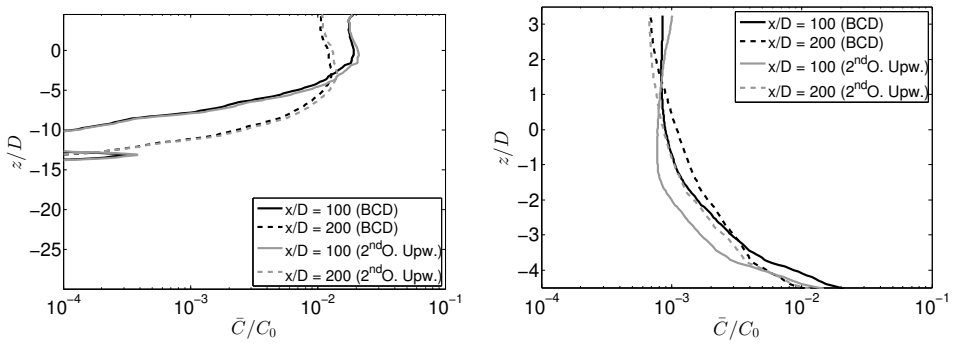

Figure 8.14: Comparison of full-scale LES results using the preferred Bounded Central Differencing Scheme (BCD) and the more diffusive 2^{nd} order upwind scheme. (a) in a plume in deep water (b) in a plume in shallow water with near-bed density current.

8.5.3 Grid resolution

8.5.4 Moving vessel approach

A simple check has been performed to determine whether the solution is sensitive for the approach with a moving wall for the sea bed. In one simulation the sea-bed velocity has been set to zero, while in the other it has not. As explained above, the sea bed is given a velocity to compensate for the ship's speed over ground while the numerical mesh is static.

It can be observed that the impact of the moving bed is not very high, although differences up to 20% occur (figure 8.15). Therefore, the moving bed approach will be kept in the remainder of the simulations.

8.5.5 Hull boundary layer

For a full-scale TSHD dredger, the hull can be considered as a rough wall. The boundary layer for a smooth wall can be estimated using the formula by Schlichting (1979):

$$\delta_r = 0.16 x Re_x^{-1/7} \approx x^{0.857} \tag{8.5}$$

For rough boundary layer, δ_r should no longer be dependent on the viscosity, but rather on a wall roughness height z_0. Elliott (1958) finds an exponent

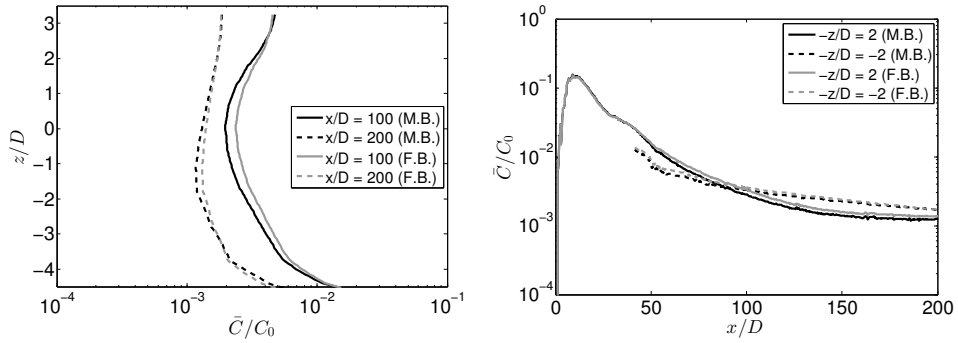

Figure 8.15: Comparison of full-scale LES results with the moving bed (M.B.) approach and with a fixes bed (F.B.). Vertical (a) and horizontal (b) profiles of C/C_0 are shown at x/D=100 and x/D=200.

of 0.8 on x, for the thickness of a growing internal boundary layer in the atmosphere:

$$\delta_r = 0.86 x^{0.8} z_0^{0.2} \tag{8.6}$$

For typical distances between 50 to 80 m from the bow, using sea water density ρ=1025 kg/m^3 and a sailing speed of 2 knots, δ_r is between 0.63 m and 0.95 m using the equation by Schlichting (1979). Presently, an equivalent sand grain roughness of 0.1 mm is commonly accepted or newbuild ships. Using the formula by Elliott (1958), with $z_0 = k_s/30$ and equivalent sand grain roughness k_s=0.1 mm, 1.6 m $< \delta_r <$ 2.3 m is found. Considering typical overflow shaft diameters between 1 m and 2 m, the dimensionless keel boundary layer thickness δ/D is thus between 0.3 and 2.3.

It is therefore likely that the relatively narrow boundary layer is not of great importance on the much larger overflow plume. However, the velocity profile determines the crossflow attack in the first $0.3D$ to $2.3D$ from the hull. An analysis is made on the soundness of the velocity profile development along the hull, before the overflow shaft location is reached. With only 4-5 cells in the boundary layer, a rough representation of the boundary layer is expected. The boundary layer thickness development along the x axis is determined in what follows.

In figure 8.16a, the evolution is shown of the boundary layer thickness δ at the TSHD hull, before reaching the influence of the overflow shaft and plume. A comparison with the theoretical boundary layer thickness is made. Even

though the LES model prediction of δ is not very steady due to the coarse grid, it still compares reasonably well with the theoretical values for δ as a function of x, mainly with the formula by Schlichting (1979). For an overflow shaft situated near the stern of the vessel, the boundary layer of the hull has a thickness between 0.4 and 1.0 m when the flow reaches the plume exit.

In figure 8.16b, the boundary layer profile is transformed to u^+=f(z/z_0). This allows to compare with the law-of-the-wall, represented as a straight line in a log-plot. The law-of-the-wall for the logarithmic profile is defined here as

$$u^+ = 2.5 \log(z/z_0) \tag{8.7}$$

where $u^+ = u/u_*$, $u_* = (\tau_w/\rho)^{1/2}$ and τ_w is the wall shear stress.

The z^+-value of the first grid cell next to the hull wall (z^+=8x10^3) is several orders of magnitude larger than the limits of the viscous sublayer (z^+=5) and the transition layer (z^+=30). The first grid cell is therefore well within the log-layer. When comparing the model boundary layer with the log-law, the simulated profile is located slightly lower than the law-of-the-wall, but the slope corresponds well between $10^4 < z/z_0 < 10^5$. Further from the wall, the outer layer starts, with a more uniform value of u^+.

In figure 8.16c, boundary layer profiles are shown of the Smagorinsky coefficient C_s, the SGS shear stress τ_{sgs} and the eddy viscosity ν. All normalised by their respective maximum values. The total shear stress τ_t should be a straight line from the wall to the end of the boundary layer. This is more or less the case here for τ_{sgs}, since $\tau_{sgs} \approx \tau_t$ (because of the high Reynolds number). Both C_s and ν should go to zero at the wall, have a peak inside the boundary layer and go back to zero in the outer layer. This is the case in the simulations, although ν goes only to about 60% of its maximum in the cell nearest to the wall.

In addition to the analysis of the boundary layer at the TSHD hull, a test has been executed in which the resolution near the hull has been doubled. The resulting plume concentration along vertical and horizontal profiles across the plume are compared in figure 8.17. Both in the vertical profiles (figure 8.17a) and in the horizontal profiles (figure 8.17b), the difference between the solution with reference hull boundary layer resolution and a doubled resolution are less than 1%. It can be concluded that the differences are insignificant, so that the base case resolution can be adopted.

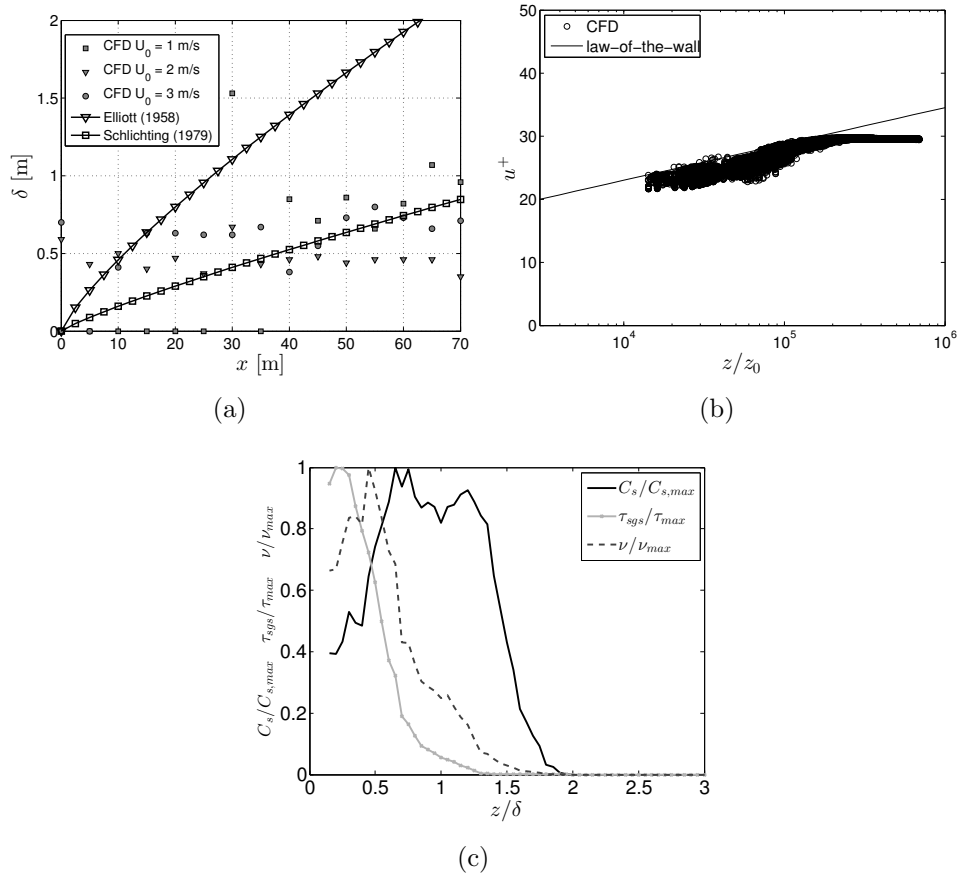

Figure 8.16: (a) Boundary layer thickness at the TSHD hull, before reaching the influence of the overflow shaft and plume. Comparison with theoretical boundary layer thickness using equation 8.5. (b) Full-scale LES velocity profile versus law-of-the-wall at 50m from the bow. (c) Profiles of the Smagorinsky coefficient C_s, the SGS shear stress τ_{sgs} and the eddy viscosity ν. All normalised by their respective maximum values.

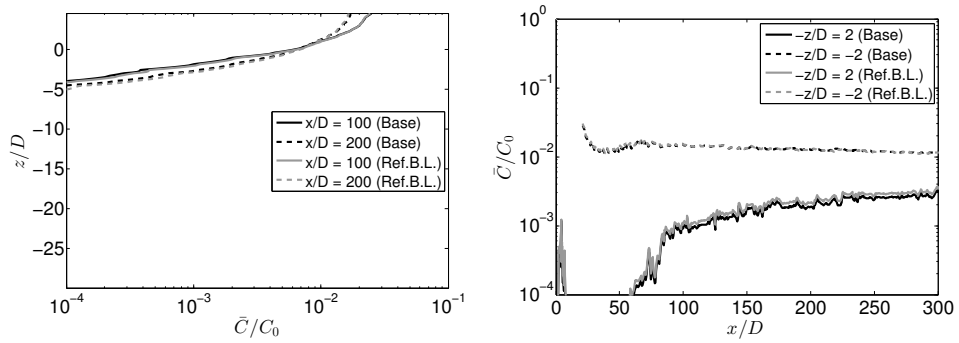

(a) (b)

Figure 8.17: LES simulation results of C/C_0 with the base resolution at the vessel hull ('Base') and with a refined region near the hull ('Ref.B.L.'). Vertical (a) and horizontal (b) profiles across the plume.

8.5.6 Time step

In this section, it is tested whether the time step determined from the criterion of maximum CFL number equal to 1 should be further decreased. A plume simulation with density current and surface plume was taken (W_0=1.9 m/s, U_0=1.0 m/s, C_0=55 g/l and D=2.0 m). The simulation has been carried out with the initial time step of dt=0.25 s and again with a time step of dt=0.125s.

The results for both simulations are again shown by vertical and horizontal profiles of the sediment concentration C/C_0, on which this modelling work focuses. The shape of the profiles is very similar, but differences exist. In the surface plume, differences of about 10-15% occur. This is probably smaller than the overall accuracy of this type of large-scale model. In the remainder, the time step of 0.25s will be used, but during the validation against in situ measurements, it will have to be re-evaluated.

8.6 In situ plume validation cases

8.6.1 Plume observations in the field

In this section a comparison is made between in situ measurements gathered in the field and LES simulations with exactly the same boundary conditions as during the field trip. Datasets of two measurement campaigns have been

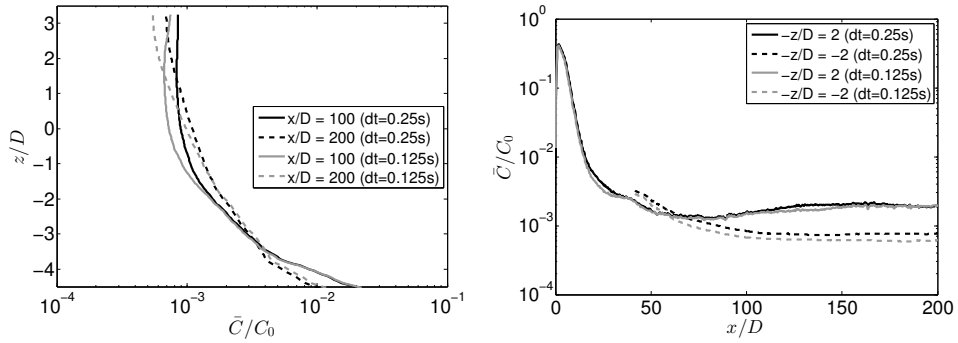

(a) (b)

Figure 8.18: LES simulation results of C/C_0 with the reference time step (dt=0.25s) and a decreased time step of dt=0.125s.

used for this validation exercise. A first dataset, described in detail in section 8.6.2, was gathered during the course of this research. A second existing dataset has been used, which is described in section 8.6.3 and in Breugem *et al.* (2009).

8.6.2 Campaign 1

In collaboration with IMDC, a measurement campaign has been set up. A 120 m long TSHD with loading capacity of 12,000 m^3 was dredging silty sand at a relatively shallow part of a tidal estuary. The mixture pumped into the dredger's hopper contained a varying percentage fine sediment particles, between 9 and 100 g/l. No environmental valve was used. The goal of the measurement campaign is to gather detailed information about the circumstances and the overflow mixture released. In this way, the dredging vessel can be simulated with all necessary boundary conditions, and the simulated plume can be compared with the observed plume.

Transects were sailed along the length of the plume as well as across the plume (Two examples are given in figure 8.19). The top panels show the positions of dredger and survey boat, as well as the positions at which a vertical profile of C has been taken. Coordinates are relative to lower left corner of the map, (X_0,Y_0). Also, the positions at which samples were taken inside the overflow shaft are shown, with the measured C_0 value in g/l. In the lower panels, the relative position of the survey boat to the dredger's position is shown. The letters B and E indicate the begin and end of a survey boat

transect, respectively. In the top panels, a red and green dot is shown to indicate the position along the dredger's track closest to the measurements at start and end time. The relative position of the survey boat to the dredger is determined. ΔX_t and ΔY_t are the longitudinal and lateral position of the survey boat in a moving coordinate system of which the x-axis is always aligned with the dredger's course. The lateral position in the plume, relative to the axis of the plume, is given by ΔY_t. Therefore, ΔY_t is always defined as the distance from the measurement location to the dredger's track, along a line perpendicular to the tangential of the track. These relative coordinates will serve to determine at which location in the simulated plume the sediment concentrations should be compared with the measurements.

The current and backscatter measurements in the plume were conducted using a Teledyne RD Instruments ADCP 1200 kHz Workhorse. This 1200 kHz ADCP system was mounted on a steel moon pole at the centre of the back deck of the vessel. The transducer set was looking vertically downwards at the bottom. ADCP backscatter data was processed to suspended sediment concentration data using the Sediview® software, based on the sonar equation. See Thorne and Campbell (1992); Hay (1991); DRLsoftware (2003) for more information. For positioning, a DGPS was installed onboard the survey vessel.

As a backup for the acoustic system, a string of optical backscatter (OBS-3A) instruments was attached to a cable and trailed behind the survey boat. A heavy metal fish was mounted at the end of the cable to minimise the uplifting of the instruments when the survey boat was sailing. One OBS-3A was logging online with a frequency of 1 Hz, two other OBS's were logging to the internal memory with a frequency of 0.1 Hz. Further attached to the string is a tube connected to a centrifugal pump, permanently pumping water from near the middle OBS's sensor. In this way water samples are collected every 5 minutes with increased frequency when entering and leaving the plume. Water samples are analysed for suspended solids and the results are used for calibration of the optical and acoustic turbidity acquisition systems.

In order to obtain complete profiles of sediment concentration between water surface and sea bed, a SiltProfiler is deployed (Zimmermann *et al.*, 2010). A picture of the instrument is shown in figure 8.20. The SiltProfiler was developed by IMDC and has the following general specifications. The data collection is executed locally (i.e. on the profiler) by an integrated data logger. Sensor cables are kept very short and connect to the interfacing electronics of the data logger. The data logger collects the sensor signals

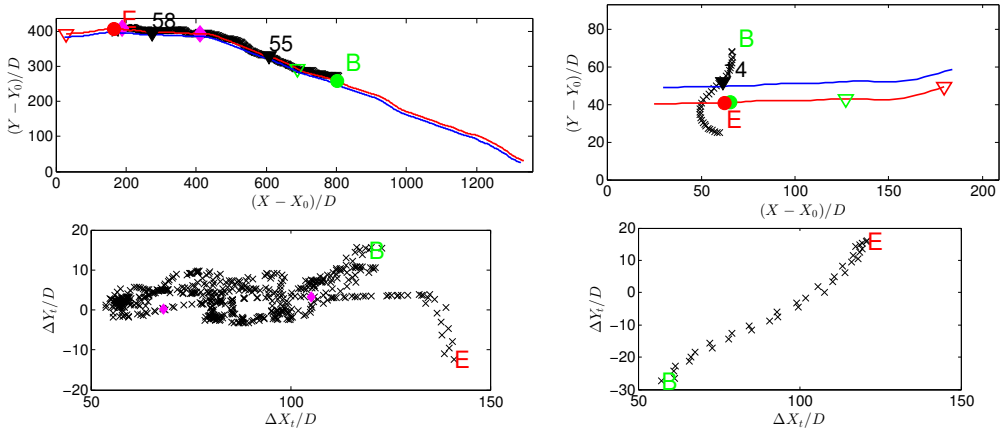

Figure 8.19: Examples of the situation during a plume measurement. Top panels: Maps of dredger midpoint(red), draghead (blue) and survey boat course (black crosses). Green and red triangles indicate the position of the dredger at start and end of the measurement, respectively. Magenta diamonds indicate locations at which a vertical profile of c has been taken. Black numbers indicate the value of C_0 (g/l) where overflow samples have been taken onboard the dredger. Letters 'B' and 'E' indicate a transect's start and end position of the survey boat. Green and red dots inducate the positions of the dredger's trajectory closest to the survey boat at the time of the start and end of a monitoring transect. Lower panels: Relative position of the survey boat to the dredger. In (a), a longitudinal measurement of the plume is taken, in (b) a cross sectional measurement.

and records the same in internal memory. The data can be retrieved upon recovery of the profiler via a short-range wireless connection. As soon as the profiler breaks the water surface the data can be accessed and transferred to the operator's PC, whereupon the profiler is ready for a new profiling session. The retrieved profile data are visualised immediately in depth profile graphs. This operational mode requires no electrical cables to be attached to the profiler. The mounted sensors are: (i) conductivity, pressure and temperature sensors with measuring ranges adequate for use in seawater; (ii) multiple turbidity sensors to cover the entire range of 0 to 55 000 mg/l suspended solids: 2 transmittance sensors (type FOSLIM) are used, in combination with a Seapoint turbidity sensor (0-400 mg/l).

As such the SiltProfiler is anticipated to rapidly profile the suspended sediment concentration as well as the salinity structure. The SiltProfiler can measure at variable frequency of up to 100 measurements per second (100

Figure 8.20: The free-fall profiler SiltProfiler.

Hz).

The vertical profiles obtained using the SiltProfiler revealed clearly a bimodal structure of the turbidity plume in all measurements of this campaign. In the lower half of the water column, a highly concentrated layer was found containing the majority of the released sediments, while in the upper layers a more diluted secondary plume can be observed (background sediment concentration was <10 mg/l) . In the surface plume, sediment concentrations of about 40 to 100 mg/l were found; in the near bed plume concentrations were up to a factor 10 higher.

However, when looking at the sediment concentrations determined using the ADCP backscatter (calibrated using water samples), it seems only a 5 m thick surface plume is found and no dense bottom layer. When two observers would use only one of both methods for plume monitoring, they would come to radically different conclusions (Decrop and Sas, 2014). It seems the acoustic measurements were disturbed by a substance inducing backscatter, which was not detected in the suspended solids analysis on the water samples, which served as calibration for the acoustics at several points along each transect. The only possible disturbance can come from the air bubbles caused by propeller and overflow. In this particular case, the air bubbles were present in

the upper layers of the water column over several 100's of meters. For that reason, the ADCP measurements of this campaign will not be used for the validation of the model. Only the (direct) measurements by the SiltProfiler and OBS will be used.

From an environmental impact point of view, the surface plume is more relevant since it has the potential to move away from the dredging area with the current, potentially moving towards environmentally sensitive areas. For this specific case, the concentration levels found in the surface plume were about a factor 1000 smaller compared to the mixture released through the overflow shaft.

In this first campaign, plumes generated by a TSHD working in a wide, tidal estuary were monitored, while the tidal flow was mostly aligned with the sailing direction of the dredging vessel. The water depth varied between 14 m and 18 m. From sea bed sample analysis, it was found that between 5% and 30% (by volume) of the sediment had a grain size smaller than 63 μm. The dredging vessel had a length L_s= 120 m, the D=2 m circular overflow shaft was located on the front end of the hopper, at L_o= 80 m from the stern (so, $L_o/D = 40$). When the dredging vessel was sailing against the current while trailing, a turbidity plume was generated behind the vessel. The water samples taken inside the overflow had on average a volume fraction of 74% silt (d <63 μm), with a standard deviation of 16%. Interestingly, the water samples taken inside the plume had almost the same silt percentage: an average of 75%, with a standard deviation of 11%. The sand fraction in the overflow samples consisted mainly of very fine sand ($d \leq$125 μm). The similarity between the silt and sand fractions in the overflow and in the plume show that the fine sand does not have the time to settle in the turbulent environment of a near-field plume. It would therefore make sense to perform near-field plume simulations of this case with a single sediment fraction.

Suspended sediment concentrations in the overflow (C_0) varied between 8.5 g/l and 167 g/l. Values of c in the plume varied between 10 mg/l and 940 mg/l, where c is taken as the concentration relative to the background concentration. The background concentration was however very low, 2-10 mg/l on all three days. Since there is no background concentration in the model, this small ambient concentration will be added to the model results for consistency.

During this campaign, measurements were taken up to very close distance behind the sailing dredger (between 50 m and 1000 m from the stern), in

order to capture the near field behaviour.

During the measurements of campaign 1, the dredging vessel sailed long transects of about 3 km during which sailing speed and sea current speed often remained fairly constant. At 3 knots sailing speed, a 3 km stretch is finished in 33 minutes, after which the dredger turned back in the opposite direction. This allows for a comparison with a numerical simulation with constant forcing at the boundaries, and a plume that has 33 minutes to form and grow. The sediment concentration inside the overflow shaft, C_0, does vary more rapidly, while all simulations are executed with stationary C_0. Therefore, for each model comparison, a period was chosen during which C_0 was relatively stable (typically 10 minutes). During such a period, a dredger covered about 1 km. All plume measurements used for comparison with model results are taken at the same day, in fair weather.

8.6.2.1 Case 1A

The plume studied during case 1A, was observed between 3:05 and 3:23 PM. The current velocity during this period was very low, while the dredging vessel sailed at about 1.1 m/s. The flow velocity relative to the dredger, U_0, was therefore taken as 1.1 m/s. The time-averaged value of the overflow concentration, C_0, was 55 g/l. The positions of the dredger, survey boat and sampling events are shown in figure 8.19a. The outflow discharge was stationary at Q_0=6 m^3/s and therefore the overflow exit velocity was W_0=$Q_0/(0.25\pi D^2)$=1.9 m/s.

The LES model was set up using these (observed) boundary conditions and was run during 500s as a warm-up period, afterwards the model was run for 1250s during which time-averaging was performed. The model results (figure 8.21) show a bimodal plume, with a density current descending to the sea bed and a surface plume separating from the main plume (figure 8.21). The time-averaged sediment concentration in the near-field plume has a wide range, from C/C_0=1 close to the overflow exit, down to about C/C_0=10^{-3} at 150 m downstream of the stern. The instantaneous concentration c/C_0 has a high variability in space, due to the resolved turbulent eddies and their interaction with rising air bubbles of different size.

In situ vertical profiles of sediment concentration closely behind the dredger (at $0.5L_s$ and $0.7L_s$ behind the stern) show that a highly concentrated near-bed layer exists as well as a more diluted surface plume (figure 8.22). The near-bed layer has sediment concentrations of 1 to 2% of the overflow con-

centration. In the surface plume this is about 0.05%.

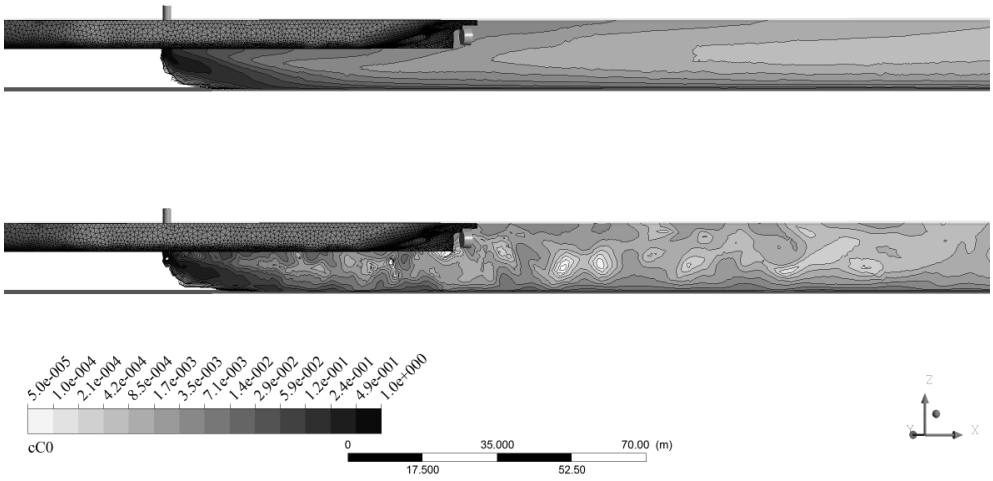

Figure 8.21: Impression of geometry of the vessel and the simulated, time-averaged (C/C_0, top) and instantaneous (c/C_0, bottom) sediment concentration field at the symmetry plane (y=0).

Results of simulations with three different initial air volume concentrations at the overflow ($\phi_{a,0}$) show the influence of the air bubbles on the time-averaged sediment concentration C in the surface plume (figure 8.22, top panels). Remind that in situ observations are in a sense instantaneous, while model output is shown in time-average form. The value of $\phi_{a,0}$=7%, obtained using the equations of Ervine (1998), result in the correct surface plume sediment concentration. Results for a lower value of 1% and a higher value of 14% show clearly that a realistic air bubble concentration is needed to obtain an accurate average surface plume sediment concentration.

Results of simulations with four different values for the initial air bubble diameter are shown for two locations, against measured values (figure 8.22, lower panels). It can be observed that the near-bed highly concentrated layer is simulated accurately for both locations and for all initial air bubble diameters. The value chosen for the initial air bubble diameter mainly influences the surface plume, albeit to a lesser extent as $\phi_{a,0}$. Based on the average root-mean-squared errors in the surface plume for all measured locations, the value of d_a=2 mm was chosen for the initial bubble diameter. Using this diameter, an average relative root-mean-squared error of 0.85 was obtained,

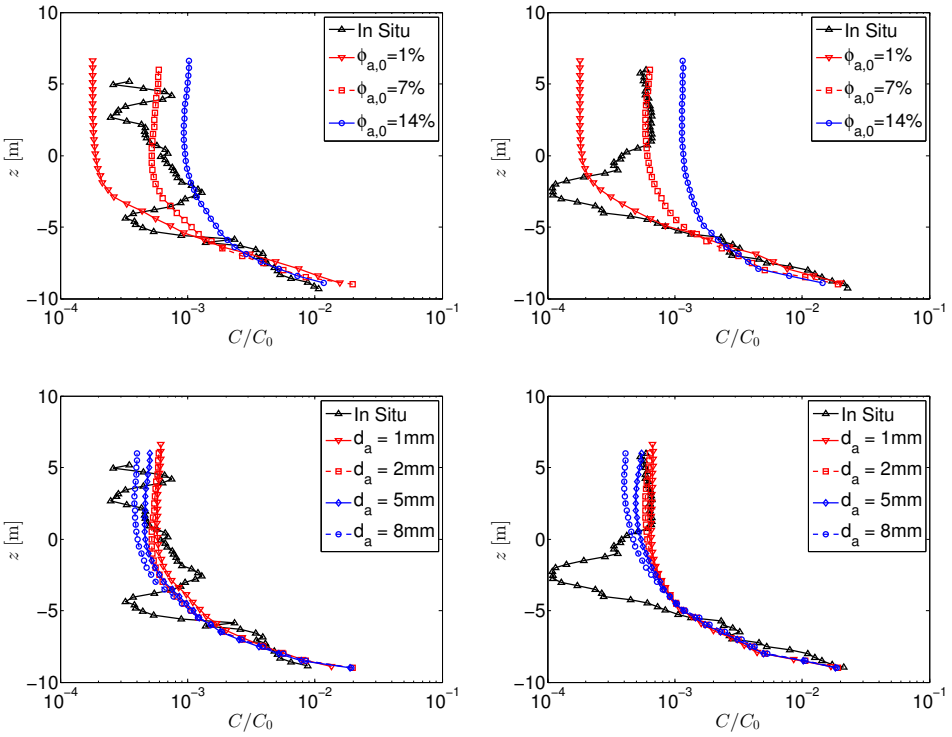

Figure 8.22: Comparison of in situ vertical sediment concentration profiles with model results. Top panels: Results using three different initial air volume fractions. Lower panels: Results using four different initial air bubble diameters. Left panels: Case 1A, right panels: Case 1C

which is a relatively low value for in situ sediment concentration matching.

In figure 8.23 (top panel), the vertical extent of the simulated air bubble plume is shown as a function of the initial air bubble diameter d_a. The longitudinal profile of time-averaged air concentration is considerably influenced by the chosen value of the initial bubble size. In figure 8.23a, the maximum depth below the surface is shown where a bubble volume concentration of $\phi_a \geq 10^{-6}$ exists at the symmetry plane. In the cases with minimum bubble diameter of 5 and 8 mm, the presence of bubbles is limited to $x/D < 40$, which is the position of the stern. These large bubbles first move to the keel and slide along the curved stern sections towards the water surface. No bubbles are found behind the vessel in these cases. In the case with minimum bubble diameter of 2 mm, coalescence forms larger bubbles with the same behaviour as described for the previous case. However, the smaller bubbles are transported with the initial momentum of the plume to a depth of 15

m, after which the maximum bubble depth decreases to a depth of 4 m at x/D=60. At that point, the propeller jets cause downward mixing. The propellers are located at x/D=38, yet, the downward mixing at the symmetry plane starts only at x/D=60. This can be explained by the fact that the two propellers are located off the symmetry plane, and both propeller jets need some distance to widen and meet each other at the symmetry plane. This phenomenon is only observed in the cases with $d_{a,0}$ <5 mm, since in the other cases all bubbles have reached the surface before they can be influenced by the propellers.

Using the value of $\phi_{a,0}$=7% the simulation result for the air volume fraction ϕ_a below and behind the dredger is shown in figure 8.23 (lower panel). Intuitively, it can be stated that the larger air bubbles should rise fast, while a smaller fraction should stay longer in the plume. In the simulation results, part of the air bubbles move very rapidly to the vessel hull and move along the sidewalls of the ship towards the surface. This has also been observed during the field campaign. Another fraction of the bubbles is advected with the plume flow and need more time to escape from the turbulent entrainment induced by the plume. These bubbles reach distances of x/D=150 (300 m) before reaching the surface. Also, this was indirectly observed by the acoustic disturbances in the ADCP results, which were not due to particulate suspended matter found in samples.

When examining the structure of the sediment plume at the surface, a relatively narrow plume is found which reaches a width of roughly twice the vessel width at a distance behind the stern of twice the length of the vessel (figure 8.24). In the top panel it can be observed that the sub-surface plume forms a density current rolling out laterally. In this way, the near-bed plume is much wider compared to the surface plume. In the instantaneous surface plume (bird's eye perspective in the lower panel of figure 8.24), internal concentration variations over the width of the plume are caused by the turbulent motions in the LES model. Turbulent variations in the surface plume have a root-mean-squared value of about 60% of the time-averaged concentrations.

8.6.2.2 Case 1B

At about 3:40 PM, the overflow shaft was slightly raised due to which the sediment concentration of the mixture going overboard decreased to C_0=14 g/l. The production volume discharge remained the same and therefore the outflow velocity was still equal to W_0=1.9 m/s. The background current

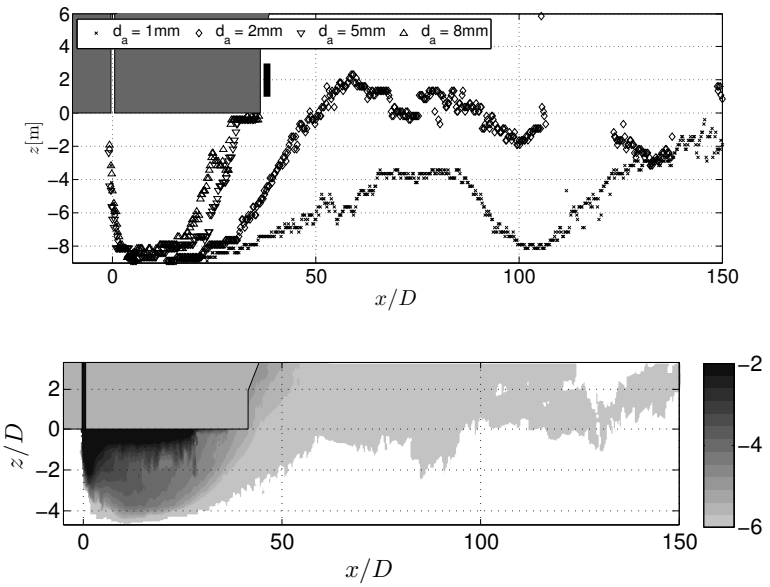

Figure 8.23: Upper panel: Lower extent of the bubble plume in Case 1A at y=0 using different initial bubble diameters. The dredging vessel hull indicated by the grey box, the propeller location is indicated by the black box. Lower panel: Simulation result of the air volume fraction distribution ($\log(\phi_a/\phi_{a,0})$ in the sediment plume at y=0.

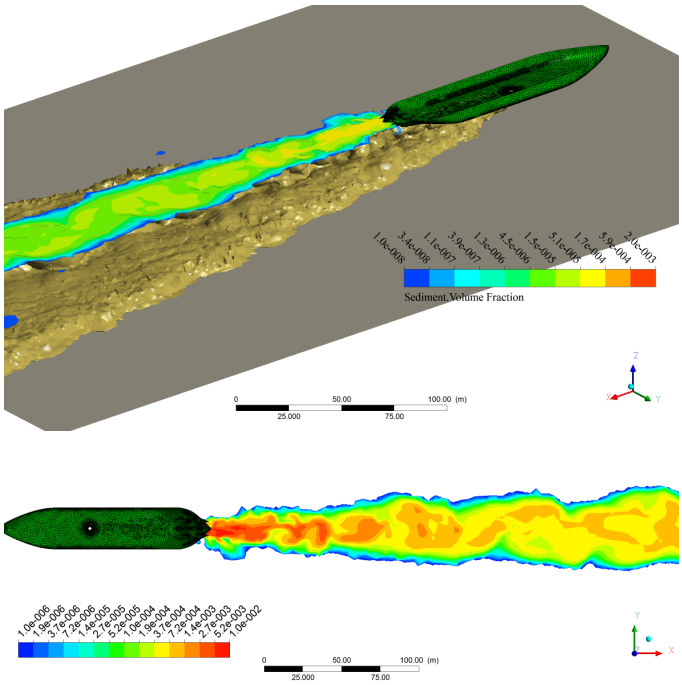

Figure 8.24: Upper panel: aerial view of the surface of the dredger in the model in Case 1A. The sub-surface plume is shown by the brown isosurface at a sediment volume fraction of 2x10^{-5}. The surface plume is shown in colorscale of the absolute sediment volume fraction. Lower panel: Separate view of relative sediment concentration c/C_0 in the surface plume.

velocity was still very low due to slack water, therefore the through-water velocity of the vessel was equal to about 2 knots, or U_0=1.0 m/s.

This time, a cross section was sailed across the plume, at $\Delta X_t/D$=110-160 (figure 8.25a). A vertical profile of c was taken at $\Delta X_t/D$=135 and a lateral position of $\Delta Y_t/D$=-20 from the centerline of the plume (figure 8.25a, lower panel). A simulated longitudinal section along the symmetry plane is shown in the top panel of figure figure 8.25. Here, it can be seen that the measured relative concentration c/C_0 is about 2x10^{-3} in the surface plume, the model result is about half of that value. Both the model result and the measurement show c/C_0 ≈2x10^{-2} near the bottom. Approximately, the lower half of the water column is occupied by a density current and the upper half by a surface plume with a concentration of an order of magnitude lower.

The concentrations measured by the OBS are compared with the model by arranging them as a function of the distance behind the TSHD (figure 8.26a,

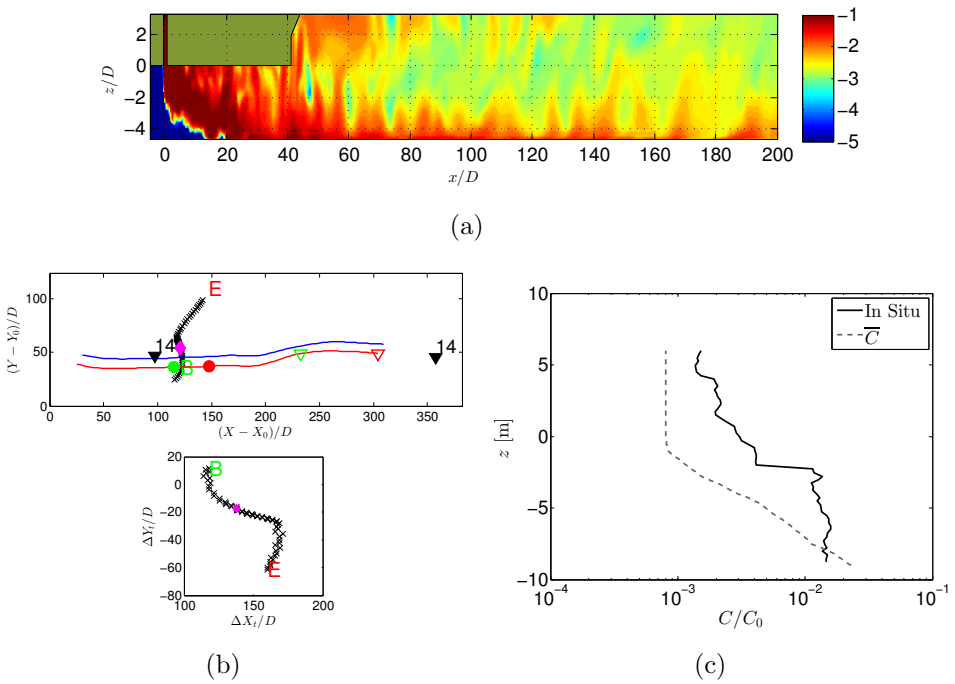

Figure 8.25: (a) Logarithm of the instantaneous concentration c/C_0 in case 1B. (b) Maps of the dredger and survey boat positions, as well as profiling positions during case 1B (colors as in figure 8.19). (c) Comparison of a measured and simulated vertical profile.

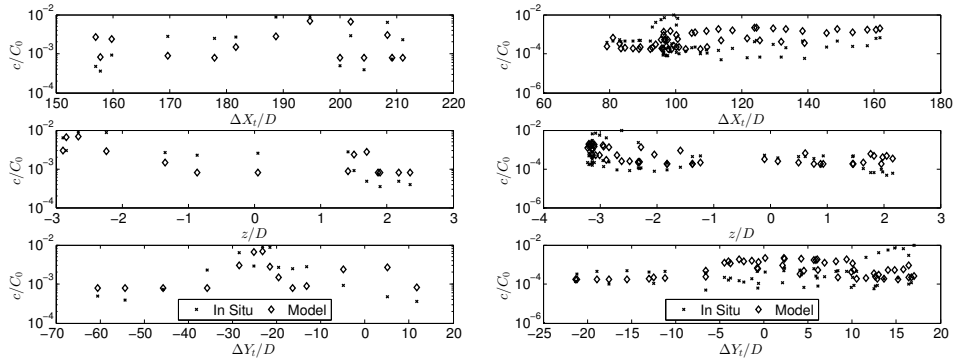

(a) (b)

Figure 8.26: Towed OBS measurements versus simulated c/C_0, as a function of distance X (top), vertical coordinate (middle) and of the lateral position relative to the course sailed by the dredger (lower panel). Case 1B shown in (a), case 1C shown in (b).

top panel). Sediment concentrations are also shown as a function of the vertical and lateral position in the plume (resp. middle and lower panel). Remind that the model results are time-averaged while the observed values have an inherent scatter due to turbulent fluctuations of c in the field. It can be seen that the measurements in the deeper locations (z/D=-3; i.e. $3D$ below the keel) are between 3 and 6x10^{-3} in the model and between 3 and 9x10^{-3} in the measurements. Closer to the surface ($z/D \approx 2$), c/C_0 is about 8x10^{-4} in the model and 4x10^{-4} in the measured data.

In the lateral profile, the same order of accuracy is found, of about a factor 2. Here, the variation of c over ΔY_t observed in the figure is not only due to the horizontal variation but also because changes in sailing speed of the survey boat caused the instruments to move up and down. The (surface) plume measured in this cross section had a width of about 60 to 80m, at $\Delta X_t/D$=110-160 behind the dredger.

8.6.2.3 Case 1C

After a breakdown due to an object tangled in the draghead, the dredger resumed work at 4:55 PM. Another longitudinal section has been sailed by the survey boat while taking measurements, between 5:49 and 5:58 PM. Due to the higher sand level in the hopper, the overflow concentration was higher, on average C_0=90 g/l. In the meantime, the tidal currents picked up and

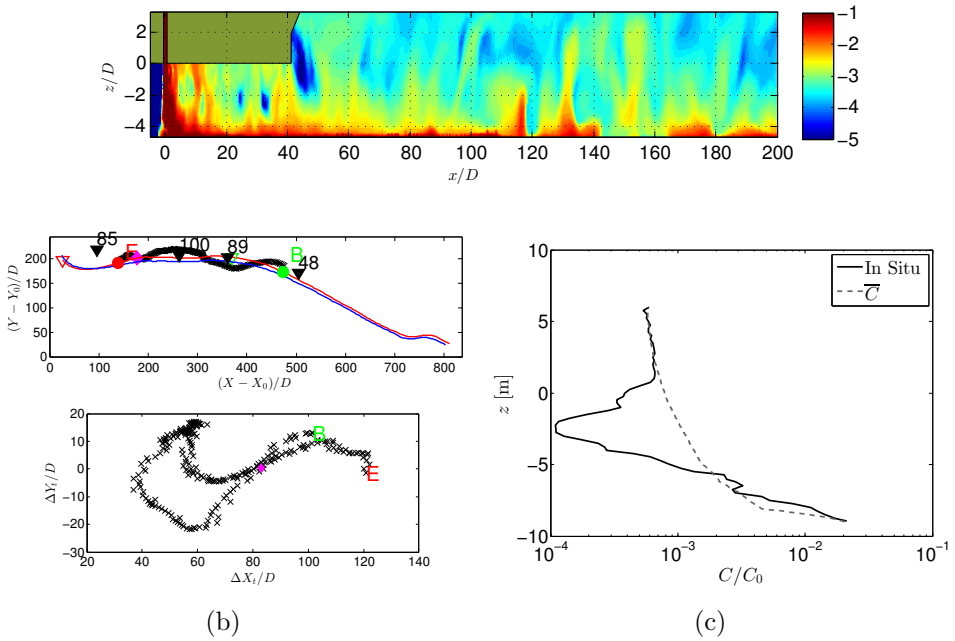

(b) (c)

Figure 8.27: Top panel: Logarithm of the instantaneous concentration c/C_0 in case 1C. (a): Maps of the dredger and survey boat positions, as well as profiling positions during case 1C (colors as in figure 8.19). (b): Comparison of a measured and simulated vertical profile.

a tail current of 0.6 m/s occurred. With a speed of 1.1 m/s over ground, the dredger had a speed through water of about U_0=0.5 m/s. The outflow velocity was still around W_0=1.9 m/s. The map of the situation is shown in figure 8.27a.

The OBS measurements are difficult to compare directly, due to the large scatter in sediment concentration caused by turbulent fluctuations in the plume. The observed c/C_0 is in the same range as the simulated, time-averaged C/C_0 when plotted as function of ΔX_t, z/D and ΔY_t (figure 8.26b).

The vertical profile taken at 160 m behind the dredger's stern (=$\Delta X_t/D$=80) and near the trajectory of the dredger ($\Delta Y_t \approx$0) is shown in figure 8.27b. It can be observed that the surface plume and near-bed density current in the simulation correspond well with the measurements. In the middle of the water column, a pocket of clearer water is found in the measurements and not in the time-averaged simulated C/C_0.

8.6.3 Campaign 2

A second data set was used to compare with the model results. An overflow dredging plume was monitored in the English Channel, 20 km off the coast of France. Compared to the first case, in this area the water depth is considerably higher (40 m on average). The dredging vessel was slightly smaller (L_s=100 m) and had a more narrow overflow shaft (D=1.1 m), which was located closer to the stern (L_o/D= 18.2). In this case, the plume was monitored by relating the backscatter of an ADCP and several OBS instruments to the sediment concentration. Due to the deep water, the OBS instruments towed on a cable were always relatively close to the surface, compared to Cases 1A-C. During this measurement campaign, air bubbles were not affecting the ADCP measurements, possibly due to the narrower overflow shaft and higher trajectory of the plume. No environmantal valve was used during the measurement campaign.

In this data set, no detailed coordinates of both vessels could be processed to ΔX_t and ΔY_t. The comparison of the data with the model is done based on the absolute distance from the survey boat to the TSHD.

8.6.3.1 Case 2A

During case 2A, the average C_0 was about 20 g/l, while the TSHD sailed at 2 knots (U_s=1 m/s). The dredger sailed in a current with average magnitude of 0.5 m/s, and angle between the dredger's course and the current between 160 and 180°. It will be assumed that the TSHD sailed head on against the current. The total speed through water of the TSHD was thus equal to U_0=1.5 m/s. The outflow discharge at the overflow was around 3 m^3/s, leading of an average outflow velocity of $W_0 = Q_0/(0.25\pi D^2)$=3.2 m/s. The water depth was about 40 m and the TSHD had a draft of 6.5 m.

The model was run with an extended downstream domain, up to x/D=900. In this case, at x/D=200, the complete plume was located in the top half of the water column in both model and ADCP measurements (figure 8.28). Further downstream, the plume reaches the bottom at x/D=500, after a sudden drop in the observed lower plume edge. The bottom edge of the simulated plume seems to be located somewhat lower than observed from the ADCP data in the range 220< x/D <470. The plume touches the bottom after x/D=600 in the model. The descent angle and the touchdown location

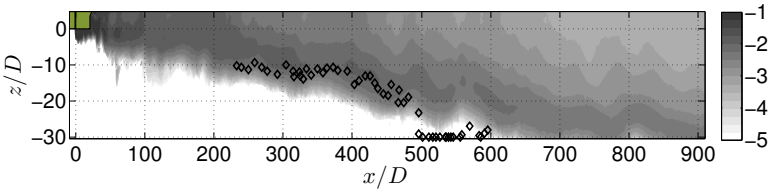

Figure 8.28: $\log(C/C_0)$ *(in grey scale) from the model results. ADCP measurements of the bottom edge of the plume are indicated with markers at values of* C/C_0*=10*$^{-3}$*.*

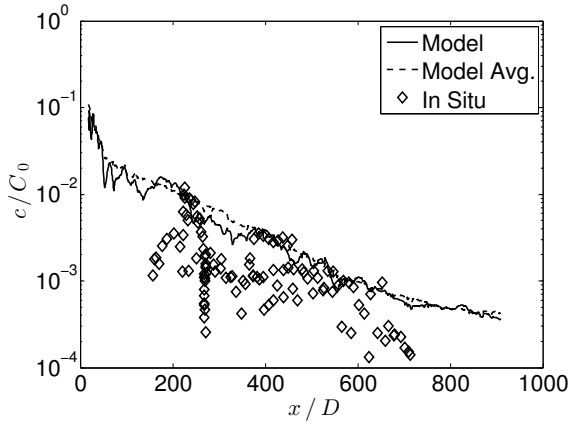

Figure 8.29: Case 2A: Comparison of simulated surface plume concentration c/C_0 *(dashed line) with in situ data (markers). Time-averaged simulation result* C/C_0 *in continuous line. In situ data represents locations outside, at the edge of and inside the plume. Model data is extracted at the symmetry plane.*

is simulated with a reasonable accuracy.

The simulated surface plume concentrations were also compared with OBS-measured surface plume values (figure 8.29). It can be seen that there exists a large spreading in the measurements, due to local variations and a position of the survey boat relative to the plume centreline changing with time. Since the survey boat was sailing back and forth across the plume and the model results are only shown at the plume centreline, it could be defended that only the highest measured values at any x-location should be compared to the time-averaged and instantaneous model results. In that case, the simulated sediment concentrations compare well with the measured concentrations in the range $200< x/D <600$.

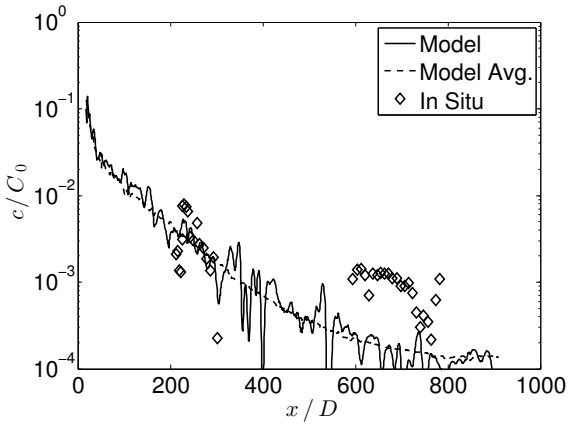

Figure 8.30: Case 2B: Comparison of simulated surface plume concentration c/C_0 (dashed line) with in situ data (markers). Time-averaged simulation result C/C_0 in continuous line. In situ data represents locations outside, at the edge of and inside the plume. Model data is extracted at the symmetry plane.

8.6.3.2 Case 2B

One more case of this data set has been simulated using the LES model. The TSHD sailed at U_s=0.6 m/s, while the current magnitude was about 0.8 m/s. Again, the dredger was sailing almost head-on against the current. Here, U_0 was therefore equal to 1.4 m/s. The overflow mixture sediment concentration was somewhat higher than in case 2A, on average C_0=39 g/l. The outflow discharge was lower, with an average outflow velocity of W_0=2.1 m/s.

For this case, a limited number of OBS data points are available (figure 8.30). When compared with the model, the measurements around x/D=250 correspond well with the model. Some measurements further downstream (x/D=600-800) show higher concentration compared to the model.

8.6.4 Conclusions for the model validation

The LES model is capable of simulating the trajectory and dispersion of the near-field sediment plume in a relatively accurate way. In the prototype cases with influence of air bubbles, an initial air bubble diameter of 2 mm gives the best results. Given the relatively small influence of the initial diameter on the surface plume results, the coalescence model is rapidly transforming the air bubble population to a size distribution that has the capability to drag part of the plume towards the surface. Even though the time-step was set to

0.25 s, rather than 0.125 s, the results are satisfactory. The model correctly distinguished between the two different modes of near-field overflow plume behaviour: (i) a density current combined with a surface plume and (ii) a plume entirely in the upper parts of the water column.

The model in its current set up is considered accurate enough for detailed analysis of the sediment concentration field of the near-field overflow plume. It will also be used in a study of the sensitivity of plumes to a variety of ambient conditions and operational parameters. These aspects will be treated in the next sections.

8.7 Plume sensitivity to boundary conditions

8.7.1 Introduction

In this section, the sensitivity of the near-field overflow plume to varying ambient conditions and operating conditions will be studied. The influence of, amongst others, dredging speed, crossflow angle, water depth and propellers will be determined. To this end, two identical simulations are carried out in which only one variable is changed.

This approach is in many cases only indicative, since the way the plume is sensitive to one ambient condition can be in turn dependent on other conditions. The fully coupled dependency of the major influence factors will be consolidated in a multivariate parameter model in chapter 10.

In de Wit *et al.* (2014c), it was shown that dredging speed, overflow location, propeller-induced advection and turbulence have a significant impact on the dispersion in the near field. In this chapter, it will be tested whether the same conclusions can be drawn using an unstructured grid in which a realistic TSHD geometry is included as well as a dynamic air bubble model. A number of additional influence factors are investigated.

8.7.2 Dredging speed

The influence of the dredging speed is investigated in this section. A simulation with typical operational conditions (C_0=90 g/l, W_0=1.9 m/s) is carried out with different values for the speed through water U_0. In the first simulation, U_0=1 m/s. For example, trailing at U_s=1 m/s through still water. The

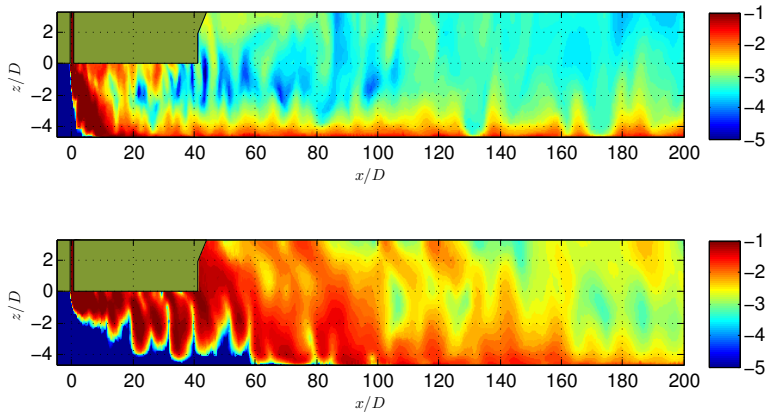

Figure 8.31: Contours of $\log(c/C_0)$. *Top panel: Overflow plume with* U_0*=1 m/s. Bottom panel: same simulation with* U_0*=3 m/s.*

resulting plume is shown in figure 8.31, top panel. In this case, the bulk of the released material moves to the sea bed rapidly, forming a density current and a more dilute surface plume, with $c/C_0 \approx 10^{-3.5}$ at x/D=100.

In the second case, the speed throug water was increased to U_0=3 m/s. For example, this situation occurs while trailing with speed over ground of 2 m/s in a current velocity of 1 m/s, head on. The resulting plume is shown in figure 8.31, lower panel. It is shown that due to the increased U_0, a large part of the plume is lifted enough to be caught by the propellers. As a result, a much higher amount of sediment is mixed towards the surface. The sediment concentration in the surface plume is $c/C_0 \approx 10^{-2.5}$ at x/D=100. A threefold increase in U_0 has therefore resulted in a tenfold increase in the surface plume concentration.

8.7.3 Crossflow

A case was simulated in which a TSHD sailed at U_s=0.9 m/s (over ground) in a perpendicular cross current of U_c=0.45 m/s. See figure 8.32a for a sketch. This results in a net speed through water of U_0=1 m/s and an angle between the ship centerline and its speed through water of ψ=26.6°. In the LES model, the ship is considered stationary with its centerline along the x-axis and the net current is imposed at the boundary. The angle of 26.6°is, however, an overestimation. Indeed, for a ship to follow its course in a cross current, it must develop some yaw angle. A ship's yaw angle is the angle

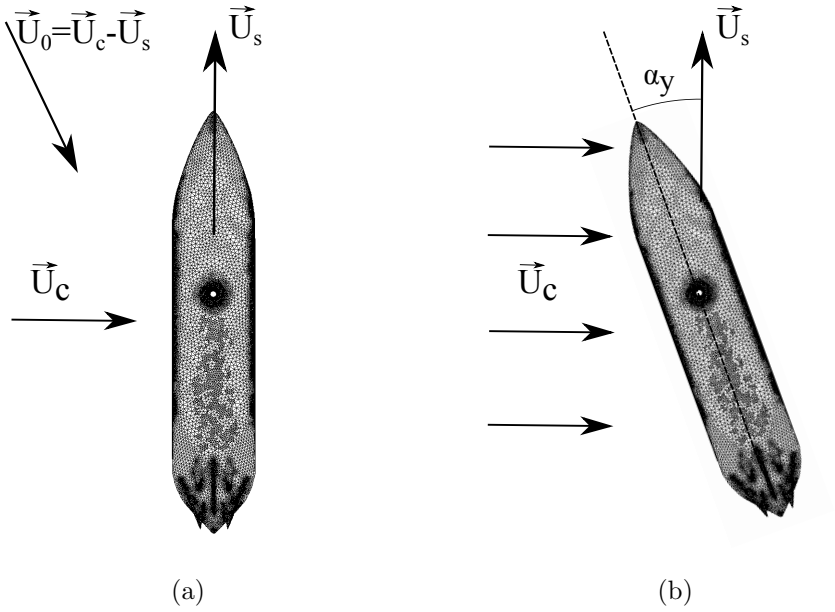

(a) (b)

Figure 8.32: (a) Modeling approach for a ship in a cross current: the through-water velocity U_0 is equal to the cross current velocity vector U_c minus the ship's course vector U_s. (b) Definition of the yaw angle α_y of a ship sailing in a cross current.

between the course and the vessel centerline (figure 8.32b). When a ship is sailing in a cross current, its yaw angle or drifting angle α_y is estimated by PIANC (2014).

$$\tan \alpha_y = \frac{U_c}{U_s} \tag{8.8}$$

This equation returns exactly the same angle as initially found for the angle between the ship centerline and the velocity vector relative to the water, U_0. This means a ship would always align itself with the relative velocity U_0. A TSHD with drag head on the sea bed has some kind of anchoring, due to which α_y might be smaller than atan(U_c/U_s). However, setting the angle ψ simply to atan(U_c/U_s) is not correct. The angle between a ship and its speed through water will be much lower. In this sense, the simulation with ψ=26.6°corresponds with a situation with a crossflow significantly stronger than 0.45 m/s, or with an anchored TSHD serving as a barge for cutter dredgers. The other plume boundary conditions were set to C_0=55 g/l and W_0=1.9 m/s.

When looking at the time-averaged C/C_0 in a cross section (x/D=50), it can be observed that the plume is asymmetric (figure 8.33, top panel). It can be seen that the surface plume is situated around y/D=15 at x/D=50. The angle of the path of the surface plume is therefore about atan(15/50)=16.7°. This is lower than the angle between the ship and the relative velocity U_0. The near-bed density current is positioned around y/D=30, corresponding to a path angle of atan(30/50)=31°. This is larger than the angle of the relative velocity U_0. The density current and the surface plume clearly feel the influence of the cross current in a different way. In order to analyse this situation, a detailed three-dimensional visualisation is needed.

The resulting surface plume and subsurface density current are shown in figure 8.33, middle panel. It can be seen that the density current follows another angle compared to the surface plume. The descending density current feels a secondary current induced by the angle between ship and flow. Therefore the density current is diverted towards a higher angle than the crossflow (towards the left of the figure). In the lower panel of the figure, a top view is shown with streamlines originating at the left side of the figure near the bed (black) and near the surface (red). The surface plume and density current are partially transparent. It can be seen that the density current is blocked by the black streamlines below the surface plume. On the other side of the density current it is widening, against the direction of the ambient current. On that side, the near-bed streamlines are also diverted with the widening density current. The surface plume is following the direction of the near-surface streamlines. The near-surface streamlines approach the TSHD from the lower-left and dive under the keel. On the downstream end of the ship, a secondary current can be distinguished by the twisted streamlines. Further downstream, the near-surface streamlines again follow the crossflow direction, and so does the surface plume.

The question is now whether the surface plume in a crossflow has significantly different concentration levels as compared to a plume without crossflow. In figure 8.34, the instantaneous concentration $\log(c/C_0)$ for a plume without crossflow and for the same plume with a crossflow is shown. The concentration levels in the surface plumes are very similar. The surface plume in the crossflow case is wider and has a larger variation in c. It can be calculated, however, that the total sediment flux in both plumes is quite similar.

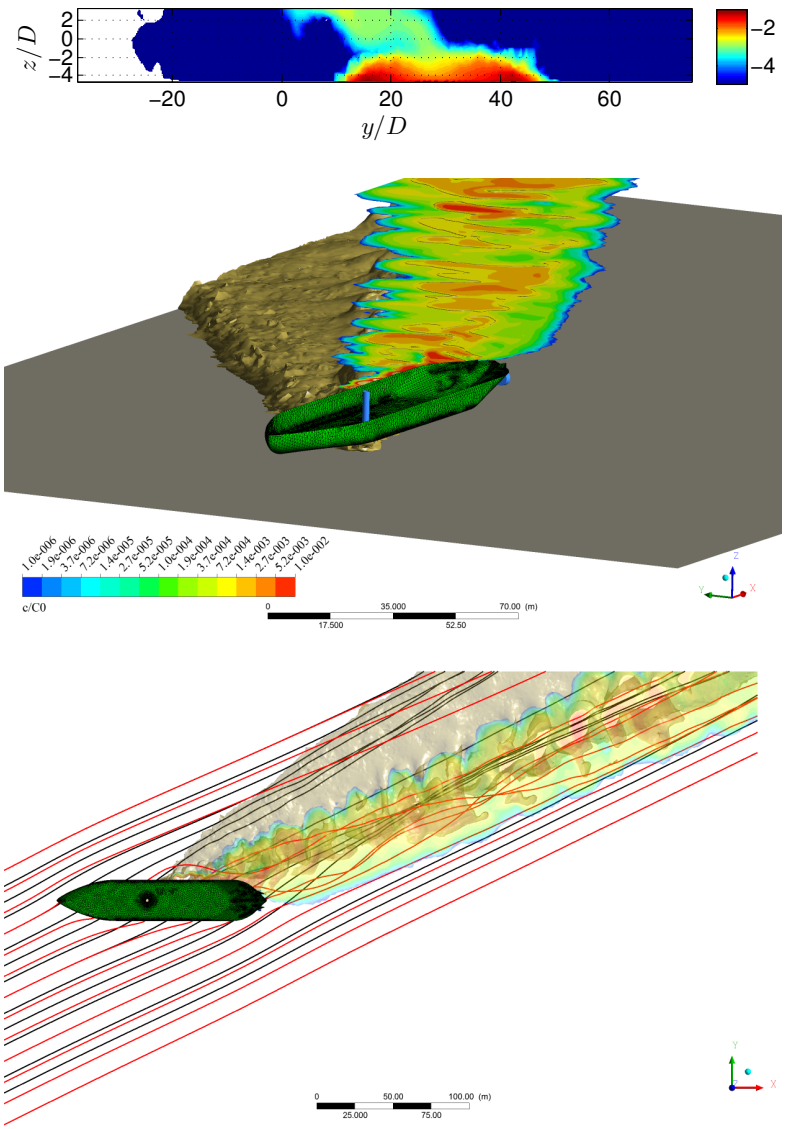

Figure 8.33: TSHD sailing in a crossflow. Top panel: Vertical cross section of time-averaged sediment concentration field $\log(C/C_0)$ *at* x/D*=50. Middle panel: Surface plume concentration* c/C_0 *in colour scale and density current in brown iso-surface. Bottom panel: Top view of the same situation with addition of streamlines originating at the left side near the bed (black) and near the surface (red).*

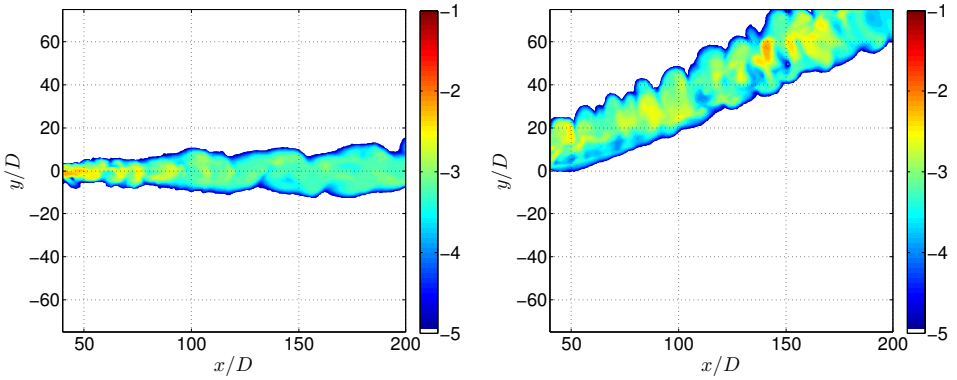

Figure 8.34: Instantaneous concentration $\log(c/C_0)$ *for a plume without crossflow (a) and for the same plume with a crossflow (b).*

8.7.4 Water depth

In this section the influence of the water depth on the sediment concentration in a surface plume is investigated. The reference case is the case shown in figure 8.31a. It will be compared with one simulation with smaller water depth and three simulations with larger depth. The water depth in figure 8.31a is 16m, and the keel clearance H_k=9.4 m.

In figure 8.35, vertical profiles of C/C_0 are given at y=0 and x/D=100 and horizontal profiles are shown in the surface plume at y=0 and at 0.5 m below the surface. It can be observed that the case with keel clearance of 5 m differs substantially from the other cases. The sediment concentration in the surface plume is about 4 times higher at x/D=100. In the horizontal profile, the concentrations are similar for the cases with $H_k \geq$9 m, but for H_k=5 m the surface concentration increases significantly at about x/D=60. This location is at 30-40 m behind the propellers.

To check the influence of the propellers at plumes in different water depths, the instantaneous streamwise flow velocity is compared for the cases with H_k=5 m and 9 m (figure 8.36). In the case with H_k=9 m, no significant propeller-induced velocity increase is found near the sea bed, where the density current related to the sediment plume is located (figure 8.36a). It is found that in the case with H_k=5 m, the propeller wash reaches the bottom at x/D=60, with a significant velocity increment (figure 8.36a). Indeed, as a consequence the sediment is drwan in the propellers and brought up to the

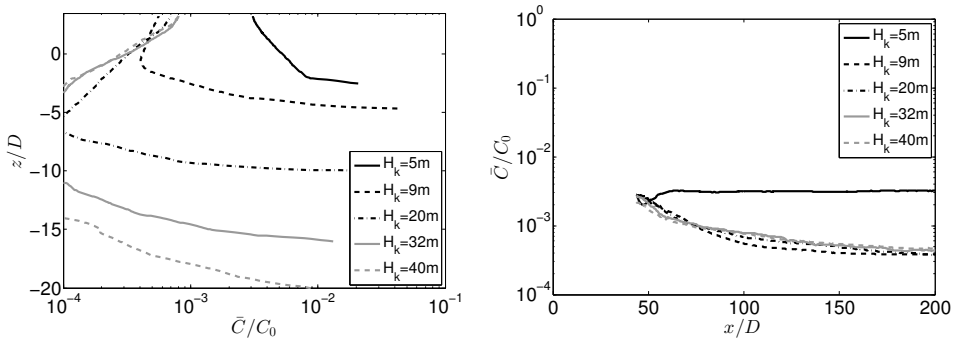

Figure 8.35: Time-averaged sediment concentration C/C_0, for three identical cases except for the different keel clearance H_k. In figure (a), vertical profiles are given at y=0 and x/D=100. In figure (b), horizontal profiles are given at y=0 and at 0.5 m below the surface.

surface by the propeller-induced turbulence (figure 8.36c).

An additional effect of shallow water is the possibility that fluffy sediment in the density current might remain available for resuspension due to waves.

8.7.5 Sediment load

The basic dimensionless numbers governing the behaviour of a buoyant jet were identified in section 2.3.2 as the densimetric Froude number F_Δ and the velocity ratio λ. The sediment load in the overflow mixture, C_0, influences directly the Froude number F_Δ. It is therefore expected that C_0 has an influence on the trajectory of near-field dredging plumes.

A total of eight cases are compared with identical water depth H=16m, W_0=1.9 m/s, U_0=1 m/s and D=2m. The overflow was located at the front end of the hopper, at L_o=80 m from the stern. The two extremes are shown in figure 8.37, with C_0=10 g/l (a) and C_0=150 g/l (b). In these plots, the sediment concentration is shown, as before, as the relative value compared to C_0. Since in this case C_0 is varied this gives a distorted view. However, it is interesting to see that in the case of C_0=10 g/l the fraction of the initial sediment discharge (C_0Q_0) present in the surface plume is about 100 times higher compared to the case with C_0=150 g/l. Evidently, in the field the absolute value of the sediment concentration is of importance. Yet, the question could be raised whether the total amount of sediment brought in suspension

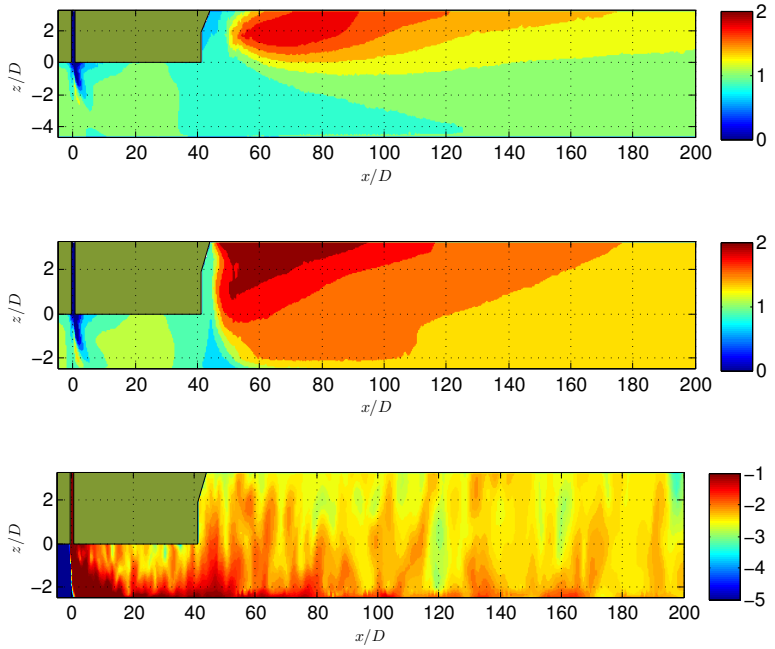

Figure 8.36: Time-averaged streamwise velocity at y=0. In figure (a) with H_k=9 m, in figure (b) with H_k=5 m. In figure (c) the instantaneous concentration $\log(c/C_0)$ *is shown for the same case as in (b).*

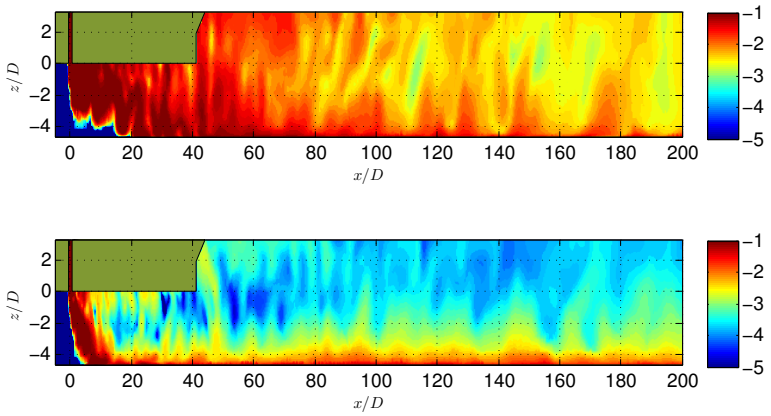

Figure 8.37: Relative sediment concentration $\log(c/C_0)$ *at the symmetry plane, with* H*=16m,* W_0*=1.9 m/s,* U_0*=1 m/s,* L_o*=80m and* D*=2m. The sediment concentration at the overflow was varied:* C_0*=10 g/l (a) and* C_0*=150 g/l (b).*

during a project could be reduced by releasing a more concentrated mixture. How this could be achieved in practise, is another question.

Nevertheless, it is needed to analyse the absolute time-averaged concentration C in the surface plume as a function of the release concentration C_0. In figure 8.38, the results for simulations with eight different values for C_0 are shown. In this figure, the absolute concentration in g/l is shown at 0.5 m below the water surface. It is surprising to see that very consistently, the sediment concentration in the surface plume decreases when the intial overflow concentration C_0 is increased. Between the stern at x/D=40 and x/D=120, the surface plume with C_0=10 g/l has sediment concentrations about twice as high as the plume with C_0=150 g/l. Further downstream, the difference becomes smaller, to about a factor 1.5.

This observation leads to the conclusion that releasing a more concentrated water-sediment mixture could significantly reduce the total amount of sediments brought in suspension. The technical aspects of how this higher C_0 can be achieved could be the topic of further research.

8.7.6 The presence of a sand fraction

In many cases, a fraction of very fine marine sand can stay in suspension in the hopper unitil the mixture reaches the overflow (Smith and Friedrichs,

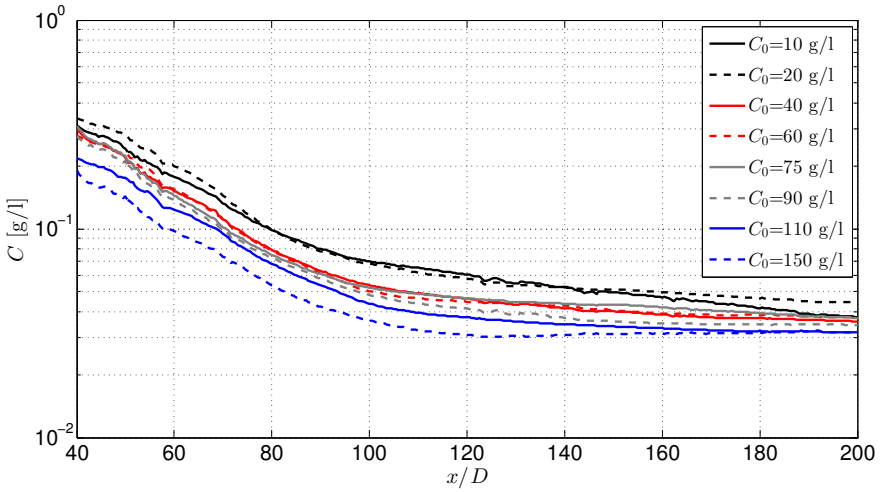

Figure 8.38: Comparison of absolute sediment concentration C as a function of the initial overflow concentration C_0.

2011). Sand concentrations are between 0% and 30%, but a large variation can exist depending on the sea bed grain size distribution, the dredging equipment and the level of the sediment load in the hopper. In our field measurements, the fraction of fine sand (125 μm < d <250 μm) was on average 7%, with a standard deviation of 5%. The relevance of a fraction of fine sand in the overflow mixture on the prediction of near-field sediment concentrations depends largely on the level of segregation of sand and mud plumes. Therefore, two simulations were executed with the same C_0. The initial sediment load consisted of two fractions.

$$C_0 = C_{0,f} + C_{0,s} \tag{8.9}$$

where $C_{0,f}$ is the mass concentration of fines and $C_{0,s}$ is the mass concentration of sand.

In one simulation $C_{0,s}/C_0$=0, in the other simulation, $C_{0,s}/C_0$=0.1. The sand fraction consisted of a uniform grain size of 125 μm. All other boundary conditions were kept equal (U_0=1.5 m/s, W_0=3 m/s, D=1.1 m and H=40 m). These conditions result in a plume in the upper half of the water column, in which the segregation of the plumes of fines and sand can be studied.

In figure 8.39, the vertical profiles of the total sediment concentration are shown for both simulations, at x/D=100 and 200. After x/D=100, no significant difference in the distribution of the total sediment concentration is

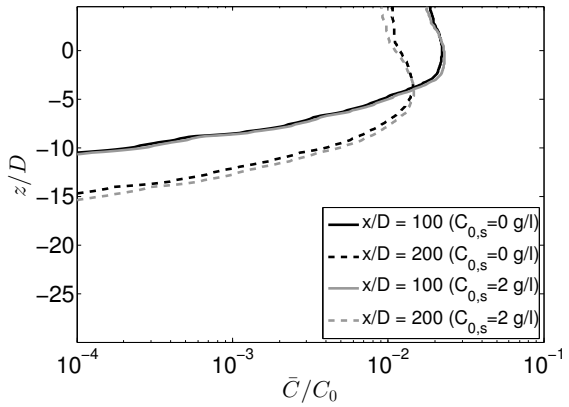

Figure 8.39: Profiles of time-averaged sediment concentration C/C_0 for a case with high trajectory. Comparison of results with (i) 100% fine sediments (sand concentration $C_{0,s}$=0 g/l) and (ii) 90% fines and 10% fine sand (sand concentration $C_{0,s}$=2 g/l).

found. A very minor shift from surface (z/D >0) to the lower parts can be seen. This shift amounts to less than 5%. At x/D=200 the same effect is found but somewhat stronger, which is logical due to the continued settling of the fine sands. Also, in the part nearest to the ship and propellers, the sand settling is counteracted more due to upward turbulent diffusion. At x/D=200, this effect is lower due to the decaying turbulence. The downward shift in mean sediment concentration after x/D=200 is, however, still small. In the surface plume, the concentration is about 10% lower in the case with fine sand, which is compensated by a slightly increased concentration in the lower part of the plume.

It can be concluded that a fraction of fine sand does segregate from the fine sediment plume, but the process is too slow to be of importance in the near field. A concentration profile can be computed with uniform sediment size in a near-field model, to be feeded in a far-field model. It can be assumed that the sand-mud ratio and the segregated settling of both fractions can subsequently be handled in the far-field model.

8.7.7 Air bubbles

The plunging jet inside the overflow shaft leads to entrainment of air bubbles in the plume (Saremi and Jensen, 2014b). In all simulations described so far, these air bubbles were taken into account. In order to isolate the effect of

these bubbles, a number of simulations have been executed with a reduced volume fraction of air. Saremi and Jensen (2014b) simulated the reduction in air entrainment that can be achieved using a valve inside the overflow shaft, choking the flow (the so-called environmental valve). They found a reduction of more than 90% of the initial air volume fraction $\phi_{a,0}$ in the overflow at a valve closing position of 15°.

The effect of the air bubble reduction is roughly indicated in this section by comparing the simulation with and without air reduction for two cases: a high plume case and a case with plume sediment mixed throughout the water column. In figure 8.40, the results are shown in terms of vertical sediment concentration profiles at the plume centerline. In the case with deep water and a high plume trajectory (figure 8.40a), the effect of removing 90% of the air bubbles is clear. The concentration near the surface is reduced drastically (factor 20), which can be explained by the absense of the vertical momentum source in the water-sediment mixture due to the wakes of the rising air bubbles (eq. 7.26). It is also observed that the bulk of the plume is situated deeper with a reduced air concentration. This effect is simply explained by the increased bulk density of the plume when the air volume fraction is lower. The bulk mass density of the water-sediment-air mixture is defined by:

$$\rho_m = (1 - \phi_s - \phi_a)\rho_w + \phi_s\rho_s + \phi_a\rho_a \tag{8.10}$$

where ϕ_s and ϕ_a are the volume fractions of sediment and air and ρ_m, ρ_s, ρ_w and ρ_a are the mass densities of respectively the mixture, the sediment, sea water and air.

It can be shown that for an air fraction of 7%, mixtures with C_0 up to 13 g/l have a positive buoyancy, which means they are lighter than the surrounding sea water. For ϕ_a=14% this is even the case up to C_0=26 g/l.

Both effects lead to a lower average position of the sediments brought in suspension. This reduces the range the sediments can travel in most cases, since they will reach the bottom after a short distance. It also reduces the potential for resuspension and upward turbulent mixing due to surface waves.

In the case with more shallow water and a near-bed density current combined with a surface plume, a different result is found (figure 8.40b). The bulk plume volume cannot descend deeper in the case with air reduction, since it is almost fully mixed throughout the water column. The surface con-

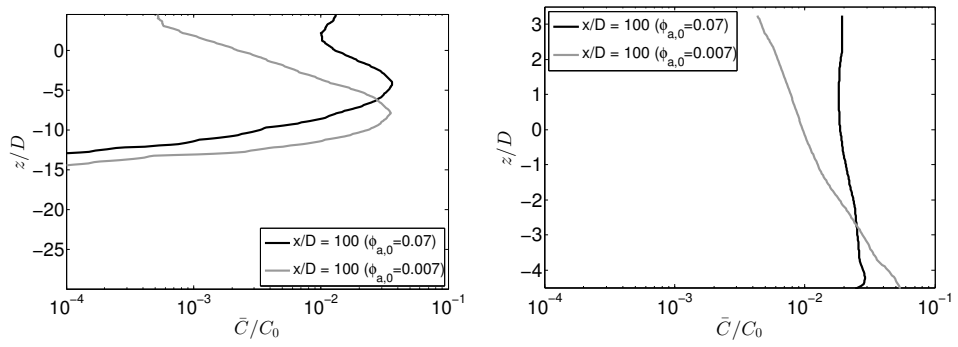

Figure 8.40: Profiles of time-averaged sediment concentration C/C_0 for a case with high trajectory (a) and a case with mixed sediments (b). For each case, a simulation is run with a regular initial air bubble volume fraction ($\phi_{a,0}$=7%) and with a 90% reduction of $\phi_{a,0}$=0.7%.

centrations, however, are also positively affected by the air reduction. It can be observed in the figure that with $\phi_{a,0}$=7%, the sediment is mixed, while with $\phi_{a,0}$=0.7%, the surface concentration is about 5 times lower than the near-bed concentration. Clearly, the air bubbles have a mixing effect on the plumes in more shallow water. Again, the effect of removing the air bubbles is that the plume has less potential to travel long distances to environmentally sensitive areas.

The efficiency of the environmental valve responsible for the air bubble reduction is assessed in more detail in section 9.1.

8.7.8 Propellers

Whether the near-field overflow plume would be different without the propeller jet influence is of course a hypothetical question. No TSHD can sail without propellers. Nevertheless, it is interesting to see how the propeller influences the streamlines around the ship and how this in turn influences the (surface) plume.

Streamlines starting from the propellers, extending upstream and downstream, show how the propeller jets evolve (figure 8.41). As also shown in section 8.4.2, it can be observed that the tangential component of the propeller jet is only short-lived. At a distance of $4D$, 90% has dissipated.

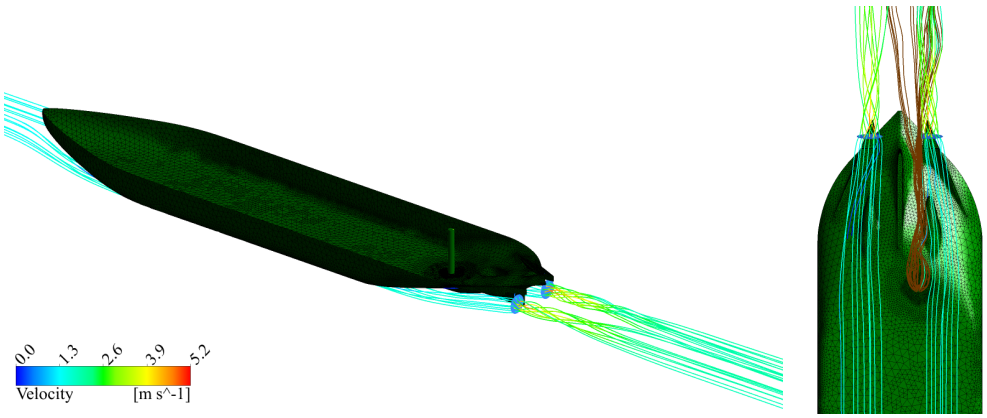

(a) (b)

Figure 8.41: Port side view of the streamlines going through the propellers (a). Bottom view of propeller streamlines and streamlines originating from an overflow with lateral shift of B_o=5 m.

Additionally, figure 8.41 shows from where the propeller jet discharge originates. It can be seen that the propeller jet discharge originates from the keel, but not from the central part of the keel. In the case of an overflow positioned along the axis of the ship, propeller streamlines do not go directly from overflow to propeller. In case of an overflow away from the ship axis (figure 8.41b), the sediment might go directly into the propellers.

The propellers also induce turbulent mixing. Following the gradient diffusion theory, turbulent mixing occurs in down-gradient direction. The vertical turbulent diffusion can be written as

$$F_z = -D_t \frac{\partial C}{\partial z} \tag{8.11}$$

where D_t is the turbulent diffusivity.

Therefore it is needed to visualise the vertical gradient of C before the plume arrives at the propeller influence. In this case, the propellers are at x/D=40, but the influence of both propellers arrives at the centerline somewhat further. The propeller jets are located at a height of $0< z/D <3$. In figure 8.42a, a case is shown with $\partial C/\partial z <0$ before arrival at the propellers (x/D=30). At x/D=50 not much influence is found yet. At x/D=100, however, the footprint of the propeller mixing is recognised. The negative vertical concentration gradient is flattened out due to turbulent mixing, and thus results in

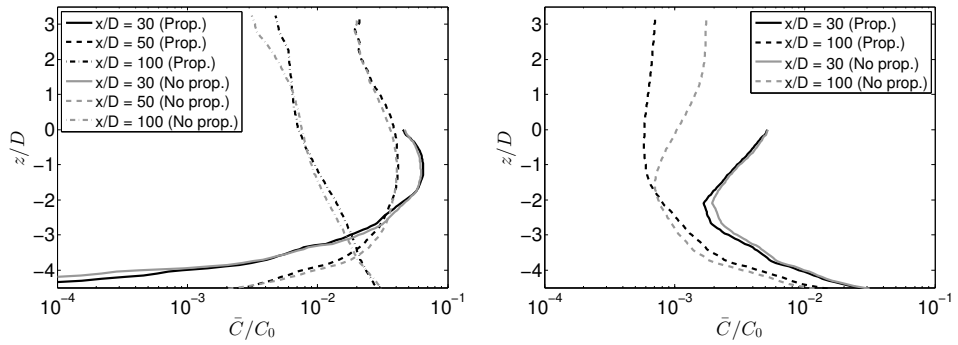

Figure 8.42: Profiles of time-averaged sediment concentration C/C_0 for two plume cases: one with $\partial C/\partial z < 0$ near the keel and under the stern (a) and one with $\partial C/\partial z > 0$ at the same location (b). For each case, a simulation is run with and without propeller jets.

an increase in the surface plume concentration.

In figure 8.42b, a case is shown with $\partial C/\partial z > 0$ at x/D=30. The turbulent sediment flux is therefore expected to be downward. Indeed, at x/D=100, the sediment in the surface plume seems to be transported by the propeller jets to deeper parts, and the surface plume has a lower C.

It can be imagined that in most cases, $\partial C/\partial z$ might be smaller than zero since the plume emerges from under keel. However, the three-dimensional situation is more complex. The two propeller jets start away from the centerline, widen and meet the centerline after a certain distance. Over the course of this distance, the plume might have risen and $\partial C/\partial z$ might be larger than zero. This is again a case of coupled interaction between multiple parameters. These effects will be consolidated in the multivariate parameter study in chapter 10.

8.7.9 Position and diameter of a single overflow

The position of the overflow relative to the stern is important, since it determines the shape of the plume at the start of the influence of the stern section and of the propeller jets. The distance between overflow and stern, L_o, as well as the lateral shift B_o are shown in figure 8.43.

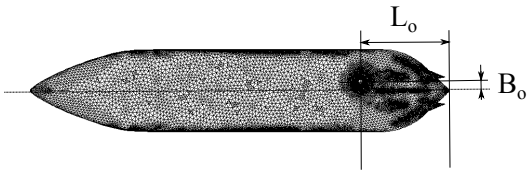

Figure 8.43: Definition of longitudinal and lateral overflow position L_o and B_o.

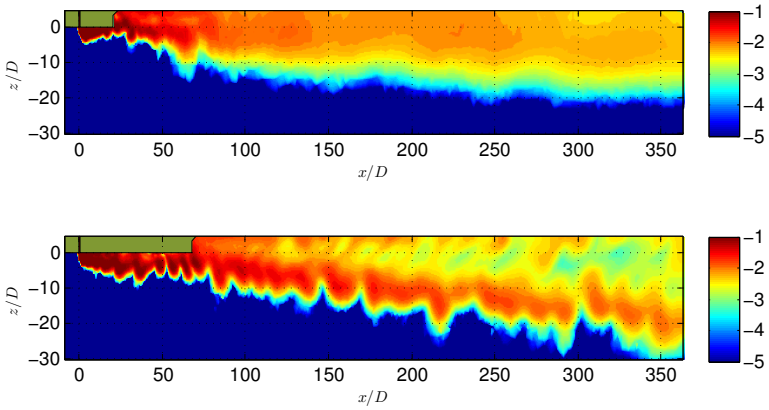

Figure 8.44: Relative sediment concentration $\log(c/C_0)$ at the symmetry plane, with H=40m, W_0=3.2 m/s, U_0=1.5 m/s, C_0=20 g/l and D=1.1m. Overflow position L_o was varied: L_o=20m (a) and L_o=80m (b).

First, the influence of L_o is investigated. It can be anticipated that a longer distance L_o is beneficial for the surface plume. When looking at the simulation results for a relatively horizontal plume (figure 8.44) the longer distance L_o seems to give the plume more time to detach from the keel and escape the propeller mixing. A smaller L_o (figure 8.44a) causes the plume to be caught in the uplifting flow behind the stern after which the propeller mixes the plume. The result is a much more uniform sediment distribution and a higher concentration in the surface plume.

When looking at the results for a more dense plume with more rapid descent, the difference between smaller and longer L_o is less evident (figure 8.45). Already after the short distance L_o=30 m (figure 8.45a), the plume has had the time to detach slightly from the hull. Therefore, the mixing of the propeller jet can just be avoided. The surface plume concentration is therefore only slightly higher compared to the case with L_o=80 m (figure 8.45b). Obviously,

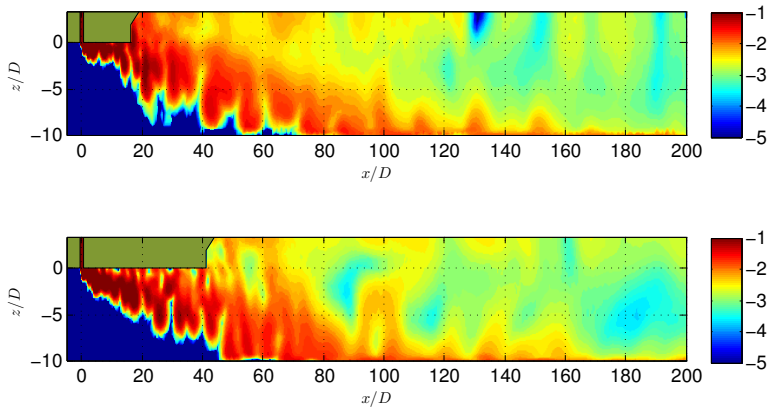

Figure 8.45: Relative sediment concentration $\log(c/C_0)$ *at the symmetry plane, with* H*=26 m,* W_0*=1.9 m/s,* U_0*=2 m/s,* C_0*=90 g/l and* D*=2 m. Overflow position* L_o *was varied:* L_o*=30 m (a) and* L_o*=80 m (b).*

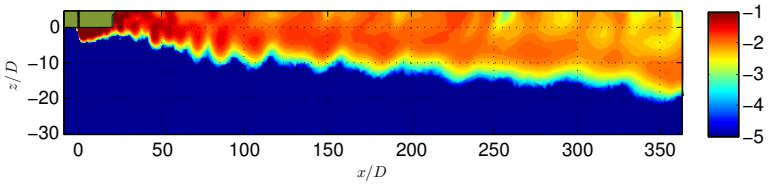

Figure 8.46: Relative sediment concentration $\log(c/C_0)$ *at the symmetry plane, boundary conditions as in figure 8.44a,* L_o*=20 m. The lateral overflow position* B_o *was changed to 5 m.*

variations in the other boundary conditions will lead to a different behaviour.

In some vessels, an overflow is located away from the centerline. The same case as in figure 8.44a has been simulated with the overflow at B_o=5 m off the centerline (figure 8.46). The effect of B_o >0 depends on the geometry of the stern section and of L_o. In this case, the strongly curved hull sections near the stern and away from the ship's centerline cause an uplifting flow, taking the plume upwards and causing an increased surface plume concentration. When the overflow is positioned at the centerline, these sloping parts are not encountered by the plume. At least in the geometry with which this model has been set up.

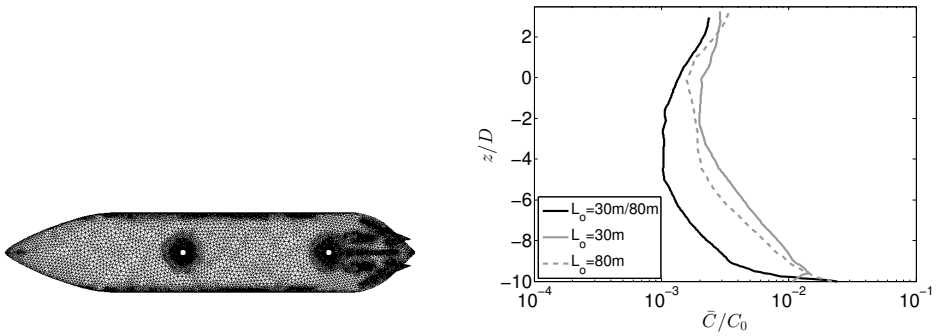

(a) (b)

Figure 8.47: (a) View of the position of the two overflows in the vessel. (b) Profiles of time-averaged sediment concentration C/C_0 for three plume cases: L_o=30 m/80 m with two overflows with distributed discharge and two cases with a single overflow at L_o=30 m and 80 m.

8.7.10 Number of overflows

In this section, the effect of multiple overflows on the sediment plumes is discussed. A case has been set up with the same boundary conditions as in figure 8.45a. In that figure, two cases are shown. One with L_o=30 m and one with L_o=80 m. In the current case, the overflow discharge has been equally distributed over two overflows by halving the outflow velocity and keeping the same pipe diameter D and concentration C_0. The resulting vertical sediment profile at x/D=100 is shown in figure 8.47. The case with multiple overflows is not in between the cases with a single overflow at 30 m and 80 m. Even though the lower exit velocity W_0 should be a disadvantage in descending deeper, the plume in the multiple overflow case has a deeper average position. The overall concentrations are also lower. In a cross section it can be observed (not shown) that the case with multiple overflows has a larger width, due to which the sediment is more diluted and the concentrations are lower. The increased width is probably caused by the upstream plume meeting the exit jet of the downstream plume and is moving around it.

8.7.11 Conclusions on boundary conditions sensitivity

It is clear that through-water velocity U_0, water depth H, initial sediment concentration C_0, air bubbles, propellers and the overflow position L_o and diameter D all have a profound influence on the plume shape and the dispersion of the sediments. Some influences, such as propeller jets, are inherent to

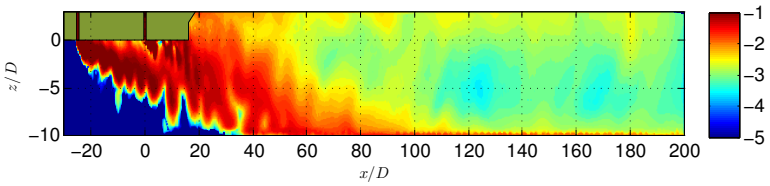

Figure 8.48: Relative sediment concentration $\log(c/C_0)$ *at the symmetry plane, boundary conditions as in figure 8.45. The overflow discharge is equally distributed over two overflows with D=2 m.*

the operation of a TSHD. However, some influencing factors might be steered due to which plume dispersion can be mitigated.

Moreover, the sensitivity of the plume dispersion to one parameter is dependent on most other parameters. The variations in plume shape demonstrated in this section are therefore indicative and do not encompass the full complexity of the plume sensitivity. Therefore, a statistical approach will be followed to extract a multivariate regression model from a large number of simulations covering the full range of boundary conditions.

8.8 Conclusions on the full-scale model

The validated laboratory-scale model was taken as a starting point for the validation of the Reynolds independency of the model. After validation of the upscaling operation, a detailed TSHD geometry has been implemented in the model domain, as well as two propellers. A number of additional validation cases for the propeller jet and for multiple plume merging have been completed sucessfully. A sensitivity analysis of the model parameters showed that the model is not excessively sensitive to parameters related to the turbulence model, the advection scheme, the grid resolution and the time step.

The final model approach has been validated against overflow plume measurements taken in the field. The simulated sediment concentration distributions are in relatively good agreement with observations in five plume cases.

Finally, an indication is given of the sensitivity of the sediment dispersion to nine conditions related to the ambient circumstances and TSHD operation.

Chapter 9

Applications of the LES model

The first section in this chapter, section 9.1, appears also in Decrop et al. *(2015c).*

9.1 The efficiency of an environmental valve

The application of an environmental valve choking the flow through the overflow has been described in literature in the past (Van Parys *et al.*, 2001; PIANC, 2010). Instead of a water level in the overflow shaft well below the crest and the resulting plunging flow (figure 9.1, left), the overflow is submerged and full pipe flow is obtained (figure 9.1, right). A 15° closing angle of the butterfly valve already leads to a reduction of air by 90%, while the discharge through the overflow is reduced by only 15% (Saremi and Jensen, 2014b).

In this section, the efficiency of this type of valve in a wide range of conditions has been simulated using the numerical modelling tool described in the previous chapters. A total of 23 cases have been simulated with full air concentration of ϕ_a=0.07 (table 9.1). For comparison purposes, the same cases have been simulated with a 90% reduction in air concentration due to the environmental valve. The liquid discharge was kept equal.

For all cases, the total horizontal sediment flux in the surface plume has been determined with and without the air bubble reduction induced by the environmental valve. An environmental valve efficiency is then determined from the resulting reduction in surface plume sediment flux. The environmental

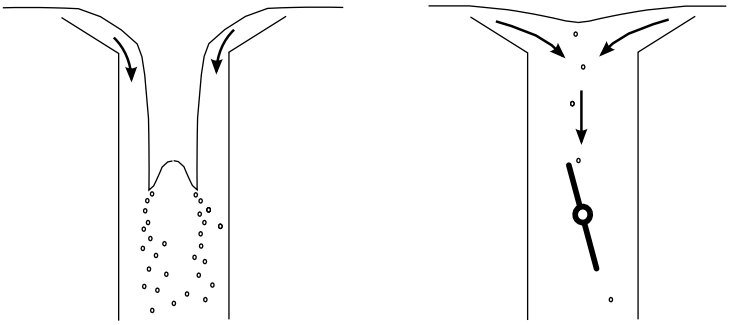

Figure 9.1: Schematic of the overflow shaft without environmental valve exhibiting plunging jet flow (left) and choked flow in the overflow with environmental valve, drastically reducing the number of entrained air bubbles (right).

valve's efficiency is computed from the model results as follows. First, the three-dimensional sediment flux field $f(x, y, z)$ is integrated in the lateral y-direction to obtain a vertical distribution of the sediment flux q_s at each location behind the dredger.

$$f(x, y, z) = C(x, y, z)U(x, y, z) \tag{9.1}$$

$$q_s(x, z) = \int_{-B_w/2}^{B_w/2} f(x, y, z)\, \mathrm{d}y \tag{9.2}$$

where B_w is the width of the plume (between nearest $|y|$-positions at which no sediment concentration C/C_0 >10^{-6} is found).

Next, a threshold level z_c is defined above which the air bubble-influenced surface plume is considered. The flux q_s is then integrated from a threshold depth z_c up to the water surface and normalised by the total sediment flux released through the overflow, $Q_{s,0}$, to obtain a relative surface plume sediment discharge Λ_s.

$$\Lambda_s(x) = \frac{1}{Q_{s,0}} \int_{z_c}^{H} q_s(x, z)\, \mathrm{d}z \tag{9.3}$$

The position x at which the surface plume flux is evaluated has to be chosen. The valve efficiency has to be determined based on passive plumes with low density difference $\Delta\rho$. One could think of a distance behind the dredger where the plume has diluted to a concentration at which it has become a passive plume. However, this would make the different cases more difficult

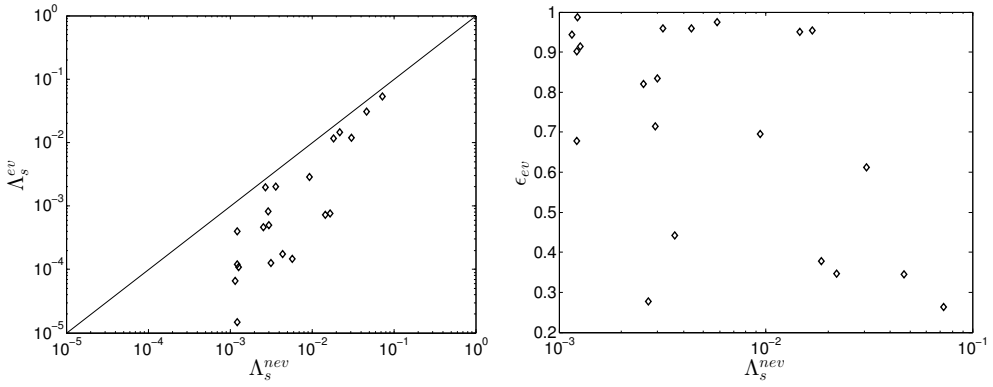

(a) (b)

Figure 9.2: Relation between surface plume sediment flux without valve (Λ_s^{nev}) and with valve (Λ_s^{ev}) (a). Relation between valve efficiency and surface plume flux (b).

to compare. The choice is made arbitrarily at x=2.5L_s, i.e. not too close to the dredger so that dynamic plumes in the evaluation are avoided, and not too far to avoid completely diluted plumes. The surface plume sediment flux without valve will be denoted as Λ_s^{nev}, the flux with the use of a valve as Λ_s^{ev}. When the Λ_s values (for z_c=0 and x/L_s=2.5) with and without environmental valve are plotted (figure 9.2a) it is found that for the 23 cases without valve, the surface plume contains a fraction of the released sediment flux (Λ_s) of between 10^{-3} and $7\text{x}10^{-2}$. It is likely that this wide range can be explained by the characteristics of the flow parameters F_Δ, λ and L_o/D.

Table 9.1: Overview of the 23 cases simulated with and without environmental valve. [a]Shallow water, [b]Deep water

$F_\infty = F_\Delta\lambda$	L_o/D	$F_\infty = F_\Delta\lambda$	L_o/D	$F_\infty = F_\Delta\lambda$	L_o/D
3.2	40	4.17	18.18	4.38	40[a]
1.07	40	5.9	18.18	2.09	18.18
1.95	40	7.62	18.18	4.38	40[b]
0.73	40	4.82	18.18	0.34	40
4.17	65.45	4.17	43.64	0.88	40[a]
0.97	40	1.64	18.18	0.49	40
2.09	65.45	3.06	18.18	0.88	40[b]
1.87	43.64	1.76	15		

Moreover, it can be seen that with environmental valve, the range of Λ_s^{ev} changes to 10^{-5} to $5\text{x}10^{-2}$. In cases with a high value of Λ_s^{nev} the valve does

not seem to have a significant influence, while in cases with a low value of Λ_s^{nev} the valve reduces the sediment flux in the surface plume by two orders of magnitude. The efficiency of the valve , ϵ_{ev} can now be defined as follows:

$$\epsilon_{ev} = 1 - \frac{\Lambda_s^{ev}}{\Lambda_s^{nev}} \tag{9.4}$$

The efficiency of the 23 cases ranges from ϵ_{ev}=0.26 to ϵ_{ev}=0.99. In other words, the air bubble reduction due to the environmental valve caused a reduction of the sediments in the surface plume by 26% to 99%. Clearly, one or more factors influence the efficiency of the valve greatly.

To investigate the reason for this wide range of efficiencies, ϵ_{ev} is plotted against the relative sediment flux without valve, Λ_s^{nev}. In figure 9.2b it can be seen that plumes containing only a small fraction of the released sediments can potentially be very effectively mitigated by an environmental valve, but plumes which are to a large extent drawn to the surface cannot. Indeed, dredging plumes of which the major part descends to the seabed as a density current, and of which a minor part is stripped due to air bubble entrainment, have small Λ_s^{nev}. In these cases, taking away the effect of air bubbles has an important impact on the turbidity. To the contrary, plumes in a relatively strong crossflow velocity U_0 or with very small initial momentum will be almost completely near the surface and have a large value for Λ_s^{nev}. It is clear that, in these cases, removing the air bubbles from the mixture will have a limited effect, resulting in a small efficiency ϵ_{ev}.

It would be useful to examine which parameters influence ϵ_{ev} and consequently attempt to optimize the operational dredging conditions as well as the construction of the overflow.

First, when a plume is allowed to descend away from the vessel over a certain distance, chances of being caught by the propeller jets are lower. A lower velocity ratio λ leads to a higher plume trajectory, as does a higher densimetric Froude number. A densimetric Froude number is defined based on the ship's relative velocity U_0 rather than the jet exit velocity:

$$F_\infty = F_\Delta/\lambda = \frac{U_0}{\sqrt{g'D}} \tag{9.5}$$

In figure 9.3a, F_∞ is plotted against the relative surface plume flux Λ_s^{nev}. It can be observed that F_∞ ranges from 0 to 8 and that there is indeed a strong correlation between both parameters. Since Λ_s^{nev} is correlated with the valve efficiency ϵ_{ev} (however poorly), F_∞ should have some degree of correlation

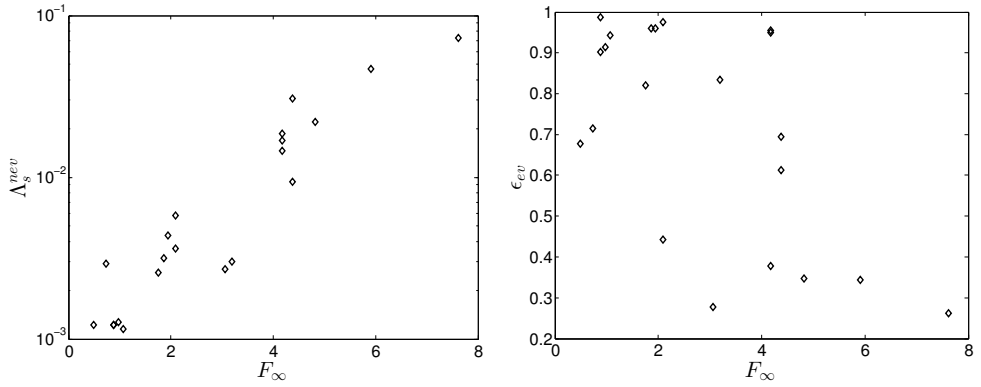

(a) (b)

Figure 9.3: Relation between densimetric Froude number and environmental valve efficiency.

with ϵ_{ev}, which is shown in figure 9.3b.

Secondly, when the relative distance from the overflow to the stern, L_o/D, is higher, the plume has a longer distance for descending before arriving at the propeller and stern. Since it is known that the stern has a lifting effect, one would expect less sediments in a surface plume when L_o/D is larger and all other circumstances stay equal.

Therefore it is investigated whether a combination of L_o/D and the previously identified F_∞ could form a predictor for the environmental valve efficiency. These parameters can be determined without computationally expensive CFD model and would allow fast a priori prediction of the valve's efficiency. The combination parameter is defined as follows

$$\Psi = \frac{(L_o/D)^n}{F_\infty^m} \tag{9.6}$$

where n and m are exponents.

An estimate of the valve efficiency ϵ_{ev}, $\hat{\epsilon}$, can now be expressed as a function of the prediction parameter Ψ. A function of the following shape was identified for least-squares fitting to the data points corresponding to the simulated valve efficiencies:

$$\hat{\epsilon} = \gamma \left[1 - \exp\left\{ \frac{-\Psi}{c_1} \right\} \right] \tag{9.7}$$

where c_1 is a fitting parameter and γ is a correction factor for the efficiency reduction at high values of Ψ (figure 9.4a). Indeed at very low values of U_0, the overflow plume sinks almost vertically to the bottom, and no surface plume is generated, both with and without valve, thereby reducing the efficiency. The valve's efficiency should go to zero asymptotically for values of U_0 going to zero. This could be achieved by defining an asymptotic function γ, with

$$\lim_{\Psi \to \infty} \gamma = 0 \tag{9.8}$$

$$\lim_{\Psi \to 0} \gamma = 1 \tag{9.9}$$

The function γ can then be defined as a Gaussian function:

$$\gamma = \exp\left\{ -\left(\frac{\Psi}{c_2}\right)^2 \right\} \tag{9.10}$$

where c_2 is an additional fitting parameter.

The coefficients were fitted using a least-squares approach. The whole procedure was repeated for values of n and m in order to optimise the fit. The optimal exponents were found to be n=1.2 and m= 1.5. The resulting function is shown in figure 9.4b. Using the above equations, the environmental valve efficiency can be predicted with a root-mean-squared error of RMSE=0.12 and a coefficient of determination of R^2=0.82, up to a value of Ψ =250. In figure 9.4b, the efficiencies simulated with the CFD model are compared with the empirical predictions.

The parameter Ψ consists of variables associated to vessel construction (L_o, D) as well as variables resulting from the dredger's operation (C_0, U_0). It would be interesting to distinguish between the influence of construction-related parameters on the one hand and the influence of operational variables on the other hand. Combining equations 9.5-9.6, Ψ can be written as

$$\Psi = \frac{{L_o}^n (g')^{\frac{m}{2}}}{{U_0}^m D^{n-\frac{m}{2}}} \tag{9.11}$$

When the operation of the dredging vessel is considered unfavourable with regard to the optimization of turbidity plumes, one can investigate the importance of the construction of the vessel in terms of overflow configuration: shaft diameter D and position L_o. Similarly, the importance of construction can be investigated in case of favourable operational conditions. The latter

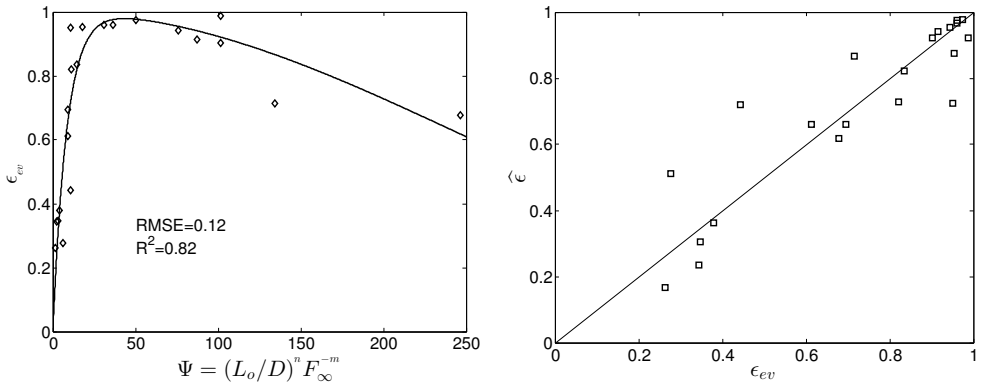

Figure 9.4: (a): Scatter plot of ϵ_{ev} as a function of predictor Ψ (markers), and the fit of eq. 9.7. (b): Correlation plot of ϵ_{ev} and estimated efficiency $\hat{\epsilon}$. Coefficients are equal to c_1=8.43 and c_2=342.

case can be realised by a high value of Ψ and thus a high sediment concentration and a low through-water velocity U_0 (e.g. U_0= 1 m/s; g'=1 m/s^2; C_0=170 g/l). The construction-related efficiency $\hat{\epsilon_c}$ can thus be defined as a function equal to $\hat{\epsilon}$, in which U_0 and g' are considered constants:

$$\hat{\epsilon_c} = \hat{\epsilon}|_{(U_0=cst, g'=cst)} \tag{9.12}$$

In order to visualise the potential effect of constructional aspects on the valve efficiency, $\hat{\epsilon_c}$ is plotted as a function of L_o, for different values of the overflow shaft diameter D (figure 9.5a). It can be seen that the efficiency drops significantly when L_o drops below 20 m. On the other hand, for D >0.5 m the shaft diameter D has limited influence on the valve efficiency in case of favourable operation.

In contrast to the above, the influence of the overflow configuration and vessel construction is determined in the case of unfavourable operation, i.e. a low value of Ψ and thus a low g' and high U_0. Realistic lower, resp. upper bounds for these values are g'=0.1 m/s^2 and U_0=3 m/s, where we remind that U_0 is the vector sum of the sailing speed and the current velocity. In figure 9.5b, the valve efficiency is shown for this case.

It can be observed that in case of unfavourable operation conditions, even the most optimal construction leads to a maximum efficiency of only about 0.75.

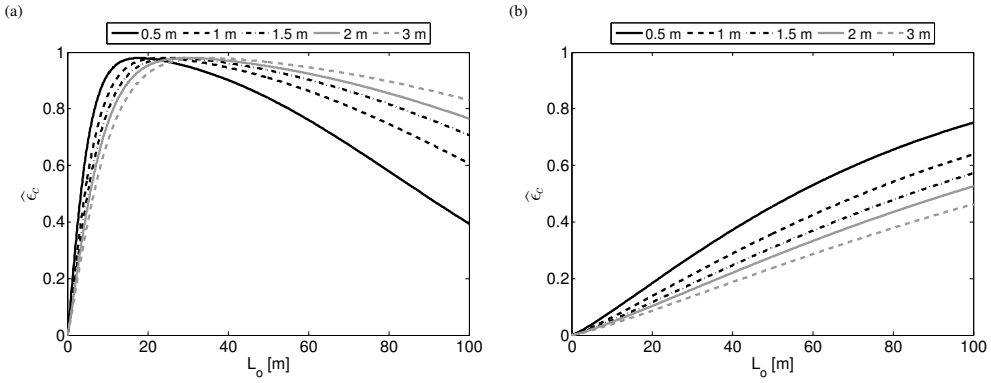

(a) (b)

Figure 9.5: Constructional efficiency under (a) favourable (U_0=1m/s; C_0=170 g/l) and (b) unfavourable (U_0=3 m/s; C_0=17 g/l) operational conditions. Lines are drawn for D=0.5, 1.0, 1.5, 2.0 and 3.0 m.

Hence, it is clear that the operational conditions have a more pronounced influence on the efficiency as compared to the construction. Therefore, for two construction cases, one favourable and one unfavourable, the influence of operational parameters U_0 and C_0 have been investigated (figure 9.6). In order to do so, the function for the operational efficiency has been defined as the efficiency $\hat{\epsilon}$ in which D and L_o are considered constants.

$$\hat{\epsilon_o} = \hat{\epsilon}|_{(D=cst, L_o=cst)} \tag{9.13}$$

In the case of a favourable construction (D=1 m, L_o=60 m), the efficiency of the valve is reasonable for most operational conditions (figure 9.6a), except for C_0 <10 g/l in combination with U_0 >1.5 m/s. For very light mixtures (C_0=1 g/l) and U_0 <0.5 m/s, the efficiency is low for all cases. However, in the case of very light overflow mixtures, only limited levels of sediment concentration will be present in the surface plume.

For the case with unfavourable construction (wide shaft of D=2 m and overflow position L_o=20 m), varying the operational parameters covers the full range of efficiencies, from 0 to 1 (figure 9.6b). While dredging at 2 knots without background current (U_0=1 m/s), the valve efficiency can be very low when the overflow concentration is low. To the contrary, the efficiency of the valve can be nearly ideal when the overflow concentration is very high (C_0 >100 g/l), which typically occurs near the end of a dredging cycle when the hopper is almost fully loaded. In this way, it is possible that the use of an environmental valve causes the situation where less sediments are found in

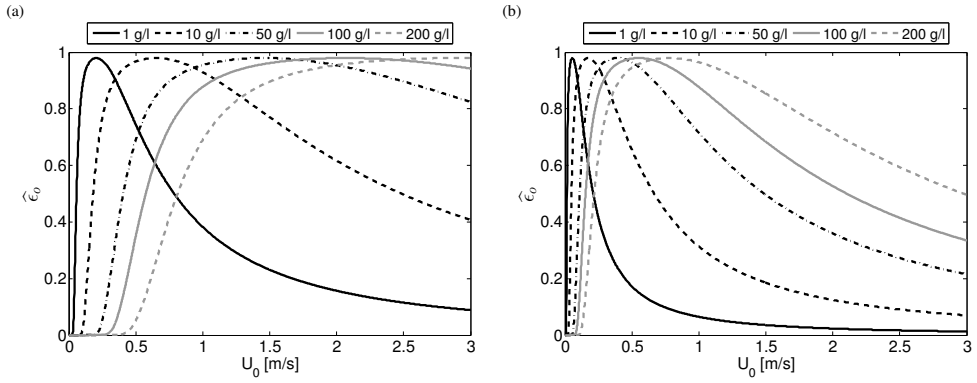

(a) (b)

Figure 9.6: Operational efficiency with (a) favourable (D=1 m, L_o=60 m) and (b) unfavourable (D=2 m, L_o=20 m) construction. Lines are drawn for overflow concentration C_0=1, 10, 50, 100 and 200 g/l.

the surface plume when the overflow concentration is very high, while more sediments are in the plume when the overflow concentration is low.

Remind that in the integrated sediment flux approach of ϵ_{ev}, the three-dimensional structure of the plume is taken into account, whereas in a plot of the sediment concentration along the x-axis at one depth at the symmetry plane, it is not. Nevertheless, x-profiles (from CFD results) at the symmetry plane at 1 m below the surface are illustrative for the effect of the environmental valve under different circumstances (figure 9.7). In this figure, all concentration values (cases A, B, C and D) are relative to the C_0 value of case A, $C_{0,A}$. On the one hand, we see that $C/C_{0,A}$ is lower in case B compared to case A, due the valve. Likewise, the concentration in case D is lower than in case C. Due to the valve, the sediment concentration at a distance x=2.5L_s is reduced with a factor 0.6 (60%, black dashed line) in the cases with high C_0 (cases C/D), whereas it is only reduced with a factor 0.4 (40%, full black line) in the cases with low C_0 (cases A/B). Moreover, at x=2.5L_s and using the valve, $C/C_{0,A}$ is 2.7 times lower in the case where C_0 is 80 g/l as compared to the case where C_0 is 10 g/l. Figure 9.7 is therefore illustrative for the fact that the efficiency of the valve can also be dependent on initial concentration C_0. The result can be a higher sediment concentration in the surface plume for a lower value of C_0.

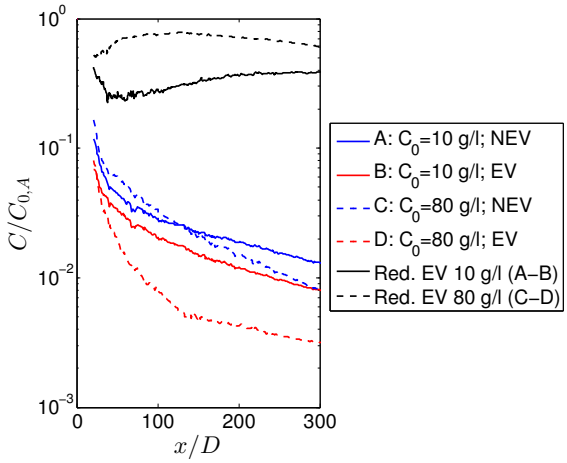

Figure 9.7: Surface plume sediment concentration along the symmetry plane. Cases with high C_0 (80 g/l) and low C_0 (10 g/l) and with/without environmental valve reduction (EV and NEV, resp.) are shown. The fractions with which the concentration dropped after using the environmental valve are shown in black full line for 10 g/l (1-C_B/C_A) and black dashed line for 80 g/l (1-C_D/C_C).

Conclusions on environmental valve efficiency

Environmental valves have been widely used in the past to mitigate the effect of surface plumes on the surrounding ecosystems. In this section, it is shown that these valves can reduce surface plumes with a high efficiency in many cases. However, it is also shown that under certain circumstances the efficiency can drop significantly, to nearly nihil in some cases.

Further, it is shown that the valve efficiency is a function of (i) the distance from the overflow to the stern, (ii) the overflow shaft diameter, (iii) the overflow sediment concentration and (iv) the relative speed of the vessel through the water.

It was found that an environmental valve positioned close to the stern increases the probability that the efficiency will drop during operation. In case of such unfavourable overflow position, the operation of the vessel is dominant in the valve's efficiency. In case an unfavourable overflow position is combined with a high sailing speed or head-on current, the efficiency of the valve drops to nearly zero.

On the other hand, in case of a favourable overflow construction - a narrow shaft, positioned at large distance from stern - only exceptional operational

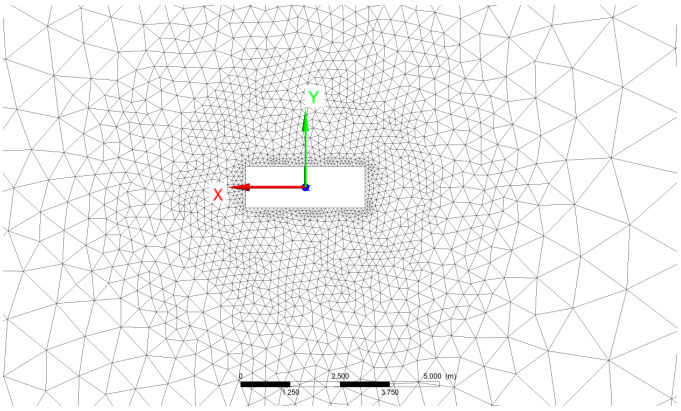

Figure 9.8: Detail of the shape of the rectangular overflow and the mesh around it.

circumstances will reduce the efficiency of the valve significantly.

It is thus demonstrated that the environmental valve can mitigate environmental effects of turbidity significantly, but not under all circumstances. Different adjustments to the overflow configuration could be thought of.

9.2 A different cross section for the overflow?

Different studies have shown that non-circular shapes of exit holes of buoyant jets in crossflows have an impact on the jet trajectory. Salewski *et al.* (2008) found that an elliptical jet exit hole with aspect ratio of 1.69 had a 10% better penetration in the crossflow compared to a circular hole with the same surface area (at x/D=10). Haven and Kurosaka (1997) also showed that high-aspect ratio openings enhance the crossflow penetration.

These findings lead to the question whether an overflow opening with higher aspect ratio could improve the plume 'escape' from the TSHD keel wall. Two test cases have been simulated with a rectangular overflow shaft cross section. The surface area of the rectangular cases was identical to the reference cases with D=2m shafts. The rectangular shafts were 3m in length (along ship axis) and $\pi/3$m in width (figure 9.8). The aspect ratio of the rectangular overflow shaft is therefore equal to π. All other conditions were kept constant.

A first case with U_0=1 m/s, C_0=55 g/l and W_0=1.9 m/s was investigated (figure 9.9a). This case is clearly of type density current, with distinct sur-

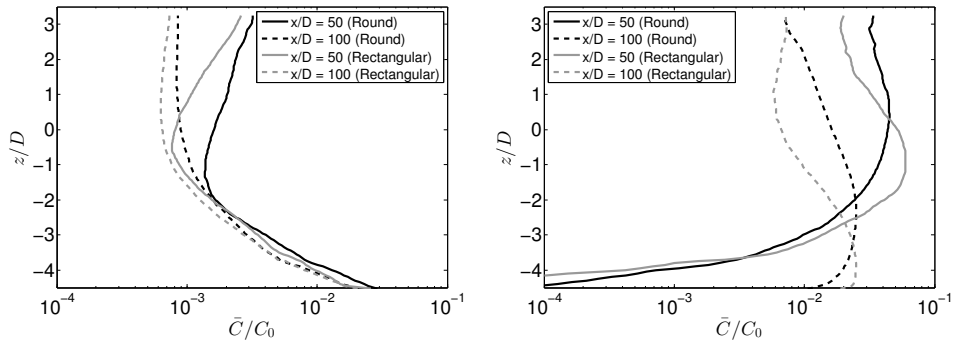

Figure 9.9: Time-averaged sediment concentration C/C_0, for 2 cases in which a round overflow shaft was compared with a rectangular shape with high aspect ratio. For both shapes the cross-sectional area of the overflow shaft was equal to π. In (a), U_0=1 m/s, C_0=55 g/l and W_0=1.9 m/s. In (b) U_0 was increased to 3 m/s.

face plume. With a round overflow shaft, the sediment concentrations in the upper half of the water column are about 25% to 50% higher compared to the case with rectangular overflow. It seems the shape of the overflow shaft does have an influence. Either the higher aspect ratio in the rectangular case leads to a better escape from the keel. Or, the more narrow shape of the plume after exit might reduce the number of air bubbles that escape per unit of time, leading to less surface plume generation in the first few meters after the exit.

In a second case, the crossflow was increased by a factor three to U_0=3 m/s. In this case, an environmental valve would not be efficient since the entire plume is lifted to the surface. It is determined in this test case whether a high-aspect ratio overflow shaft would lead to a reduction of the surface plume concentration. The result of the simulations of this case with round (D=2m) and equivalent rectangular shape is shown in figure 9.9b.

At x/D=50, it can clearly be observed that the bulk of the plume is situated lower for the rectangular case compared to the round shaft. The surface concentration is 40% lower in the rectangular case. After x/D=100, the difference in concentration near the surface has reduced, but it is clear that less sediments are present in the water column in the near-field overflow plume.

The influence of the shape of the overflow shaft needs more investigation to draw definite conclusions, but it seems that variations in the aspect ra-

tio of the shaft cross section have the potential to reduce the sediments in suspension in the overflow plume.

9.3 Telescopic overflow extension

The concept of an extension of the overflow shaft below the keel of the TSHD was first introduced to the author by IHC Holland (personal comm., 2012). The hypothesis is that an extension of the overflow can deliver the sediment mixture in a zone closer to the sea bed and can reduce the influence by the vessel hull and propellers. It is anticipated that this would reduce the dispersion of the sediments. Of course, air bubbles still play an important role, which makes that the efficiency of the overflow extension has to be seen in relation with the environmental valve. However, no environmental valve in combination with an overflow extension will be considered. A number of tests in a numerical model have been executed by de Wit (2015). It was found that a 3 m extension reduces the suspended sediment flux by 1%, an 8 m extension by 17% and a 16 m extension by up to 35%. These cases were simulated at a keel clearance of 18 m. It seems, however, questionable whether a ship can sail safely with an overflow extension down to 2m above the sea bed, on average. Some surface waves and sea bed undulations could bring the extension dangerously close to the sea bed. Also, a quick calculation learns that the torque around the point where the extension is attached to the hull could rise to order 10^6 N.m for a 16 m extension. Therefore, smaller values for the overflow extension length h_e will be assumed here.

In order to confirm and complement the finding by de Wit (2015) that the surface flux can be reduced, a number of challenging test cases are simulated using the currently presented model. The present model has some advantages, due to the unstructured grid. The overflow pipe extension ejected into the water flow produces important wake effects with increased turbulence. To model this, a good representation of the boundary is required. The present model uses the unstructured grid to lay computational cells in the correct cylindrical shape, and a proper wall boundary condition can thus be imposed. Near the inner wall as well as near the outer wall of the overflow extension, refined layers of grid cells are placed to resolve the boundary layers.

A TSHD-case has been used in which the overflow is positioned near the stern of the ship, with a slight lateral shift off the centerline of B_o=4 m. It was shown previously that this is a very unfavourable setup for surface plumes, due to the specific geometry of TSHD's stern sections (figure 8.4).

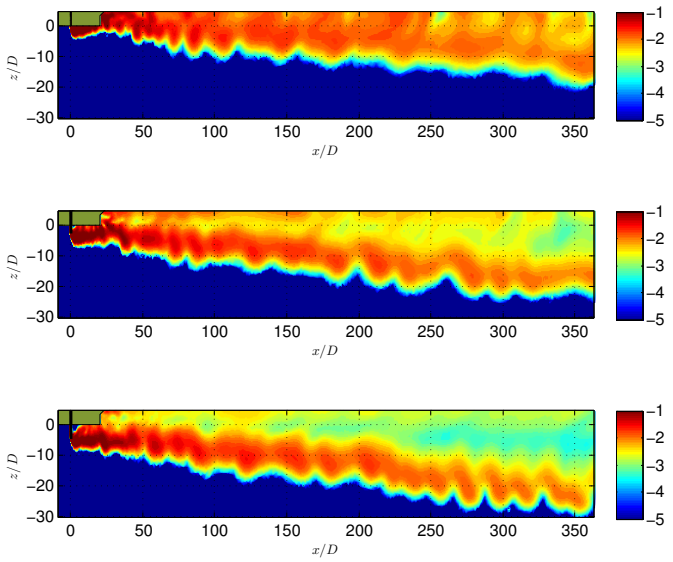

Figure 9.10: Relative sediment concentration $\log(c/C_0)$ *at the symmetry plane, with* H*=40 m,* W_0*=3.2 m/s,* U_0*=1.5 m/s,* C_0*=20 g/l and* D*=1.1 m. Top panel: Overflow extension* h_e*=0 m; Middle panel:* h_e*=3 m; Bottom panel:* h_e*=5 m.*

In this setup, an environmental valve will also often be inefficient. It will be tested whether the overflow extension can make a difference in these cases. A base case is simulated while dredging (or mining) without extension in a water depth of H=40 m, as well as cases with extensions with length h_e=3 m and 5 m. No environmental valve is taken into account in these simulations.

The resulting sediment plumes are shown in figure 9.10. It can clearly be observed that in this case the overflow plume moves completely to the surface without extension (top panel). With an extension of h_e=3 m, the main plume is allowed to escape the uplifting effect of the curved stern sections, but a relatively high sediment concentration remains present in a surface plume (middle panel). This can be explained by the fact that the plume was not deep enough to escape the propeller jet. For an extension of h_e=5 m, the plume escapes both the uplifting of the stern and the propeller jet mixing (bottom panel). The main plume descends steadily towards the sea bed. Air bubbles still have an influence, which cannot be avoided unless an overflow extension is combined with an environmental valve. It can be seen that even in the h_e=5m case, some sediment is torn off above the plume right after the exit, due to air bubble entrainment.

The behaviour of the air bubbles is shown in figure 9.11. It can clearly be

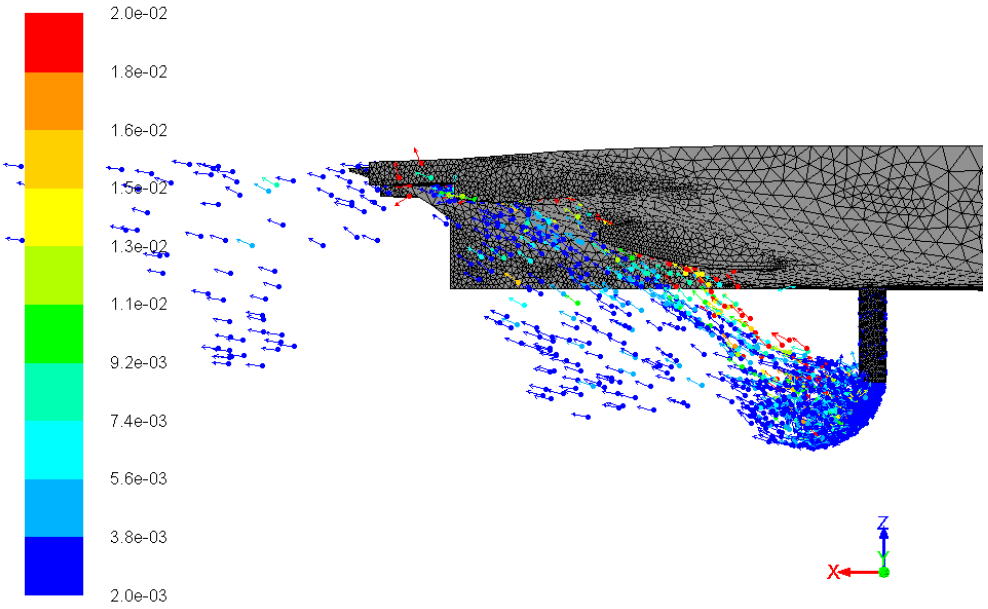

Figure 9.11: Case of the lower panel in figure 9.10. Snapshot of the position of air bubble parcels with velocity vector. The parcels and vectors are coloured according to the air bubble diameter. The smallest bubbles (blue) are 2 mm, the largest (red) around 2 cm.

observed that most air bubbles ascend steeply after release, with the largest bubbles of d_a >1 cm at the steepest angle. It makes clear that mainly at x/D <10, bubbles impose a vertical momentum source on the sediment mixture due to drag. This occurs of course mainly in the top part of the plume, where most bubbles are located. By this mechanism, the top part of the plume is torn of to form a surface plume.

Additionally, an overview is shown of vertical profiles of C/C_0 at the centerline for the different extension lengths and at two distances behind the dredger (figure 9.12). In figure 9.12a, the profiles are shown at x/D=100. It can be observed that the maximum concentration in the plumes remains similar, but that the plume center is deeper for longer h_e. It is noteworthy that the difference between the depth of the concentration maxima for the h_e=3 m and h_e=5 m plumes is larger than the difference in h_e (2 m). More important is the fact that the surface concentration decreases a factor 2.5 with a 3 m extension and a factor 5 with a 5 m extension. When looking further downstream (x/D=300; figure 9.12b), the same pattern is found, where plumes with increasing extension are deeper and have a lower surface

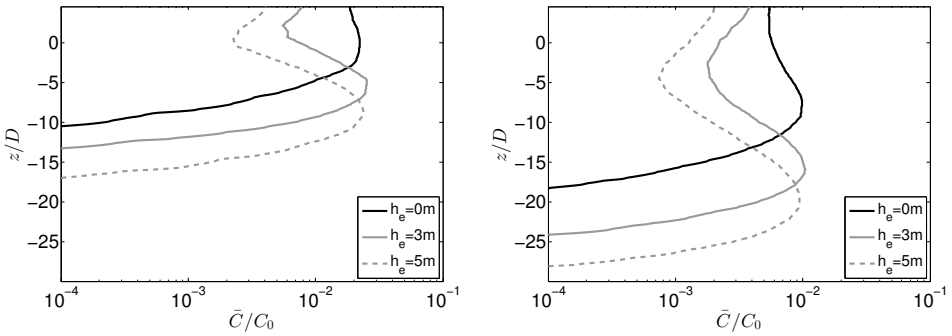

Figure 9.12: Vertical profiles of time-averaged sediment concentration C/C_0 at y=0 for three extension lengths h_e=0, 3 and 5 m. Profiles shown at x/D=100 (a) and at x/D=300 (b).

concentration. The surface plume reductions at x/D=300 are smaller, but still significant.

Conclusions on the overflow extension

It is likely that the overflow extension can be a valuable mitigation measure against turbidity. The efficiency of extensions with different lengths, as a function of overflow location and the many other boundary conditions, remains to be further investigated. A similar approach could be followed as for the environmental valve efficiency towards the surface plumes fluxes (section 9.1).

Chapter 10

Grey-box plume dispersion model

10.1 Introduction

In engineering practice, a CFD model can provide a wealth of information on the plume behaviour. In some phases of a dredging project, however, the long simulation times are not always acceptable. In the feasibility phase of dredging projects, the fate of the fine sediment plumes needs to be predicted in order to assess the need for mitigation measures. At this point in time the CFD model is availble for detailed computations. In the operational project phase, real-time plume predictions might be needed to assess the timing and location of dredging in the day-by-day planning of works. At this stage, the long simulation times of the CFD model might be prohibitive.

The large-scale simulation of the far-field plumes is generally executed with a shallow-water equations based hydrodynamic flow model with a sediment transport equation and a source term for the overflow releases. The source term which has to be supplied to the large-scale model is the fraction of the overflown sediments that is released into the water column, preferrably as a vertical profile. The determination of this source term can be done using the process-based CFD models, or by means of a faster parameterised prediction model. A parameterised model will have to be a trade-off between speed and accuracy. It will be less accurate compared to a CFD model, but will be applicable in cases where the CFD model is not possible, e.g. real-time forecasting simulations.

The parameter model will be composed of theoretical solutions as well as on

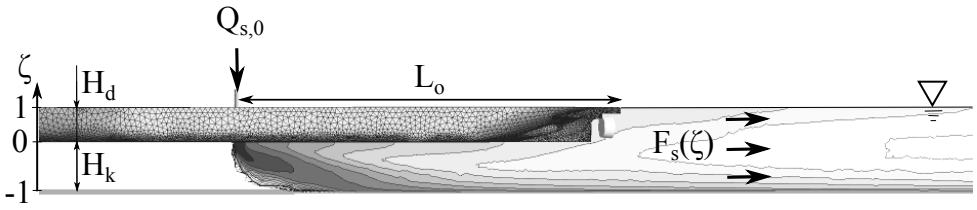

Figure 10.1: Sketch of the different length scales and sediment fluxes.

multivariate regression analysis, thefore the term 'grey-box model' is used.

The parameters in the model will be fitted by means of a large data set of CFD model output, based on 75 CFD model simulations. The development of the parameter model structure, the fitting of its parameters and the assessment of its quality are presented in this chapter.

10.2 Formulation and principles

Before the formulation of a parameterised model can start, the different length scales and fluxes need to be condensed into non-dimensional numbers. This makes the parameterisation of the vertical flux profiles more generic.

In figure 10.1 the different scales are sketched. The water depth H is the sum of the TSHD draft H_d and keel clearance H_k. As before, the distance between the overflow and the stern is denoted as L_o. The vertical coordinate z can now be transformed to a dimensionless coordinate ζ, equal to -1 at the sea bed, to 0 at the keel and to 1 at the water surface:

$$\zeta = \left(\frac{z}{H_d}\right)\mathcal{H}(z) + \left(\frac{z}{H_k}\right)\mathcal{H}(-z) \tag{10.1}$$

where $\mathcal{H}$ is the Heaviside step function.

The time-averaged sediment flux f in the sediment plume (in kg/s/m), is determined as before, based on the CFD results:

$$f(x, y, \zeta) = C(x, y, \zeta)U(x, y, \zeta) \tag{10.2}$$

with C and U the time-averaged sediment concentration and flow velocity.

The laterally integrated flux q_s is determined as:

$$q_s(x,\zeta) = \int_{-B_w/2}^{B_w/2} f(x,y,\zeta)\,\mathrm{d}y \tag{10.3}$$

where B_w is the width of the plume.

At this point we have a sediment flux in kg/s at every location along x and ζ. A choice should be made at which distance x_p the vertical profile of q_s will be evaluated. Different options were considered. The result of the parameter model will be a vertical profile q_s to be implemented in a large-scale far-field plume model. These models cannot cope well with vertical accelerations. For that reason, the distance x_p cannot be too close to the vessel so that an important buoyancy is still present in the plume. The distance x_p can also not be chosen too far from the vessel since the plume might have diluted excessively. One option would be to determine the distance at which the buoyancy has decreased to a certain threshold. This is, however not practical since the result might be that the profile is defined at a very short distance or a very large distance from the ship. Another option would be selecting a point at which the plume profile resembles a standard Rouse profile for sediment transport. But this would lead to the same limitation. Finally, the option was chosen to define a fixed distance at which the CFD model output is evaluated and by consequence at which the parameter model is valid. The distance x_p was chosen at two and a half vessel lengths, $2.5L_s$.

The vertical profile of the flux that will be parameterised is non-dimensionalised and defined by:

$$F_s(\zeta) = \frac{q_s(x_p,\zeta)}{Q_{s,0}} \tag{10.4}$$

where $Q_{s,0} = C_0 Q_0$ is the sediment outflow from the overflow.

For each CFD result in the data set, the profile $F_s(\zeta)$ is determined at x_p=$2.5L_s$, or about 3 TSHD lengths, behind the dredger.

The next step is to parameterise the resulting profiles. The parameters describing the shape of the profiles will then be linked through a multivariate regression to the input parameters. As was already identified during the discussions of the CFD model results, two distinct types of plumes can be distinguished: the near-bed density current with surface plume and the sea bed-detached plume. The shape of the vertical flux profile of both types of

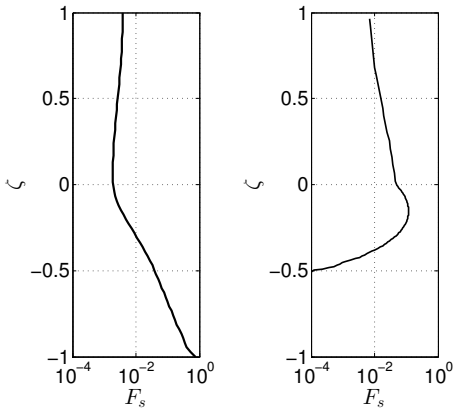

Figure 10.2: Vertical profile of F_s for two types of plumes: (a) Near-bed density current type and (b) the detached plume.

plumes is obviously different (figure 10.2). Both types can be characterised with a surface flux at the top of the water column, F_t=$F_s(\zeta = 1)$, and a ζ-level at which $\mathrm{d}F_s/\mathrm{d}\zeta$ changes rapidly.

If a subdivision is to be made between both types in a predictive parameter model, the decision must be made as a precursor. If an estimate of the ζ-level of the centre of the plume would be available, the decision could be made thereupon. For this purpose, the Lagrangian model for the trajectory of buoyant jets of Lee and Cheung (1990) and Lee and Chu (2003) is used as a start. The outflow velocity W_0, pipe diameter D, sediment concentration C_0 and the crossflow velocity U_0 are used to determine the trajectory of the buoyant jet, and the centerline height ζ_c at x_p=$2.5L_s$. This solution is an estimate of the trajectory without TSHD-specific influence factors, see the diamond markers in figure 10.3. In general, the ship and air bubbles have the tendency to move the sediment plume higher than what would be expected from a plain buoyant jet.

The plume centre at x_p=$2.5L_s$ can be extracted from the LES model results and can be compared with the Lagrangian model. The uplifting effect of the vessel is related to the boundary conditions F_Δ and λ. A multivariate linear model fit is executed. The independent variables are the initial plume centre height ζ_c, the crossflow-based Froude number $F_\infty = F_\Delta\lambda$ and the ratio H_d/L_o. The dependent variable is the plume height based on the LES model results, $\zeta_{c,LES}$.

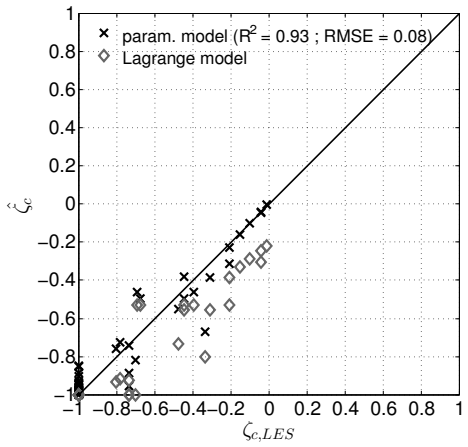

Figure 10.3: Relation between Lagrangian estimates (diamonds) for a simple buoyant jet and corresponding LES results for TSHD plumes ($\zeta_{c,LES,i}$). Improvement of the estimates by applying a general linear regression is shown by black crosses.

$$\zeta_{c,LES,i} = \beta_0 + \beta_1\,\zeta_{c,i} + \beta_2\,F_{\infty,i} + \beta_3\,(H_d/L_o)_i + \varepsilon_i \qquad (10.5)$$

where i is the number of observations, β_0, β_1, β_2 and β_3 are the coefficients to fit and ε_i are error terms.

After solving for the coefficients β_0 to β_3 by a least-squares approach, the estimated plume height $\hat{\zeta}_c$ (at x_p=2.5L_s) can be determined. The resulting estimated plume heights $\hat{\zeta}_c$ can be compared with the 'true' plume heights from the LES model in a scatter plot. The Root-Mean-Squared-Error and coefficient of determination R^2 can be determined (figure 10.3).

It is shown that the corrected version of the Lagrange-estimates can be used as a good indication for the height of the plume center at x_p. When $\hat{\zeta}_c$ <-0.75, the plume can be considered of type 'near-bed density current', when $\hat{\zeta}_c \geq$-0.75, of type 'bottom-detached'. For both types, the model follows a different approach in terms of the parameterisation of the shape of the vertical profile of F_s.

The density current type has a relatively smooth profile, and can be approximated using Chebychev polynomials, see e.g. Lopez (2001). In this method, a weighted sum of polynomials with order zero to n is considered. The coefficients in the weighted sum are fitted to each case in the data set of CFD model-based plumes. Here, n=3 was found to be sufficient:

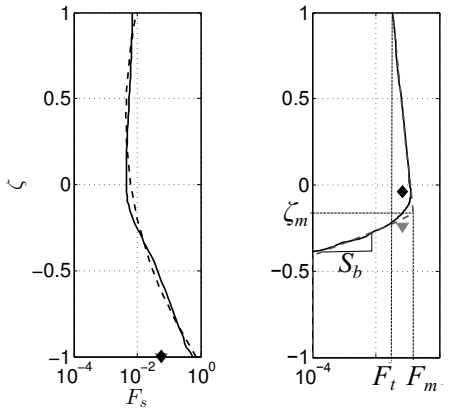

(a) (b)

Figure 10.4: Vertical profile of F_s for two types of plumes. (a): Near-bed density current type with Chebychev parameterisation (dashed line), with initial (grey triangle) and corrected plume center position. Both initial and corrected estimate of the plume center is located at the seabed. (b): The detached plume type with step-wise parameterisation (dashed line), defined by points (F_t,1), (F_m,ζ_m) and slope S_b.

$$\widehat{F_s(\zeta)} = \sum_{i=0}^{n} \psi_i \, T_i(\zeta) \tag{10.6}$$

where T_i are the Chebychev polynomials and ψ_i are $n+1$ coefficients fitted to the data set.

The so-called Chebychev polynomials of the first kind can be found by the recurrence relation:

$$T_0(\zeta) = 1 \tag{10.7}$$

$$T_1(\zeta) = \zeta \tag{10.8}$$

$$T_{n+1}(\zeta) = 2\zeta T_n(\zeta) - T_{n-1}(\zeta) \tag{10.9}$$

The Chebychev polynomials are defined in the range [-1,1], for which reason the transformation from z to ζ is particularily practical.

An example of a Chebychev parameterisation of a density current type plume is shown in figure 10.4a.

The second type of plume flux profile is the seabed-detached plume. For this type, a step wise parameterisation of the flux profile is proposed. The reason for the different parameterisation is that the profile is often less smooth, with a sharp edge at the position of the bottom of the plume where the sediment concentration goes to zero rapidly. Fitting using Chebychev polynomials induces wiggles due to the sharp edge. In figure 10.4b, the step-wise parameterisation (dashed line) is shown. It is defined by the points (F_t,1), (F_m,ζ_m) and the slope S_b. This gives a total of four parameters to fit to the data set, as for the Chebychev approach.

10.3 Model training

A training data set of 50 CFD simulations was used to relate the coefficients ψ_i (for the density current type) or F_t, F_m, ζ_m and S_b (for the detached plumes) to the different boundary conditions of the plume. These boundary conditions consist of F_Δ, λ, H_d/L_o, etc. The ranges of these conditions covered by the training data set are shown in figure 10.5. The model is therefore valid for $1.2< F_\Delta <14.2$, $0.5< \lambda <4$, $0.07< H_d/L_o <0.26$ and $1< H_k/D <30.4$.

The Chebychev coefficients were found to depend mainly on F_∞ and the ratio H_k/D. For each coefficient, a multivariate regression is fitted with these two dependent variables. The training data set cases are used for finding $\beta_{c,i}$ (3x4=12 coefficients):

$$\psi_i = \beta_{c,i,0} + \beta_{c,i,1}\, F_{\infty,m} + \beta_{c,i,2}\, (H_k/D)_m + \varepsilon_{i,m} \tag{10.10}$$

where i=0,...,3 is the number of the Chebychev coefficients, m=1,...,M, with M the number of CFD simulations in the data set, $\beta_{c,0}$, $\beta_{c,1}$ and $\beta_{c,2}$ are the coefficients to fit and $\varepsilon_{i,m}$ are error terms.

The parameters for the step-wise profile of the seabed-detached plumes were found to be best represented as a function of the following plume conditions: F_∞, the ratio H_d/L_o and the ratio H_k/D. For each parameter, a multivariate regression is fitted with these three dependent variables. The training data set cases are used for finding β_d (4x4=16 coefficients):

$$(F_t, F_m, \zeta_m, S_m) = \beta_{d,0} + \beta_{d,1}\, F_{\infty,m} + \beta_{d,2}\, (H_d/L_o)_m + \beta_{d,3}\, (H_k/D)_m + \varepsilon_m \tag{10.11}$$

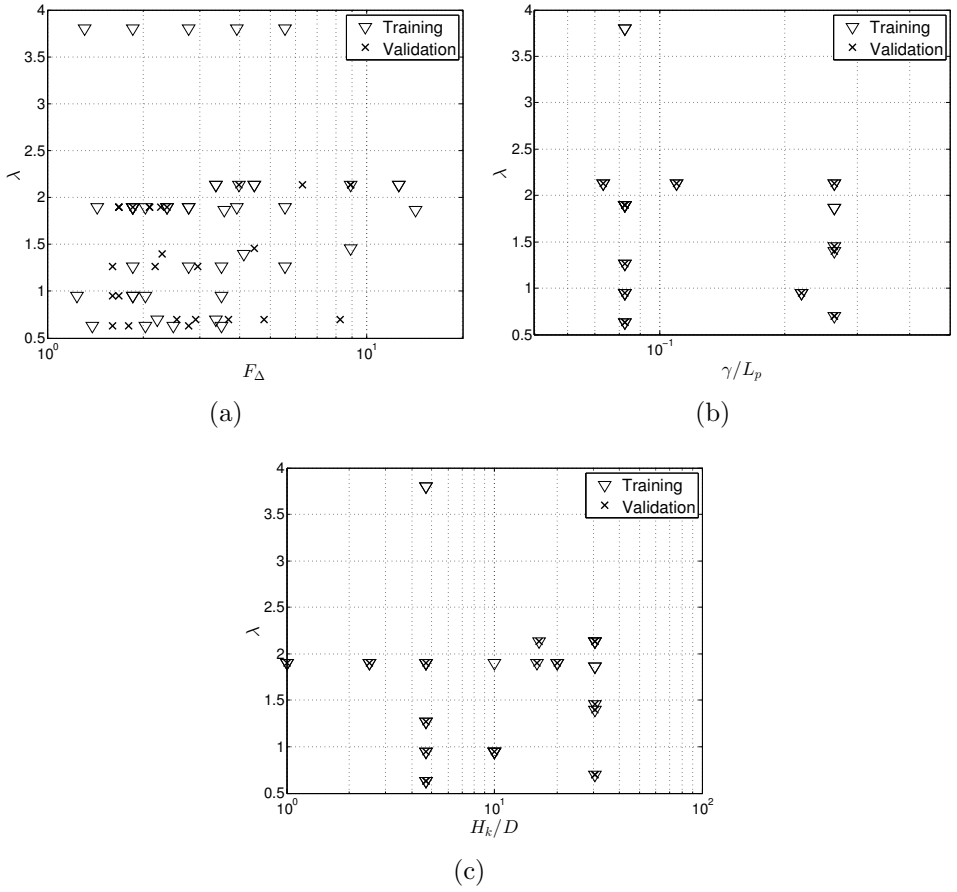

Figure 10.5: Properties of the plumes in the data sets for training the parameter model and for validating the parameter model.

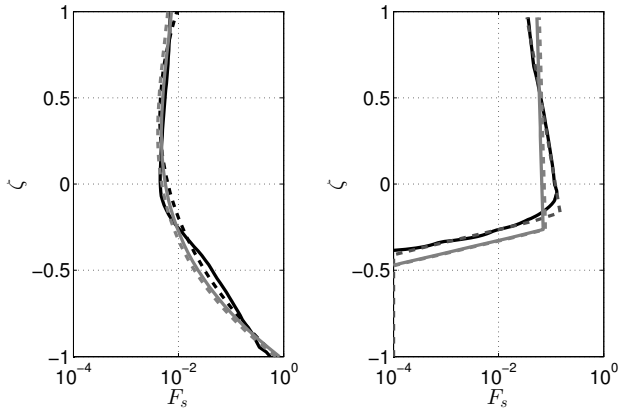

Figure 10.6: Vertical profile of F_s for two types of plumes, as in figure 10.4. Here the parameter model predictions are added to the figure in magenta (dashed line, first step) and full magenta line (after corrector step).

where, m=1,...,M, with M the number of CFD simulations (with seabed-detached plume) in the data set, $\beta_{d,0}$, $\beta_{d,1}$, $\beta_{d,2}$ and $\beta_{d,3}$ are the coefficients to fit for each profile parameter (F_t,F_m,ζ_m,S_m). ε_m are error terms.

When all coefficients β have been fitted to the training data set, a parameter model prediction can be compared with the original profile (from CFD) and with the parameterised profile. In figure 10.6, the dashed magenta lines indicate the predictions from the parameter model. At this point, the vertical integral of $F_s(\zeta)$ might not be equal to 1. This should be the case, since F_s is the sediment flux in the plume normalised by the overflow flux Q_s. Also, the total sediment flux in the plume must be equal to the sediment flux from the overflow, since deposition (i.e. near-bed removal of sediment from the CFD domain) is not allowed in the detailed near-field CFD model.. A corrector step is thus added in which a (small) correction factor is multiplied by F_s. The factor is determined by the inverse of the integrated $F_s(\zeta)$, so that for the corrected profile the vertical integral of $F_s(\zeta)$ becomes equal to one. In figure 10.6, the full magenta lines show the corrected flux profile predictions.

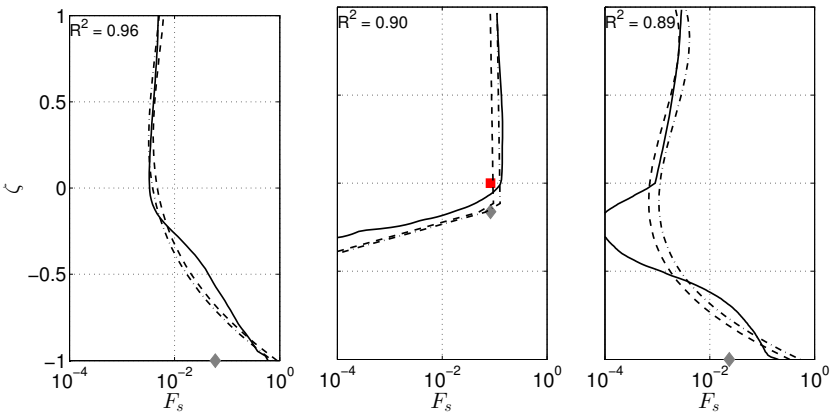

Figure 10.7: Examples of parameter model predictions of the F_s-profiles. Black line indicates full CFD solutions, dot-dashed (dashed) line shows the uncorrected (corrected) parameter model prediction. Preliminary determinations of plume center levels are shown in diamond and square markers.

10.4 Model validation

10.4.1 Against CFD runs

A dataset of 25 CFD runs were not used in the training of the parameter model. This data set is used to validate the performance of the simple profile prediction model. In figure 10.7, a number of examples are given of the predictions of the parameter model against CFD solutions. In figures 10.7a and 10.7c, the model correctly identified the plume as of type 'density current', whereas in figure 10.7b the type 'seabed-detached' was correctly identified. In most cases, the typical profile shapes are found. In some cases, very specific profile shapes of the deeper part of the plume were found in the CFD model. In these cases, the exact shape is not reproduced by the parameter model, given the limited number of parameters (figure 10.7c). Nevertheless, the sediment flux near the surface is reproduced well.

A general overview of the performance of the parameter model, both for the training data set and for the validation data set, is shown (figure 10.8). The fraction of cases is shown for which the coefficient of determination (R^2) has a certain value. Also the cumulative values are shown. It is shown that for the validation cases, 75% of the predicted profiles had a R^2 value of more than 0.7. In about 18% of the cases, the predictions were not very accurate

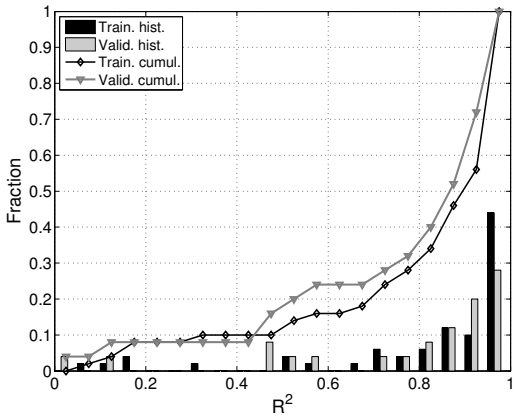

Figure 10.8: Statistics of the parameter model performance, for the training data set and for the validation data set. Histograms are shown for each class of R^2 values. The lines with diamond markers are drawn for the cumulative fraction of cases with R^2-value lower than or equal to the value on the x-axis.

with $R^2 \leq 0.5$. Taking into account the simple semi-analytical setup of the parameter model, the overall performance is relatively good.

10.4.2 Multiple overflow superposition

In many of the largest TSHD's, multiple overflows are mounted. They are not necessarily active at the same time, but the situation of multiple overflow plumes is possible. Therefore, a check is performed on how well the CFD model results compare with superimposed parameter model plumes. The profiles are obtained from the parameter model for each overflow plume separately. Afterwards, the values of F_s of both plume profiles are simply added together.

Two cases have been simulated in the CFD model in which two overflows are active. In these cases, the overflow concentration for both overflows was the same, while the discharge was equally distributed. In this case the following boundary conditions were imposed: H=40 m, U_0=1.5 m/s, W_0=3.2 m/s, C_0=20 g/l and D=1.1 m. The latter three conditions are valid for both overflows. In figure 10.9a, the result is shown after adding both parameter model results together and comparing with the CFD simulation. The plume with L_o=20m is of type 'seabed-detached' (grey dashed line), while the plume with L_o=72m is of type 'density current'. When both are added together, the shape is similar to the CFD result of the multiple plume. The surface plume, however, is overestimated. This can be explained by the shielding of the

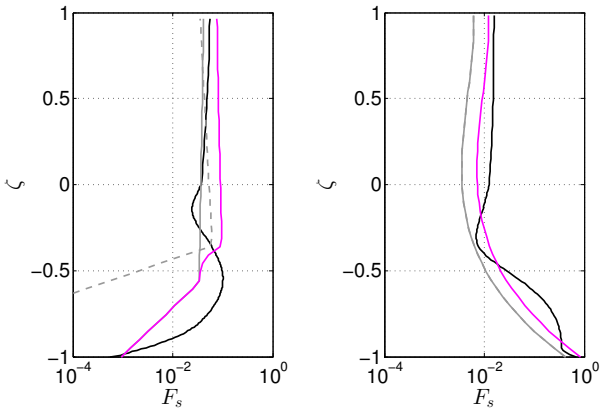

Figure 10.9: Parameter model predictions of multiple overflow plumes. Figure (a): two plumes for which H=40m, U_0=1.5 m/s, W_0=3.2 m/s, C_0=20 g/l and D=1.1m. One plume originated at L_o=20 m, the other at L_o=72 m. Figure (b): two plumes for which H=26 m, W_0=1.9 m/s, U_0=2 m/s, C_0=90 g/l and D=2 m. L_o=30 m for one plume and 80 m for the second. Grey lines indicate individual plume results, of which the magenta line is the sum. The black line shows the CFD model result.

plume closest to the stern. Due to the wake of the plume closest to the bow, the other plume experiences less crossflow. Therefore the L_o=20m-plume generates a lower added sediment concentration compared to the single-plume situation.

The second case equally consists of two overflows at the symmetry plane, but with larger diameter, D=2 m. Also, H=26 m, W_0=1.9 m/s, U_0=2 m/s and C_0=90 g/l. L_o=30 m for the rear end plume, while L_o=80 m for the front end overflow plume. In this case, both separate plumes are of type 'density current'. This type of plume is not dependent on the overflow position in the parameter model. Therefore both parameter model profiles are equal (grey line). The superimposed plume profile is thus simply equal to twice the F_s-values from the individual plumes. In this case, this seems to correspond quite well with the CFD result of the multiple plumes. In this case, the surface plumes formation is more dominated by air bubbles than by crossflow. Both plumes are therefore less influenced by each other, and hence can be superimposed with good result.

Superimposing multiple plumes from a simplified parameter model seems to

be allowed in some cases. In other cases deviations from the CFD model results seem to occur. Further investigation is needed to clarify under which circumstances multiple plumes can be superimposed and under which circumstances corrections are needed to the simple addition of plumes.

10.5 Application and conclusions

Though less accurate than the CFD model, the parameter model is much faster (order of magnitude of seconds). The parameter model predicts the sediment flux in the overflow plume still with reasonable accuracy. It is therefore well suited to be applied in situations where limited or not enough time is available for CFD simulations. These situations include real-time forecasting simulations of overflow turbidity throughout the wider area around a dredging project. In such situations, the tidal flow velocity and water depth can vary, and thus varying boundary conditions for the near-field plume simulations are needed. This can only be achieved in a real-time forecasting model when a simple prediction module can be implemented in the large-scale tidal model. The parameter model presented above would be suited for this application.

The parameters in the parameter model were fitted based on a wide range of boundary conditions. Within this range of conditions, the model is valid. In some cases, however, the model is not valid. For example an anchored TSHD in a crossflow, or in the case of salinity stratification in deep water. In these cases, CFD model results still need to be generated to estimate the overflow plume turbidity.

Chapter 11

General conclusions & Recommendations

In this section, the general outcome of the research is evaluated according to the goals set before the start. The research objectives were twofold:

- The development of a CFD model for the accurate representation of all relevant processes in the near-field overflow plume, and
- The development of a simplified model for fast approximations of the vertical profile of the sediment flux in the plume.

11.1 Near-field CFD model

Lab experiments

The first objective can only be met when highly detailed validation data can be made available for a CFD model of a sediment plume. This was achieved by performing laboratory experiments of sediment plumes, including the influence of a schematised ship hull and air bubbles. In order to capture turbulent properties of the water-sediment mixture, a new processing technique was developed for Acoustic Doppler Velocimeter (ADV) data. This processing technique corrects for high-frequency noise in the signals of velocity and sediment concentration. In this way the turbulent fluctuations of sediment concentration and the turbulent fluxes of sediment could be measured.

It was shown in the experiments that a fine sediment plume behaves in a very similar way to a buoyant jet. It was also shown that both the stern

section of a ship hull and air bubbles can strip off part of the plume, to form a secondary plume near the surface.

Laboratory-scale CFD

A highly detailed CFD model has been built in different steps of increasing complexity.

First, a CFD model of the simplified geometry of the laboratory experiments was set up. Using this geometry, first a vertical sediment plume without crossflow was simulated and compared with experimental results. Afterwards, crossflow was added and the results were again compared to experimental results. Subsequently the same was done after adding a schematised dredging vessel hull. The plume trajectory as well as the turbulent structures in the flow field were reproduced accurately by the model. The Large-Eddy Simulation technique was applied, which allows to resolve a large part of the turbulence explicitly on the numerical mesh.

Additionally, the model performance was validated against a number of relevant cases found in the literature. These cases include a jet in a crossflow, a wall-impinging sediment jet and an air bubble plume in crossflow.

Prototype-scale CFD

After validation of the mean flow properties as well as the turbulent characteristics of the simulated plumes, the CFD model was scaled to the prototype scale. It was demonstrated through similarity laws that the resulting upscaled plume trajectories were still accurate.

In a next step, the geometry of an actual Trailing Suction Hopper Dredger was added into the unstructured grid of the CFD model. The influence of the propellers on the mean flow and the turbulence was incorporated with the actuator disc method. The model contains three different phases: water, sediment and air bubbles.

The prototype-scale model was further tested by comparing simulation results against a number of benchmark cases from the literature. Additionally, an in situ measurement campaign was executed in this research project. During this campaign several sediment plumes have been monitored by means

of sailing with a survey boat behind a TSHD at work at sea and taking measurements of the sediment concentration. The most interesting data gathered consisted of detailed vertical profile of the sediment concentration, from the water surface down to the last few centimetres above the sea bed. In this way, not only the plume in the central part of the water column was monitored, but also the sediment concentration in a density current near the sea bed was recorded. It was also found that when using acoustic profilers (ADCP) for dredging plumes, it is often hard to distinguish between air bubble plumes and sediment plumes. The resulting dataset was used to validate the prototype-scale CFD model.

A number of observations were deduced from the CFD model simulation results:

- The presence of **air bubbles** in the overflow has the potential to increase surface plume concentrations with a factor 5 to 10 and to raise the near-field plume trajectory by several pipe diameters.
- The streamlines going through the **propellers** run over the port and starboard sides of the keel, and therefore do not draw sediments from the overflow shaft directly into the propellers in most cases. In some cases, however, sediment is drawn in the propellers leading to increased amounts of sediment in the surface plume in some cases. More specifically, in cases with (i) high sailing speed, (ii) high current velocity, (iii) a narrow overflow shaft, (iv) a short distance from overflow to stern or (v) an overflow shaft located off the ship axis.
- Depending on the sign of the vertical sediment concentration gradient at keel level near the stern, the propellers can cause both a reduction and an increase in surface plume concentration.
- In many cases, the sediment concentration in the surface plume drops when the sediment concentration of the overflow mixture is raised.
- The surface plume sediment concentration is up to 10 times higher when the TSHD **speed-through-water** is increased with a factor 3.
- The **water depth** is not of significant influence on the surface plume, unless the under keel clearance drops below 1.5 times the TSHD draft.
- Due to turbulent mixing and a small settling velocity, a **fine sand fraction** in the overflow discharge is not segregated from the main plume until at least 2 vessel lengths behind the dredger.

Additionally, several practical applications of the CFD model gained a number of insights:

- A full investigation of the **efficiency of the environmental valve** was undertaken. It was confirmed that such a valve can be very efficient in reducing surface plume sediment concentrations. However, the efficiency of the valve is a function of the boundary conditions and the configuration of the overflow. Under certain conditions the efficiency is nearly optimal, but under other conditions and/or overflow configurations the efficiency is drastically reduced.
- Indications that a **telescopic overflow extension** can reduce the surface plumes were shown by de Wit (2015). In the present work, using a more advanced model for air bubbles and a realistic TSHD geometry, the potential of such extension can be confirmed. However, the conditions under which the efficiency of the extension is significant, must be further investigated.
- A different cross-sectional shape of the overflow shaft was tested. It was shown that a **rectangular shape of the overflow**, with an aspect ratio of about 3 and aligned with the vessel axis, has the potential to reduce the surface plume sediment concentration. Again, a full investigation is needed to reveil under which conditions the efficiency of different shapes and aspect ratios is significant.

11.2 Grey-box parameter model

A grey-box model was developed, based both on theoretical plume solutions and multivariate regression. The regression parameters have been fitted to a large data set of CFD simulations. The grey-box model is less accurate than the CFD model, but it is much faster (order of magnitude of seconds). However, the parameter model predicts the sediment flux in the overflow plume still with reasonable accuracy.

The grey-box model is therefore specifically well-suited to be applied in situations where limited time is available. These situations include real-time forecasting simulations of overflow turbidity throughout the wider area around a dredging project. In such situations, the tidal flow velocity and water depth can vary, and thus varying boundary conditions for the near-field plume simulations are needed. This can only be achieved in a real-time forecasting model when a simple near-field plume prediction module can be implemented

in the large-scale tidal model. The parameter model presented above would be suited for this application.

The parameters in the grey-box model were fitted based on a wide range of boundary conditions. Within this range of conditions, the model is valid.

11.3 Recommendations

1. For future environmental impact assessments of overflow dredging plumes, it is recommended to perform near-field modelling first, before applying the sediment fluxes in a far-field turbidity model. Either a process-based CFD model or a parameterised model can be applied to this end.

2. Even though the validation cases show that the CFD model can reproduce the overflow plumes observed in the field with good accuracy, more in situ measurements are required in different circumstances to complete the validation of the model.

3. Different shapes of the overflow shaft cross-section seem to have a potential to reduce the surface plume sediment concentrations. However, a detailed analysis of the potential improvement by using different shapes under different boundary conditions is required.

4. Similarly, it is confirmed that an overflow extension has the potential to reduce surface plume concentrations. However, a detailed efficiency study for the overflow extension is still lacking.

5. The CFD model could be applied to optimise multiple overflow control for the minimisation of turbidity during dredging.

6. An on-board application for on-line turbidity predictions is possible. With input data based on the dredger's log files, the grey-box model developed in this work can be converted to an operational (surface) plume predictor.

References

Andreopoulos, J. (1985). On the structure of jets in a crossflow. *Journal of Fluid Mechanics*, 157, 163–197.

Antonia, R., Chambers, A. and Hussain, A. (1980). Errors in simultaneous measurements of temperature and velocity in the outer part of a heated jet. *Physics of Fluids*, 23(5), 871–874.

Argus (2007). *Argus Surface Meter*.

Armaly, B. F., Durst, F., Pereira, J. and Schönung, B. (1983). Experimental and theoretical investigation of backward-facing step flow. *Journal of Fluid Mechanics*, 127, 473–496.

Becker, J., van Eekelen, E., van Wiechen, J., de Lange, W., Damsma, T., Smolders, T. and van Koningsveld, M. (2015). Estimating source terms for far field dredge plume modelling. *Journal of environmental management*, 149, 282–293.

Bel F'Dhila, R. and Simonin, O. (1992). Eulerian prediction of a turbulent bubbly flow downstream a sudden pipe expansion. In *Sixth workshop on two-phase flow prediction, Erlangen*.

Black, K. P. and Parry, G. D. (1999). Entrainment, dispersal, and settlement of scallop dredge sediment plumes: field measurements and numerical modelling. *Canadian Journal of fisheries and aquatic sciences*, 56(12), 2271–2281.

Bray, R. N. (2008). *Environmental aspects of dredging*. CRC Press.

Breugem, W., Bollen, M., Sas, M. and Vandenbroeck, J. (2009). A field survey of a dredging plume during gravel mining. In *CEDA Dredging Days 2009 - Dredging Tools for the Future, Rotterdam*.

Breugem, W. and Uijttewaal, W. (2007). Sediment transport by coherent structures in a turbulent open channel flow experiment. In *Particle-Laden Flow*, pages 43–55. Springer.

Breugem, W. A. (2012). *Transport of suspended particles in turbulent open channel flows*. Ph.D. thesis, Delft University of Technology.

Cambonie, T. and Aider, J.-L. (2014). Transition scenario of the round jet in crossflow topology at low velocity ratios. *Physics of Fluids*, 26(8), 084101. doi:http://dx.doi.org/10.1063/1.4891850.

Cambonie, T., Gautier, N. and Aider, J.-L. (2013). Experimental study of counter-rotating vortex pair trajectories induced by a round jet in crossflow at low velocity ratios. *Experiments in Fluids*, 54(3), 1–13.

Carrica, P., Drew, D., Bonetto, F. and Lahey Jr, R. (1999). A polydisperse model for bubbly two-phase flow around a surface ship. *International journal of multiphase flow*, 25(2), 257–305.

Celik, I., Cehreli, Z. and Yavuz, I. (2005). Index of resolution quality for large eddy simulations. *Journal of Fluids Engineering*, 127(5), 949–958.

Celik, I. and Rodi, W. (1988). Modeling suspended sediment transport in nonequilibrium situations. *Journal of Hydraulic Engineering*, 114(10), 1157–1191.

Cellino, M. (1998). *Experimental study of suspension flow in open channels*. Ph.D. thesis, EPFL.

Cellino, M. and Graf, W. (2000). Experiments on suspension flow in open channels with bed forms. *Journal of Hydraulic Research*, 38(4), 289–298.

Chanson, H. (1996). *Air bubble entrainment in free-surface turbulent shear flows*. Academic Press.

Chanson, H., Trevethan, M. and Aoki, S. (2008). Acoustic Doppler velocimetry (ADV) in small estuary: Field experience and signal post-processing. *Flow Measurement and Instrumentation*, 19(5), 307–313.

Chowdhury, M. R. and Testik, F. Y. (2014). Axisymmetric underflows from impinging buoyant jets of dense cohesive particle-laden fluids. *Journal of Hydraulic Engineering*.

CoastlineSurveys (1998). Marine aggregate mining benthic and surface plume study. report prepared by arc marine ltd, south coast shipping company ltd, united marine dredging ltd and hr wallingford.

Cortelezzi, L. and Karagozian, A. R. (2001). On the formation of the counter-rotating vortex pair in transverse jets. *Journal of Fluid Mechanics*, 446, 347–373.

Coussement, A., Gicquel, O., Degrez, G. *et al.* (2012). Large eddy simulation of a pulsed jet in cross-flow. *Journal of Fluid Mechanics*, 695, 1–34.

Crowe, C. (1982). Review of numerical models for dilute gas-particle flows. *Journal of Fluids Engineering*, 104(3), 297–303.

Cushman-Roisin, B. (2010). *Environmental Fluid Mechanics*. Wiley.

Dai, Z., Tseng, L. and Faeth, G. (1994a). Structure of round, fully developed, buoyant turbulent plumes. *ASME Transactions Journal of Heat Transfer*, 116, 409–417.

Dai, Z., Tseng, L. and Faeth, G. (1994b). Velocity statistics of round, fully developed, buoyant turbulent plumes. *Transactions of the ASME-Journal of Heat Transfer*, 117(1), 138–145.

Dai, Z., Tseng, L. and Faeth, G. (1995). Velocity/mixture fraction statistics of round, self-preserving, buoyant turbulent plumes. *Transactions of the ASME-Journal of Heat Transfer*, 117, 918–926.

de Wit, L. (2015). *3D CFD modelling of overflow dredging plumes*. Ph.D. thesis, Delft University of Technology.

de Wit, L., Talmon, A. and van Rhee, C. (2014a). 3D CFD simulations of trailing suction hopper dredger plume mixing: Comparison with field measurements. *Marine pollution bulletin*, 88(1), 34–46.

de Wit, L., van Rhee, C. and Keetels, G. (2014b). Turbulent interaction of a buoyant jet with cross-flow. *Journal of Hydraulic Engineering*, 140(12).

de Wit, L., van Rhee, C. and Talmon, A. (2014c). Influence of important near field processes on the source term of suspended sediments from a dredging plume caused by a trailing suction hopper dredger: the effect of dredging speed, propeller, overflow location and pulsing. *Environmental Fluid Mechanics*, pages 1–26.

Decrop, B., De Mulder, T. and Toorman, E. (2012a). Mean and fluctuating suspended sediment concentration measurements using ADV. In *Hydraulic Measurement and Experimental Method conference 2012*, pages 1–6.

Decrop, B., De Mulder, T., Toorman, E. and Sas, M. (2015a). New methods for ADV measurements of turbulent sediment fluxes - application to a fine sediment plume. *Journal of Hydraulic Research*, 53(3), 317–331. doi: 10.1080/00221686.2015.1037871.

Decrop, B., De Mulder, T., Troch, P., Toorman, E. and Sas, M. (2012b). Experimental investigation of negatively buoyant sediment plumes resulting from dredging operations. In *Coastlab 2012, Proceedings, 573-582*.

Decrop, B., Mulder, T. D., Toorman, E. and Sas, M. (2015b). Large-eddy simulations of turbidity plumes in crossflow. *European Journal of Mechanics - B/Fluids*, 53(0), 68 – 84. ISSN 0997-7546. doi:http://dx.doi.org/10.1016/j.euromechflu.2015.03.013.

Decrop, B., Mulder, T. D., Toorman, E. and Sas, M. (2015c). Numerical simulation of near-field dredging plumes: the efficiency of an environmental valve. *Journal of Environmental Engineering*.

Decrop, B. and Sas, M. (2014). Challenges in the acoustic measurements of dredging plumes. In *Particles in Europe 2014*, pages 35–41.

Decrop, B., Sas, M., De Mulder, T. and Toorman, E. (2013). Physical modelling based assessment of some influence factors on overflow plume behaviour. In *WODCON XX*.

Decrop, B., Sas, M., De Mulder, T. and Toorman, E. (2014). Large-eddy simulations of a sediment-laden buoyant jet resulting from dredgers using overflow. In *International Conference on Hydroscience and Engineering*, pages 737–744.

Diez, F., Bernal, L. and Faeth, G. (2005). PLIF and PIV measurements of the self-preserving structure of steady round buoyant turbulent plumes in crossflow. *International journal of heat and fluid flow*, 26(6), 873–882.

Dimitrova, D. N. *et al.* (2011). *On the reliability of large-eddy simulation for dispersed two-phase flows*. Ph.D. thesis, TU Darmstadt.

Doherty, J., Ngan, P., Monty, J. and Chong, M. (2007). The development of turbulent pipe flow. In *16th Australasian fluid mechanics conference, University of Queensland, Brisbane*, pages 266–270.

Douglas, J., Gasiorek, J. and Swaffield, J. (1995). Fluid mechanics (essex: Longman scientific & technical).

DRLsoftware (2003). Sediview user guide v3.

Einstein, A. (1906). Effect of suspended rigid spheres on viscosity. *Ann. Phys*, 19, 289–306.

Elçi, S., Aydın, R. and Work, P. (2009). Estimation of suspended sediment concentration in rivers using acoustic methods. *Environmental monitoring and assessment*, 159(1-4), 255–265.

Elghobashi, S. (1994). On predicting particle-laden turbulent flows. *Applied Scientific Research*, 52(4), 309–329.

Elliott, W. P. (1958). The growth of the atmospheric internal boundary layer. *Eos, Transactions American Geophysical Union*, 39(6), 1048–1054.

Ervine, D. (1998). Air entrainment in hydraulic structures: A review. *Proceedings of the ICE-Water Maritime and Energy*, 130(3), 142–153.

Fettweis, M., Francken, F., Van den Eynde, D., Verwaest, T., Janssens, J. and Van Lancker, V. (2010). Storm influence on SPM concentrations in a coastal turbidity maximum area with high anthropogenic impact (southern north sea). *Continental Shelf Research*, 30(13), 1417–1427.

Fischer, H. (1979). *Mixing in inland and coastal waters*. Academic Press.

Fric, T. and Roshko, A. (1994). Vortical structure in the wake of a transverse jet. *Journal of Fluid Mechanics*, 279(1), 1–47.

Galerpin, B. and Orszag, S. (1996). Large eddy simulation of complex engineering and geophysical flows. *Phys D*, 98, 481–491.

García, C. M., Cantero, M. I., Niño, Y. and García, M. H. (2005). Turbulence measurements with acoustic Doppler velocimeters. *Journal of Hydraulic Engineering*, 131(12), 1062–1073.

George Jr, W., Alpert, R. and Tamanini, F. (1977). Turbulence measurements in an axisymmetric buoyant plume. *International Journal of Heat and Mass Transfer*, 20(11), 1145–1154.

Germano, M., Piomelli, U., Moin, P. and Cabot, W. H. (1991). A dynamic subgrid-scale eddy viscosity model. *Physics of Fluids A: Fluid Dynamics (1989-1993)*, 3(7), 1760–1765.

Goring, D. and Nikora, V. (2002). Despiking acoustic Doppler velocimeter data. *Journal of Hydraulic Engineering*, 128, 117.

Gratiot, N., Mory, M. and Auchere, D. (2000). An acoustic Doppler velocimeter (ADV) for the characterisation of turbulence in concentrated fluid mud. *Continental Shelf Research*, 20(12), 1551–1567.

Ha, H., Hsu, W., Maa, J., Shao, Y. and Holland, C. (2009). Using ADV backscatter strength for measuring suspended cohesive sediment concentration. *Continental Shelf Research*, 29(10), 1310–1316.

Hanes, D. M. (2012). On the possibility of single-frequency acoustic measurement of sand and clay concentrations in uniform suspensions. *Continental Shelf Research*, 46, 64–66.

Haven, B. and Kurosaka, M. (1997). Kidney and anti-kidney vortices in crossflow jets. *Journal of Fluid Mechanics*, 352, 27–64.

Hay, A. E. (1991). Sound scattering from a particle-laden, turbulent jet. *The Journal of the Acoustical Society of America*, 90(4), 2055–2074.

Hinze, J. (1975). Turbulence, McGraw-Hill. *New York*.

Hitchcock, D. R. and Bell, S. (2004). Physical impacts of marine aggregate dredging on seabed resources in coastal deposits. *Journal of Coastal Research*, pages 101–114.

Hoitink, A. and Hoekstra, P. (2005). Observations of suspended sediment from ADCP and OBS measurements in a mud-dominated environment. *Coastal engineering*, 52(2), 103–118.

Hosseini, S., Shamsai, A. and Ataie-Ashtiani, B. (2006). Synchronous measurements of the velocity and concentration in low density turbidity currents using an Acoustic Doppler Velocimeter. *Flow Measurement and Instrumentation*, 17(1), 59–68.

Hough, G. and Ordway, D. (1964). The generalized actuator disk. Technical report, DTIC Document.

Hsu, C. M. and Huang, R. F. (2012). Effects of crossflow on puff and oscillation modes of a pulsed elevated transverse jet. *European Journal of Mechanics - B/Fluids*, 31(0), 140 – 148. ISSN 0997-7546. doi: http://dx.doi.org/10.1016/j.euromechflu.2011.09.003.

Hunt, J. C., Wray, A. and Moin, P. (1988). Eddies, streams, and convergence zones in turbulent flows. In *Studying Turbulence Using Numerical Simulation Databases, 2*, volume 1, pages 193–208.

Ishii, M. and Hibiki, T. (2006). Thermo-fluid dynamics.

Issa, R. I. (1986). Solution of the implicitly discretised fluid flow equations by operator-splitting. *Journal of computational physics*, 62(1), 40–65.

Jensen, J. H. and Saremi, S. (2014). Overflow concentration and sedimentation in hoppers. *Journal of Waterway, Port, Coastal, and Ocean Engineering*, 140(6).

Kaltenbach, H.-J. (2004). Turbulent flow over a swept backward-facing step. *European Journal of Mechanics - B/Fluids*, 23(3), 501 – 518. ISSN 0997-7546. Invited papers from the 9th EUROMECH European Turbulence Conference.

Kashinsky, O. and Randin, V. (1999). Downward bubbly gas–liquid flow in a vertical pipe. *International journal of multiphase flow*, 25(1), 109–138.

Kaye, N. (2008). Turbulent plumes in stratified environments: a review of recent work. *Atmosphere-Ocean*, 46(4), 433–441.

Kaye, N. and Linden, P. (2004). Coalescing axisymmetric turbulent plumes. *Journal of Fluid Mechanics*, 502, 41–63.

Kelso, R. M., Lim, T. and Perry, A. E. (1996). An experimental study of round jets in cross-flow. *Journal of Fluid Mechanics*, 306, 111–144.

Khorsandi, B., Mydlarski, L. and Gaskin, S. (2012). Noise in turbulence measurements using Acoustic Doppler velocimetry. *Journal of Hydraulic Engineering*, 138(10), 829–838.

Kim, S. *et al.* (2004). Large eddy simulation using unstructured meshes and dynamic subgrid-scale turbulence models. *AIAA paper*, 2548, 2004.

Kim, S.-E. (2004). Large eddy simulation using an unstructured mesh based finite-volume solver. In *34th AIAA fluid dynamics conference and exhibit*, volume 2548, pages 1–7. Portland.

Kim, W.-W. and Menon, S. (1997). Application of the localized dynamic subgrid-scale model to turbulent wall-bounded flows. *AIAA Paper No. AIAA-97-0210*.

Kolář, V. (2007). Vortex identification: New requirements and limitations. *International Journal of Heat and Fluid Flow*, 28(4), 638–652.

Kolmogorov, A. N. (1941). The local structure of turbulence in incompressible viscous fluid for very large reynolds numbers. In *Dokl. Akad. Nauk SSSR*, volume 30, pages 299–303.

Kotsovinos, N. E. (1991). Turbulence spectra in free convection flow. *Physics of Fluids A: Fluid Dynamics (1989-1993)*, 3(1), 163–167.

Kumar, S., Nikitopoulos, D. and Michaelides, E. (1989). Effect of bubbles on the turbulence near the exit of a liquid jet. *Experiments in fluids*, 7(7), 487–494.

Lam, W., Hamill, G., Robinson, D., Raghunathan, S. *et al.* (2011). Experimental investigation of the decay from a ship's propeller. *China Ocean Engineering*, 25(2), 265–284.

Lam, W., Robinson, D., Hamill, G., Raghunathan, S., Kee, C. *et al.* (2006). Simulations of a ship's propeller wash. In *The Sixteenth International Offshore and Polar Engineering Conference*. International Society of Offshore and Polar Engineers.

Lam, W.-H., Hamill, G., Robinson, D. and Raghunathan, S. (2010). Observations of the initial 3D flow from a ship's propeller. *Ocean Engineering*, 37(14), 1380–1388.

Law, A. and Wang, H. (2000). Measurement of mixing processes with combined digital particle image velocimetry and planar laser induced fluorescence. *Experimental thermal and fluid science*, 22(3-4), 213–229.

Lee, J. and Chu, V. (2003). *Turbulent jets and plumes: A Lagrangian approach*. Springer.

Lee, J. H. and Cheung, V. (1990). Generalized Lagrangian model for buoyant jets in current. *Journal of Environmental Engineering*, 116(6), 1085–1106.

Leggett, D., Black, K. and KM, R. (2013). Environmental monitoring and control of sediments around dredging and reclamation works, thames, uk. In *WODCON XX*.

Lelouvetel, J., Tanaka, T., Sato, Y. and Hishida, K. (2014). Transport mechanisms of the turbulent energy cascade in upward/downward bubbly flows. *Journal of Fluid Mechanics*, 741, 514–542.

Lemmin, U., Lhermitte, R., Nikora, V. and Goring, D. (1999). ADV measurements of turbulence: Can we improve their interpretation? *Journal of Hydraulic Engineering*, 125, 987.

Leonard, A. (1974). Energy cascade in large-eddy simulations of turbulent fluid flows. In *Turbulent Diffusion in Environmental Pollution*, volume 1, pages 237–248.

Leonard, B. and Mokhtari, S. (1990). Beyond first-order upwinding: The ultra-sharp alternative for non-oscillatory steady-state simulation of convection. *International Journal for Numerical Methods in Engineering*, 30(4), 729–766.

Lewis, R. (1997). *Dispersion in estuaries and coastal waters*. Wiley Chichester, UK.

Lilly, D. (1992). A proposed modification of the Germano subgrid-scale closure method. *Physics of Fluids A: Fluid Dynamics*, 4, 633.

Lim, T., New, T. and Luo, S. (2001). On the development of large-scale structures of a jet normal to a cross flow. *Physics of Fluids (1994-present)*, 13(3), 770–775.

Lipari, G. and Stansby, P. K. (2011). Review of experimental data on incompressible turbulent round jets. *Flow, turbulence and combustion*, 87(1), 79–114.

Lohrmann, A., Cabrera, R., Kraus, N. *et al.* (1994). Acoustic-Doppler velocimeter (ADV) for laboratory use. In *Proc. Conf. on Fundamentals and Advancements in Hydraulic Measurements and Experimentation*, pages 351–365.

Lopez, R. J. (2001). *Advanced engineering mathematics*, volume 1158. Addison-Wesley.

Manninen, M., Taivassalo, V., Kallio, S. *et al.* (1996). *On the mixture model for multiphase flow*. Technical Research Centre of Finland.

Manning, A. and Dyer, K. (2007). Mass settling flux of fine sediments in Northern European estuaries: measurements and predictions. *Marine Geology*, 245(1), 107–122.

Mathey, F., Cokljat, D., Bertoglio, J.-P., Sergent, E. *et al.* (2006). Specification of LES inlet boundary condition using vortex method. *Progress in Computational Fluid Dynamics*, 6, 58–67.

Medwin, H. and Blue, J. (2005). *Sounds in the sea: From ocean acoustics to acoustical oceanography*. Cambridge University Press.

Mehta, A. J., Hayter, E. J., Parker, W. R., Krone, R. B. and Teeter, A. M. (1989). Cohesive sediment transport. I: Process description. *Journal of Hydraulic Engineering*, 115(8), 1076–1093.

Merckelbach, L. and Ridderinkhof, H. (2006). Estimating suspended sediment concentration using backscatterance from an acoustic Doppler profiling current meter at a site with strong tidal currents. *Ocean Dynamics*, 56(3), 153–168.

Meyers, J. and Sagaut, P. (2006). On the model coefficients for the standard and the variational multi-scale Smagorinsky model. *Journal of Fluid Mechanics*, 569, 287–319.

Morsi, S. and Alexander, A. (1972). An investigation of particle trajectories in two-phase flow systems. *Journal of Fluid Mechanics*, 55(02), 193–208.

Morton, B., Taylor, G. and Turner, J. (1956). Turbulent gravitational convection from maintained and instantaneous sources. *Proceedings of the Royal Society of London. Series A. Mathematical and Physical Sciences*, 234(1196), 1.

Muldoon, F. and Acharya, S. (2010). Direct numerical simulation of pulsed jets-in-crossflow. *Computers & Fluids*, 39(10), 1745–1773.

Muppidi, S. and Mahesh, K. (2007). Direct numerical simulation of round turbulent jets in crossflow. *Journal of Fluid Mechanics*, 574, 59–84.

Muppidi, S. and Mahesh, K. (2008). Direct numerical simulation of passive scalar transport in transverse jets. *Journal of Fluid Mechanics*, 598, 335–360.

Neto, I. E. L., Zhu, D. Z. and Rajaratnam, N. (2008). Bubbly jets in stagnant water. *International Journal of Multiphase Flow*, 34(12), 1130–1141.

Newell, R., Hitchcock, D. and Seiderer, L. (1999). Organic enrichment associated with outwash from marine aggregates dredging: a probable explanation for surface sheens and enhanced benthic production in the vicinity of dredging operations. *Marine Pollution Bulletin*, 38(9), 809–818.

Nicoud, F. and Ducros, F. (1999). Subgrid-scale stress modelling based on the square of the velocity gradient tensor. *Flow, turbulence and Combustion*, 62(3), 183–200.

Nieuwstadt, F. (1998). Turbulentie. *Theorie en toepassingen van turbulente stromingen. Epsilon Uitgaven*.

Nikora, V. and Goring, D. (2002). Fluctuations of suspended sediment concentration and turbulent sediment fluxes in an open-channel flow. *Journal of Hydraulic Engineering*, 128(2), 214–224.

Odar, F. and Hamilton, W. S. (1964). Forces on a sphere accelerating in a viscous fluid. *Journal of Fluid Mechanics*, 18(02), 302–314.

O'Rourke, P. J. (1981). *Collective drop effects on vaporizing liquid sprays*. Ph.D. thesis, Princeton University, Princeton.

Panchapakesan, N. and Lumley, J. (1993). Turbulence measurements in axisymmetric jets of air and helium. part 1. air jet. *Journal of Fluid Mechanics*, 246, 197–223.

Papanicolaou, P. and List, E. (1988). Investigations of round vertical turbulent buoyant jets. *Journal of Fluid Mechanics*, 195, 341–391.

Parthasarathy, R. and Faeth, G. (1990). Turbulence modulation in homogeneous dilute particle-laden flows. *Journal of Fluid Mechanics*, 220, 485–514.

Parthasarathy, R. and Faeth, G. M. (1987). Structure of particle-laden turbulent water jets in still water. *International journal of multiphase flow*, 13(5), 699–716.

Peterson, S. and Plesniak, M. (2004). Evolution of jets emanating from short holes into crossflow. *Journal of Fluid Mechanics*, 503, 57–91.

Pham, M. V., Plourde, F. and Kim, S. D. (2006). Effect of swirl on pure turbulent thermal plume development. *International journal of heat and fluid flow*, 27(3), 502–513.

PIANC (2010). Port construction around coral reefs. *United Nations Environment Programme World Conservation Monitoring Centre*.

PIANC (2014). Harbour approach channels-design guidelines. *Maritime Navigation Commision*, 121.

Poindexter, C., Rusello, P. and Variano, E. (2011). Acoustic Doppler velocimeter-induced acoustic streaming and its implications for measurement. *Experiments in fluids*, 50(5), 1429–1442.

Pope, S. B. (2004). Ten questions concerning the large-eddy simulation of turbulent flows. *New Journal of Physics*, 6(1), 35.

Rayleigh, J. (1945). The theory of sound, vols. 1 and 2.

Recker, E., Bosschaerts, W. and Hendrick, P. (2009). Large eddy simulation of mixing in a round jet in crossflow. In *39th AIAA Fluid Dynamic conference, San Antonio, Texas. AIAA 2009-3561.*.

Romagnoli, M., García, C. and Lopardo, R. (2012). Signal postprocessing technique and uncertainty analysis of ADV turbulence measurements on free hydraulic jumps. *Journal of Hydraulic Engineering*, 138(4), 353–357.

Rusello, P. (2009). A practical primer for pulse coherent instruments. *Nortek Technical Notes*, (TN-027).

Saffman, P. (1965). The lift on a small sphere in a slow shear flow. *Journal of fluid mechanics*, 22(02), 385–400.

Salehi, M. and Strom, K. (2009). Suspended sediment concentration measurements of muddy sediments with an ADV. In *World Environmental and Water Resources Congress 2009@ Great Rivers*, pages 1–7. ASCE.

Salehi, M. and Strom, K. (2011). Using velocimeter signal to noise ratio as a surrogate measure of suspended mud concentration. *Continental Shelf Research*, 31(9), 1020–1032.

Salewski, M., Stankovic, D. and Fuchs, L. (2008). Mixing in circular and non-circular jets in crossflow. *Flow, Turbulence and Combustion*, 80(2), 255–283.

Sangras, R., Kwon, O. and Faeth, G. (2002). Self-preserving properties of unsteady round nonbuoyant turbulent starting jets and puffs in still fluids. *Journal of heat transfer*, 124, 460.

Saremi, S. and Jensen, J. H. (2014a). Multiphase CFD modeling of nearfield fate of sediment plumes. In *3rd IAHR Europe Congress*.

Saremi, S. and Jensen, J. H. (2014b). Numerical modelling of the effect of the green valve on air entrainment at hopper overflow. *Coastal Engineering Proceedings*, 1(34), posters–21.

Sassi, M., F Hoitink, A. and Vermeulen, B. (2013). Quantified turbulent diffusion of suspended sediment using acoustic Doppler current profilers. *Geophysical Research Letters*, 40(21), 5692–5697.

Schlichting, H. (1979). *Boundary-Layer Theory*. Mc-Graw-Hill Book Company, New York.

Shabbir, A. and George, W. (1992). *Experiments on a round turbulent buoyant plume*. Lewis Research Center, Institute for Computational Mechanics in Propulsion.

Sheen, H., Jou, B. and Lee, Y. (1994). Effect of particle size on a two-phase turbulent jet. *Experimental Thermal and Fluid Science*, 8(4), 315–327.

Smagorinsky, J. (1963). General circulation experiments with the primitive equations: I. the basic experiment. *Monthly weather review*, 91(3), 99–164.

Smith, S. and Friedrichs, C. (2011). Size and settling velocities of cohesive flocs and suspended sediment aggregates in a trailing suction hopper dredge plume. *Continental Shelf Research*, 31(10), S50–S63.

Smith, S. and Mungal, M. (1998). Mixing, structure and scaling of the jet in crossflow. *Journal of Fluid Mechanics*, 357(1), 83–122.

Socolofsky, S. and Adams, E. (2002). Multi-phase plumes in uniform and stratified crossflow. *Journal of Hydraulic Research*, 40(6), 661–672.

Socolofsky, S. A. (2001). *Laboratory experiments of multi-phase plumes in stratification and crossflow*. Ph.D. thesis, Massachusetts Institute of Technology.

Spalding, D. B. (1981). A general purpose computer program for multi-dimensional one-and two-phase flow. *Mathematics and computers in simulation*, 23(3), 267–276.

Su, L. and Mungal, M. (2004). Simultaneous measurements of scalar and velocity field evolution in turbulent crossflowing jets. *Journal of Fluid Mechanics*, 513, 1–45.

Sykes, R., Lewellen, W. and Parker, S. (1986). On the vorticity dynamics of a turbulent jet in a crossflow. *Journal of Fluid Mechanics*, 168, 393–413.

Talaia, M. A. (2007). Terminal velocity of a bubble rise in a liquid column. *World Academy of Science, Engineering and Technology*, 28, 264–268.

Tennekes, H. and Lumley, J. (1972). *A first course in turbulence*. The MIT press.

Thorne, P. and Hanes, D. (2002). A review of acoustic measurement of small-scale sediment processes. *Continental Shelf Research*, 22(4), 603–632.

Thorne, P. D. and Campbell, S. C. (1992). Backscattering by a suspension of spheres. *The Journal of the Acoustical Society of America*, 92(2), 978–986.

Tian, X. and Roberts, P. J. (2003). A 3D LIF system for turbulent buoyant jet flows. *Experiments in fluids*, 35(6), 636–647.

Tomiyama, A., Kataoka, I., Zun, I. and Sakaguchi, T. (1998). Drag coefficients of single bubbles under normal and micro gravity conditions. *JSME International Journal Series B*, 41(2), 472–479.

Toorman, E. A. (2008). Vertical mixing in the fully developed turbulent layer of sediment-laden open-channel flow. *Journal of hydraulic engineering*, 134(9), 1225–1235.

Townsend, A. (1976). *The structure of turbulent shear flow*. Cambridge Univ Pr.

Van Eekelen, E. (2007). *Experimental research on dynamic dredge overflow plumes*. TU Delft, Delft University of Technology.

Van Parys, M., Dumon, G., Pieters, A., Claeys, S., Lanckneus, J., Van Lancker, V., Vangheluwe, M., Van Sprang, P., Speleers, L. and Janssen, C. (2001). Environmental monitoring of the dredging and relocation operations in the coastal harbours in Belgium. In *Proceedings of the XVIth World Dredging Congress Dredging for Prosperity, Achieving Social and Economic Benefits, 14 pp*.

van Rhee, C. (2002). *On the sedimentation process in a trailing suction hopper dredger*. Ph.D. thesis, Delft University of Technology.

van Rijn, L. C. (1993). *Principles of sediment transport in rivers, estuaries and coastal seas*. Aqua publications, Amsterdam, The Netherlands.

Vermeulen, B., Hoitink, A. and Sassi, M. (2011). Coupled ADCPs can yield complete reynolds stress tensor profiles in geophysical surface flows. *Geophysical Research Letters*, 38(6).

Veron, F. and Melville, W. (1999). Pulse-to-pulse coherent Doppler measurements of waves and turbulence. *Journal of Atmospheric and Oceanic Technology*, 16(11), 1580–1597.

Versteeg, H. K. and Malalasekera, W. (2007). *An introduction to computational fluid dynamics: the finite volume method*. Prentice Hall.

Viollet, P. and Simonin, O. (1994). Modelling dispersed two-phase flows: closure, validation and software development. *Applied Mechanics Reviews*, 47(6S), S80–S84.

Visonneau, M., Queutey, P. and Deng, G. (2006). Model and full-scale free-surface viscous flows around fully-appended ships. In *Proceedings of the European Conference on Computational fluid dynamics (ECCOMAS CFD), Egmond aan Zee, The Netherlands*, pages 5–8.

Voulgaris, G. and Trowbridge, J. (1998). Evaluation of the Acoustic Doppler Velocimeter (ADV) for turbulence measurements. *Journal of atmospheric and oceanic technology*, 15(1), 272–289.

Wahl, T. (2003). Discussion of despiking Acoustic Doppler Velocimeter data by derek g. goring and vladimir i. nikora. *Journal of Hydraulic Engineering*, 129, 484.

Walters, D. and Leylek, J. (2000). A detailed analysis of film-cooling physics: part I - streamwise injection with cylindrical holes. *Journal of turbomachinery*, 122(1), 102–112.

Webb, A. and Mansour, N. (2000). Towards LES models of jets and plumes. *Center for Turbulence Research, Annual Research Briefs*, 2000, 229–240.

Westerweel, J., Fukushima, C., Pedersen, J. and Hunt, J. (2009). Momentum and scalar transport at the turbulent/non-turbulent interface of a jet. *J. Fluid Mech*, 631, 199–230.

Wilkinson, D. and Wood, I. (1971). A rapidly varied flow phenomenon in a two-layer flow. *Journal of Fluid Mechanics*, 47(02), 241–256.

Williams, E. and Simpson, J. H. (2004). Uncertainties in estimates of reynolds stress and TKE production rate using the ADCP variance method. *Journal of Atmospheric and Oceanic Technology*, 21(2), 347–357.

Winterwerp, J., Manning, A., Martens, C., De Mulder, T. and Vanlede, J. (2006). A heuristic formula for turbulence-induced flocculation of cohesive sediment. *Estuarine, Coastal and Shelf Science*, 68(1), 195–207.

Worthy, J. (2003). Large eddy simulation of buoyant plumes.

Wright, S. J. (1977). Effects of ambient crossflows and density stratification on the characteristic behavior of round, turbulent buoyant jets.

Wright, S. J. (1984). Buoyant jets in density-stratified crossflow. *Journal of Hydraulic Engineering*, 110(5), 643–656.

Xu, G. and Antonia, R. (2002). Effect of different initial conditions on a turbulent round free jet. *Experiments in fluids*, 33(5), 677–683.

Yuan, L. L., Street, R. L. and Ferziger, J. H. (1999). Large-eddy simulations of a round jet in crossflow. *Journal of Fluid Mechanics*, 379, 71–104.

Zedel, L., Hay, A., Cabrera, R. and Lohrmann, A. (1996). Performance of a single-beam pulse-to-pulse coherent Doppler profiler. *Oceanic Engineering, IEEE Journal of*, 21(3), 290–297.

Zhang, W. (2012). *Air injection for river water quality improvement*. Ph.D. thesis, University of Alberta.

Zhang, W. and Zhu, D. Z. (2013). Bubble characteristics of air–water bubbly jets in crossflow. *International Journal of Multiphase Flow*, 55, 156–171.

Zhou, X., Luo, K. H. and Williams, J. J. (2001). Large-eddy simulation of a turbulent forced plume. *European Journal of Mechanics-B/Fluids*, 20(2), 233–254.

Zimmermann, N., Melotte, J., Breugem, W., Sas, M. and Lehay, D. (2010). Monitoring the behaviour of sediments disposed by a TSHD in the external estuary of the loire. In *WODCON XIX, Beijing, China*.

Zorn, T., Heimann, J. and Bertram, V. (2006). CFD analysis of a ducts effectiveness for model scale and full scale. In *13th Numerical Towing Tank Symposium, 10-12 October, Duisburg, Germany*.

List of Symbols

a	Sediment particle radius (m)
A_d	Surface area of the actuator disk (m^2)
AMP	Backscatter amplitude (counts)
$a_{i,j}$	Element (i,j) of the ADV transformation matrix (-)
B_0	Initial overflow buoyancy flux (m^4/s^3)
B_r	Volume acoustic intensity (dB)
B_o	Lateral distance from overflow to ship axis (m)
b_c	Plume concentration half-width (m)
b_w	Plume velocity half-width (m)
C	Time-averaged suspended sediment concentration (mg/l)
C_D	Drag coefficient
C_s	Smagorinsky coefficient (-)
C_c	Centreline value of C (mg/l)
C_0	Overflow sediment concentration (g/l)
c_s	Speed of sound (m/s)
D	Plume source pipe diameter (m)
D_p	Propeller diameter (m)
d_a	Air bubble diameter (m)
$da, 0$	Initial air bubble diameter (m)
D_t	Turbulent mass diffusivity (m^2/s)
$E(f)$	Amplitude spectrum (unit of Fourier transformed quantity)
f	Frequency of the acoustic wave (Hz)
f_N	Nyquist frequency (Hz)
F_Δ	Densimetric Froude number (-)
F_∞	Densimetric Froude number, based on U_0 (-)
h_{ws}	Height of the BFS (m)
h_e	Length of the overflow extansion (m)
H_k	Under keel clearance (m)
H_d	Draft (m)
I	Volume backscatter (dB)
I_0	Emitted acoustic intensity (dB)

k	Acoustic wave number (m^{-1})
k	Turbulent kinetic energy (m^2/s^2)
k_{res}	Resolved turbulent kinetic energy (m^2/s^2)
k_{sgs}	Subgrid-scale turbulent kinetic energy (m^2/s^2)
l_M	Characteristic momentum length scale for buoyant jets (m)
L_o	Distance from overflow to stern (m)
L_s	Ship length (m)
M	Turbulence resolution (-)
M_0	Initial overflow momentum flux (m^4/s^2)
P	Propeller Power (W)
p_d	Pressure jump across the actuator disk (Pa)
R	Acoustic path length (m)
R_p	Propeller radius (m)
r/z	Radial distance in plume, relative to distance from source (-)
$\mathrm{Re_p}$	Pipe Reynolds number
$\mathrm{Re_w}$	Plume wake Reynolds number
s	Sub-grid activity (-)
SNR	Signal to noise ratio (dB)
$\mathrm{Sc_t}$	Turbulent Schmidt number (-)
S_a	Factor containing acoustic particle properties (-)
S_f	Factor containing ADV instrument properties (-)
S_y	Horizontally integrated dilution (-)
SVH	Sampling volume height ADV (mm)
TL	Pulse transmit length ADV (mm)
u, v, w	x,y and z direction velocity components (m/s)
u', v', w', c'	Fluctuations of u,v,w and c (m/s, mg/l)
u'_*, v'_*, w'_*	Uncorrected fluctuations of u,v,w (m/s)
U_0	Crossflow velocity magnitude (m/s)
U_a	Axial component of the propeller jet velocity (m/s)
U_t	Tangential component of the propeller jet velocity (m/s)
u_a	Velocity of the air phase (m/s)
u_d	Velocity at the actuator disk (m/s)
$u_{dr,s}$	Drift velocity of the sediment phase (m/s)
$u_{dr,w}$	Drift velocity of the water phase (m/s)
u_w	Velocity of the water phase (m/s)
u_s	Velocity of the sediment phase (m/s)
u_{sw}	Slip velocity of the sediment phase (m/s)
u_m	Velocity of the water-sediment mixture (m/s)
V'_d	Doppler noise (m/s)
w_c	Centreline vertical velocity in plume (m/s)
W_0	Overflow exit velocity magnitude (m/s)

x	Streamwise coordinate (m)
x_{ws}	x-position of the BFS (m)
y	Lateral coordinate (m)
y^*	Dimensionless lateral coordinate (-), eq.7.45
z	Vertical coordinate, along the pipe axis (m)
z	Vertical distance in plume from source (m)
$\overline{z}$	Level of the concentration maximum (m)
z^*	Dimensionless vertical coordinate (-), eq.7.46
z_m	Plume merging height (m)
z_M	Momentum height (m)
z_B	Buoyancy height (m)
z_C	Far field momentum height (m)

α_r	Sediment attenuation coefficient (-)
α_l	Water attenuation coefficient (-)
α_i	Amplification coefficient for Doppler noise in $\overline{u_i'^2}$ (-)
β	Merging plume density ratio (-)
δ	Wall boundary layer thickness (m)
$\Delta\rho = \rho_s - \rho$	Excess mass density of sediment in ambient fluid (kg/m^3)
Δ	LES grid filter width (m)
Δx_0	Multiple plume exit distance (m)
ΔX_t	Distance to the dredger along its trajectory (m)
ΔY_t	Perpendicular distance to the dredger trajectory (m)
ϵ_{ev}	Efficiency of the environmental valve (-)
ε	Turbulent dissipation (m^2/s^3)
ϕ	Sediment volume fraction (-)
ϕ_a	Volume fraction of air (-)
η	Kolmogorov length scale (m);
κ	Eddy wave number (1/m)
λ	Jet-to-crossflow velocity ratio (-)
Λ_s	Relative surface plume sediment discharge, eq.9.3 (-)
Λ_s^{ev}	Q_s with environmental valve (-)
Λ_s^{nev}	Q_s without environmental valve (-)
ν_t	Turbulent eddy viscosity (m^2/s)
μ_m	Molecular dynamic viscosity of water-sediment mixture (N s/m^2)
μ_w	Molecular dynamic viscosity of water (N s/m^2)
ω_z	Vertical component of the vorticity vector (1/s)
ρ_a	Mass density of air (kg/m^3)
ρ_s	Mass density of sediment (kg/m^3)

ρ_w	Mass density of ambient water (kg/m^3)
ρ_m	Mass density of water-sediment mixture (kg/m^3)
σ_{AMP}	Noise variance in the amplitude signal (dB)
τ_m	Molecular shear stress (N/m^2)
τ_{sgs}	Turbulent sub-grid scale shear stress (N/m^2
τ_w	Wall shear stress (Pa)
$(...)^*$	Nondimensionalised field-variables, eq.7.42-7.44
ξ	Self-similarity form of the horizontal distance, table 6.2
ζ	Self-similarity form of the vertical distance, table 6.2

List of Abbreviations

ADCP	Acoustic Doppler Current Profiler
BDFF	Buoyancy-Dominated Far Field
BDNF	Buoyancy-Dominated Near Field
BFS	Backward-Facing Step
CFD	Computational Fluid Dynamics
CFL	Coutant-Friedrichs-Lewy
CRVP	Counter-rotating Vortex Pair
DNS	Direct Numerical Simulation
FP	Field probe
LES	Large-Eddy Simulation
MDFF	Momentum-Dominated Far Field
MDNF	Momentum-Dominated Near Field
OBS	Optical BackScatter instrument
RANS	Reynolds-averaged Navier Stokes
RMSE	Root-Mean-Squared Error
SGS	Sub Grid Scale
SP	Sidelooking probe
TKE	Turbulent Kinetic Energy
TSHD	Trailing Suction Hopper Dredger
WALE	Wall-Adapted Local Eddy viscosity
WMLES	Wall Modelled LES
ZEF	Zone of Established Flow
ZFE	Zone of Flow Establishment

Acknowledgements

This work would not have been possible without the financial and moral support of many people.

First of all, I would like to give special thanks to Jos Smits and Marc Sas (IMDC). Without their decision to support this research project from the private sector, it could not have been started. After funding was granted and the project started, I have been grateful to them for allowing me to spend sufficient time to work on the research.

A special thanks goes out to my supervisors, prof. Tom De Mulder and prof. Erik Toorman, among many other things for their help with improving the many manuscripts for papers and this thesis. The toughest challenge while getting technical research published in international publications is not the research in itself, but the way to present it in a clear manner understandable for a wider public.

After initiating the project proposal from IMDC, the remaining funding was granted by IWT, due to which I should also thank the Belgian tax payer. However, the investments made for this project will be obviously returned by the valorisation of the project.

For the support in the initial stages of project proposal and project start-up, I wish to thank prof. Renaat De Sutter. He encouraged me to continue with the project application after funding was not obtained after first submission.

Further, I would like to express my gratitude to prof. Peter Troch and prof. Johan Meyers, members of the doctoral advisory committee, for sharing their ideas and measurement equipment with me. Members of the examination committee prof. Jean Berlamont, prof. Jacob Jensen, prof. Cees van Rhee and prof. Jan Vierendeels have also contributed by giving their comments

during the internal defence, which further increased the quality of this thesis.

I would like to thank Robert van de Ketterij, Dick Stander and Edwin Munts at Royal IHC Merwede, for their help with the TSHD geometry.

Also, the colleagues at the Hydraulics Laboratory at Ghent University have been great fun to spend time with during normal lunches but mainly during special (birthday) lunch parties, in which prof. Ronny Verhoeven was always a highly motivated participant. But of course also the other colleagues at the Laboratory: Davy, Dieter, Jan, Laurent, Rebecca, Sieglien, Stephan, Stefaan, Thomas, Tomas and Vicky. Thanks for all the fun we had and for the interesting talks over lunch.

Not to be forgotten: Stefaan Bliki and Davy Haerens, thanks for the assistance with the much needed adaptations to the flume in the sediment lab Tito. And also master students Stijn Bruggeman and Laurens Aelvoet: thanks for the assistance with performing that many experimental runs during your thesis research. Even after a pipe rupture in the lab, resulting in a mud bath and broken laptops, the two of you stayed motivated.

Last but not least, I have to express my special gratitude to Katrien, who endured me being out of temper at times, especially during the stressy months of writing this thesis. But, there is one advantage: one can only write one PhD thesis in his or her life!

With that said, I'll put an end to it.

Curriculum Vitae

In 2002, Boudewijn Decrop obtained a Master of Science degree in Industrial engineering at the KU Leuven, campus Groep T. He went on to obtain a Master of Science in Water Resources Engineering, a joint degree organized by the KU Leuven and the Free University of Brussels. After a period as a teaching assistant at the Hydraulics Laboratory at KU Leuven, he joined IMDC in 2006 where he conducted several studies in the field of hydraulic engineering.

In 2009, a research project on dredging plumes was conceived and in 2011 funding was obtained from IWT and IMDC. Boudewijn then started part-time doctoral research at the Hydraulics Laboratories at the universities of Ghent and Leuven. During the course of this research, he has authored eight articles in international journals and conference proceedings.

List of Publications

International Journal Articles

- Decrop, B., De Mulder, T., Toorman, E. and Sas, M. (2015a). New methods for ADV measurements of turbulent sediment fluxes - application to a fine sediment plume. *Journal of Hydraulic Research*. doi:10.1080/00221686.2015.1037871.

- Decrop, B., Mulder, T. D., Toorman, E. and Sas, M. (2015b). Large-eddy simulations of turbidity plumes in crossflow. *European Journal of Mechanics - B/Fluids*, 53, 68 - 84. ISSN0997-7546.
doi: http://dx.doi.org/10.1016/j.euromechflu.2015.03.013.

- Decrop, B., Mulder, T. D., Toorman, E. and Sas, M. (2015c). Numerical simulation of near-field dredging plumes: the efficiency of an environmental valve. *Journal of Environmental Engineering*.

International Conference Proceedings

- Decrop, B., De Mulder, T. and Toorman, E. (2012a). Mean and fluctuating suspended sediment concentration measurements using ADV. In: *Hydraulic Measurement and Experimental Method conference 2012* , pages 1-6.

- Decrop, B., De Mulder, T., Troch, P., Toorman, E. and Sas, M. (2012b). Experimental investigation of negatively buoyant sediment plumes resulting from dredging operations. In: *Coastlab 2012, Proceedings*, 573-582.

- Decrop, B. and Sas, M. (2014). Challenges in the acoustic measurements of dredging plumes. In: *Particles in Europe 2014* , pages 35 - 41.

- Decrop, B., Sas, M., De Mulder, T. and Toorman, E. (2013). Physical modelling-based assessment of some influence factors on overflow plume behaviour. In: *WODCON XX proceedings*.

- Decrop, B., Sas, M., De Mulder, T. and Toorman, E. (2014). Large-eddy simulations of a sediment-laden buoyant jet resulting from dredgers using overflow. In: *International Conference on Hydroscience and Engineering*, pages 737 - 744.